University
of Basel

Swiss Nanoscience Institute

SNI
Swiss Nanoscience Institute
Center of Excellence supported
by the University of Basel
and the Canton of Aargau

Annual Report 2024 Supplement

Swiss Nanoscience Institute

Contents

PhD projects

Nano-Argovia projects

Gold Nanoparticle Assemblies for Raman Visualization of Ovarian Cancer Cells

Project P1802: Gold nanoparticle assemblies for SERS based detection of EGFR expressing ovarian cancer cells in tumor xenografts.
Project Leaders: S. Saxer, S. McNeil, V. Heinzelmann, and F. Jacob
Collaborator: A. Stumpo (SNI PhD Student)

Introduction

Ovarian cancer (OC) is often referred to as the "silent killer" among women in Europe, as it accounts for more fatalities than any other malignancy of the female reproductive system. The main reason is that OC symptoms are often misattributed to other diseases, and as a result, it is diagnosed at a late stage when it is difficult to treat it. Despite its lethality, there are currently no effective screening techniques for ovarian cancer nor simple tests to diagnose it.[1]
To address this challenge, we employed Surface-Enhanced Raman Scattering (SERS) microscopy. This approach involves utilizing gold nanoparticles (AuNPs) functionalized with a Raman reporter molecule and anti-human epidermal growth factor receptor (EGFR) antibodies on their surface. These functionalized nanoparticles specifically target ovarian cancer (OC) cells that overexpress EGFR on their membrane, allowing differentiation from EGFR-negative OC cells. EGFR was selected as the target biomarker due to its overexpression in OC, which has been associated with poorer patient outcomes. Additionally, EGFR plays a critical role in tumor growth and resistance to radiotherapy and chemotherapy.[2] The Raman signal from the reporter molecule is significantly enhanced by the gold nanoparticles, enabling precise discrimination between cells with elevated EGFR expression and control cells. For our initial experimental cell line setup the following cell lines are employed: OVCAR5 and OVCAR8 that exhibit positive EGFR expression; TOV-112D that is EGFR-negative (Figure 1).

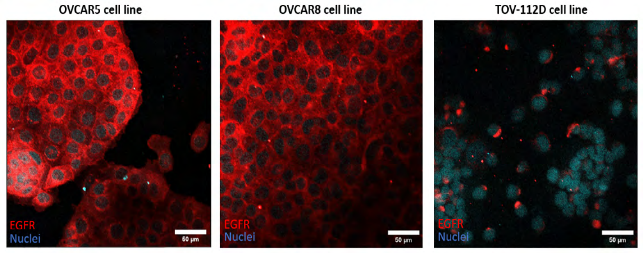

Figure 1: Confocal microscopy pictures of the EGFR expression of 3 selected ovarian cancer cell lines: OVCAR8, OVCAR5 and TOV-112D. OVCAR5 and OVCAR8 show a strong EGFR expression while TOV-112D is negative for EGFR, with some nonspecific staining. EGFR expression in red; Nuclei stained in blue. Scale bar: 50 µm.

However, to obtain a significant signal, it is necessary to fix the cells onto glass slides, as visualization in a buffer or cell culture media solution does not provide adequate signal intensity. Therefore, we use gold nanoparticles assemblies (aAuNPs) to achieve an increased sensitivity of Raman imaging in liquid. The assemblies are made of three key components: a) a cucurbit[7]uril/methyl viologen complex (CB[7]/MV) serves as the linker to assemble AuNPs with an interparticle gap of approximately 1 nm, this "hot spot" generates a strong SERS [3] signal from methyl viologen, b) Anti-human EGFR antibodies as targeting proteins to ensure specific binding to EGFR-expressing cancer cells and c) polyethylene glycol (PEG) as stabilizing polymer to enhance the stability and biocompatibility of the assemblies. (Figure 2)

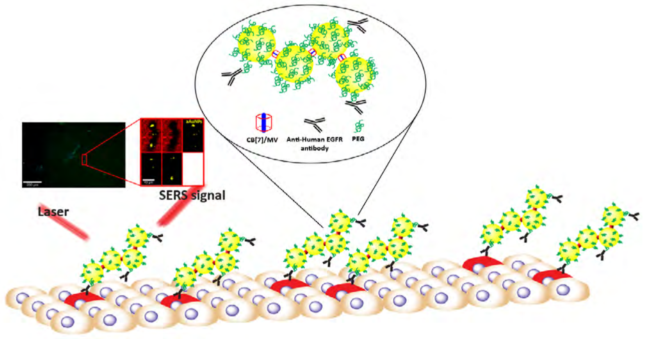

Figure 2: Schematic illustration of gold nanoparticle assemblies (aAuNPs) targeting ovarian cancer cells expressing EGFR protein on their surface.

Results and discussion

Cucurbit[7]uril (CB[7]), a barrel-shaped macrocyclic molecule, was selected as the linker for aAuNPs due to its unique structural and functional properties: the molecule has carbonyl groups on both its upper and lower rims, enabling the simultaneous binding of two gold nanoparticles; its height of approximately 1 nm provides an ideal interparticle gap for achieving an extremely strong enhanced Raman signal; the cavity of CB[7] can encapsulate guest molecules, such as Methyl Viologen (MV), which is known for its strong Raman spectrum. MV forms a highly stable 1:1 host-guest complex with CB[7], facilitated by its aromatic rings and positive charge in solution.[4] For these attributes, we used CB[7]/MV complex to link 40 nm AuNPs to assemblies. Notably, Raman measurement revealed that the signal from MV positioned in the interparticle gaps of the assemblies was approximately 5 times stronger than that from MV simply adsorbed to single AuNPs (Figure 3). This demonstrates that the interparticle localization of Methyl Viologen within the assemblies substantially amplifies the Raman signal compared to single AuNPs. As targeting molecule anti-human EGFR antibodies were selected. The conjugation of these antibodies to the aAuNPs surface is achieved using Light-Activated Site-Specific Conjugation (LASIC).[5] A copper-free click reaction is used to link dibenzocyclooctyne (DBCO) PEG-thiol to oYo-Link Azide (alphaThera). The oYo-Link Azide contains an engineered Protein G that covalently binds the heavy chains of our anti-human EGFR IgG antibodies upon UV light exposure.

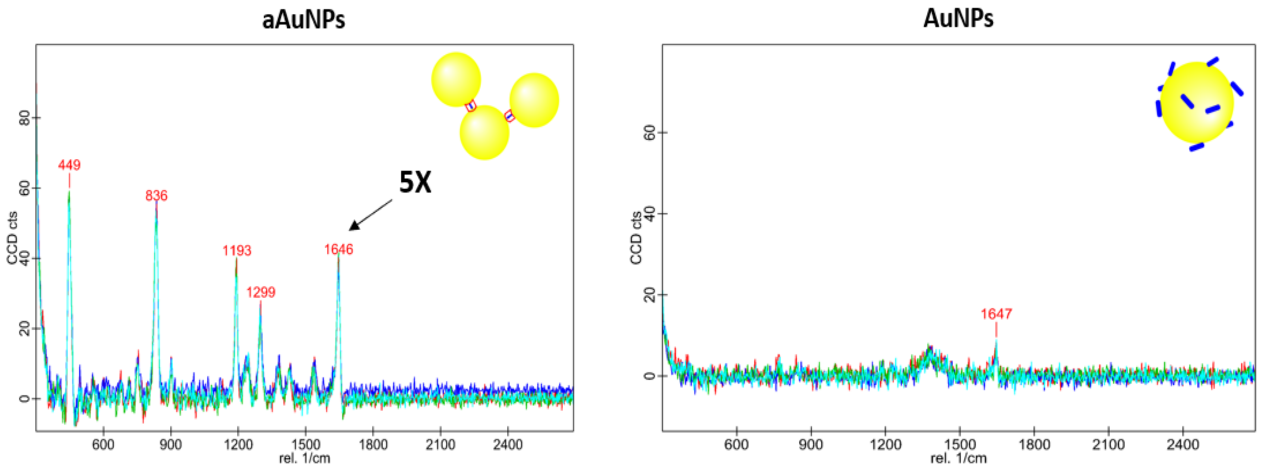

Figure 3: Comparison of Raman spectra of MV on aAuNPs and MV adsorbed on single AuNPs. The peak at 1646 rel. 1/cm, which was the only detectable signal for AuNPs, was used to compare signals. The Raman intensity resulted approx. 5 times stronger for aAuNPs than for AuNPs. Measurements were conducted by placing 500 uL [0.2 nM] of the AuNPs and aAuNPs in sodium citrate buffer solution onto a cavity slide. A 10X objective was used to focus the 785 nm (60mW) into the AuNP solutions. Each sample was measured three times, with each measurement lasting 10 seconds and an integration time of 0.5 seconds.

Once assembled, this complex is attached to the aAuNPs surface through the thiol group of the DBCO PEG-thiol. Excess DBCO PEG-thiol is removed using Amicon Ultra 0.5 mL Filters (MWCO: 100 kDa). The successful assembly of the complex was confirmed using high-performance liquid chromatography (HPLC) and Western blot analysis (Figure 4). The functionality of the conjugated antibodies was validated through immunofluorescence assay (data not shown). Finally, the complete complex is bound to aAuNPs via thiol-gold interaction. Preliminary data suggest that the Nanoflow Cytometry (NanoFCM) and QSense Analyzer (Biolin Scientific) hold promise for analyzing the effective attachment of antibodies on the aAuNPs surface and assessing their antigen recognition capability.

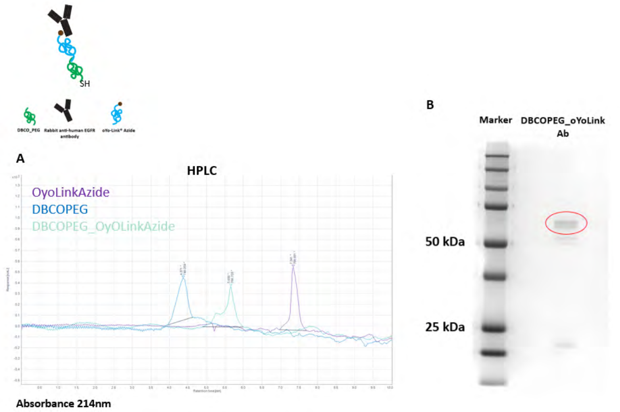

Figure 4: Schematic illustration of the complex and its components. (A) HPLC analysis; a new absorbance peak at retention time of 5.6 min. distinct from the peaks of unconjugated DBCO PEG-thiol and oYo-Link Azide indicates successful conjugation. The disappearance of unconjugated molecule peaks further supports this result. (B) Western blot analysis; the attachment of the antibody (Ab) to the DBCO PEG-oYoLink Azide complex is confirmed by detecting a band (red circle) approx. 10 kDa larger than the unconjugated heavy chain at 50kDa. The light chain band is also visible at 25 kDa.

Conclusion and outlook

Ovarian cancer remains a challenging disease to be diagnosed. The development of our aAuNPs-enhanced Raman microscopy, distinguished by its remarkably intense Raman signal relative to single nanoparticles, offers promising potential for precise cancer visualization and possibly diagnosis in vitro and in vivo. To ensure specificity, anti-human EGFR antibodies were conjugated to the assemblies' surface using the LASIC method. This approach guarantees the proper orientation of antibodies, with their binding site exposed for optimal interaction. Establishing the appropriate antibody and PEG density on the assemblies' surface is the next critical step. Once optimized, these assemblies will be tested for their ability to distinguish EGFR-positive and EGFR-negative ovarian cancer cells using Raman microscopy. We consider this initial experimental cell line setup as optimal approach to evaluate the specificity & selectivity of SERS as an imaging tool for follow-up experiments, to continue for in vivo visualization of tumor cells.

References

[1] European Institute of Women's Health (EIWH)

[2] Q Sheng & J Liu, The therapeutic potential of targeting the EGFR family in epithelial ovarian cancer, British Journal of Cancer Vol. 104, pp. 1241-1245 (2011).

[3] Samuel T. Jones et al., Gold Nanorods with Sub-Nanometer Separation using Cucurbit[n]uril for SERS Applications, small Vol. 10, pp. 4298–4303 (2014)

[4] Daniel O. Sigle et al., Observing Single Molecules Complexing with Cucurbit[7]uril through Nanogap Surface-Enhanced Raman Spectroscopy, The Journal of Physical Chemistry Letters Vol. 7, pp. 704-710 (2016)

[5] James Z. Hui, Shereen Tamsen, Yang Song, Andrew Tsourkas, LASIC: Light Activated Site-Specific Conjugation of Native IgGs, Bioconjugate Chem. Vol. 26, pp. 1456-1460 (2015)

Quantifying bacterial responses to antibiotics at the single-cell level

Project P1805: High-throughput multiplexed microfluidics for antimicrobial drug discovery
Project Leaders: E. van Nimwegen and V. Guzenko
Collaborator: M.-E. Alaball Pujol (SNI PhD Student)

Introduction

Without effective antimicrobials, the success of modern medicine would be at risk for treating infections including during major surgery and cancer chemotherapy. Misuse and overuse of antimicrobials are the main drivers in the development of resistant pathogens; however, it has also become clear in the last decades that the sensitivity to treatment varies from cell to cell, even in an isogenic population. In particular, some cells are in physiological states that allow them to survive antibiotic treatment without any resistance mutations [1]. Yet, most *in vitro* assays used to discover and study antimicrobial compounds are based on the study of macroscopic growth in liquid cultures where single-cell resolution is lacking. Consequently, the determinants of sensitivity to antibiotics are only poorly understood at the single-cell level due to the lack of quantitative data.

In recent years, powerful methods have been developed to quantitatively measure behaviour and responses in single bacterial cells. By combining microfluidics with time-lapse microscopy, it is possible to track growth, gene expression, division, and death within lineages of single cells. An especially attractive microfluidic design is the so-called Mother Machine, where bacteria grow within narrow growth channels that are perpendicularly connected to a main flow channel, which supplies nutrients and washes away cells growing out of the growth channels. In this field, our lab has developed an integrated microfluidic and computational setup to study the response of single bacteria to controlled environmental changes [2]: the dual-input Mother Machine (DIMM). The DIMM allows arbitrary time-varying mixtures of two input media, such that cells can be exposed to a precisely controlled set of varying external conditions. The companion image analysis software Mother Machine Analyser (MoMA) segments and tracks cell lineages from phase-contrast images with high throughput and accuracy.

In the present project, we use this setup to quantify how the response of individual bacteria to treatment with antibiotics depends on their physiological state at the time the treatment commences. For this, we focus on treating Escherichia coli (E. coli) cells with a variety of clinically relevant antibiotics at clinically relevant concentrations. Moreover, we developed new microfluidic designs to enable the study of multiple antibiotics and strains in parallel. Such designs can for example be used to identify compounds that specifically target subpopulations of pathogenic bacteria.

New microfluidic circuits to study the bacterial response to antibiotic treatments in parallel

Classical Mother Machine designs consist of narrow dead-end channels located perpendicular to a main channel where the media flow (Figure 1A). By concentrating a bacterial cell culture and through diffusion, the cells are trapped in the dead-end channels and can be exposed to different media. However, it has been observed that a nutrient gradient exists acros the channels and that the growth rates vary depending on where a cell is located along this gradient (Figure 1D).

To enable multiplexed testing of different strains and media, we have designed filtering Mother Machine channels. In such channels the closed end is replaced by constrictions that act as filters. The openings are connected to a backflow channel that collects the media, without letting the cells escape. This improves and accelerates the cell loading procedure as a diluted culture can be used, as well as mitigating the nutrient and growth rate gradient along the channel (Figure 1D). To create such filtering channels two features can be used: lateral (Figure 1B) or vertical constriction (Figure 1C). The lateral constriction consists of an opening at the back of the channel, with a narrower width than the growth channel to avoid cells escaping [3]. Because of the small size of these structures, they are very challenging to manufacture, and require e-beam lithography which is not widely available. Together with Dr. Vitaliy Guzenko at PSI we used the e-beam lithography system Raith EBPG 5000Plus to microfabricate lateral constrictions. With this strategy the design consists of two layers of different thicknesses, one for the main flow channels (20µm wide and 10µm deep), connected to the narrow (<1µm) and shallow (900nm deep) growth channels. The lateral constriction reduces the width of the channels to 250nm. The vertical constriction consists of adding a layer in the design with a shallower height than connects the growth channel to the collecting flow channel. This strategy led by Dr. Thomas Julou is based on a 3-layer design, where the third layer is shallow enough to produce a vertical constriction, reducing the channel height by 250nm. The vertical constriction consists of a reservoir-like structure surrounding the growth channel.

After testing both designs, we concluded that cells could escape the lateral constriction, but we obtained successful results by reducing the area of contact of the vertical constriction with the growth channel. Additionally, together with the mechanical workshop of Biozentrum we developed a prototype pressurized box to multiplex the reservoirs for the input media, which is being used in our experiments.

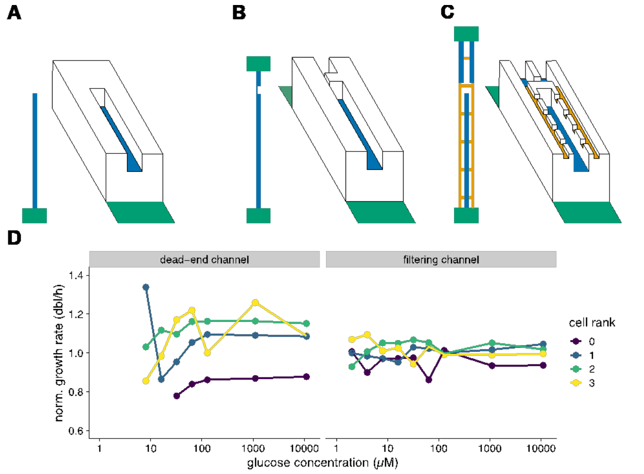

Fig. 1: Mother Machine filtering channel designs. (A) 2-layer design with a dead end. (B) 2-layer design with a lateral constriction at the back of the channel, connected to a back-flow channel. (C) 3-layer filtering design with a shallow ladder-like structure around the channel, connected to a back-flow channel. In panels (A-C) the growth layer (blue) has 0.9µm height, the flow layer (green) has 10µm height, and the filter layer (orange) has 0.25µm height. (D) Normalised growth rate of cells by position in the growth channel (cell rank) from the bottom (rank 0) to the top (rank 3), in dead-end channels and filtering channels, in various glucose concentrations.

Mother Machine experiments to characterize bacterial responses to antibiotic treatment

We focused on 3 clinically relevant antibiotics for Urinary Tract Infection (UTI) treatment: Ciprofloxacin (CIP), Ceftriaxone (CEF), and Gentamicin (GEN). The experiments consisted of treating cells of E. coli strain MG1655 with different concentrations of each antibiotic, ranging from sub-Minimal Inhibitory Concentration (MIC) values to the maximum concentration measured in serum during clinical treatment. The experimental timeline consisted of 6 hours of exponential growth in M9 minimal media supplemented with 0.2% glucose, followed by the antibiotic treatment that lasted 2 hours, after which the survival was assessed by exposing the bacteria to fresh media for 16 hours.

We calculated the survival rates for all the conditions by tracking the 'mother' cells (i.e. cells at the bottom of the growth channels) across the treatment and counting the cells that produced viable progeny after it. We found that, although the fraction of surviving cells drops as a logistic function with concentration for each antibiotic, the concentration range over which survival rates fall varies strongly across antibiotics (Figure 2A).

We obtained quantitative data from the experiments using the DeepMoMA software, a new version of the MoMA software, that integrates the U-Net convolutional neural network architecture, developed by Dr. Michael Mell in our group. DeepMoMA allows quantifying single-cell response to antibiotic treatment, and has been specifically adapted to different cell morphologies that result from treatment with antibiotics. These morphologies include lysis, filamentation, and loss of phase contrast, which are observed at different rates across the different antibiotics and concentrations.

We reconstructed cell lineages across the experimental time courses, and quantified various single-cell variables. Using RealTrace, a Bayesian inference method developed by Björn Kscheschinski in our group (based on maximum entropy process priors), we can remove measurement noise from raw traces and obtain de-noised traces of cell length from which the instantaneous growth rate can be inferred. We then analysed how the physiological state of the cell just before the treatment affected its subsequent survival. As shown in Figure 2B, surviving cells generally were growing slower just before the CIP and CEF treatment, compared to cells that died. We also observed cells late in their cell cycle for GEN and early in their cell cycle in CEF to be more likely to survive (Figure 2C). Additionally, we could also follow each cell throughout the antibiotic treatment and once the compound is removed identify how the surviving and susceptible population's dynamics change over the course of the experiment.

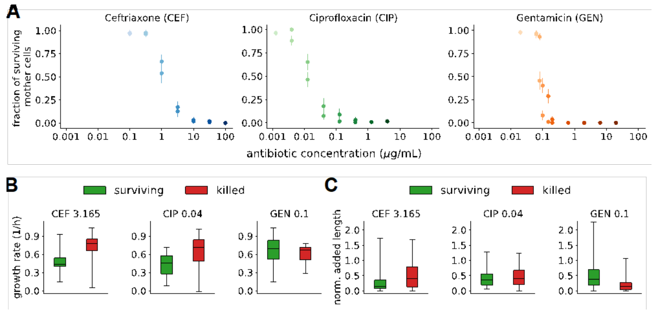

Fig. 2: Bacterial single-cell response to antibiotic treatments. (A) Dose-response curves at the single-cell level. Fractions of mother cells with viable progeny in each condition replicate, with ±2 standard deviations error bars, and a hill curve fitted for each antibiotic compound. (B) In CEF and CIP, surviving cells (cells with viable offspring) after the treatment, grew slower during the 30 min before the treatment than killed cells. (C) The added size since birth normalized by the average added length in fresh media, which serves as a proxy for the cell cycle stage, is smaller for surviving cells than killed cells in CEF, in GEN surviving cells are later in their cell cycle.

The present study could be extended to other strains and media, for example to compare our results to a more clinically relevant strain such as Uropathogenic E. coli (UPEC) CFT073. Furthermore, other antibiotic treatment strategies could be tested, such as new antibiotic compounds or combinations of treatments, which are possible thanks to the multiplexing accomplished with the new microfluidic designs.

References

[1] D. Hughes and D.I. Andersson, "Environmental and genetic modulation of the phenotypic expression of antibiotic resistance", FEMS microbiology reviews 41 (2017).

[2] M. Kaiser, F. Jug, T. Julou, S. Deshpande, T. Pfohl, et al., "Monitoring single-cell gene regulation under dynamically controllable conditions with integrated microfluidics and software ", Nature Communications 9 (2018).

[3] Ö. Baltekin, A. Boucharin, E. Tano, D. I. Andersson, J. and Elf, "Antibiotic susceptibility testing in less than 30 min using direct single-cell imaging", Proceedings of the National Academy of Sciences 114 (2017)

Investigation of skyrmion bubbles using NV magnetometry and simulations

Project P1806: Image the twist!
Project Leaders: P. Maletinsky and V. Scagnoli
Collaborator: S. Treves (SNI PhD Student), K. Wagner

Introduction and motivation

The aim of this project is to determine the formation mechanism of skyrmions, a topologically protected magnetic structure [1]. Currently it is not fully understood what drives the formation and annihilation events in skyrmion hosting materials; such knowledge is particularly important if skyrmions are to be employed in future advanced information processing devices [2]. Observations of such creation/anihilation events are made easier through the use of materials which host skyrmions in ambient conditions.

A system of recent interest for hosting room temperature skyrmions with no applied magnetic field is $NdMn_2Ge_2$, a rare-earth based centro-symmetric material. This bulk material has been observed to host different metastable magnetic textures stabilized by high- and low- magnetic field cooling protocols. Metastable skyrmions have been nucleated with a field cooling procedure and then observed using topological Hall effect measurements [3,4] and Lorentz transmission electron microscopy [5]. We have confirmed these findings in previous years of the project using scanning transmission x-ray microscopy (STXM), where we investigated the effects of temperature and an applied magnetic field on Skyrmion formation and stability.

This year, we used nitrogen-vacancy magnetometry to obtain a quantitative map of the magnetic stray field emanating from a lamella of $NdMn_2Ge_2$. The results complement our previous measurements from STXM on a similar lamella. Furthermore, by quantifying the strength of the stray field we could make a comparison to our simulation models and justify the parameters used and behaviours observed experimentally.

Key experimental results

Nitrogen vacancy magnetometry measurements were performed on a circular, 4 µm diameter NdMn2Ge2 lamella of 190 nm thickness, that was FIB-cut from the same crystal as the lamella studied thus far. The skyrmion bubble lattice was initialised via the following protocol. First, the lamella was heated above its Curie temperature ($Tc = 330\,K$), via the application of a mA current through the Pt heater strips on the membrane at a rate of $1.6\,\Omega K^{-1}$. A small magnetic field of 50 mT was applied out-of-plane (perpendicular to the sample's surface) while the sample was still being heated. This arrangement was maintained for one minute, after which the current was gradually decreased and then turned off. The sample was allowed to cool for an additional 30 s to reach room temperature. The resulting skyrmion bubble lattice was then imaged under ambient conditions in a small bias field of 8.3 mT, to allow for quantitative NV magnetometry [6].

A representative result of our NV measurements is shown in Fig.1a and shows a stray field map of a highly regular, triangular NdMn2Ge2 SkBL, with a periodicity, $p_{skyr} \sim 490\,\text{nm}$, largely consistent with our previous STXM findings. This image directly yields a quantitative estimate of the stray magnetic field strength at the scan-height, $h_{NV} \approx 300\,\text{nm}$ of the NV sensor. By taking a line cut of this data we can see how the strength of the stray field changes from the center (~1 mT) to the edges of the skyrmion bubbles (~0 mT).

To benchmark this quantitative measurement against our model, we conducted a set of simulations, using the same material parameters used previously. This time however, we initialized the system with a Bloch skyrmion lattice that we subsequently relaxed, rather than relaxing the system from a random magnetic state with an external magnetic field. With this initialisation, it was possible to obtain a skyrmion bubble lattice configuration closely resembling the NV experimental results (see Fig. 1b). The stray field was then computed up to 500 nm away from the sample surface and projected onto the known direction of the NV spin quantization axis (55° ± 4° from the sample normal, azimuthal angle 30° ± 4°) to reproduce the anticipated NV magnetometry image from the simulations. Figure 1b shows an example of such a simulated stray field map, evaluated at a position $h_{NV} \approx 300$ nm above the sample surface. Our comparison shows that the measured field strength is ~ 7× weaker than the one predicted from our simulations, as seen in the linecuts in Fig. 1c.

This difference in stray field magnitude between the simulation and the experimental results may result from several factors, which we discuss in the following:

First, given that the stray field strength scales directly with the magnetisation strength M_{sat}, the observed discrepancy could be explained by the choice of the value of M_{sat} in our simulations. There, we initially set M_{sat} to the full sublattice magnetisation of $NdMn_2Ge_2$, in accordance with past works [5]. However, previous studies [3, 7] indicate that for $240\,K < T < 340\,K$, a canting of the sublattice magnetisation occurs as the out-of-plane ferromagnetic state transitions to an in-plane antiferromagnetic state. At $T = 285\,K$, a canting angle of 58° is reported [7], which would reduce the ferromagnetic moment of $NdMn_2Ge_2$ by a factor of two over the value we chose for $T = 300\,K$, where our experiments were conducted.

Second, due to manufacturing by focused ion beam (FIB) there is a surface layer where the material's crystalline structure is damaged. The thickness of these "dead-layers" is on the order of a few 10 nm on each side of the lamellae [8] and would further reduce the stray field strength from the expected value. Based on standard theory for field propagation away from thin magnetic films [9], these factors can be used to estimate the resulting reduction in stray field magnitude B through the "thickness loss factor".

$$B \propto \exp\left(-\frac{2\pi d_{top}}{p_{skyr}}\right) - \exp\left(-\frac{2\pi d_{bot}}{p_{skyr}}\right)$$

With $d_{top} = h_{NV} + t_d$ and $d_{bot} = h_{NV} - t_d + t$, where t, t_d are the thicknesses of the magnetically ordered part of the $NdMn_2Ge_2$ lamella and dead layer respectively.

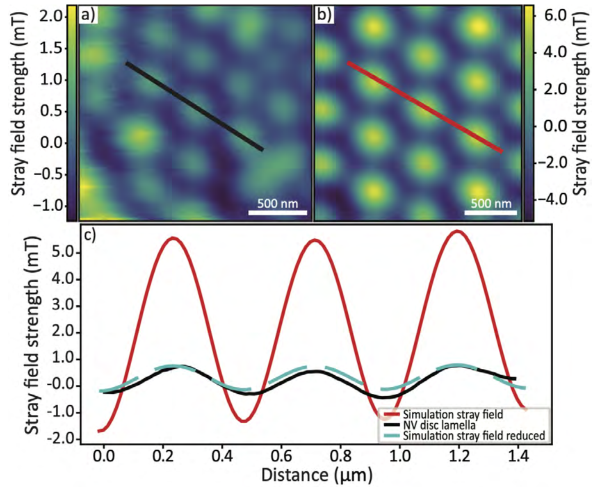

Fig. 1: a) Stray field map measured using NV magnetometry on a NdMn2Ge2 disk lamella, at a lift height of 300 nm. These stray field maps directly reflect the ferromagnetic moment of the canted antiferromagnetic sublattice. b) A stray field map calculated from the disk lamella simulation at a lift height of 300 nm. c) The black line profile shows the strength of the stray field for three skyrmion bubbles from the NV stray field map. A line profile for three skyrmion bubbles from simulations is plotted in red. Also plotted is the line profile (blue) calculated (using Eq. 2) from the simulation stray field data when accounting for dead layers of material and a different NV height.

Considering all these factors, the observed discrepancy in stray field strength could be explained by a realistic set of parameters, such as a canting angle of 68°, $h_{NV} = 340\,nm$ and $t_d = 35\,nm$ (see blue dashed curve in Fig. 1c). While it is beyond the scope of the current project to disentangle the different possible contributions, the quantification of the reduced stray field values may provide valuable information in future studies on the canting angle or non-magnetic dead layers.

Outlook

In summary, we have scrutinised the nature of skyrmionic objects in NdMn2Ge2 using micromagnetic simulations, scanning transmission X-ray microscopy imaging and nitrogen-vacancy magnetometry. As previously reported, with an appropriate field cooling protocol, the system is capable of hosting a metastable skyrmion bubble lattice at room temperature, in zero magnetic field. This lattice is robust to some extent to various changes in external stimuli such as, temperature and application of a magnetic field. Finally, our NV magnetometry measurements provide a quantitative assessment of the magnetic stray field of the sample at a height of 300 nm above the sample surface, suggesting that the micromagnetic simulations overestimated the field strength by a factor of seven. This can be accounted for by considering the dead layers arising from the sample preparation, a slightly higher NV lift height, and the canting of the sublattice magnetisation.

References

[1] T. H. R. Skyrme, "A unified field theory of mesons and baryons.", Nuclear Physics 31, 556–569 (1962).

[2] S. S. P. Parkin, et al., "Magnetic Domain-Wall Racetrack Memory.", Science, 320, 190 (2008).

[3] S. Wang, et al., "Giant Topological Hall Effect and Superstable Spontaneous Skyrmions below 330 K in a Centrosymmetric Complex Noncollinear Ferromagnet NdMn2Ge2.", ACS Applied Material Interfaces, 12, 24125 (2020)

[4] X. Zheng, et al., "Giant topological hall effect around room temperature in noncollinear ferromagnet NdMn2Ge2 single crystal.", Applied Physics Letters 118, 072402 (2021).

[5] Z. Hou, et al., "Emergence of room temperature stable skyrmionic bubbles in the rare earth based REMn2Ge2 (RE = Ce, Pr, and Nd) magnets.", Materials Today Physics, 17, 100341 (2021).

[6] L. Rondin, et al., "Stray-field imaging of magnetic vortices with a single diamond spin", Nature Communications 4, 2279 (2013).

[7] R. Welter, et al., "Neutron diffraction study of CeMn2Ge2, PrMn2Ge2 and NdMn2Ge2: evidence of dominant antiferromagnetic components within the (001) Mn planes in ferromagnetic ThCr2Si2-type manganese ternary compounds", Journal of Alloys and Compounds 218, 204 (1995).

[8] L. Giannuzzi and F. Stevie, "A review of focused ion beam milling techniques for TEM specimen preparation", Micron 30, 197 (1999).

[9] E. Meyer, et al., "Scanning Probe Microscopy" (Springer-Verlag Berlin Heidelberg, 2004).

A single cell preparation platform for correlative light and electron microscopy

Project P1901: Microfluidics to Study Huntington's Disease by Visual Proteomics
Project Leaders: T. Braun, and H.Stahlberg
Collaborators: A. Fränkl (SNI PhD Student), A. Bieri, E. Schneider, L. Rima, M. Zimmermann

Introduction

Electron microscopy of vitrified specimens (cryo-EM) is a powerful technique for examining cellular structures and ultrastructures at high resolution. However, several challenges hinder the direct application of electron tomography to adherent eukaryotic cells. First, the thickness of cell somas often exceeds the limits for effective transmission EM imaging. Second, the cell's thickness and heat conduction properties limit efficient vitrification. Therefore, current approaches frequently rely on harsh blotting methods with filter paper, which can distort cellular morphology and damage delicate structures such as dendrites. Third, while EM provides high-resolution snapshots of cellular features, it cannot capture real-time dynamics, limiting its use for studying ongoing biological processes.

One approach to addressing the first bottleneck is to create a thin lamella in the cell soma using focused ion beam milling. Alternatively, EM can focus selectively on thin cellular structures like dendrites. In our work, we developed a novel platform that enables the direct growth of adherent (neuronal) eukaryotic cells on cryo-EM sample carriers (grids) designed for gentle, blotting-free vitrification (as detailed in the FuncEM report). This platform integrates with "minimalistic tissue" microfluidics, facilitating the selective outgrowth of dendrites onto the EM grid. These dendrites are thin enough for direct transmission EM analysis, eliminating the need for lamella milling.

Additionally, our system supports fluorescence light microscopy both before and after vitrification, allowing for real-time monitoring of dynamic processes before vitrification and three-dimensional confocal characterization afterward. We are now exploring the fate of amyloid particles within neuronal model systems using these new methods.

Biological background

In Parkinson's disease (PD) and related synucleinopathies, the intrinsically disordered protein alpha-synuclein (alpha-syn) adopts a pathogenic structure that can propagate by inducing misfolding in healthy alpha alpha syn molecules. This process leads to the formation of fibrillar alpha-syn aggregates, or amyloids, which progressively spread through the neuronal network, driving disease progression. The cellular machinery that maintains protein homeostasis, comprising chaperones and other quality control systems, helps typically prevent such misfolding. However, with age, the efficiency of this network declines, making aging the primary risk factor for the spontaneous onset of neurodegenerative diseases.

Our research aims to investigate how these amyloid particles are handled once they enter cells, likely through endocytosis, and how cellular components process them.

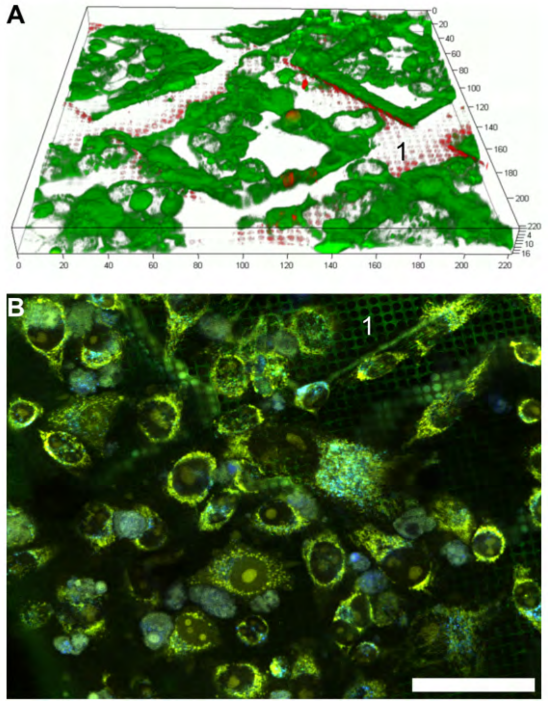

Fig. 1: Fluorescence microscopy of vitrified cells grown directly on cryo-EM grids, visible in the background (1). A) 3D-overview of the vitrified cell on the cryo-EM grid. All dimensions are given in µm. B) Projection of the cells grown on the grid at higher magnification. In yellow, a mitochondrial substrate is shown, and α-syn "seeds" are labeled in blue. Manuscript in preparation.

Fluorescence microscopy of vitrified cells

Adherent human cells were cultivated in a proliferative state under standard cell culture conditions. The cells were then incubated with fluorescently labeled alpha-syn particles for 3 days to introduce the amyloid seeds. Following this incubation, the cells were replated onto a cryo-EM grid mounted on our newly developed cell cultivation platform (refer to FuncEM report, Fig. 3) and allowed to grow for an additional 24 hours. Replating was crucial for effectively removing non-internalized seeds, ensuring only internalized particles remained.

Before vitrification, the cryo-EM grid cells were imaged using a simple fluorescence microscope. Excess liquid was then carefully removed, and a controlled gas stream helped to thin the remaining liquid around the grid. The CryoWriter system was used to plunge the grid into liquid ethane, vitrifying the sample. The vitrified cells ' fluorescence images (Fig. 1) clearly show the internalized alpha-syn seeds.

Subsequent analysis of the vitrified cells was performed using cryo-EM imaging and tomography. To do so, a thin lamella was milled from the cell, enabling the detailed imaging of a small cellular region. In addition to lamella-based analysis, we also investigated naturally thin cellular structures, such as dendrites of neurons, which are particularly suited for direct cryo-EM imaging without the need for lamella milling.

Controlled dendrite outgrowth on cryo-EM grids

We previously developed a microfluidic chip for co-pathological interactions between two neuronal cell populations. Building on this, we created a modified version designed to direct the selective outgrowth of dendrites directly onto a cryo-EM grid. This modified chip features a sizeable cell-growth chamber approximately 30 µm high, connected to narrower selection channels measuring 3 µm in height and 4 µm in width (Fig. 2A).

Using live-cell imaging with a fluorescent label, we observed dendrites extending from the selection zones onto the cryo-EM grid (Fig. 2B). The rapid removal of the grid helped preserve the structural integrity of the dendrites, as confirmed by light microscopy (data not shown). An overview image (Fig. 2B) highlights the extensive dendritic coverage across the perforated carbon film of the cryo-EM grid.

Conclusion and outlook

We are currently analyzing the results of the seeding experiments and comparing them across several complementary approaches (see also the FuncEM report): (i) single-cell lysis experiments, which provide detailed ultrastructural insights into the seeds [2]; (ii) amyloid structures derived from patient brain extractions, isolated using the cryoWriter system's isolation module [1]; and (iii) processing experiments involving synthetic fibrils immobilized on beads and exposed to various neuronal extracts, including cell lysates and patient brain homogenates.

This comparative analysis will deepen our understanding of amyloid seed and degradation, potentially paving the way for more refined models and therapeutic strategies.

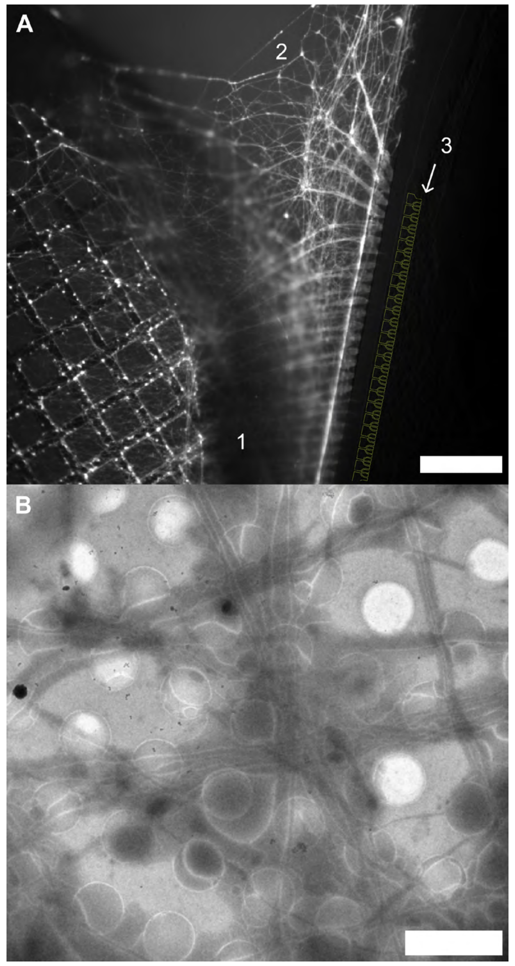

Fig. 2: Selective outgrowth of dendrites (dopaminergic neuron-like, human cells) onto the cryo-EM grid. Manuscript in preparation. A) Fluorescence microscopy of the chip and cyo-EM grid (1) before vitrification. The dendrites (2) are selected by the chip's filter region (3, highlighted in yellow), which retain the the cell somas in the cell-growth chamber of the chip. Scale bar: 500 µm. B) cryo-EM (overview) of the cell's dendrites. Scale bar: 5 µm.

References

[1] C. Schmidli, S. Albiez, L. Rima, R. Righetto, I. Mohammed, et al., "Microfluidic Protein Isolation and Sample Preparation for High-Resolution Cryo-EM", Proc. Natl. Acad. Sci. U.S.A. 116(30), 15007 (2019)

[2] [1] A. Syntychaki, L. Rima, C. Schmidli, T. Stohler, A. Bieri, et al., "`Differential visual proteomics': Enabling the proteome-wide comparison of protein structures of single-cells," J. Proteome Res., 18(9), 3521–3531 (2019)

Dual-Scale hybrid patches micmicking native combining 3D-bioprinted constructs with directional nanofiber network to mimic native myocardium towards in-vitro heart models

Project P1902: Directional 3D nanofiber network to mimic in-vivo myocardial syncytium towards guiding contraction patterns in in-vitro heart models
Project Leaders: M. R. Gullo, A. Marsano and M. Poggio
Collaborator: F. Züger (SNI PhD Student)

Introduction

In cardiac tissue engineering, there is a high demand for innovative biofabrication methods, particularly because myocardial infarction is one of the leading causes of hospitalization and death globally.[1] When heart functionality is impaired following a myocardial infarction, coupled with the limited regenerative capacity of cardiomyocytes (CMs), it results in a loss of cardiac tissue. This lost tissue needs to be replaced with constructs that closely mimic natural tissue and its environment to achieve physiologically relevant conditions.[2,3]

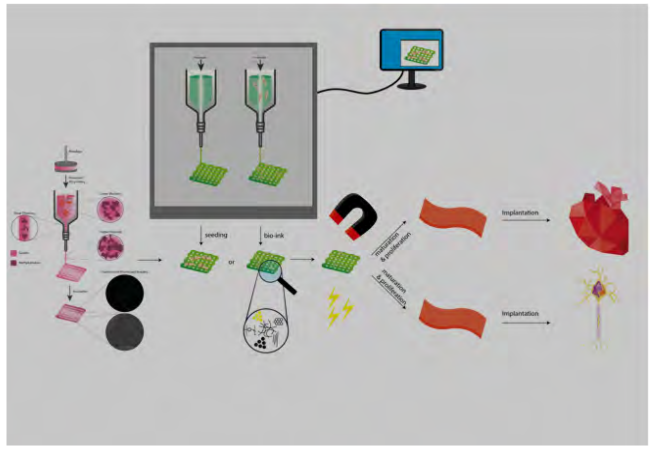

Fig. 1: Schematic representation of a typical workflow of a biofabrication process to produce cardiac dual-scale constructs.

To achieve such a biomimicking construct the idea of a dual-scale approach was pursued within the scope of this PhD thesis. This approach combines 3D-printed micrometer scale and electrospun nanometer scale structures resembling natural cardiac tissue and cardiac environment very closely. Therefore, the findings of conductive nanofiber production and the formulation and refinement of our custom-made bioink were used to fabricate a dual-scale cardiac construct. The whole biofabrication process was optimized for high cell survival, sterile handling and smooth integration of all production steps. The constructs could successfully be used for long-term cell culture experiments (21d) and were assessed for cell viability and functional behavior at several timepoints.

Fabrication and Analysis of Dual-Scale Cardiac Constructs

After successful fabrication of nanofibers and the development of a custom-made bioink with high cell viability (both fabrication steps described in earlier reports) the DSC was being created by combining both pre-produced structures. For that, all the individual production steps, needed to be coordinated with each other, to minimize cell handling outside of the incubator. The whole process, worked for a small batch number of constructs, but was difficult to apply for higher batch numbers. The resulting construct (Fig. 2a/b) was placed in the incubator for long-term cell experiments. Viability of NRCMs in a 5-layered 3D-biofabricated full DSC construct were at: 74.86% ±4.5 (1-day postprint), 75.21% ±5.3 (7-days postprint), and 70.64% ±7.8 (21-days postprint). The corresponding controls, where no electrospun NFs were transferred onto the 3D-bioprinted constructs, were 87.45% ±4.16, 88.89% ±5.8 and 89.41% ±3.7, respectively (Fig. 2c).

As a final step in the fabrication of novel cardiac patches the combination of electrospun nanocomposite fibers and the 3D-bioprinted cell-laden construct, using custom-made bioink, to form a dual-scale construct was tackled. After sorting out contamination issues, due to the transfer of the DSC between different production sites (hoods) and coordination of all necessary production steps, we were able to biofabricate a cardiac patch. Viability tests indicate cell survival of >70% for up to 21d of DSC incubation. This is compared to the solely 3D-bioprinted case (viabilities >90%) lower and can be explained through longer production time and an overall more complicated coordination of DSC fabrication. This is generally a challenge of such multiscale biofabricated constructs. The combination of different fabrication processes together with cells, leads to a lot of individual steps, susceptible to errors and increased workload in production. Only small batches of a fully 'equipped' CNT-PCL NF dual-scale construct were possible to be produced at a time, otherwise the individual procedures did not interlock smoothly anymore leading to decreased cell survival. As in the increased cell viability during the course of 3D-bioprinting cardiac cells within our custom-made bioink, it is assumed that with more time for improving coordination of all the separate manufacturing steps and advancing the workflow, higher cell survival would have been possible.
Overall, in this thesis we report for the first time a dual-scale (or multiscale) construct for cardiac patch engineering, combining conductive NFs and a custom-made cell-laden bioink ready for 3D-bioprinting. The herein developed and studied DSC shows favorable features for cardiac regeneration applications with a novel kind of approach. This dual-scale arrangement closely resembles the extracellular matrix (ECM) found in actual tissues, providing a more realistic microenvironment, which allowed for high cell survival and functional cardiac tissue. This enables a promising strategy for engineering tissues with structural and functional characteristics similar to native heart tissue. This research facilitates and optimizes the design, fabrication and availability of multiscale constructs, providing a robust platform on which additional experimental data can be obtained on.

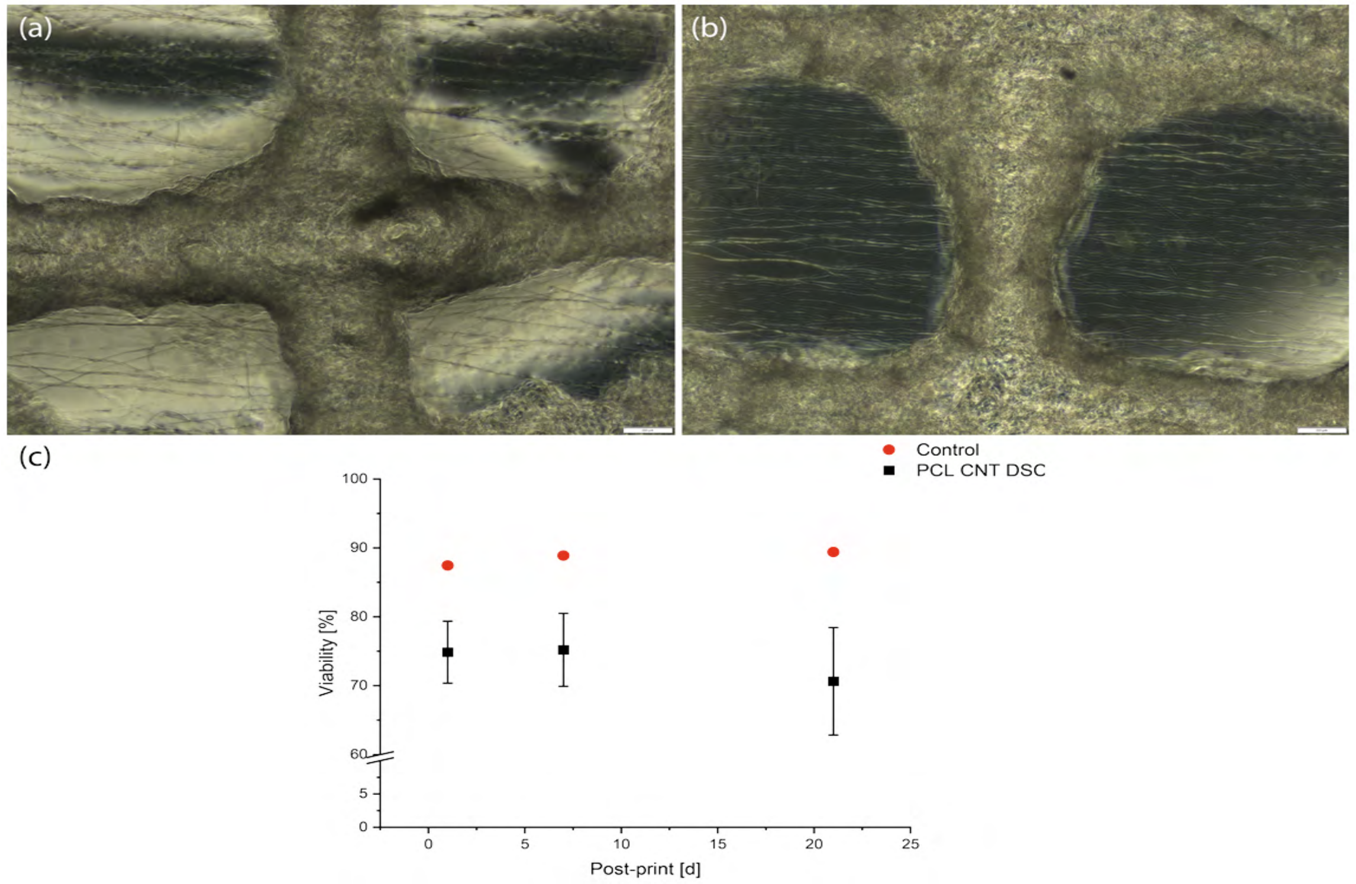

Fig. 2: Graphical representation of NRCM viability in full CNT-PCL DSC vs NRCM viability in a control print (5 layers, only 3D-bioprinted without NF): (a) and (b) Micrographs of CNT-PCL nanofibers transferred onto a previously 3D-bioprinted NRCM construct, scale bar = 200µm; (c) Viability of NRCMs in a 5-layered 3D-biofabricated full DSC construct: 74.86% ±4.5 (1-day postprint), 75.21% ±5.3 (7-day postprint), and 70.64% ±7.8 (21-days postprint). Controls viability were 87.45% ±4.16, 88.89% ±5.8, and 89.41% ±3.7, respectively. Live/Dead staining with dual-stained cells PI/Hoechst. Bioink contains NRCMs (5.4mio/mL).

Outlook

Further improvement and development of these described cardiac patches is manifold. From reconsidering the workflow, to increased cell density and the use of hiPSC derived cardiac cells. While a facilitated workflow would optimize the whole biofabrication process, higher cell numbers and more human like cell types would raise bio-similarity of our constructs and produce more translatable experimental data. Furthermore, maturation and functionality of the cardiac cells within the construct needs to be studied in more detail and with it the influence of conductive nanofibers on the hydrogels resistivity

References

[1] Gopinathan, J. & Noh, I., "Recent trends in bioinks for 3D printing", Biomaterials Research 22:11 (2018)

[2] Freemantle, N., Cleland, J., Young, P., Mason, J. & Harrison, J. "Beta Blockade after myocardial infarction: systematic review and meta regression analysis". BMJ 318, 1730–1737 (1999)

[3] Züger, F., Marsano, A., Poggio, M. & Gullo, M. R. "Nanocomposites in 3D Bioprinting for Engineering Conductive and Stimuli-Responsive Constructs Mimicking Electrically Sensitive Tissue". Advanced NanoBiomed Research 2, 2100108 (2022)

Integration of neutron nanomediators in fuel cells

Project P1903: Neutron nanomediators for non-invasive temperature mapping of fuel cells
Project Leaders: M. Kenzelmann and P. Boillat
Collaborator: A. Ruffo (SNI PhD Student)

Introduction

In this project, we integrate magnetic particles into fuel cell porous media called gas diffusion layers (GDLs) in order to measure the spatial temperature variation *in-situ*. The general measurement concept is to use the depolarization of a neutron beam as a measurement of the particle's magnetic saturation, which is temperature dependent. In previous work, we characterized how different materials and particle sizes impact the neutron beam depolarization and its temperature dependence. Here, we demonstrate how such particles can be introduced in a real fuel cell structure to conduct *in-situ* measurements.

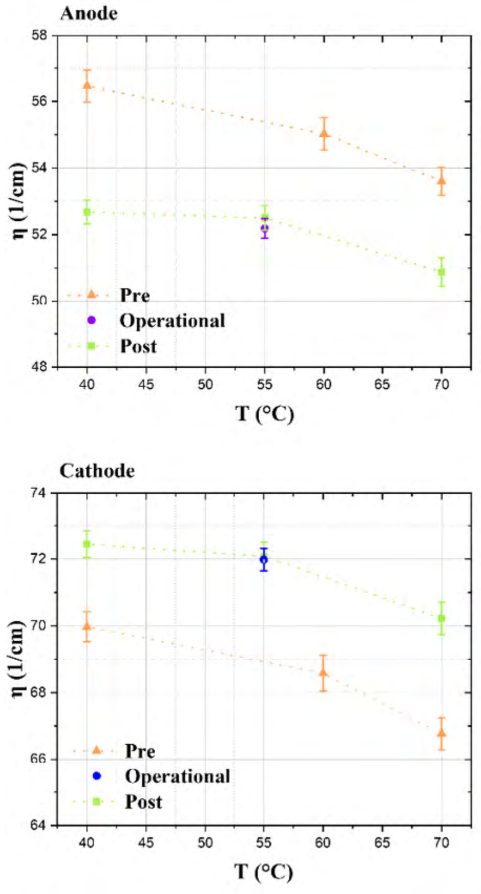

Fig. 1: Depolarization coefficients of samples taken from the anode (top) and cathode (bottom) at various stages of the operation. The data is segmented into three distinct periods: before operation, during operation, and after operation.

Measurement of the temperature in a fuel cell structure

To conduct the measurements, we included micrometric size magnetic particles. These particles were synthesized by ball milling from a coarser NdFeB powder. The milled powder is denominated NdFeB-415 based on the parameters used for the milling (4 hours, 15g of balls). The particles were integrated into the fuel cell GDLs by spray coating them together with a PTFE powder dispersion used as a hydrophobic treatment for the material. In order to be able to work with a neutron imaging setup with a limited resolution (aprox. 200 µm), we used a thicker porous layer than is usual fuel cell structures by stacking 5 GDL pieces on each side of the fuel cell.

As seen in Fig.1, the impact of artificially imposed temperature variation could be observed in the real fuel cell structure, both before and after operation. Meaning that the mediators are functional even after being exposed to the fuel cell operating conditions. A measurement during operation shows a deviation from the measurement at the same temperature which could be indicative of a temperature elevation to cell operation.

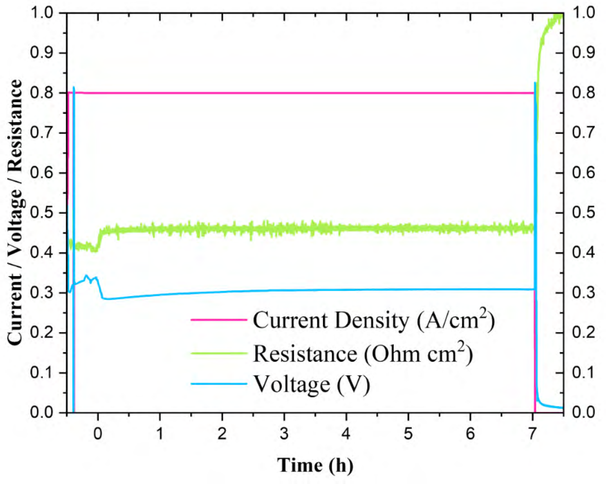

Fig. 2: Outcomes of an operating fuel cell containing a stack of GDLs coated with NdFeB-415, capturing three main parameters over a 7-hour operation period: the selected current density (red), the high-frequency resistance (green), and the cell voltage (blue).

Stability of cell operation

A potential concern with the proposed approach is whether part of the NdFeB particles could leach and poison either the catalyst or the membrane of the fuel cell. In the present study, the cell was operated for approximately eight hours at a temperature of 55 °C. As seen in Fig.2, the stability of the cell high frequency resistance (indicative of the membrane conductivity) indicates that these is no significant poisoning of the membrane. If it would occur, catalyst poisoning would be evidenced as a decrease of voltage over time. As the voltage is stable (the slight increase is commonly observed in fuel cell testing and is attributed to catalyst surface change during fuel cell operation), we conclude that there is no indication of catalyst poisoning.

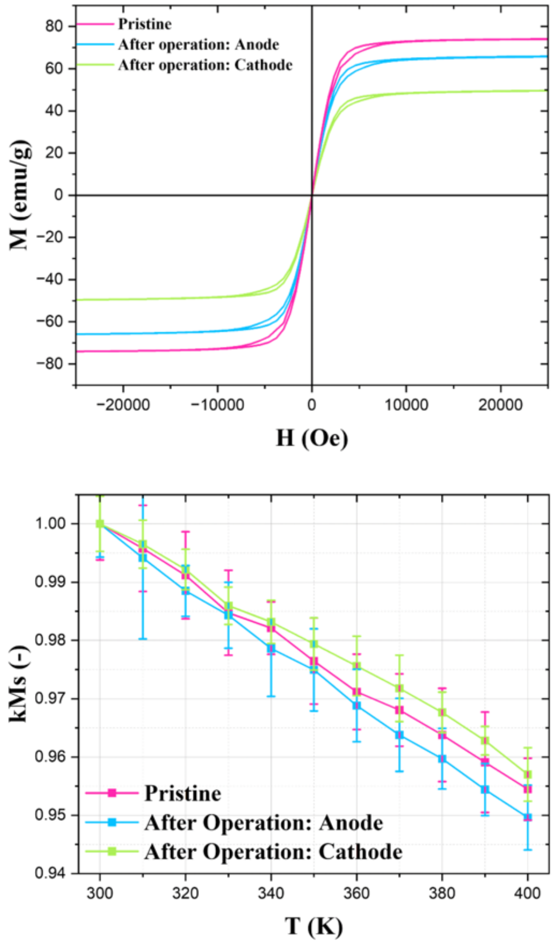

Fig. 3: Top: Magnetic hysteresis loops of various samples: the pristine sample (in pink), and samples after operation in both the anode (in blue) and cathode (in green) sections. Bottom: Relative magnetic saturation variation of the pristine (pink), anode (blue), and cathode (green) samples over a temperature range extending from 300 K to 400 K.

Stability of mediators

Besides the potential damage to the fuel cell, a further concern was the possible degradation of the mediator particles following their exposure to the fuel cell operating conditions. To assess this, magnetometer and EDX measurements were conducted on pristine samples and on samples having been used for the fuel cell anode and cathode. For Fig 3a, we can see that the estimated magnetic saturation is reduced for the samples used after operation when compared to one of the pristine samples. However, a second pristine sample shows an even lower saturation, which means that the differences are possibly related to the uncertainties in the coating process by hand spraying, resulting in imprecisions in the amount of coated material. In Fig. 3b, we can see the relative saturation as a function of temperature. Because this value is normalized to the saturation at 30°C, the effect of the imprecisions in the amount of coated material is compensated. In this case, the temperature dependence is the same for the materials before and after exposure to fuel cell conditions. This indicates that the use of the particles in fuel cell does not significantly alter their composition, at least not in a way affecting their function as temperature sensors. This is consistent with the neutron depolarization measurements presented in Fig.1.

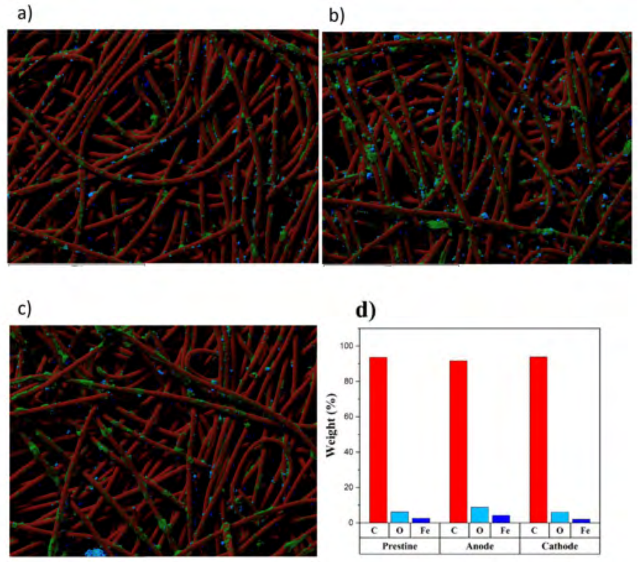

Fig. 4: EDX results of a) pristine, b) used in the anode, c) used in the cathode samples, with elemental mapping shown in distinct colors: iron (dark blue), oxygen (light blue), neodymium (yellow), carbon (red), and fluorine (green), and d) the weight percentages of the elements in these three different samples.

The SEM-EDX results presented in Fig. 4 also shows no significant qualitative differences between the pristine and used GDLs. In conclusion the results show that the NdFeB-415 powder used in this study can effectively be integrated in fuel cells without resulting in poisoning or being degraded by operation.

Applying nanowire MFM to 2D materials

Project P1905: Magnetic force microscopy with nanowire transducers
Project Leaders: M. Poggio and E. Meyer
Collaborator: L. Schneider (SNI PhD Student)

Introduction

Recent years have seen rapid progress in nanometer-scale magnetic imaging technology, with scanning probe microscopy driving remarkable improvements in both sensitivity and resolution. Among the most successful tools are magnetic force microscopy (MFM), spin-polarized scanning tunneling microscopy, as well as scanning magnetometers based on nitrogen-vacancy centers in diamond, Hall-bars, and superconducting quantum interference devices. Over the past 3 years, we have been using nanowire (NW) force sensors as ultra-sensitive MFM probes. Using NWs functionalized with magnetic tips, we strive to map magnetic fields and dissipation with enhanced sensitivity and resolution compared to the state of the art and to apply these new capabilities to study magnetization in 2D materials.

The key component of a force microscope is the force sensor, which consists of a mechanical transducer, used to convert force into displacement, and an optical or electrical displacement detector. In MFM, "top-down" Si cantilevers with sharp tips coated by a magnetic material have been the standard transducer for years. Under ideal conditions, state-of-the-art MFM can reach spatial resolutions down to 10 nm, although more typically around 100 nm. These cantilevers are well-suited for the measurement of the large forces and force gradients produced by strongly magnetized samples. The advent of NWs and carbon nanotubes grown by "bottom-up" techniques now gives researchers access to much smaller force transducers than ever before. This reduction in size implies both a better force sensitivity and potentially a finer spatial resolution. Sensitivity to small forces provides the ability to detect weak magnetic fields and therefore to image subtle magnetic patterns; tiny concentrated magnetic tips have the potential to achieve nanometer-scale spatial resolution, while also reducing the invasiveness of the tip on the sample under investigation. Such improvements are crucial for imaging nanometer-scale magnetization textures in 2D systems.

Recent efforts have demonstrated the use of single NWs as sensitive scanning force sensors [1]. When clamped on one end and arranged in the pendulum geometry, i.e. with their long axes perpendicular to the sample surface to prevent snapping into contact, they probe both the size and direction of weak tip-sample interactions. NWs have been demonstrated to maintain excellent force sensitivities around 1 aN/Hz$^{1/2}$ near sample surfaces (<100 nm), due to extremely low noncontact friction. As a result, NW sensors have been used as transducers in force-detected nanometer-scale magnetic resonance imaging and in the measurement of tiny optical and electrical forces. In a proof-of-principle microscopy experiment in the Poggio lab, we showed that a magnet-tipped NW can be sensitive to magnetic field gradients of just a few mT/(m Hz$^{1/2}$), equivalent to the gradient produced by a few tens of Bohr magnetons or a few nA of flowing current at a distance of a few hundred nanometers [2]. Such sensitivity compares favorably to that of other magnetic microscopies, including scanning Hall microscopy, scanning SQUID microscopy, and scanning nitrogen-vacancy magnetometry [3].

Goals

Despite these promising features, until now, only proof-of-principle NW MFM experiments have been carried out on the well-known magnetic field profile of a current-carrying wire [2, 4]. We intend to move past this demonstration stage by:

1. optimizing the magnet-tipped NW transducers to achieve the highest possible sensitivity and resolution.
2. using the new scanning probes to image magnetism in 2D vdW systems and the surface of bulk chiral magnets.

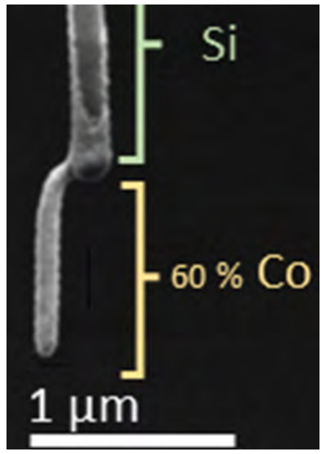

Figure 1: Scanning electron micrograph of a Co tip deposited by FEBID (at the SNI Nano Imaging Lab) on the free end of a Si NW. The Si NW (length: 20 µm) was grown by the Budakian group (Waterloo).

Results

In the fourth year of work, we have been focusing on imaging experiments on 2D magnets as well the surface of bulk chiral magnets. Both of these systems present a number of open questions relating to the spatial configuration of magnetic phases and phase transitions. NW MFM, which combines high magnetic field sensitivity and high spatial resolution, is ideally suited for this task. In collaboration with the Maletinsky group, who is studying the 2D magnet EuGe$_2$ using scanning nitrogen-vacancy (NV) microscopy (SNVM), we have studied bilayer samples of EuGe$_2$ [4] via NW MFM. The NW MFM images are complementary to the SNVM images, because they provide different contrast, i.e. magnetic field gradients and magnetic susceptibility, and can function under much higher magnetic fields. Using our NW MFM technique, we find a phase-separated state and follow its evolution with temperature and magnetic field. Spatial maps reveal that the characteristic length-scale of magnetic domains is in the hundreds of nanometers. These observations strongly shape our understanding of the magnetic states in 2D materials at the monolayer limit and contribute to engineering of ultra-compact spintronics. A manuscript on this work has been written and is currently under submission.

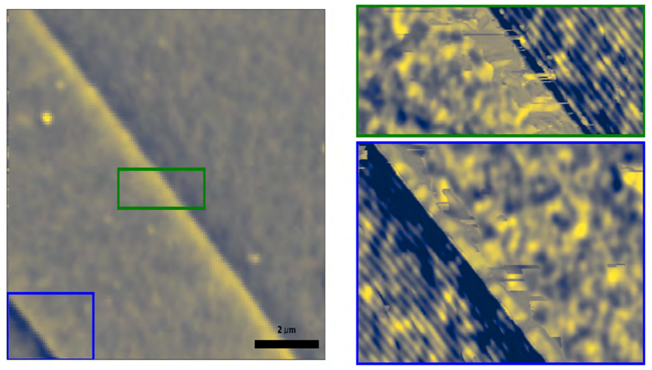

Figure 2: NW MFM images of the (001) surface of Cu2OSeO3, The images show the sample after zero-field cooling in an applied field of 32 mT applied along [001]. 3 domains of the helical phase with modulations of 60 nm along <100> are visible. The domains with clear modulation visible have in-plane modulation vectors while the third domain has an out-of-plane modulation vector.

To exploit the high-spatial resolution of around 50 nm offered by NW MFM, we have also started imaging periodically modulated magnetic phases in the insulating cubic helimagnet Cu$_2$OSeO$_3$. These measurements complement scanning superconducting quantum interference device (SQUID) microscopy (SSM) measurements carried out in our own group on the same material. They have given us new insights about modulated phases with spatial periods around 60 nm, which were too small to be apparent in SSM images [5].

Recently, we have also studied the magnetically-controlled vortex dynamics in a ferromagnetic superconductor, using our NW MFM. In particular, we investigated the material EuFe$_2$(As$_{1-x}$P$_x$)$_2$, which is an iron-based superconductor with a maximum critical temperature of 25 K. It is unique in that it exhibits full coexistence with ferromagnetic order below 19 K. We study the interplay between superconductivity and magnetism in this regime by imaging the magnetic field gradients at the sample surface via NW MFM, as shown in Figure 3. The results are summarized in a manuscript submitted with our collaborators [6].

The success of NW MFM in local magnetic susceptibility imaging of EuGe$_2$ has also led us to start new and very promising measurements of the dependence on thickness of the magnetic phase transitions in other 2D magnets, including Cr$_2$Ge$_2$Te$_6$.

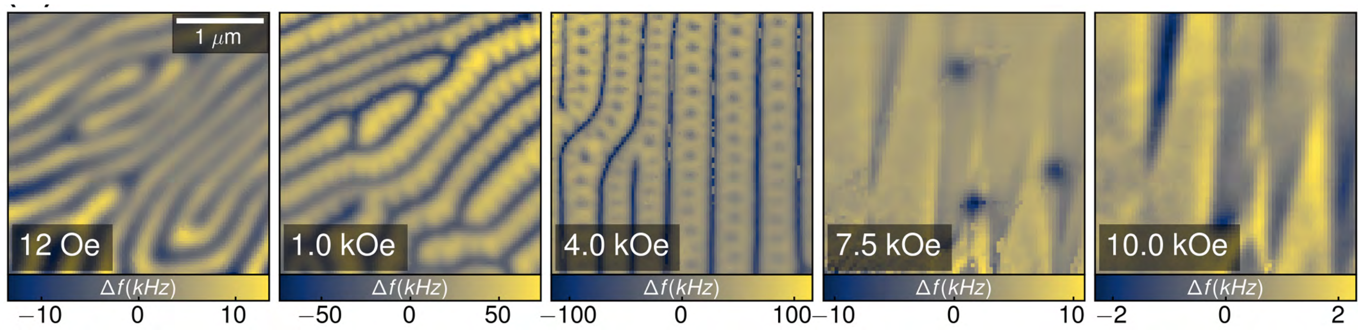

Figure 3: Evolution of the domain vortex state in EuFe2(As1-xPx)2 with applied field 3 µm x 3 µm NW MFM images captured at T = 4.3 K.

References

[1] N. Rossi, F. R. Braakman, D. Cadeddu, Denis Vasyukov, G. Tütüncüoglu, A. Fontcuberta i Morral, and M. Poggio, "Vectorial scanning force microscopy using a nanowire sensor", Nat. Nanotechnol. 12, 150 (2017).

[2] N. Rossi, B. Gross, F. Dirnberger, D. Bougeard, and M. Poggio, "Magnetic Force Sensing Using a Self-Assembled Nanowire", Nano Lett. 19, 930 (2019).

[3] E. Marchiori, L. Ceccarelli, N. Rossi, L. Lorenzelli, C. L. Degen, and M. Poggio, "Nanoscale magnetic field imaging for 2D materials", Nat. Rev. Pys. 4, 49 (2022).

[4] A. M. Tokmachev, D. V. Averyanov, A. N. Taldenkov, O. E. Parfenov, I. A. Karateev, I. S. Sokolov, and V. G. Storchak, "Lanthanide f7 metalloxenes – a class of intrinci 2D ferromagnets", Mater. Horizons 6, 1488 (2019).

[5] E. Marchiori, G. Romagnoli, L. Schneider, B. Gross, P. Sahafi, A. Jordan, R. Budakian, P. R. Baral, A. Magrez, J. S. White, and M. Poggio, "Imaging magnetic spiral phases, skyrmion clusters, and skyrmion displacements at the surface of bulk Cu2OSeO3", Commun. Mater. 5, 202 (2024)

[6] J. A. Wilcox, L. Schneider, E. Marchiori, V. Plastovets, A. Buzdin, P. Sahafi, A. Jordan, R. Budakian, T. Ren, I. Veshchunov, T. Tamegai, S. Friedemann, M. Poggio, and S. J. Bending, "Magnetically-controlled vortex dynamics in a ferromagnetic superconductor", arXiv:2412.04098 (2024).

Hybrid atom-optomechanical system in the quantum regime

Project P1907: Spin-opto-nanomechanics
Project Leaders: P. Treutlein and P. Maletinsky
Collaborator: G.-L. Schmid (SNI PhD Student), M. Bosch Aguilera, A. Huot de Saint-Albin, A. Mitchell Galvao de Melo

Quantum technologies have seen an impressive progress, leading to the development of numerous individual systems performing very well in one specific task. For instance, photons can be used to transmit quantum information over long distances, spins serve as precise magnetometers or atomic clocks, and mechanical oscillators are very precise force sensors. However, many real-world problems require quantum devices that can combine different functionalities, making hybrid quantum systems particularly intriguing. By combining quantum systems with complementary functionalities, hybrid systems can leverage the strengths and mitigate the weaknesses of individual components. Hybrid spin-mechanical systems are a very interesting in this context. While spins are microscopic systems for which quantum control is well established, mechanical oscillators are macroscopic systems which can be functionalized to couple to various forces [1].

In our experiment, we couple the collective spin of an atomic ensemble to the vibrations of a nano-mechanical membrane. Exploiting the strong coupling of the membrane to the spin ensemble [2], we performed classical state-swaps between the membrane vibrational state and the atomic spin [3]. In this way, the membrane can be cooled to 216 mK in 200 µs. These experiments were performed in the strong coupling regime. In order to implement quantum protocols with the coupled system, we have to reach the regime of quantum coherent coupling. While in the so-called strong coupling regime, the coupling rate $2g$ is larger than the average decay rate of the systems, $2g > \gamma_s + \gamma_m$, for quantum coherent coupling the coupling rate must exceed the average decoherence rate, $2g > \gamma_{s,\mathrm{dec}} + \gamma_{m,\mathrm{dec}}$.

In our system, the coupling is mediated by light (see below for details). To achieve quantum coherent coupling between the systems, the coupling of each individual system to the light must be stronger than the total decoherence of the system $\gamma_{i,\mathrm{dec}}$. The total decoherence rate consists of the stochastic drive by the measurement backaction, by the thermal environment and by technical noise. The figure of merit is the cooperativity $C_i = \Gamma_i/\gamma_{i,\mathrm{dec}}$, which is the ratio between the coupling strength to the light Γ_i and the total decoherence rate $\gamma_{i,\mathrm{dec}}$.

In the following, we describe first the effort of bringing both individual systems to the regime of large cooperativity $C_i > 1$. Then we discuss the coupling between the two systems mediated by light.

Atomic Spin

The collective atomic spin is formed by an ensemble of 2×10^7 ultracold 87Rb atoms in an optical dipole trap. The atoms are pumped into the state $|F = 2, m_F = -2\rangle$. Using a static magnetic field, the atomic Larmor frequency can be tuned into resonance with the membrane frequency. The atomic spin interacts with the light by the off-resonant Faraday interaction. To characterize the spin-light coupling, we measure the light after the first interaction with the spin (instead of sending it to the membrane as in the coupling experiment). If the atoms are well polarized and not excited, we can detect the quantum noise of the atoms imprinted on the light.

A measurement of the atomic noise signal on the light as function of the number of atoms in the cloud is shown in Fig. 1. Together with the data, a theory curve is plotted which is calculated from the geometry of the atomic cloud and the coupling beam. The theory reproduces the measurement well, which suggests that we understand the processes which drive the atomic spin in this limit.

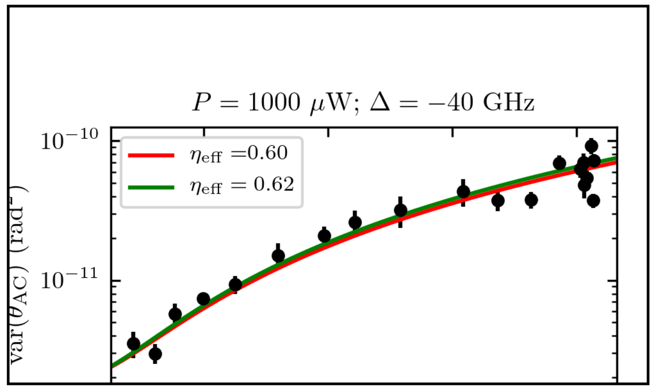

Fig. 1: Measurement of the quantum noise on the light after the interaction with the spin. The vertical axis shows the noise on the light measured with the spin aligned orthogonal to the probe beam. The horizontal axis shows the DC Faraday signal measured with the spin parallel to the probe beam, which is proportional to the atom number. The green line shows the theoretical expectation calculated from the geometrical overlap of the coupling beam and the atomic cloud. The red line shows a fit to the data with one fitting parameter, the overall spin-light coupling strength.

Optomechanical System

In the optomechanical system, the membrane with a phononic bandgap shield in the frame, which was used in our previous work [2,3], has been replaced by a nano-pillar membrane [4]. The nano-pillar membrane exhibits a mechanical quality factor of $Q_m = 5.1 \times 10^7$ at a temperature of 10 K, more than an order of magnitude higher than that of the previous membrane. This improvement, combined with cryogenic cooling, enables the optomechanical system to achieve high quantum cooperativity.

One way to measure the cooperativity of the optomechanical system is by performing a cooling experiment by cavity dynamical backaction cooling (shown in Fig. 2). At a cryostat temperature of 10 K the membrane was cooled to an occupation of 11 phonons, which is the theoretical limit for our current cavity with a linewidth of $\kappa = 2\pi \times 96$ MHz, placing the system in the unresolved sideband regime. When cooled to this theoretical limit, the optomechanical system is driven predominantly by quantum noise of the light, equivalent to an optomechanical cooperativity exceeding unity.

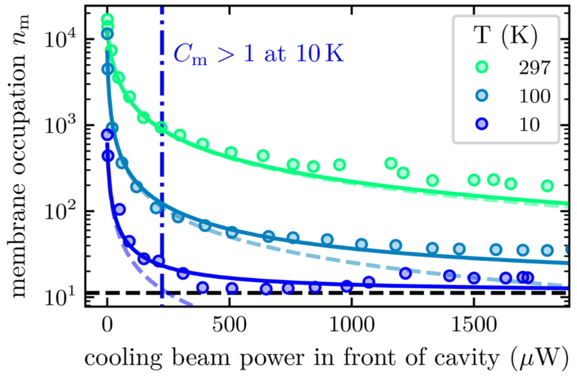

Fig. 2: Cavity dynamical backaction cooling of the membrane at three different cryostat temperatures. Together with the data, the theoretical expectations are plotted as solid lines. The dashed (colored) lines show the membrane occupation when neglecting the backaction noise of the light. At high temperatures, neglecting the backaction gives a good estimate. The dashed black line shows the theoretical cavity dynamical backaction cooling limit for our system. At 10 K, the limit of $C_m > 1$ is reached for high optical power (dash-dotted line), where the driving force is dominated by quantum noise of the light.

Hybrid setup

Now that both the spin-light interface and the optomechanical interface can be operated in the regime of large quantum cooperativity, the two systems can be coupled in the quantum coherent coupling regime. Here, we introduce briefly the coupling mechanism between the two systems:

The coupling of the atomic spin to the mechanical oscillator is mediated by light so that the two systems can be separated by a macroscopic distance, in our case by about one meter [2]. To achieve a Hamiltonian coupling between the two systems, the light forms a loop: The coupling laser interacts first with the spin, then with the membrane, and then once again with the spin, as sketched in Fig. 3 and detailed in [2]. By shifting the phase of the quantum signal on the light by $\phi = \pi$ before the second interaction with the spin, the second spin-light interaction is the time-reversal of the first one, cancelling the backaction of the light onto the spin.

Summary and Outlook

Previously, coupling experiments were performed with a membrane at room temperature, resulting in strong coupling between the two systems [2,3]. With our improved system, reaching the regime of quantum coherent coupling is feasible. The next step is to perform the coupling experiment with the nano-pillar membrane at cryogenic temperatures and the improved atomic system. The parameters of our improved setup should allow us to achieve ground-state cooling of the membrane by coherent feedback with the spin [3]. Exploiting the quantum coherent coupling, we could then create quantum entanglement of the spin and the membrane over a distance of more than one meter.

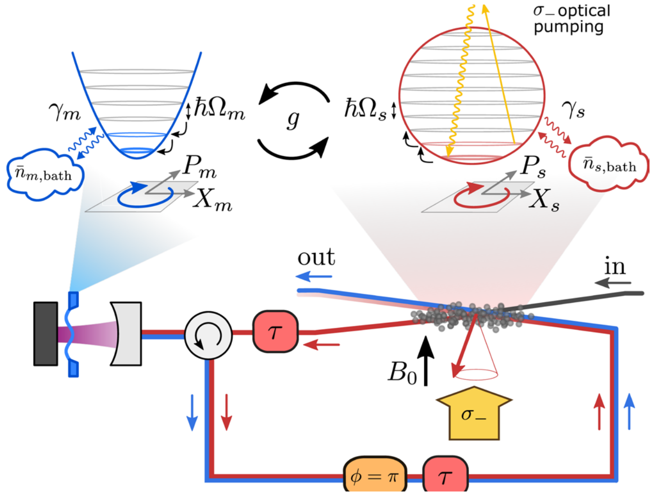

Fig. 3: Sketch of the light-mediated spin-membrane coupling. Light interacts first with the spin, then with the membrane, and then again with the spin. On the way back from the membrane to the spin, a π-phase is imprinted on the light, rendering the spin-membrane interaction effectively Hamiltonian for zero delay τ = 0. The systems can be approximated by harmonic oscillators of frequencies Ω_m and Ω_s with damping rates γ_m and γ_s coupling them to a bath with $\bar{n}_{m,\mathrm{bath}}$ and $\bar{n}_{s,\mathrm{bath}}$ phonons, respectively. The oscillators are coupled at a rate g. coupled at a rate g.

References

[1] P. Treutlein, C. Genes, K. Hammerer, M. Poggio, and P. Rabl. Hybrid Mechanical Systems. In: Cavity Optomechanics: Nano- and Micromechanical Resonators Interacting with Light. Ed. by M. Aspelmeyer, T.J. Kippenberg, and F. Marquardt. Berlin, Heidelberg: Springer Berlin Heidelberg, pp. 327–351 (2014)

[2] T. M. Karg, B. Gouraud, C. T. Ngai, G.-L. Schmid, K. Hammerer, and P. Treutlein, Light-mediated strong coupling between a mechanical oscillator and atomic spins 1 meter apart, Science 369, 174 (2020).

[3] G.-L. Schmid, C. T. Ngai, M. Ernzer, M. Bosch Aguilera, T. Karg, and P. Treutlein, Coherent feedback cooling of a nanomechanical membrane with a spin, Phys. Rev. X 12, 011020 (2022).

[4] D. Høj, U. B. Hoff, U. L. Andersen, Ultracoherent Nanomechanical Resonators Based on Density Phononic Crystal Engineeering, Phys. Rev. X 14, 011039 (2024).

Chiral luminescent Pt(II) complexes – enantiomer recognizing nanowires

Project P1908: Chiral Recognition in Molecular Nanowires from Square-Planar Platinum(II) Complexes
Project Leaders: O.S. Wenger and C. Sparr
Collaborator: A. Huber (SNI PhD Student)

In the context of chiral recognition, we designed new nanostructured “chiral nose”-type materials to selectively sense chiral volatile organic compounds (VOCs).[1,2] Controlled helical superstructures composed of stacked square planar platinum(II) complexes were of main interest to us. Interactions of small chiral molecules within a crystal lattice can provoke changes in photoluminescence, vapochromism,[3] or electrical conductance, thus leading to sensing behavior. Chiral recognition based on molecular nanowires seems underexplored until now.

Ideally, stereoisomers of specific VOC analytes could interact with the nanowire crystal lattice by intercalation, or through C-H-π, π-π, or other interactions directly at the atropisomeric moieties of the complexes.

The tendency of square planar Pt(II) complexes to form stacked aggregates arises from weak metal-metal interactions between the $5d_{z2}$ orbitals upon close contact (<3.5 Å).[4] Thus, Pt(II) complexes are known to form aggregates with distinct properties.[5,6] Application of such systems for chiral recognition is however underexplored so far.[7]

Stereogenic Pt(II) isocyanide complex

Taking advantage of the atroposelective arene forming method developed in the Sparr group, we prepared conformationally well defined 1,2-binaphthyl moiety.[8] The atropisomeric scaffold was then transformed into the isocyanide ligand, following methods developed in the Wenger group (Scheme 1).[9]
Complex (1) was obtained after applying optimized reaction conditions using a precursor Pt(II) complex with the bisanionic tridentate bis(trifluoro-methyltriazolyl)pyridine ligand

Absorption and aggregation of complex (1)–tested enantiomer recognition

With the desired complex (1) in hand, we first studied the absorption and aggregation in solution. Figure 1 a) shows the UV-vis absorption spectra of complex 1 (1.0×10^{-5} M) in varying ratios of CHCl3 /n-hexane. In polar solvent, 1 shows the typical intra-ligand and inter-ligand charge transfer bands below 400 nm and weak metal-to-ligand charge transfer bands between 400 – 450 nm. In less polar $CHCl_3$ /n-hexane, 1/9, a new absorption band was formed at 385 nm, indicative for metal–metal-to-ligand charge transfer. In addition, the solution turned into a colloidal dispersion within seconds, which supported the hypothesis of a nanowire assembly. Scanning electron microscope images (SEM) showed bent nanowires with up to 12 µm length.

Figure 1 b) shows the characteristic UV-vis absorption band of complex **1** (1.0×10^{-5} M) in $CHCl_3$ /n-hexane, 1/9 in the aggregated state (light blue). Upon addition of excess R/S 2-butanol (BuOH), the absorbance changed significantly. While R-BuOH had a minor effect on the band at 385 nm, addition of S-BuOH led to a drastic decrease in the absorbance. This behavior was reproducible and reversible. This observation represents a proof of principle for chiral recognition. Similar effects could be measured upon addition of enantiomers from 2-phenylethanol, alpha-pinene, and limonene.

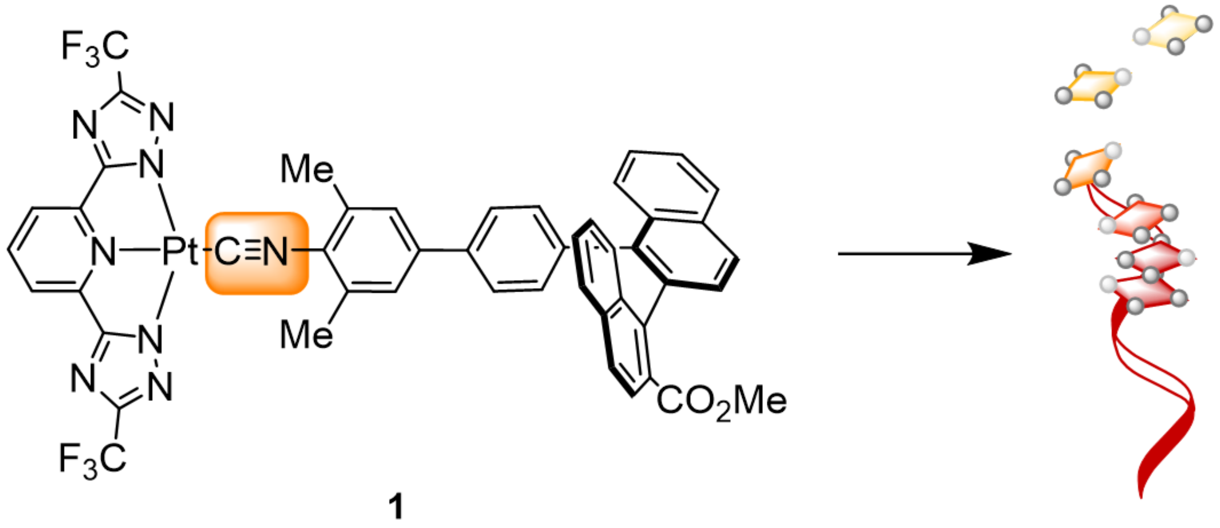

Scheme 1: Molecular structure of complex 1 and schematic representation of the anticipated supramolecular aggregation.

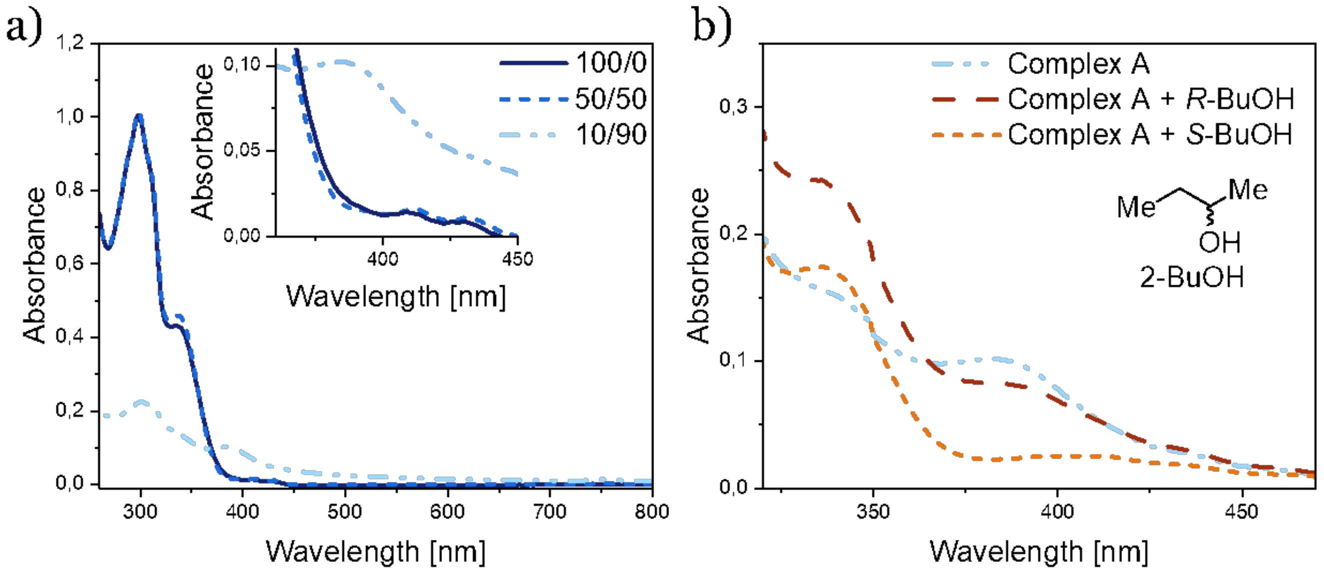

Figure 1: UV-vis 2absorption (a) spectra of (1) in $CHCl_3$ /nhexane (1.0×10^{-5} M).

Conclusion

The chiral Pt complex was synthesized and characterized by UV-Vis absorbance, photo-luminescence, circular dichroism, and SEM. Under specific conditions, the complex showed the expected aggregation behavior. More importantly, the aggregated nano-assembly exhibited remarkable changes in the UV-vis absorption upon exposure to chiral VOC analytes. With these results, we successfully completed the SNI project. A publication of our results is in preparation.

References

[1] A. Prabodh, D. Bauer, S. Kubik, P. Reb-mann, F. G. Klärner et al. “Chirality Sensing of Terpenes, Steroids, Amino Acids, Peptides and Drugs with Acyclic Cucurbit[n]urils and Molecular Tweezers”, Chem. Commun. 56, 4652–4655 (2020).

[2] Z. A. De los Santos, C. Wolf, “Optical Terpene and Terpenoid Sensing: Chiral Recognition, Determination of Enantiomeric Composition and Total Concentration Analysis with Late Transition Metal Complexes”, J. Am. Chem. Soc. 142, 4121–4125 (2020).

[3] O. S. Wenger, “Vapochromism in Organometallic and Coordination Complexes: Chemical Sensors for Volatile Organic Compounds”, Chem. Rev. 113, 3686–3733 (2013).

[4] W. B. Connick, R. E. Marsh, W. P. Schaefer, H. B. Gray, “Linear-Chain Structures of Platinum(II) Diimine Complexes”, Inorg. Chem. 36, 913–922 (1997).

[5] S. Chakraborty, A. Aliprandi, L. De Cola “Multinuclear PtII Complexes: Why Three is Better Than Two to Enhance Photophysical Properties” Chem. Eur. J. 26, 11007–11012 (2020).

[6] V. W. Yam, V. K. Au, S. Y. Leung “Light-Emitting Self-Assembled Materials Based on d8 and d10 Transition Metal Complexes” Chem. Rev. 115, 7589–7728 (2015).

[7] M. J. Cich, I. M. Hill, A. D. Lackner, R. J. Martinez, T. C. Ruthenburg, Y. Takeshita, A. J. Young, S. M. Drew, C. E. Buss, K. R. Mann “Enantiomerically selective vapochromic sensing” Sensors and Actuators B 149, 199–204 (2010).

[8] D. Lotter, A. Castrogiovanni, M. Neuburger, C. Sparr, “Catalyst-Controlled Stereodivergent Synthesis of Atropisomeric Multiaxis Systems”, ACS Cent. Sci. 4, 656–660 (2018).

[9] L. Büldt, X. Guo, A. Prescimone, O. S. Wenger “A Molybdenum(0) Isocyanide Analogue of Ru(2,2’-Bipyridine)32+: A Strong Reductant for Photoredox Catalysis”, Angew. Chem. Int. Ed. 55, 11247–11250 (2016).

Surface chemistry of hafnium oxide nanocrystals as X-ray computed tomography contrast agents

Project P2001: Imaging cardiovascular macro- and micro-structure using HfO2 nanocrystals as X-ray tomography
Project Leaders: J. De Roo and A. Bonnin
Collaborator: Elizaveta Maksimova (SNI PhD Student)

Introduction

With the rapid development of nanotechnology and nanomedicine, there is a growing research interest in employing nanomaterials to improve the efficiency of disease diagnosis and treatment. The surface modification of the nanomaterials impacts the performance and success of carious applications by enabling selective and precise targeting. [1] Over the last years, click and biorthogonal reactions have become one of the most reliable and frequently used approaches for payloads coupling on the surface of nanoparticles. [2] However, there is still a lack of standardized and precise procedures for the preparation of nanoparticles with such functional groups.

In this work, we study the surface chemistry of hafnium oxide nanocrystals as they have been recently reported as promising contrasts agents for x-ray computed tomography. [3] To retain colloidal stability in conditions close to physiological, nanocrystals were coated with biocompatible ligands. To provide the targeting moiety, nanocrystals were further modified with azide groups to open the possibility of bioconjugation via strain-promoted azide-alkyne cycloaddition. Two independent methods for the quantification of azide functional groups were developed and validated.

Preparation of HfO_2 nanocrystals

Hafnium oxide nanoparticles were synthesized via well-established solvothermal process. [3] Hafnium tert-butoxide and benzyl alcohol were heated at 220°C for 96 hours in muffle furnace (Fig. 1a). After synthesis, the nanocrystals are isolated, purified and stabilized with 2-[2-(2-methoxyethoxy) ethoxy]acetic acid (MEEAA) to impart colloidal stability of nanoparticles.

The synthesis resulted in the formation of monoclinic (Fig. 1b) ellipsoidal nanoparticles with major axis length of (3.8 ± 0.6) nm and minor axis length of (2.4 ± 0.3) nm, as confirmed by TEM (Fig. 1c).

From the variety of bioconjugation options, we have chosen strain promoted alkyne azide cycloaddition also known as copper-free click-chemistry as highly specific, biocompatible and bioorthogonal reaction. It is a fast reaction with no catalyst required and it occurs under physiological conditions. [4] To enable this reaction, we have to provide azide groups on the surface of nanocrystals and functionalize biomolecules of interest with dibenzocyclooctyne (DBCO) group.

To prepare nanocrystal with functional groups, the weakly binding carboxylate ligand MEEAA was subsequently exchanged for a mixture of nitrodopamine-based ligands in which the ratio of purely PEGylated to azide-terminated catechols was varied to obtain particles with 2, 5 or 10 azides per nanoparticle. The PEGylated ligands provide colloidal stability in aqueous buffers, whereas the azides determine the valency of the particle and enable the click-chemistry reaction.

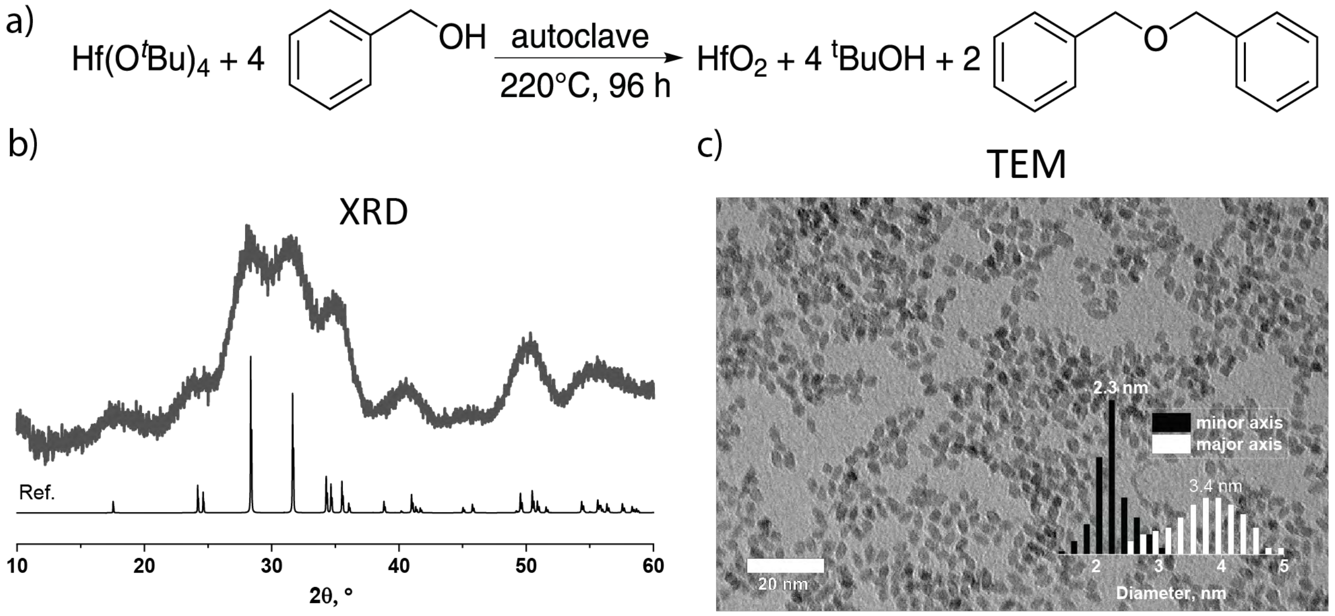

Fig. 1: a) Synthetic route of HfO2 nanoparticles; b) powder x-ray diffraction analysis of the formed nanocrystals; c) TEM picture of nanocrystals

Azide groups quantification by fluorescence quenching

We varied the amount of azide-carrying catechols in the ligand shell from 0 to 10 per NP to test the possibility of quantification of low amounts of functional groups necessary for precise bioconjugation.

The first method that we developed to quantify azide groups on the surface of NPs leverages the fluorescence quenching effect of the nitrocatechol ligands on covalently bound dye molecules by photoinduced charge transfer (PCT) (Fig.2a). The fluorescence of AF488 was quenched until the dye:NP ratio in the reaction mixture was equal to the actual valency of NPs. Above that concentration, the dye remains in its free form, and thus is fluorescent. By fitting two linear regions of the graph, we were able to find their intersection point that was lower than the target value of N_3/NP and represents the actual ligand density on the surface. The repeatability and reproducibility of this method was proved by repeating this experiment three times.

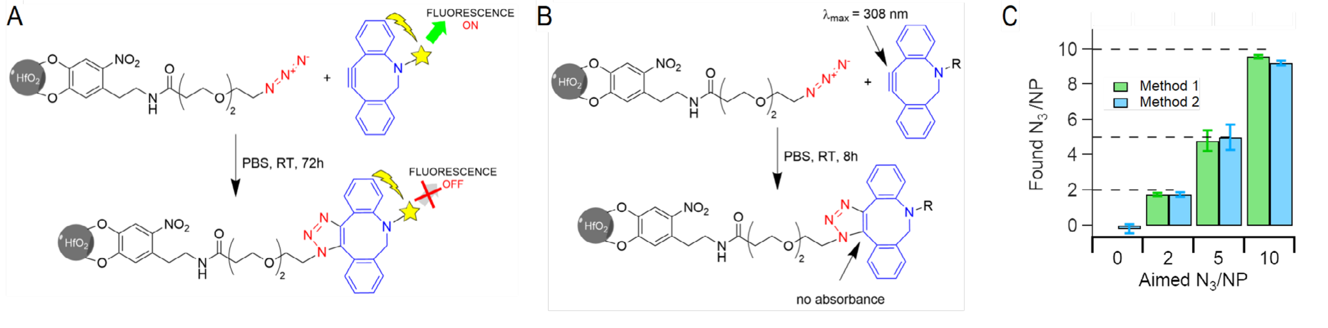

Fig.2: a) Schematic process behind the quantification method 1: DBCO-functionalized dye emits green light in the free form, but the fluorescence is quenched upon click reaction with surface azide groups due to PCT to acceptor nitrodopamine groups of the ligands; b) Chemical reaction behind the method 2: UV-tracking of azide-carrying nanoparticles with alkyne; c) Comparison of the quantification results by two developed methods.

The second method represents a general strategy based on following the alkyne absorbance during the click reaction, which is independent on the core or ligand composition of NPs (Figure 2b). In this method, the ligand density was calculated from the kinetic curves of alkyne consumption and was found to be similar to the one found by Method 1. The limit of detection of Method 2 was found to be as low as 0.53 N_3/NP. From Figure 1c it can be seen that both methods show a similar result of azide surface density, proving that the methods can be used interchangeably depending on the limitations of the studied system.

Conclusions

In conclusion, we have proposed two methods to quantify azide groups on the surface of the nanoparticles that are in agreement with each other. We believe that quantitative analysis of surface functional groups will play an important role in precise bioconjugation that is crucial for cell targeting. Both methods do not require purification and can be applied to colloidally stable NPs of different core and ligands nature. Our approach could be beneficial in the precise design of targeted contrast agents for x-ray computed tomography or magnetic resonance imaging.

References

[1] S.V.Kaymaz, H.M.Nobar, H.Sarigül, C.Soylukan, L.Akyüz, et al., “Nanomaterial surface modification toolkit: Principles, components, recipes, and applications“, Adv. Colloid Interface Sci 322, 103035 (2023)

[2] L.Taiariol, C.Chaix, C.Farre, E.Moreau, “Click and Bioorthogonal Chemistry: The Future of Active Targeting of Nanoparticles for Nanomedicines? “, Chem.Rev. 122, 1 (2022)

[3] J.Marill, N.M.Anesary, P.Zhang, S.Vivet, E.Borghi, et al., “Hafnium oxide nanoparticles: toward an in vitropredictive biological effect? “, Radiat.Oncol. 9, 150 (2014)

Outer membrane damage activates a bacterial attack response

Project P2002: A Death-Dealing Nanomachine
Project Leaders: R.Y.H Lim, M. Basler
Collaborator: M. Brüderlin (SNI PhD Student)

Introduction

Bacterial cells activate specific signaling pathways in response to environmental stimuli [1]. However, bacterial cells are also sensitive to interbacterial and bacteria-host contact interactions. Recent studies have attributed many of these interactions to mechanosensitive pathways [2]. In this project, we investigated the reaction of bacteria to mechanical stress by means of correlative atomic force microscopy (AFM) and live-cell fluorescence microscopy (FM) (Fig. 1) [3].

Bacteria employ a sophisticated response mechanism(s) through the assembly and activation of multiprotein complexes. These highly specialized systems enable bacteria to retaliate against competing organisms, delivering toxic proteins in a targeted and efficient manner. To understand these bacterial mechanisms is to provide deep insight into their dynamic survival strategies, pathogenesis, and potential therapeutic interventions.

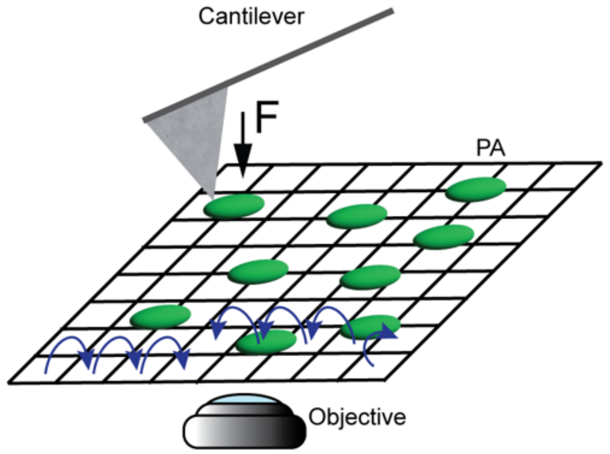

Fig. 1: Correlative AFM/FM of live bacterial cells. The green rods indicate bacterial cells, and the blue arrows show the path of the AFM cantilever during force mapping.

Force dependency of response

Mechanical indentations applied using an AFM tip were found to induce the multiprotein complex assembly in a highly localized manner. Forces as low as 7 nN were sufficient to prompt a response, with higher forces increasing the likelihood of activation. This threshold-based mechanism ensures that the bacteria respond specifically to sufficiently strong mechanical insults, avoiding unnecessary activation of its defense system.

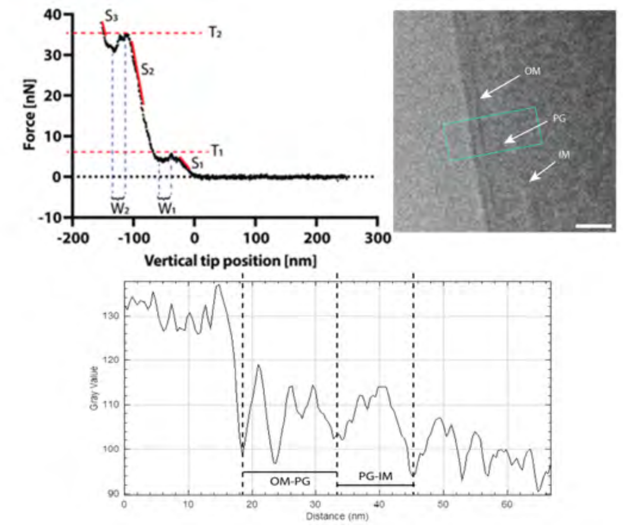

Fig. 2: Analysis of AFM force curves and corresponding EM image. The force curve (top left) shows two distinct puncture events T1 and T2 with consistent thicknesses W1 and W2. The EM image (top right) and corresponding plot profile confirm those distance to be OM-PG and Pg-IM.

By analyzing force curves obtained during AFM experiments, we observed that two distinct puncture events could be observed (Fig. 2). These observed barriers were shown to correspond to distances between the outer membrane-peptidoglycan-inner membrane borders by electron microscopy. This finding indicates that the puncture of one or both membranes serves as a primary sensor for environmental threats, translating mechanical stimuli into a biochemical response.

Outer membrane damage induced trigger

The use of correlative AFM/FM allowed us to observe this process in real time, revealing that the multiprotein complex assembles within seconds of membrane damage (Fig. 3). The dynamic nature of this response underscores the efficiency of bacteria in mobilizing its defense system against potential threats. By localizing the assembly of the multiprotein complex to sites of membrane damage, the bacteria minimize energy expenditure while maximizing the effectiveness of its response.

Using polymyxin B nonapeptide (PMBN), an outer membrane-destabilizing agent, we confirmed that outer membrane damage alone is sufficient for activating the multiprotein complex. This finding suggests that the outer membrane functions as a critical sensory interface, enabling the bacteria to distinguish between harmless environmental fluctuations and genuine threats.

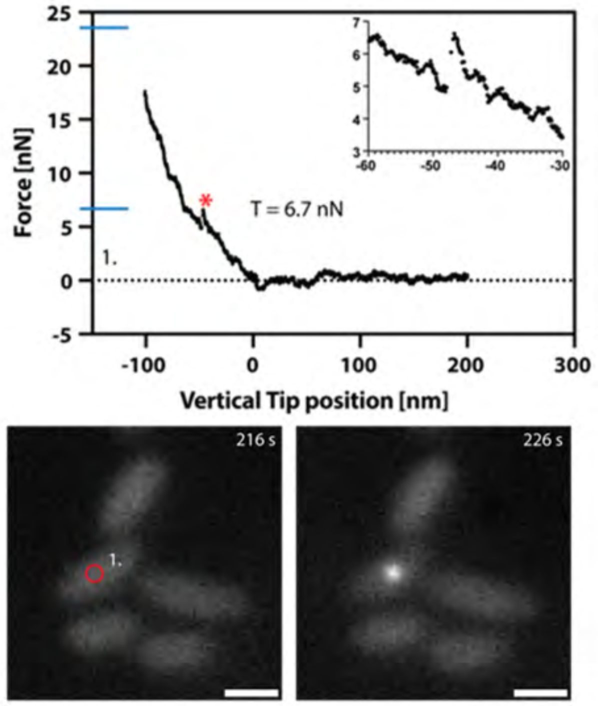

Fig. 3: Single puncture event still leads to assembly. The AFM force curve (top) shows a single puncture event (red asterisk) and the corresponding FM image series (bottom) shows the point of AFM indentation (red circle) and the resulting assembly.

Signaling pathway

Hence, the activation of the multiprotein complex begins with the detection of outer membrane breaches, which likely expose signaling molecules normally confined within the periplasmic space. These signals activate the inner membrane kinase, a protein in the pathway, leading to the phosphorylation of downstream targets. This phosphorylation event initiates the assembly of the multiprotein complex.

Because multiprotein complex assembly is highly localized to sites of membrane damage, the bacteria ensure that its retaliatory response is both efficient and targeted. This level of precision minimizes collateral damage and optimizes resource use, enhancing the bacteria's ability to compete with other microorganisms in its environment.

Conclusion and outlook

By elucidating the triggers, dependencies, and signaling pathways involved in the multiprotein complex activation, our study provides valuable insights into the bacteria's defense strategies. These findings have important implications for the development of antimicrobial therapies, as they highlight potential targets for disrupting the bacteria's ability to sense and respond to environmental threats.

Moving forward, further studies are needed to explore the broader applicability of these findings. Investigating how similar mechanisms operate in other bacterial species could reveal universal principles underlying microbial defense systems. Additionally, understanding the interplay between mechanical and chemical stimuli in triggering the multiprotein complex activation may uncover new strategies for controlling bacterial infections.

In conclusion, our work underscores the remarkable adaptability of bacteria and its ability to precisely calibrate its responses to environmental challenges. By combining advanced imaging techniques with molecular biology, this study has laid the groundwork for future research aimed at unraveling the complexities of bacterial survival and competition.

References

[1] Laventie, B.-J. and Jenal, U. Surface Sensing and Adaptation in Bacteria. Annual Review of Microbiology 74:735-760 (2020).

[2] Peterson, S., Bertolli, K. and Mougous, J. The Central Role of Interbacterial Antagonism in Bacterial Life. Current Biology 30.19 (2020): R1203-R1214.

[3] Marek Basler et al., Tit-for-tat: Type VI secretion system counterattack during bacterial cell-cell interactions. Cell, V 152, (2013)

Multi-scale surface characterization of a multiferroic Rashba semiconductor

Project P2004: Local manipulation of spin domains in a multiferroic Rashba semiconductor
Project Leaders: M. Muntwiler and T. Jung
Collaborator: M. Heinrich (SNI PhD Student)

Introduction

To fulfill the need of smaller and faster computational devices, non-traditional possibilities of quantum state manipulation move into the spotlight of current research. One such option, which is known as spintronics, makes use of the electron spin as a carrier of information. In particular, multiferroic materials, coupling multiple ferroic orders, such as ferroelectricity, ferromagnetism and ferroelasticity, in the same system [1], and Rashba materials are promising candidates towards spin control on the atomic level via energy-efficient electric fields (magnetoelectric coupling).

Project goals

In this project, we are studying rhombohedral alpha-GeTe, which is a ferroelectric-ferroelastic semiconductor. It recently received renewed attention when ARPES studies revealed a large Rashba spin-splitting in both bulk and surface electronic bands [2]. The addition of Mn into the crystal structure also renders the system ferromagnetic and studies suggest the possibility of switching its surface spin polarizations via external electric fields [3]. We are conducting a multi-scale and multi-technique investigation of the surface atomic, electronic and magnetic structures and interactions present in (GeMn)Te(111), with an emphasis on the correlation between ferroic polarizations, domains and atomic structure.
The combination of large area techniques, like synchrotron based X-ray photoelectron diffraction (XPD, PhD) and spectroscopy (XPS, ARPES), and local techniques, such as scanning tunneling microscopy and spectroscopy (STM, STS), allows us to probe complementary aspects of surface atomic and electronic structures. In particular, we combine experimental XPD and PhD measurements with multiple scattering calculations to reveal the surface atomic inter-layer distances, and apply an external gate voltage to study the effect of electric fields on atomic displacements. Angle resolved photoelectron spectroscopy (ARPES) together with scanning tunneling spectroscopy (STS) and quasiparticle interference (QPI) reveal the 3D dispersions of electronic states and their variations between different areas and doping levels. Finally, we want to use spin-polarized scanning tunneling microscopy (SP-STM) to visualize the magnetic domain structure and manipulate the spin polarizations on an atomic level with the electric field of the STM tip.

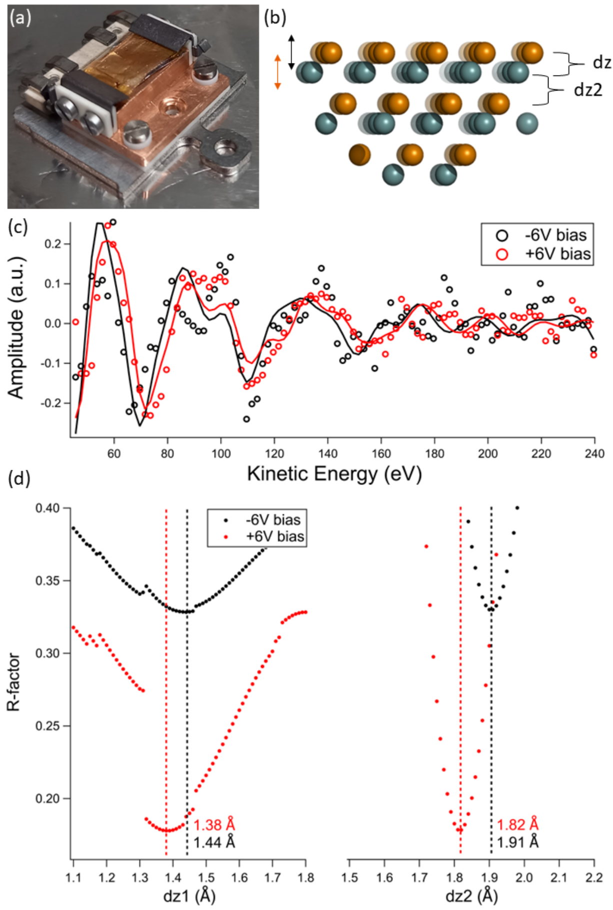

Fig. 1: Operando PhD measured on GeTe(111). (a): Sample setup with a gold mesh top electrode. (b): Surface atomic layer structure of GeTe(111) with the first two inter-layer distances dz1 and dz2 to be optimized. (c): Bias dependent PhD modulations measured on the Ge 3d peak (circles) and corresponding best fitting simulations (lines). (d): R-factors from a number of simulations with varied dz1 and dz2 parameters. Best fits (R-factor minima) for positive and negative polarity are indicated by vertical lines.

Results

The project started in July 2021. After studying the surface layer structure of alpha-GeTe(111) and finding a surface relaxation with respect to the bulk structure, we recently employed operando PhD measurements to measure the surface layer response to external electric fields. To this goal, we assembled a sample setup, which consists of a top electrode made of a gold micro-mesh covered with insulating Al2O3 placed on top of the sample surface. A photo of the setup is shown in fig. 1 (a). We applied an out-of-plane electric field and studied its impact on the surface atomic layer structure, fig. 1 (b), by measuring the Ge 3d photoemission peak along the [100] direction for a series of photoelectron kinetic energies. The resulting signal modulation was compared to multiple scattering calculations, with the best fitting structure fitted in figure 1 (c). Figure 1 (d) illustrates the structure optimization process, by plotting the R-factor, a measure of the goodness of fit of the simulated pattern to the experiment, in dependence of the first two inter-layer distances. We find that the applied bias shifts the surface layers by about 0.06 - 0.09 Å with respect to each other, meaning the electric field is contracting and expanding the crystal structure at the surface. This is an important result in the context of the material's multiferroicity and towards understanding the coupling of its ferroic orders.

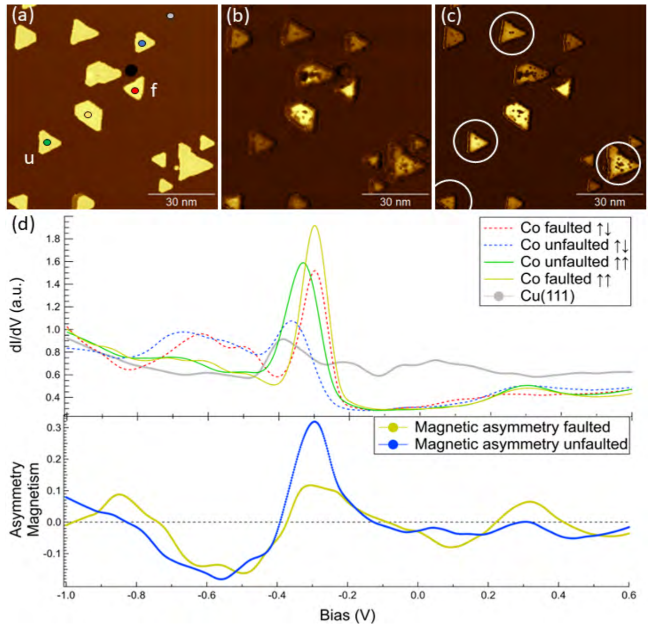

Fig. 2: Detecting spin-polarized signals in Co/Cu(111). (a): STM image of Co bilayers grown on Cu(111), forming faulted (f) and unfaulted (u) islands. (b): Spin-averaged LDOS map measured at U = -270 mV showing faulted islands in bright and unfaulted islands in dark. (c): Spin-polarized LDOS map at U = -270 mV showing an intensity difference for certain islands compared to the spin-averaged case in (b). (d): STS curves measured on Cu(111) and some islands as indicated in (a) (upper panel), with the extracted magnetic asymmetry illustrated in the lower panel.

With the goal of imaging the surface magnetic structure of GeMnTe(111), we have prepared spin-polarized MnNi and Co covered PtIr STM tips. A reference sample in the form of Co islands on Cu(111) was prepared via e-beam evaporation and used to test the out-of-plane spin polarization of the STM tips [4]. Co/Cu(111) grows in the form of bilayer high triangular ferromagnetic islands, which either follow the fcc structure of the substrate (unfaulted) or have a stacking fault, which results in a rotated hcp stacking (faulted), see figure 2 (a). This leads to a shift in the Co surface state detected via STS, i.e. when measuring the local density of states (LDOS) at a certain bias, islands of opposite stacking will give signals of different intensities. This is shown in figure 2 (b), where the spin-averaged LDOS map at a bias of -270 mV shows faulted islands in bright and unfaulted islands in dark. Additionally, each island possesses an out-of-plane spin polarization, which can randomly be up or down. This means, measuring the same area with an out-of-plane spin polarized tip will give rise to different signal intensities for the same type of island, but with differently oriented spin polarizations with respect to the tip. Figure 1 (c) shows the LDOS map measured in the same area and at the same voltage as in (b) using a cobalt covered tip. The result is an observed intensity difference of certain islands coming from an increased or decreased spin-polarized current depending on the relative spin alignment between tip and island. This example shows, that with our tips we are able to detect spin-polarized states.

Outlook

Our focus in the coming months lays on imaging the surface spin structure of $Ge_{1-x}Mn_xTe(111)$ on an atomic level by means of spin-polarized STM and STS, making use of our prepared and tested bulk MnNi and Co covered tips. In addition, we plan on testing the magnetoelectric coupling by manipulating the magnetic surface structure with the electric field of the STM tip.

References

[1] N. Spaldin et al., "Multiferroics: Past, present, and future", Physics Today 63, 38-43 (2010).

[2] J. Krempaský et al., "Surface versus bulk contributions to the giant Rashba splitting in the ferroelectric alpha-GeTe semiconductor", arxiv:1503.05004 (2015).

[3] J. Krempaský et al., "Operando Imaging of All-Electric Spin Texture Manipulation in Ferroelectric and Multiferroic Rashba Semiconductors", Phys. Rev. X 8, 021067 (2018).

[4] O. Pietzsch et al., "Spin-Polarized Scanning Tunneling Spectroscopy of Nanoscale Cobalt Islands on Cu(111)", Phys.Rev.Lett. 92, 057202 (2004).

Development of biomimetic systems

Project P2005: Transmembrane protein-mediated loading of synthetic compartments
Project Leaders: C.G. Palivan, R.A. Kammerer, S. Gros
Collaborator: P. Jasko (SNI PhD Student)

Compartmentalization, a prerequisite for the spatiotemporal control of biochemical pathways in cells, is a fundamental concept in designing new materials for medical and technological applications. Synthetic nano- and micro-compartments (NCs, MCs), with their chemical versatility and superior stability provide the basis for developing specifically designed catalytic compartments, artificial organelles, or cell mimics [1]. However, the development of more advanced, integrated systems that closely mimic cellular processes remains a hurdle that could be overcome by establishing efficient and straightforward methods for creating stable synthetic compartments, ensuring communication and material exchange between them and the external environment by providing better compartment permeability. Employing bacterial toxin components for controlled compartment fusion in artificial systems

Membrane fusion is a crucial process underlying numerous biological functions, including subcellular compartmentalization, cell growth, and exo- and endocytosis. It is also essential for the construction of artificial membrane structures, such as vesicles. Despite its importance, achieving membrane fusion in vitro under neutral pH conditions without the use of fusion-promoting biomolecules to modify vesicles remains a considerable challenge. This obstacle has limited the advancement of biomimetic fusion systems and their practical applications. In this study, we introduce diphtheria T-domain as an innovative fusogenic agent that addresses these challenges by eliminating the need for membrane modifications [2][3].

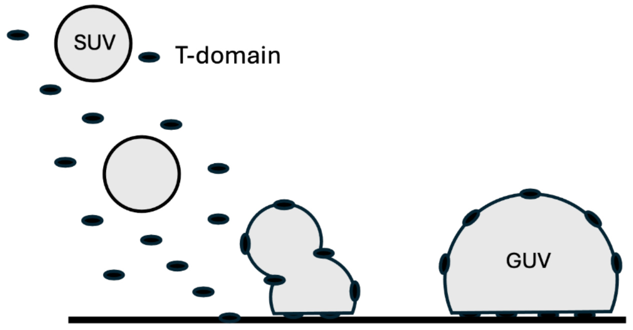

Fig. 1: Model of compartment fusion mediated by bacterial toxin-based. Our engineered bacterial toxin component (T-domain) binds to anionic small unilamellar vesicles (SUV) simultaneously mediating the surface adsorption of our vesicular systems inducing tension on the membrane that we found to be a trigger for the vesicle fusion and formation of MCs – giant unilamellar vesicles (GUV).

We applied molecular biology techniques that allowed us to establish the production of recombinant proteins. In order to study the interaction between the recombinant toxin and the native-like membranes, we introduced mutations in key basic amino-acid residues expected to mediate this interaction. Using characterisation methods, such as circular dichroism (CD) and nano-differential scanning fluorimetry (nanoDSF), we examined the protein variants' proper fold and stability, respectively. We produced small lipid unilamellar vesicles (SUVs) with varied negative charge content to mimic cell membranes for in situ functionality assessment of protein variants. In addition, we monitored the interaction of the purified toxin variants with vesicle membranes by a calcein-release assay. We evaluated the stability of protein-SUVs by means of light scattering techniques, and electron microscopy (EM) under neutral pH conditions. Next, the fusion process was examined using confocal laser scanning microscopy (CLSM) which uncovered that bacterial toxin could mediate vesicle adsorption onto the glass surface inducing tension on the SUV membrane leading to the vesicle fusion (Fig. 1). To visualize giant unilamellar vesicles (GUVs), we enhanced our SUV preparations by implementing fluorescent lipids. Mutated variants exhibited lower vesicle binding capability and surface adsorption confirming their role in membrane interaction and subsequent vesicle fusion. Our results indicate a novel role in nano-vesicle fusion for one of the bacterial toxins. In the bulk solution our recombinant bacterial toxin interacts with the anionic vesicle membrane in an undisrupting and non-fusogenic manner. Once the mixture of protein and SUVs is exposed to the glass surface, GUVs emerge driven by the induced membrane tension (Fig. 2).

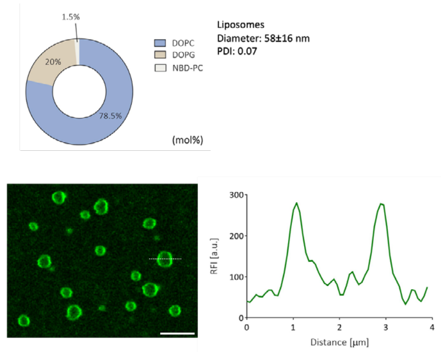

Fig. 2: The presence of DOPG ensures a negative charge whereas NBD-PC fluorescent signal is further recorded by CLSM in fused liposomes upon T-domain addition. Emerged GUVs are of homogenous size with a typical 2 µm diameter. Scale bar 5 µm.

Controlled enzymatic reactions by programmed confinement in clusters of polymersomes and Janus nanoparticles

One of the key aspects in developing biomimetic systems incorporating NCs is establishing communication, or material flow, between them. This can be achieved by integrating highly stable beta-barrel membrane proteins, such as outer membrane porin F (OmpF), which tolerate harsh conditions. These proteins enable the formation of supramolecular assemblies with amphiphilic block copolymers (BCP), resulting in permeable NCs capable of supporting enzymatic reactions and exchanging materials with the external environment and adjacent NCs.

In our studies, we optimized the production of OmpF and adapted a simpler approach to reconstitute the pore in the membrane of NCs at the stage of organic solvent evaporation. The rehydration of the copolymers and protein mixtures by aqueous solution containing an enzyme we constructed catalytic nanocompartments (CNCs). CNCs were selectively attached on one of the lobes of Janus nanoparticles (JNP), giving rise to complex and stable communication platform. Such JNP-CNC clusters provide both spatial and directional control of enzymatic reactions at the nanoscale and have high potential in biomedical applications, including protein therapy and theranostics [4].

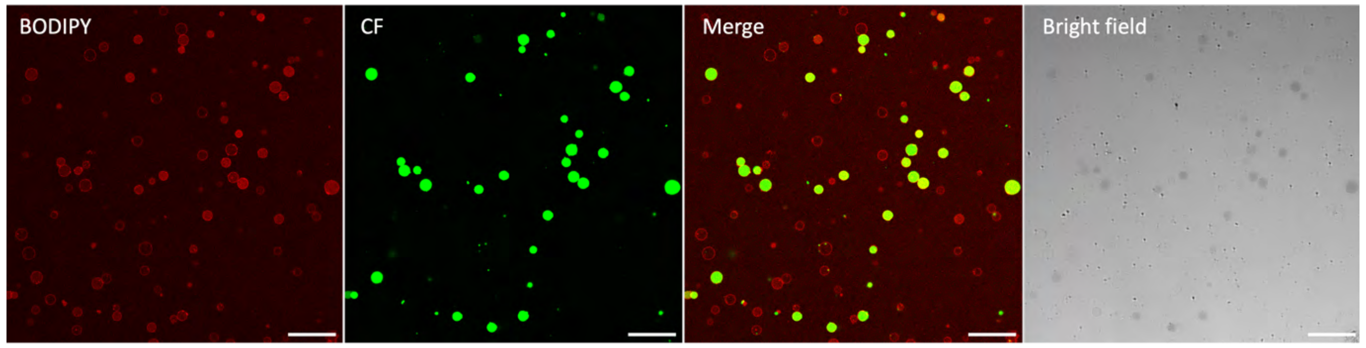

Fig. 3: CLSM studies at GPMVs demonstrating catalytic activity of enzymes transferred from the parental cells. GPMVs were stained with BODIPY dye, and a precursor molecule was introduced, giving rise to an enzymatically converted fluorescent product CF. Scale bars 30 µm.

Exploring the functional proteome and biophysical characteristics of GPMVs derived from neuroblastoma cells

In this part of our project we investigated whether cell-derived giant plasma unilamellar vesicles, GPMVs could serve as minimal cell models in establishing simpler environments for studying cellular processes in biomedical applications or development of protocells. GPMVs from donor cells, have gained attention because of their straightforward preparation and handling in contrast to cells [5]. However, little is known about the GPMV protein content that is derived from the parental cell as well as its functional status crucial in determining application directions.

We obtained GPMVs from a neuroblastoma cell line that had been engineered to stably express a water channel AQP1. The expression of AQP1 in the engineered cells reflects a key feature of the tumor microenvironment, as AQP1 is upregulated in response to hypoxic conditions commonly found in tumors [6]. Additionally, AQP1 was used as a marker to evaluate how much biologically functional cell membrane was transferred to the GPMVs. To complement this, we performed proteomic analysis to investigate the membrane and luminal content of GPMVs, revealing thousands of protein entries. We demonstrated that GPMVs carry enzymatically active proteins and retain biomacromolecules within the vesicles (Fig. 3). Furthermore, we characterized GPMV stability under physical stress conditions, such as osmotic shock, to highlight their flexibility and adaptability to external stimuli. Lastly, we aim to establish a detailed map of the GPMV proteome, which we envision to be valuable for biomedical research. This comprehensive proteomic analysis could provide new insights into molecular mechanisms underlying vesicle formation, particularly in the context of cancer, where altered vesicle dynamics play a critical role in tumor progression and metastasis. On the other hand, the GPMV's proteome could serve as a foundation for mimicking the cytosolic environment in the development of protocells for nanotechnological applications.

By combining our hybrid approaches, we aim to bridge the gap between synthetic and natural systems. The versatile platforms that we have achieved also support the engineering of biomimetic systems for drug delivery, biosensing, and synthetic biology applications.

References

[1] Maffeis V, Belluati A, Craciun I, Wu D, Novak S, Schoenenberger CA, Palivan CG. "Clustering of catalytic nanocompartments for enhancing an extracellular non-native cascade reaction", Chem Sci. 12, 37 (2021).

[2] Richard A. Kammerer, Roger M. Benoit, "Botulinum neurotoxins: new questions arising from structural biology", Trends Biochem. Sci. 39, 11 (2014).

[3] Dehua Pei, "How Do Biomolecules Cross the Cell Membrane?", Acc. Chem. Res. 55, 3 (2022).

[4] Voichita Mihali, Piotr Jasko, Michal Skowicki, Cornelia G. Palivan. „Controlled enzymatic reactions by programmed confinement in clusters of polymersomes and Janus nanoparticles". Mater. Today. 80, (2024).

[5] Alter CL, et al. „High efficiency preparation of monodisperse plasma membrane derived extracellular vesicles for therapeutic applications". Commun. Biol. 6, 478 (2023)

[6] Huo Z, et al. „AQP1 Is Up-Regulated by Hypoxia and Leads to Increased Cell Water Permeability, Motility, and Migration in Neuroblastoma". Front. Cell Dev. Biol. 9, (2021).

Surface chemistry and self-assembly studies of zirconium and hafnium oxo clusters

Project P2006: RESTRAIN – Reticular chemistry at interfaces as a form of nanotechnology
Project Leaders: P. Shahgaldian and J. De Roo
Collaborator: A. Roshan (SNI PhD Student)

While group 4 metal oxo clusters can be used as metal–organic frameworks (MOFs) building blocks, their discrete clusters are used in polymer composites, and as catalysts.[1] Conceptually, discrete oxo clusters are close to metal oxide nanocrystals. Both have an inorganic core capped with an organic ligand shell, mostly carboxylates (Fig. 1A,B). One can regard the prototypical $Zr_6O_8H_4(OOCR)_{12}$ (**Zr6**) cluster as the smallest possible nanoparticle, with the advantage that the cluster is atomically precise in contrast to nanocrystals that display size heterogeneity. [2] Despite their structural similarities, oxo clusters exhibit, however, subtle variations in chemistry due to their smaller surface curvature. Here, we study the surface chemistry of zirconium and hafnium oxo clusters through ligand exchange reactions. Through experimental spectroscopic techniques, we determined the interaction between the $M_6O_8^{8+}$ (M = Zr, Hf) cluster surface and various ligands: carboxylates (RCOOH), phosphonates ($RPO(OH)_2$), dialkylphosphinates ($R_2PO(OH)$), and mono-substituted phosphinates (RHPO(OH)).[3] These insights into cluster surface chemistry are further utilized for the controlled synthesis of 2D metal-organic networks (MONs).

Surface chemistry of oxo clusters

We chose Zr12-acetate clusters, a dimer of Zr6 clusters as starting point and modified their surface with a variety of phosphonate and mono/di-substituted phosphinate ligands in chloroform. The extent of ligand exchange was monitored through solution 31P NMR (nuclear magnetic resonance) spectroscopy. When titrated with dioctylphosphinic acid, expressed in equivalents relative to a Zr6O8H412+ core, six distinct resonances were observed between 51 and 55 ppm in the 31P spectrum upon addition of one equivalent (Fig. 1D). These resonances correspond to bound phosphinate ligands and highlight the complexity of binding sites on Zr12 clusters. The absence of a signal for free dioctylphosphinic acid indicated quantitative replacement of acetate ligands. At three equivalents, the most downfield resonance at 55 ppm disappeared, suggesting structural reorganization, possibly into a Zr6 structure. For six equivalents of dioctylphosphinic acid, we observed the resonance of free phosphinic acid, which further increased in intensity for 9 and 12 equivalents. We infered that the full exchange of all 12 carboxylates per Zr6O8 core was sterically impeded for di-substituted phosphinic acids.

In contrast, with the less sterically hindered phenylphosphinic acid, no free acid resonances were observed until 12 equivalents, suggesting an irreversible and complete ligand exchange (Fig. 1E). At 15 equivalents, a broad resonance for free phenylphosphinic acid emerged, implying a dynamic equilibrium between free and coordinated acids. To isolate fully phosphinate-capped clusters, Zr12-acetate was reacted with 13.2 equivalents of phenylphosphinic acid in dry DCM at room temperature and purified via precipitation. Single crystals of Zr6-phenylphosphinate (CCDC-2358676) were obtained, revealing a preserved Zr6O8H412+ core with 12 phosphinate ligands bound in a bridging mode (Fig. 1C). Interestingly, when hexylphosphonic acid was titrated with Hf12-acetate clusters, the solution immediately formed a gel, precluding 31P NMR analysis. Pair distribution function (PDF) analysis (Fig. 1F) revealed a dual-phase structure: phase I as a 3 × 3 hafnium phosphonate layer (Fig. 1H) and phase II as an Hf6 core (Fig. 1G), extracted from the Hf12-acetate crystal structure. We conclude that upon ligand exchange, a significant fraction of the clusters decomposes into metal phosphonates, whereas the rest of the clusters get trapped in the gel with an intact M6O8 core. These results highlight critical differences in the surface chemistry of metal oxo clusters with oxide nanocrystals, providing essential insights for designing materials based on clusters.

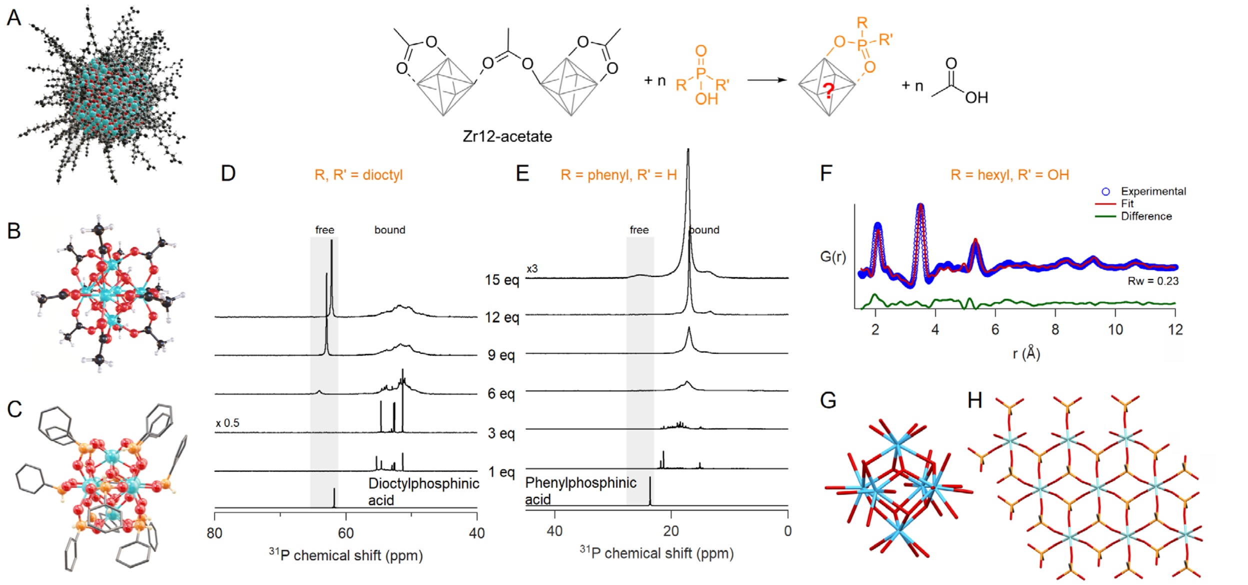

Fig. 1: Schematic representation of (A) colloidally stable zirconium/hafnium oxide nanocrystal, (B) $M_6O_8H_4(OOCR)_{12}$ carboxylate cluster (M = Zr/Hf) and (C) Zr6-phenylphosphinate cluster – $Zr_6O_8H_4(O_2PHPh)_{12}$. Cyan atoms represent Zr/Hf and all other atoms follow conventional CPK coloring. 31P NMR spectra of the titrations of Zr12-acetate with (D) dioctylphosphinic acid (expressed as equivalents with respect to a monomer unit) and (E) phenylphosphinic acid. The cluster concentration is 20 mg mL–1 in CDCl3. The reference 31P NMR spectrum of free phosphinic acids with one equivalent acetic acid is also provided. (F) (E) Dual-phase PDF fit for hexylphosphonate exchanged Hf clusters with Hf6 chelating bridging acetate (G) and a 3 × 3 layer of Hf phenylphosphonate (H).

Self-assembly of oxo clusters with amphiphiles

2D metal-organic networks (MONs) are highly desirable materials, consisting of either a single layer or stacked layers of organic-inorganic hybrid nanosheets oriented in one direction. This unique layered structure provides 2D MONs with enhanced properties, including increased active metal sites, higher catalytic activity, improved porosity, greater specific surface area, and superior electrical conductivity compared to 3D MOFs.[4] While Group 4 metal oxo clusters have been widely employed as precursors for the synthesis of nanocrystals and MOFs, [5,6] their potential for developing 2D MONs has remained unexplored.

In this work, we report the first air-water interface-assisted synthesis of Group 4 2D MONs, using metal oxo cluster secondary building units at room temperature. To assess the stability of these clusters in water prior to the self-assembly, we employed PDF analysis (Fig. 2C). Interestingly, dissolving Hf12-acetate in water led to the exchange of inter-cluster carboxylates with oxo-bridges, while the core structure of the cluster remained intact (Fig. 2A). To restrict the anisotropic growth of 2D MONs at the air-water interface, we designed a series of amphiphilic terephthalates featuring hydrophobic alkyl chains and hydrophilic carboxylate groups (Fig. 2B). When spread over a 10 µM aqueous solution of Zr12/Hf12-acetate, these amphiphilic molecules spontaneously formed self-assembled monolayers with clusters. A combination of characterization techniques, including atomic force microscopy, ellipsometry, and X-ray photoelectron spectroscopy, confirmed the molecular structure and composition of the resulting metal-organic network (Fig. 2D).

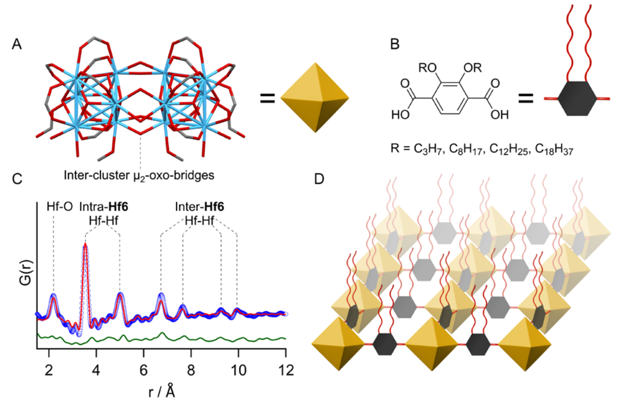

Fig. 2: Structure of (A) μ_2-oxo-bridged Hf12-formate cluster and (B) amphiphilic terephthalate linkers. (C) PDF fit for 10 mM aqueous solution of Hf12-acetate cluster with the structure model of μ_2-oxo-bridged Hf12-formate. (D) Schematic model of 2D MON at the air-water interface.

References

[1] Van den Eynden, D. et al. Nonaqueous chemistry of group 4 oxo clusters and colloidal metal oxide nanocrystals. Chem. Rev. 122, 10538–10572 (2022).

[2] Van den Eynden, D. et al. Fatty acid capped, metal oxo clusters as the smallest conceivable nanocrystal prototypes. Chem. Sci. 14, 573-585 (2023).

[3] Unniram Parambil, A. R. et al. Atomically precise surface chemistry of zirconium and hafnium metal oxo clusters beyond carboxylate ligands. Chem. Sci. 15, 17380-17396 (2024).

[4] Chakraborty, G.; Park, I.-H.; Medishetty, R.; Vittal, J. J. Two-dimensional metal- organic framework materials: synthesis, structures, properties and applications. Chem. Rev. 121, 3751–3891 (2021).

[5] Sliem, M. A. et al. Surfactant-induced nonhydrolytic synthesis of phase-pure ZrO2 nanoparticles from metal–organic and oxocluster Precursors. Chem. Mater. 24, 4274–4282 (2012).

[6] Wang, C. et al. High-Valence Metal-organic framework materials constructed from metal-oxo clusters: opportunities and challenges. ChemPlusChem, 88, e202200462 (2023).

Hybrid acoustic tweezers for cells and soft matters driven by surface acoustic wave

Project P2007: Development of nanoscale acoustic tweezers for mechanobiology application
Project Leaders: S. Tsujino and R.Y.H. Lim
Collaborator: S. Jia (SNI PhD Student)

Introduction

In the annual report of last year, we showed the ongoing development of our acoustic tweezers driven by surface acoustic wave (SAW) ultrasonic transducers. In this report, we will demonstrate the capability of our acoustic tweezers of handling micron-scale particles and soft matters in a liquid environment.

SAW ultrasonic transducers have been extensively used to generate high frequency ultrasound in acoustic tweezers for sample handling at a high spatial resolution. The components housing samples in liquid in such devices are commonly made of PDMS (polydimethylsiloxane) due to its optical transparency and bio-compatibility [1]. Nevertheless, PDMS attenuates vibration and leads to a low acoustic transmission from the SAW transducers to the liquid [2]. Alternatively, rigid materials, such as silicon and glass, are used to build microfluidic (MF) chips that are coupled with SAW transducers. This construction reduces the loss of acoustic energy and resultantly heat dissipation [2,3]. Thus, high acoustic pressure can be generated in the liquid more efficiently without generating excessive heat that may be detrimental to biological samples. In our study, we combine a planar SAW transducer fabricated from a piezoelectric substrate with a MF chip made from a silicon wafer via deep reactive etching (DRIE). Owing to the enhanced acoustic coupling, our device is demonstrated to be able to trap highly motile cells and deform soft matters at a spatial resolution < 20 µm.

Materials and methods

The SAW transducers were made from a 127.86°C Y-cut and X-propagating lithium niobate ($LiNbO_3$) wafer. The aluminum interdigitated electrodes were fabricated using direct laser writer (DWL66+, Heidelberg Instruments) and wet etching. For the SAW transducers to work at around 50 MHz, each interdigitated transducer is composed 20 µm wide fingers with spacing of 20 µm, following by reflector strips of 20 µm in width and spacing.

The fabrication of the Si MF chips mainly involves photolithography and deep reactive ion etching (DRIE) on a Si wafer. Using two chromium photomasks fabricated by direct laser writer, the MF channels (front side) and the chip structures (back side) were patterned using a mask aligner and then defined from the front- and back-sides of the Si wafer, respectively, via DRIE. The fabricated MF channels are 200 µm wide, 120 µm deep, and 5 mm long. The chip structures were defined by etching though the wafer. The dry etching process of the MF chips obviated protective coatings which are typically required by wet etching. The Si chip is then bonded to the SAW chip and capped by thin glass plates using UV-cured negative-tone photoresist.

Enhancing acoustic radiation by acoustic horns

To evaluate the acoustic field in the MF channel, we infused a DI water suspension of 3-micron polyethylene (PE) particles into the MF channel in the Si chip and apply ultrasound pulses. Upon each pulse, a standing acoustic wave is formed between the channel walls, and particles are moved by acoustic radiation force to the pressure nodes. The sequence of the recorded images in Figure 1 displays the distribution of the particles, from the left to the right, as the particles, initially randomly distributed, are moved along the lines with the spacing of ~17 micron as 100 ms ultrasound pulses are applied multiple times. The spacing corresponds to the ½ wavelength of the 49.2 MHz ultrasound in water.

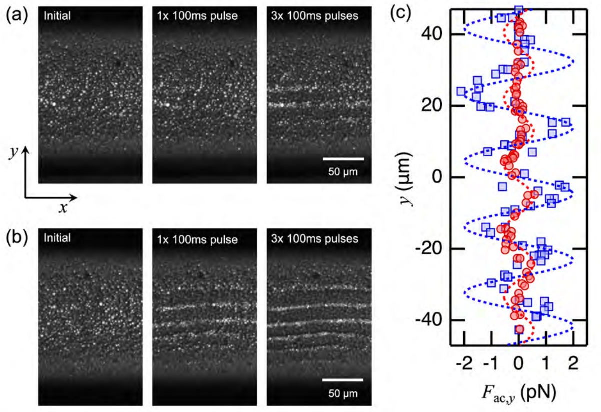

Fig. 1: (a)-(b) From the left to the right: particle distribution in the initial state, and after one, two, and three 100 ms ultrasound pulses, observed in the silicon chip with and without acoustic horns, respectively. (c) Estimated acoustic radiation force as function of particle position in the y axis inside the channel. Red circle – without horn. Blue squares: with horn. Dashed line are their sinusoidal fits.

Compared to Fig. 1 (a), particles in Fig. 1 (b) are moved to the acoustic pressure nodes much more quickly, and a single pulse would move particles to form clear nodes. This is owing to the enhanced coupling of acoustic radiation into the MF channel by shaping the Si chip as a focusing horn. To estimate the acoustic radiation force on particles, we analysed the particle trajectories and calculated their velocities. Then the acoustic radiation force F_y^{rad} is obtained by equating it with the viscous Stokes drag force in y direction (transverse direction) [4], i.e., $F_y^{rad} = 6\pi\eta r v_y$, where η, r, and v_y are the dynamic viscosity of water, the radius of particle, and the particle velocity in the y direction (transverse direction), respectively. The results are shown in Figure 1 (c), and the acoustic pressure is estimated to be enhanced by the horn by twofold.

Trapping of motile cells

To test the tweezing capability of the developed device, we first used it to trap a highly motile cell species, Tetrahymena. It has an ellipsoidal shape, ~20 µm in its minor axis and ~50 µm in its major axis. As shown in Fig. 2 (a), when the ultrasound was turned off, it swam swiftly along its major axis at a root-mean-square (rms) velocity of 0.54 mm/s. Once the 49.2 MHz ultrasound is turned on, it was trapped vertically in the pressure nodes (visualized by the aggregation of ~3-µm PE particles) and swam horizontally (the horizontal part of the orange arrows in Fig. 2 (b)). It tried to escape one pressure node but ended up being trapped in another, as indicated by the zig-zag part of the orange arrows, respectively, in Fig. 2 (b). The swimming speed of this Tetrahymena was reduced by over 40% due to acoustofluidic trapping.

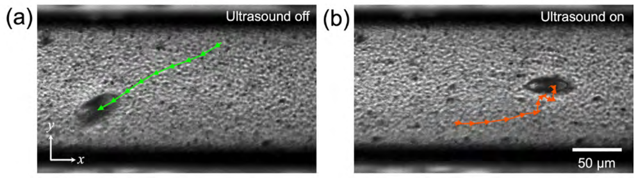

Fig. 2: (a) Snapshot of a single Tetrahymena moving freely (the dark ellipsoid) when the ultrasound is off. The green arrows illustrate the frame-by-frame movement of the cell during t =0 – 0.36s under white LED illumination. (b) Snapshot of the same Tetrahymena when ultrasound was on. The orange arrows show the frame-by-frame movement during t = 1.68 – 2.48 s.

Deformation of inactivated cells

We notice that, after being exposed to UV for ~12 min, a Tetrahymena lost its motility and turned from an ellipsoid into a sphere, as shown by Figs. 3 (a)-(b). We applied 3 ms ultrasound pulses at 45.1 V_{rms}. As captured by the Figs. 3 (c)-(d), we observed significant vertical compression and accordingly horizontal elongation of the cell upon each acoustic pulse. We measured the diameters along AB and CD, as denoted in Figure 3 (d) and plotted them in Figure 3 (e). Each deformation was followed by a slow recovery, which is a typical behavior of a viscoelastic material. When the morphological change finished, the cell turned into a sphere. From then on, applying ultrasound pulses did not deform the entire cell but instead aggregated the substance inside the cell into lines with a separation approximately equal to one half of the wavelength. This suggests that the acoustic wave penetrated into the cell and moved intracellular substances to acoustic pressure nodes.

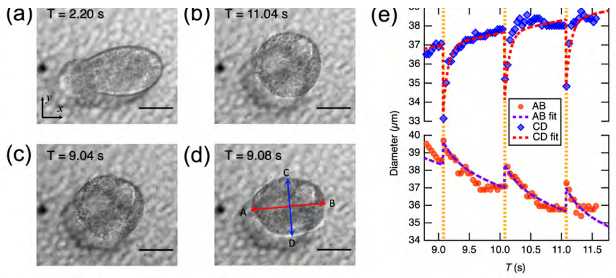

Fig. 3: (a)-(b) Snapshots of the change of cell morphology from an ellipsoid. From (c) to (d), the deformation of the cell upon the application of a 3 ms ultrasound pulse was observed. Scale bar = 20 µm.

It can be observed that some substances in the medium (bottom part in Figure 4 (b)) also aggregated into lines, with their separation approximately equal to that inside the cell. This implies that the cell might have lost its internal rigidity, which could be due to the observed emission of some substances from the cell during the ultrasound-induced deformation. The presumed lack of acoustic contrast between the cell and the medium also explains why the cell in its spherical shape could not be deformed anymore.

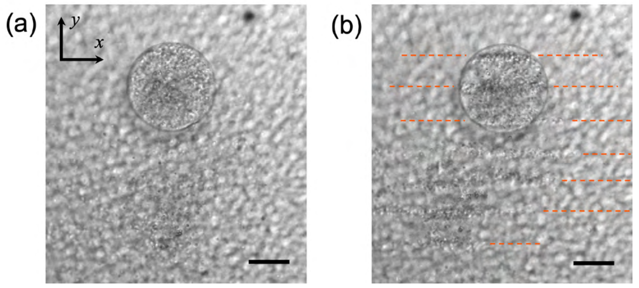

Fig. 4: (a) An inactivated Tetrahymena that became a sphere after 12 min UV illumination. (b) Aggregation of intracellular substance inside the inactivated Tetrahymena. Scale bar = 20 µm.

Summary

With our acoustic tweezers of a hybrid construction, we have introduced a new way of improving the acoustic radiation force for efficient sample handling. Owing to the achieved strong acoustic radiation force, we were able to trap highly motile cells and deform cellular samples. The result suggests the feasibility of the developed device not only in the handling of cellular samples but also in the study of mechanical properties of cells and other viscoelastic samples.

References

[1] X. Ding, Z. Peng, S. S. Lin, M. Geri, S. Li, et al., Proc. Natl. Acad. Sci. U.S.A., 2014, 111, 12992–12997.

[2] M. Cui, M. Kim, P. B. Weisensee, and J. M. Meacham, Lab on a Chip, 2021, 21, 2534-2543

[3] M. Cui, S. K. Dutcher, P. V. Bayly, and J. M. Meacham, Proc. Natl. Acad. Sci. U.S.A., 2023, 120 (25) e2218951120

[4] H. Bruus, Microscale Acoustofluidics, The Royal Society of Chemistry, 2014, ch. 4, pp. 65-80

Integrating a nanowire quantum dot on a scanning probe tip

Project P2008: Scanning nanowire quantum dot
Project Leaders: D. Zumbühl and M. Poggio
Collaborator: L. Forrer (SNI PhD Student)

Introduction

In this project, we intend to develop a new kind of scanning probe microscope, which employs gated quantum dots (QDs) embedded in semiconductor nanowires (NWs), integrated on the tips of standard force microscopy cantilevers. These sensors will be sensitive scanning probes of charge and electronic density [1]. The sensors will be used to characterize the spatial profile of charge noise, quantum dots, and electric fields [2] in spin qubit devices, aiding the design of coherent quantum computation processors. This is particularly relevant here in the Department of Physics of the University of Basel, where the NCCR SPIN, aimed at producing scalable spin qubits in Si was established in the summer of 2020.

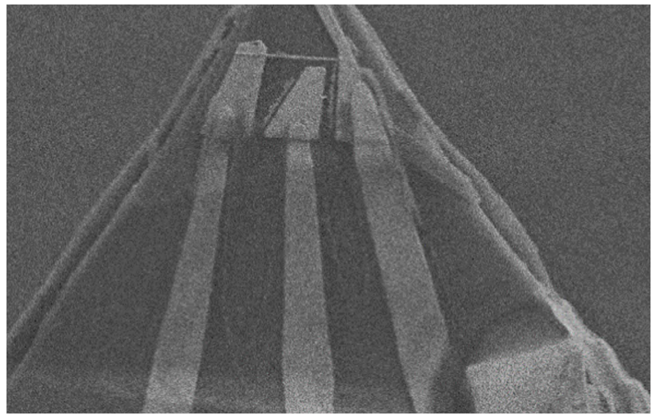

Figure 1: A scanning electron micrograph of a patterned cantilever tip with a gate-controlled NW QD at its tip. We have recently realized such a working device and will soon implement it as a scanning probe as a highly sensitive tool for measuring small electric fields with nanometer-scale resolution.

Our scanning probe method builds on previously developed scanning single-electron transistors (SETs) made from metallic islands [1] and scanning QDs defined in carbon nanotubes (CNTs) [2]. Research efforts using such devices have been extremely fruitful, due to the high sensitivity to electric field. Indeed, QD-based sensors are the preferred sensors of charge in applications in quantum computation with spins in QDs, where they are incorporated on the same substrate as the sample of interest. Such charge sensors make use of sharp spikes in the electrical conductance of the QDs (Coulomb peaks) and are capable of detecting a small fraction of an electronic charge at micron distance. Until now, however, both scanning SETs and scanning QDs in CNTs have been relatively cumbersome to use, extremely delicate, and limited in their design. These drawbacks are a result of the specialized processes involved in their fabrication.

Our approach addresses this shortcoming by using standard AFM cantilevers as the scanning probe combined with NWs as the QD hosts. By developing a scheme for patterning leads, gates, and contacts directly to the cantilever tip [3], we will have maximum flexibility for the design of our sensors. AFM levers allow easy tip-sample distance control, topographic contrast. NW QDs possess many qualities that make them suitable for use in scanning probes: they are small (~10-50 nm), need few gates because of the natural 1D confinement, and can due to the low-dimensional geometry of the NW be easily brought closer than 100 nm to a sample. Importantly, their strong confinement and tunable nature endows NW QDs with a higher sensitivity to electric fields and nearby charges than their SET counterparts. Moreover, NW crystals can be grown with an exceptional control over material composition. The specific NW material composition can pass on useful properties to the embedded probe QDs, such as a strong spin-orbit interaction, which may offer interesting new modalities of sensing.

Goals

The main goals of this project are to: 1) Fabricate scanning probe cantilevers hosting a NW with embedded gated QDs (**T**); 2) Image the electronic density of nanoscale samples with unprecedented sensitivity (**F**); 3) Implement high-bandwidth scanning probe imaging using microwave reflectometry techniques (**T**); 4) Image and study the dynamics of charge fluctuators in semiconducting devices (**F**).

Results

Early in this project, we developed new methods to pattern scanning probe cantilevers with nanostructures such as gate electrodes and contacts, using electron-beam lithography [3]. Our process involves coating cantilevers with a floating resist layer, which is then patterned with nanometer resolution, as shown in Figure 1. We have tested the method for various kinds of cantilever shapes, which we pattern using focused-ion-beam milling. Summarizing, we are now able to make wide variety of gates, with dimensions down to 50 nm, and contacts suitable for QD control. This method gives us the opportunity to fabricate gates on the tip of our lever and contact NWs by evaporation of metal as done on conventional planar substrates [4,5].

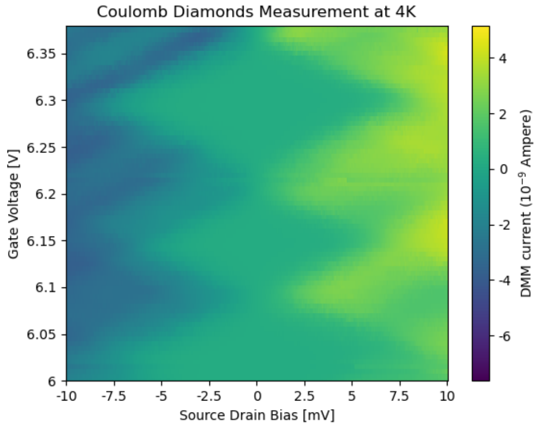

Figure 2: : Source-drain current measured as a function of source-drain bias and gate voltage in a NW QD device. Recently, we have realized a similar measurement for the NW QD on a cantilever tip shown in Figure 1 [3].

We have demonstrated QD formation on substrates using our fabrication techniques and we have successfully fabricated a NW QD on the tip of a cantilever designed for atomic force microscopy (AFM), seen in Figure 1. The next step is to produce more such devices and to use them in a scanning probe experiment both to demonstrate its function and to take advantage of its capabilities to sensitively image electric fields.

Recently, we have also taken advantage of our ability to pattern nanometer-scale electrodes on cantilever tips to develop probes for scanning multi-gate microscopy, as shown in Figure 3. With these probes we aim to induce quantum dots in materials underneath the probe, such as Si, planar Ge, or Ge/Si NWs. By inducing such dots and studying their behavior much about the electronic properties of the material can be learned, in some cases without patterning any structures or making any contacts. The mobility of the scanning probe also allows these studies to be carried out at arbitrary positions on the substrate, potentially allowing for a detailed characterization of a materials' homogeneity.

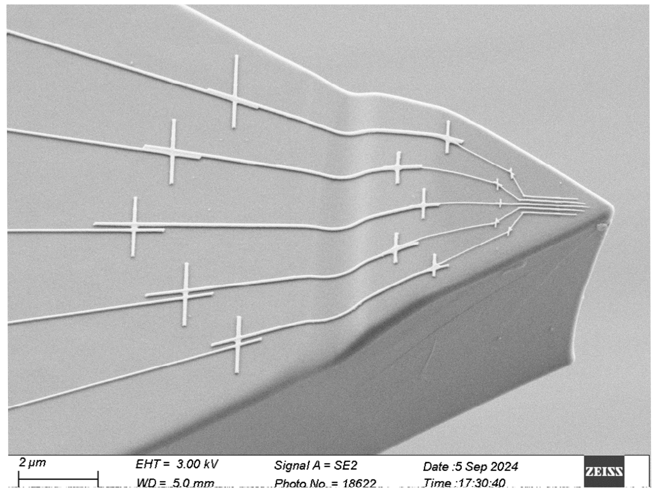

Figure 3: A scanning electron micrograph of a patterned cantilever with a multi-gate pattern at its tip.

Having assembled all the necessary instrumentation for implementing high-bandwidth microwave reflectometry readout techniques and having developed a fabrication technique for patterning contacts and gates on AFM tips, we are also preparing advanced scanning gate microscopy experiments. In these measurements, we use our multiple on-tip gates to induce QDs in the substrate below and measure their charge state using both DC and microwave reflectometry techniques.

Outlook

In the final part of the project, we will apply the techniques that we have developed so far to to study defects and charge noise, which are the main source of decoherence in spin and superconducting qubit devices. Furthermore, by combining our multi-gate cantilevers with microwave reflectometry read-out techniques, we will be able to image QD formation and QD properties such as energy level splittings in pristine samples, such as ungated heterostructures, thin Si quantum wells, and NWs.

References

[1] M. J. Yoo, T. A. Fulton, H. F. Hess, R. L. Willett, L. N. Dunkleberger, R. J. Chichester, L. N. Pfeiffer, and K. W. West, "Scanning Single-Electron Transistor Microscopy: Imaging Individual Charges". Science 276 (1997), p. 579.

[2] L. Ella, A. Rozen, J. Birkbeck, M. Ben-Shalom, D. Perello, J. Zultak, T. Taniguchi, K. Watanabe, A. K. Geim, S. Ilani, and J. A. Sulpizio, "Simultaneous voltage and current density imaging of flowing electrons in two dimensions", Nat. Nanotechnol. 14 (2019), p. 480.

[3] L. Forrer, A. Kamber, A. Knoll, M. Poggio, and F. Braakman, "Electron-beam lithography of nanostructures at the tips of scanning probe cantilevers", arXiv: 2209.11503 (2022)

[4] F. S. Thomas, A. Baumgartner, L. Gubser, C. Jünger, G. Fülöp, M. Nilsson, F. Rossi, V. Zannier, L. Sorba, C. Schönenberger, "Highly symmetric and tunable tunnel couplings in InAs/InP nanowire heterostructure quantum dots", Nanotechnology. 31 (2020)

[5] F. N. M. Froning, M. Rehmann, J. Ridderbos, M. Brauns, F. A. Zwanenburg, A. Li, E. P. A. M. Bakkers, D. M. Zumbühl, F. R. Braakman, "Single, double, and triple quantum dots in Ge/Si nanowires", APL. 113 (2018)

A Schrödinger-cat qubit in a tantalum-based planar architecture

Project P2101: A planar nanofabrication process for coupled Schrödinger-cat qubits in parametrically-driven nonlinear superconducting resonators
Project Leaders: A. Grimm and C. Bruder
Collaborator: A. Bruno (SNI PhD Student)

Introduction

Quantum two-level systems are routinely used to encode qubits but tend to be inherently fragile, leading to errors in the encoded information. Quantum error correction (QEC) addresses this challenge by encoding effective qubits into more complex quantum systems. Unfortunately, the hardware overhead associated with QEC can quickly become very large.

In contrast, a qubit that is intrinsically protected against a subset of quantum errors can be encoded into superpositions of two opposite-phase oscillations in a resonator, so-called Schrödinger-cat states. This "Schrödinger-cat qubit" has the potential to significantly reduce the complexity of QEC, because it can replace a large number of two-level-system qubits in a QEC code [1]. In a recent experiment, we have demonstrated the stabilization and operation of such a qubit through the interplay between Kerr nonlinearity and single-mode squeezing in a superconducting microwave resonator [2]. This type of Schrödinger-cat qubit is typically referred to as the "Kerr-cat qubit".

Previous implementations of Kerr-cat qubits (KCQs) relied on three-dimensional microwave cavities. This counteracts the reduction in hardware complexity achievable with this system and is not fundamentally required. In this project, we are developing a nanofabrication process for fully planar Kerr-cat qubits. This will result in an easily scalable platform enabling us to investigate interactions between several such qubits.

In the first year of this SNI project we built up the basics required for the fabrication, measurement, and operation of Kerr-cat qubits in line with the ramping up of the research activities of the host group. In addition to experimental tasks, such as building a measurement and control setup, we implemented an Al/AlO$_x$/Al Josephson junction fabrication process for standard superconducting transmon qubits and benchmarked it by characterizing the coherence times of these devices. We furthermore reported on building a first prototype of a quantum-limited parametric amplifier in our group. In the second year of this SNI project we implemented a fabrication process for tantalum-based superconducting resonators. We performed all fabrication steps except for the thin-film deposition in-house. We furthermore designed the resonator test chips and measured them in our dilution refrigerator showing state-of-the-art quality factors.

This year, we have built on these results by integrating Al-AlO$_x$-Al Josephon junctions with tantalum structures to form superconducting tantalum transmon qubits. After this initial benchmarking step, we proceeded to design, fabricate, and measure a planar Kerr-cat qubit. We will describe our work in more detail in the following.

Reasoning for using tantalum as a material for bosonic superconducting qubits

Even though bosonic qubits are intrinsically robust against errors, they profit from high coherence properties of the underlying superconducting circuits. Therefore, we can build on developments made for standard superconducting qubits and apply them to our devices. A standard superconducting qubit consists of a capacitive element connected to one or several Josephson junctions acting as a nonlinear inductor. The capacitive element and the embedding superconducting circuitry is generally made from thin metal films, such as aluminum or niobium, patterned on a substrate, such as Si:SiO$_2$ or sapphire. In bosonic or protected qubits, more complex circuit elements are used, but the basic fabrication principle is similar.

Losses in high-coherence superconducting circuits originate primarily in the three interfaces present in the devices: metal-vacuum, substrate-metal, and substrate-vacuum [4]. It is therefore crucial to improve the quality of these surfaces and interfaces. This has led to the emergence of tantalum (Ta) as a new circuit material in recent years [3,5]. Ta can be deposited directly and cleanly onto sapphire and has a naturally low-loss surface oxide that is stable at room temperature. It furthermore resists aggressive cleaning steps aimed are removing contaminants at the substrate-vacuum interface.

Testing of tantalum superconducting circuits

We initially benchmarked our process by fabricating and measuring tantalum-based superconducting transmon qubits. This means that the capacitive transmon pads, and in the case of a planar sample, the readout resonator and filter circuitry are made from tantalum structures using the process described in last year's report.

Only the Josephson junction is made with an aluminum-based fabrication process. Great care has to be taken when integrating the two processes to avoid losses through contact resistance. We fabricate our Josephson junctions using a Dolan shadow-angle recipe in a Plassys evaporator at the IBM BRNC cleanroom. We added an ion-beam milling step inside the evaporator before the first aluminum deposition to our standard process. This step needs to be carefully calibrated to remove the tantalum surface oxide while not collapsing the EBEAM resist bridges essential for the junction fabrication.

Our initial transmon samples were so-called "3D" transmons, meaning that they were electrically floating in a three-dimensional microwave cavity, which acted as the readout resonator. We chose this geometry because it avoids packaging losses and gives a more straightforward measure of the fabrication-related surface and interface losses on the sample chip. With these samples we obtained very encouraging T_1 relaxation times and T_2 Ramsey times in excess of 100 μs. We have very recently achieved similar results in a fully planar device resembling one of the two lateral qubit islands shown in Fig. 1. The best T_1 time measured on a planar transmon in our lab is ~200 μs.

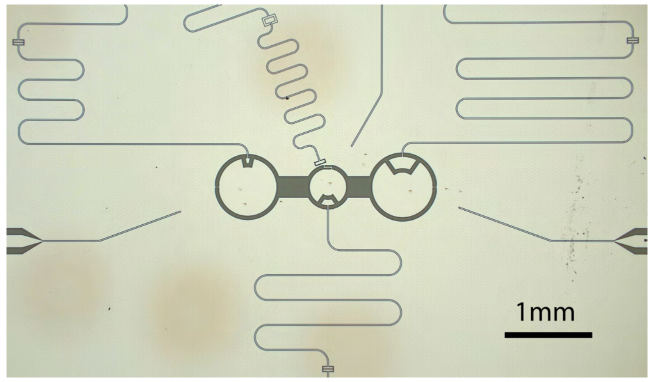

Fig. 1: Optical microscope image of a representative example chip showing three coupled qubits (islands in the middle of the image), several drive lines (e.g. lines entering the image from the left and right), as well as readout resonators and filtering structures. The tantalum film (light color) has been etched away in some regions of the chip (dark color) to define the device structures. All resonators and transmission lines are coplanar waveguides.

Measuring a planar Kerr-cat qubit

We then progressed to the next milestone on our project: the implementation of a planar Kerr-cat qubit. This required us to update the design to accommodate additional transmission lines and filters for the parametric pump used to activate the single-mode squeezing drive (visible at the top of Fig. 1). To prove that we can stabilize a KCQ we conducted the following experiment described by the schematic pulse sequence given in Fig. 2: We initialize the system in the vacuum state through passive cooling and then ramp on the squeezing drive. This maps the vacuum state (first excited state) onto the so-called even (odd) parity Schrödinger-cat states, which are the basis states of the KCQ. We then apply an additional resonant drive to induce Rabi oscillations on the KCQ Bloch sphere. After a variable wait time, we map the resulting state back onto the vacuum/first excited state and measure the population in that basis. Due to the error-suppression capabilities of the KCQ, it is only possible to drive these oscillations with a well-defined phase [2]. If the phase of the drive is not correctly aligned with the phase of the coherent states of the KCQ the oscillations are suppressed. This can be observed by repeating the experiment for different drive phases (see Fig. 3) and is direct evidence of the stabilization and operation of a Kerr-cat qubit [2].

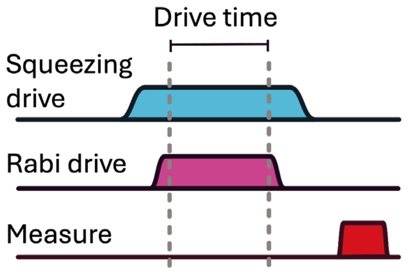

Fig. 2: Pulse sequence of the experiment. See text for description. Adapted from [2]

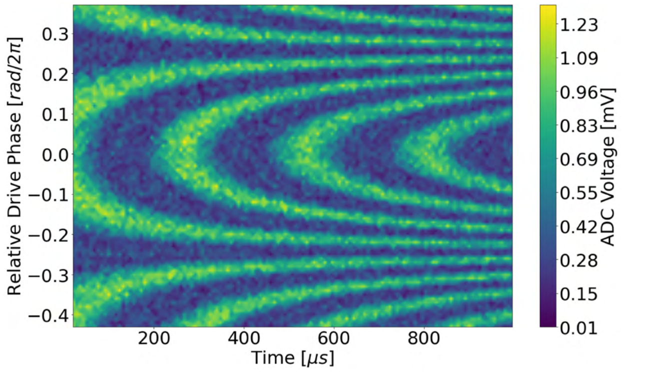

Fig. 3: Drive-phase-dependent Rabi oscillations of a Kerr-cat qubit. Color scale is the analog-to-digital converter voltage corresponding to the measured signal. Dark color indicates the vacuum state, while light color indicates the first excited state. The abscissa gives the time for which the Rabi drive is applied (see drive time in Fig. 2) and the ordinate gives the phase of the drive relative to the phase of the Kerr-cat qubit basis states. It is calibrated such that zero phase corresponds to the maximum oscillation rate.

Outlook

In the coming year, we will begin to couple KCQs both to standard qubits and to other KCQs to demonstrate gate operations and parametric interactions between these systems.

References

[1] Darmawan, A. S., et al. Practical Quantum Error Correction with the XZZX Code and Kerr-Cat Qubits. PRX Quantum 2, 030345 (2021).

[2] Grimm, A., Frattini, N.E., et al. Stabilization and operation of a Kerr-cat qubit. Nature 584, 205-209 (2020).

[3] Place, A. P. M., et al. New material platform for superconducting transmon qubits with coherence times exceeding 0.3 milliseconds. Nature Communications 12, 1779 (2021).

[4] Wang, C., et al. Surface participation and dielectric loss in superconducting qubits. Appl. Phys. Lett. 107, 162601 (2015).

[5] Crowley, K. D., et al. Disentangling Losses in Tantalum Superconducting Circuits. Phys. Rev. X 13, 041005 (2023).

Structural basis of NINJ1-mediated plasma membrane rupture in cell death

Project P2102: Structure and Assembly Mechanism of the Ninjurin-1 Membrane Perforation Pore in Executing Cell Death
Project Leaders: S. Hiller and D.J. Müller
Collaborator: M. Degen (SNI PhD Student)

Introduction

This project is centred on deepening our understanding of how cells die – a fundamental process essential for multicellular life. Cells can naturally undergo a process called Programmed Cell Death (PCD), which is vital for maintaining healthy tissues. However, when PCD goes awry, it can cause serious illnesses like cancer, neurodegenerative diseases, autoimmune disorders, and chronic inflammation. Our focus is on a 19 kDa protein named Ninjurin-1 (NINJ1), which plays a pivotal role in the final stages of certain subtypes of lytic PCDs such as pyroptosis and secondary necrosis [1].
The membrane protein NINJ1 is crucial for PCD. Its primary role is to facilitate the completion of lytic PCD by breaking apart the plasma membrane. This event releases important molecules, such as HMGB1 and LDH, which trigger further immune responses.

Establishing recombinant protein expression and purification

Our initial steps involved producing NINJ1 in a controlled environment. We inserted human NINJ1 into a suitable vector for expression in *Escherichia coli*. To purify NINJ1, we isolated it from the cells, solubilized it from the bacterial membranes using detergents and then utilized a combination of different chromatography-based purification techniques [2].

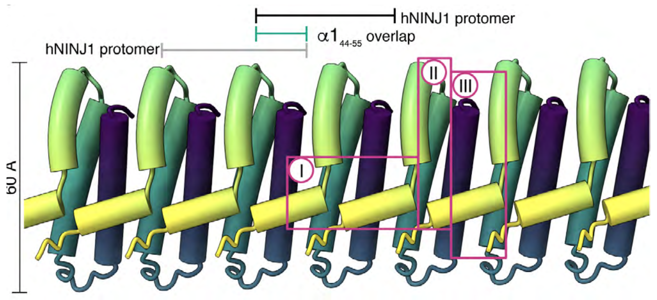

Fig. 1: NINJ1 Cryo-EM Structure of the NINJ1 filament. Individual protomers are colored by gradient (yellow-green-purple). Main interfaces of NINJ1 protomers are indicated by magenta boxes.

After purification, we used two types of electron microscopy to study NINJ1. Negative stain transmission electron microscopy helped us understand the size and overall arrangement of NINJ1 assemblies at a basic and low-resolution level. For a more detailed view, we employed cryogenic electron microscopy (cryo-EM), revealing the three-dimensional structure of NINJ1 at atomic resolution (Fig. 1).

Interaction of NINJ1 with bilayer is mediated by phosphatidylserine-dependent interaction helix 1

It is well known that cells become symmetric in their lipid composition upon pyroptosis. The normal asymmetry is no longer maintained and flippases switch phosphatidylserine (PS) to the outer leaflet. We could show in unique experiments that helix 1 of NINJ1 is specifically binding to PS-containing membranes (Fig. 2). This feature might play a crucial role in pyroptotic signalling and gives a unique outlook for the mechanism of NINJ1 action. It seems that helix 1 has unique abilities to specifically detect the PS molecule. For example, it could bind to its head group and thus recognize its chemistry. This feature has now been shown consistently in three different biophysical experiments.

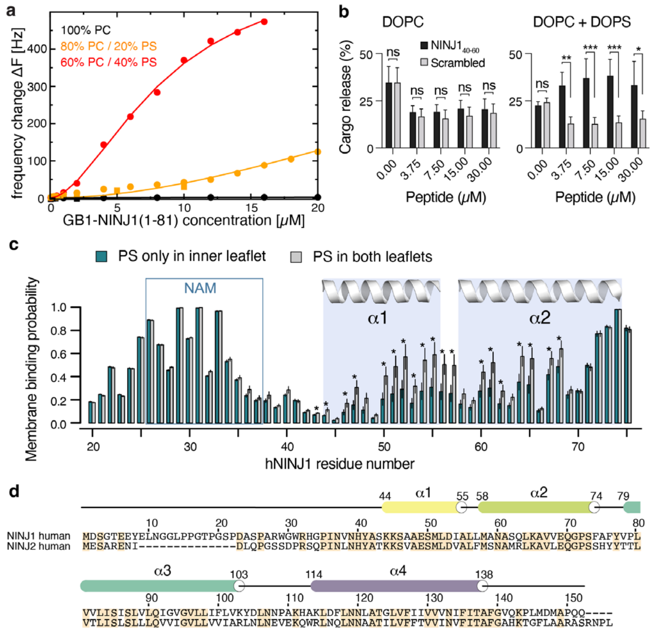

Fig. 2: Interaction of helix 1 with the lipid bilayer is PS-dependent. a Binding of NINJ1 helix 1 to bilayers with different composition measured by bilayer interferometry. b NINJ1 helix 1 releases cargo from bilayer vesicles, but only in bilayers with PS. c Binding propensity of NINJ1 to bilayers. Grey in presence, blue in absence of phosphatidylserine.

Molecular Dynamics and Mutagenesis Studies

Molecular dynamics simulations further supported our structural findings. These simulations demonstrated the stability of NINJ1 filaments at membrane edges and their ability to form variable arrangements, proving crucial for membrane perforation. The simulations also highlighted the importance of specific helices, in maintaining the structural integrity of NINJ1 filaments (Fig. 3). NINJ1 is not only able to stabilize membrane edges – it also shows a large malleability to undergo transformations of the pore shape. This might be a unique property to act as a universal cell killer irrespective of the local topology and morphology.

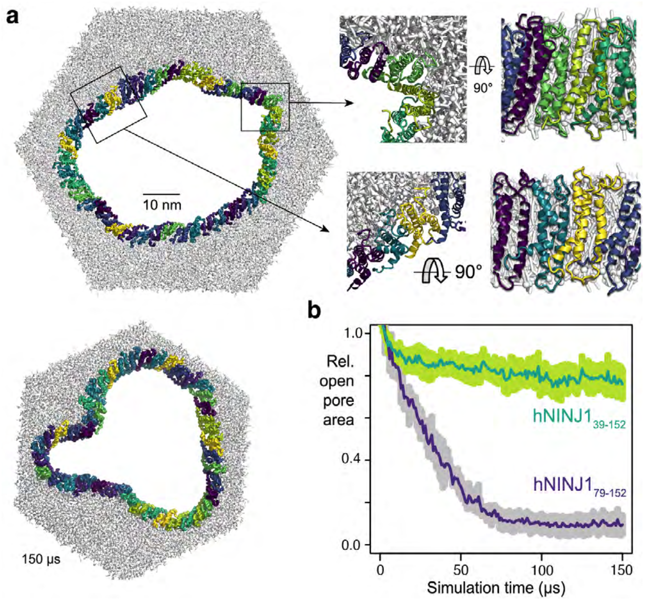

Fig. 3: MD simulations of the NINJ1 pore. a Starting conformation of the MD simulation and atomic details. Bottom: structure of the pore after 150 µs. b Time-dependence of the pore are for wildtype and mutant NINJ1.

To validate our structural model, we engineered single-amino-acid mutants of NINJ1 and assessed their impact on in vitro filament formation and cell lysis. Mutants designed to disrupt filament formation generally reduced or abolished cell lysis, aligning with our structural understanding of NINJ1. These findings were corroborated in both in vitro settings and in cellular models, cementing the functional significance of NINJ1's structural arrangement in mediating cell death.

Conclusion

Overall, a functional model emerged of NINJ1 pore formation in pyroptosis and other cell deaths (Fig. 4). The mechanism is of crucial biological relevance in all cell types. Connections to cell adhesion seems plausible. This project has thus so far illuminated the critical role of NINJ1 in PCD, particularly in the context of pyroptotic cell death (Fig. 4). By elucidating the structural and functional aspects of NINJ1, we have advanced the understanding of the molecular mechanisms underpinning inflammatory active, lytic cell death. This knowledge not only contributes to basic biological science but also opens new avenues for therapeutic interventions in diseases characterized by dysregulated cell death [3].

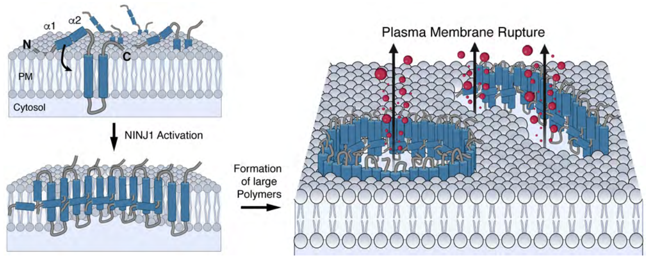

Fig. 4: Schematic model summarizing the current understanding of NINJ1-mediated plasma membrane rupture.

As an outlook, we have now made substantial progress in reconstitution of NINJ1 for atomic force microscopy (AFM). Initial recordings have shown that NINJ1 in lipid bilayers forms pores that can be imaged faithfully. We will thus be able to observe and possibly quantify membrane disruptions, which we anticipate to further elucidate the mechanisms triggering NINJ1 activation. Emerging studies suggest that this activation might be linked to cellular blebbing which is a common hallmark across different forms of PCD [4]. In addition, it has been proposed by us and others that membrane lipid composition and therefore fluidity / rigidity could play a role in activation which we aim to investigate further.

References

[1] Kayagaki, N., Kornfeld, O.S., Lee, B.L. et al. NINJ1 mediates plasma membrane rupture during lytic cell death. Nature 591, 131–136 (2021).

[2] Degen, M., Santos, J.C., Pluhackova, K. et al. Structural basis of NINJ1-mediated plasma membrane rupture in cell death. Nature 618, 1065–1071 (2023).

[3] Kayagaki, N., Stowe, I.B., Alegre, K. et al. Inhibiting membrane rupture with NINJ1 antibodies limits tissue injury. Nature 618, 1072–1077 (2023).

[4] Dondelinger, Y., Priem, D., Huyghe, J. et al. NINJ1 is activated by cell swelling to regulate plasma membrane permeabilization during regulated necrosis. Cell Death Dis 14, 755 (2023).

RT-Xray as a tool to explain cofactorindependent hydrolytic C-S bond cleavage

Project P2104: Methods to understand the role of ordered waters and disordered residues in enzyme
catalysis using macromolecular crystallography at physiological temperatures
Project Leaders: F.P. Seebeck and J.H. Beale
Collaborators: S. Bolotova (SNI PhD Student)

Abstract

Nucleophilic activation of water is a key catalytic strategy employed by hydrolytic enzymes. The hydrolysis of substrates with low electrophilicity necessitates the use of highly activated water-derived nucleophiles, such as metal-coordinated hydroxides, or covalent catalysis involving active-site cysteine or serine residues as primary nucleophiles. This year, we investigated an enzyme that catalyzes hydrolytic C-S bond cleavage through a novel mechanism.

Introduction

Ergothioneine (**1**, Figure 1) is a histidine-derived sulfur metabolite found in bacteria, archaea, fungi, plants, and animals. Multiple biosynthetic pathways for ergothioneine have been described, and the key enzymes involved have been extensively studied for their structure and mechanisms. In contrast, ergothioneine catabolism is much less well understood. We have previously outlined a five-step pathway for the complete degradation of ergothioneine (**1**) and S-methyl ergothioneine (**2**, Ref. 1 and 2). S-methyl ergothioneine likely forms from ergothioneine via uncatalyzed alkylation by methyl halides, which are known electrophilic metabolites in plants and bacteria. The first two degradation steps are catalyzed by specific lyases and hydratases, which are closely related to enzymes involved in histidine catabolism. The final two steps are mediated by metal-dependent hydrolases that show strong homology to enzymes in uracil catabolism. The pathway's early and late stages are connected by an entirely novel type of enzyme that catalyzes the desulfurization of thiohydantoin. We have solved the crystal structure of the desulfurase (S-Me-THD) from Variovorax species (strain JCM 16519 / RA8) in a complex with hydanthionine (5). Comparison with the structure and activity of THD from *Paenibacillus sp*. suggests that this enzyme catalyzes C-S bond cleavage through a previously uncharacterized mechanism.

Results and Discussion

Production of S-Me-THD. The gene coding for S-Me-THD was purchased from Biocat GmbH and cloned into a pET28a(+) expression plasmid. This plasmid was transformed into *E. coli* BL21 pLysS (DE3) strain expressing *S. coelicolor* chaperonins GroEL/GroES by heat shock method. Transformed cells were cultivated at 37°C, 180 rpm until OD_{600} reached 0.6, and then induction with 0.2 mM IPTG was performed. After induction, the cultures were

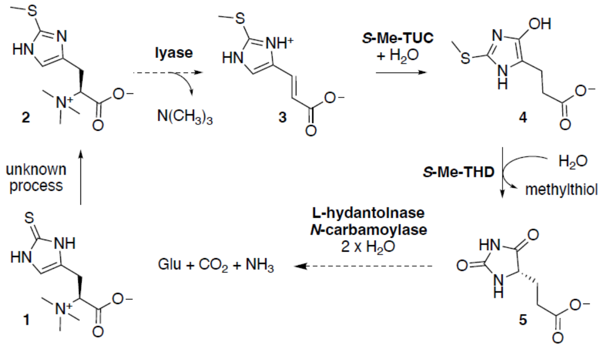

Figure 1: Bacterial degradation of S-methylergothioneine

Protein purification and crystallization. S-Me-THD was purified from cell-free lysates over Ni^{II}NTA agarose dialyzed in a cellulose bag (MW 12-14 MWCO) against 20 mM Tris, 200 mM NaCl, pH 8.0, at 4°C. After concentration (10K MWCO, 20 mL, Thermo Scientific) this protein was used for crystallization. The sitting drop vapor diffusion method was applied for the crystallization of VasTHD using commercial protein crystallization screens Morpheus® II and PACT premier™ (Molecular Dimensions). The protein samples were used for crystallization in a final concentration of 15 mg/mL (0.39 mM), also supplemented with Hydantoin in a final concentration of 0.5 mM.

Crystals for VasTHD in complex with Hydantoin were obtained in Morpheus II screen, in a crystallization buffer consisting of 10% w/v PEG 20000, 20% v/v PEG MME 550, 0.1 M MES/imidazole pH 6.5, 0.02 M of carboxylic acids. The diffraction data were collected at the i03 beamline of Diamond Light Source (Oxfordshire, UK), equipped with an Eiger2 XE 16M detector (Dectris). High-resolution data sets were collected at an X-ray energy of 12.7 keV (l = 0.9763 Å). Diffraction data were indexed, integrated, scaled, and merged with DIALS (Diamond Light Source, Lawrence Berkeley National Laboratory, and STFC).

VasTHD crystals grew into space group P 1 2$_1$ 1 with unit cell dimensions of a = 49.8 Å, b = 87.5 Å, c = 70.9 Å, alpha = 90.0°, beta = 94.9°, gamma = 90.0°, unit cell volume is 308026.84 Å^3.

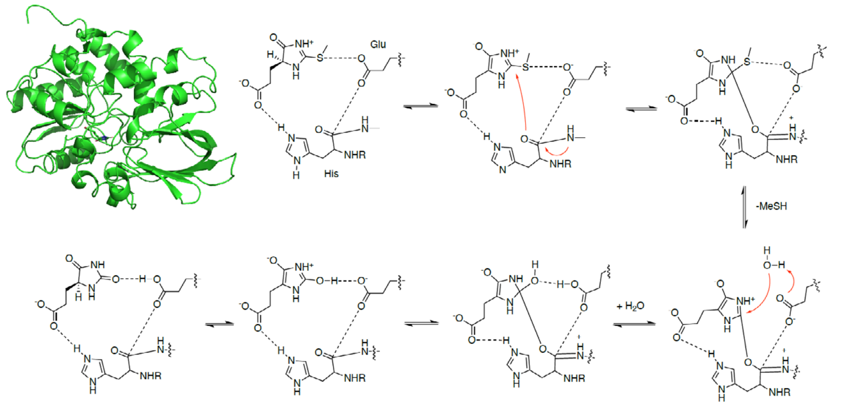

Figure 2: Top left: overall view of the structure of S-Me-THD in complex with hydantoin. Right: Proposed mechanism of THD-catalyzed hydrolysis of S-methyl thiohydantoin. An active site Glu residue forms an S-O chalcogen bond with the positively charged 2-thiohydantoin ring. The negative charge of the same Glu residue also stabilizes the positive charge developing on the amid bond after nucleophilic attack onto the substrate. The resulting first covalent intermediate collapses upon expulsion of methyl thiol (MeSH). The second covalent intermediate is attacked by a water molecule that is activated by the active site Glu. The catalytic cycle concludes with stereoselective protonation of the hydantoin ring.

Table 1. Data collection and refinement statistics.

	VasTHD:Hyd, PDB ID:
Wavelength (Å)	0.9763
Resolution range (Å)	87.44 - 1.30 (1.32 - 1.30)
Space group	P 1 2$_1$ 1
Unit cell dimensions	
a, b, c (Å)	49.92, 87.44, 70.73
α, β, γ (°)	90.00, 94.84, 90.00
Total reflections	705763 (2360)
Unique reflections	119174 (1258)
Multiplicity	5.9 (1.9)
Completeness (%)	80.3 (16.9)
<I/σ(I)>	19.6 (0.4)
R_{merge}	0.052 (0.881)
R_{meas}	0.056 (1.168)
R_{pim}	0.022 (0.758)
$CC_{1/2}$	0.999 (0.347)
Reflections used in refinement	119076 (3057)
Reflections used for R-free	2049 (61)
R-work	
R-free	
Number of non-hydrogen atoms	5895
macromolecules	5288
ligands	24
solvent	583
Protein residues	722
r.m.s deviations	
bond lengths (Å)	0.005
bond angles (°)	1.21
Ramachandran favored (%)	96.94
Ramachandran allowed (%)	2.79
Ramachandran outliers (%)	0.28
Rotamer outliers (%)	0.00
Clashscore	2.98
Average B-factor (Å^2)	21.60
macromolecules	20.47
ligands	22.34
solvent	31.79

Two protein molecules were contained per unit cell. The Matthews coefficient is 2.02 Å^3/Da, and the estimated solvent content is 39.12%.

Iterative cycles of the manual and automated model building into the interpretable electron density map and refinement were done by using COOT and phenix.refine (Table 1). Aside from protein chains, the asymmetric unit cell contained additional electron density in the active sites that was modeled by the addition of the hydantoin molecule.

Mechanistic implications. The structure of S-Me-THD combined with previous biochemical observations suggest that this enzyme-type mediates hydrolysis of compound **4** via a two-step process. In the first step, a specific amid function of the enzyme backbone attacks the electrophilic C2 on the thiohydantoin of **4**. In the second step, the covalent adduct is hydrolyzed by an activated water molecule. Currently, we are developing experiments to visualize one of the proposed covalent intermediates.

Conclusion

We have determined the crystal structure of a novel type of desulfurase. This enzyme mediates the hydrolytic substitution of a C-S bond by recruiting a backbone amid function for nucleophilic covalent catalysis.

References

[1] M.A. Beliaeva, F. Leisiner, F.P.Seebeck. In Vitro Reconstitution of a Five-Step Pathway for Bacterial Ergothioneine Catabolism. ACS Chem. Biol. 16 (2): 397-403. (2021)

[2] C.M. Vasseur, D. Karunasegaram, F.P. Seebeck Structure and Substrate Specificity of S-Methyl Thiourocanate Hydratase. ACS Chem. Biol. 19 (3): 718-724. (2024)

Gated monolayer MoS_2

Project P2105: Ferromagnetism of mobile electrons in a two dimensional semiconductor
Project Leaders: R.J. Warburton and M. Poggio
Collaborator: R.M. Kaiser (SNI PhD Student)

Recently, it has been shown that mobile electrons in various two-dimensional (2D) materials are ferromagnetic at low temperature. Ferromagnetism has been observed in the semiconductors monolayer MoS_2 [1], an AlAs quantum well [2], and monolayer WSe_2 [3]. Graphene, a 2D semi-metal, also exhibits ferromagnetism [4]. There is evidence in MoS_2 for an abrupt loss of the ferromagnetism, i.e., a phase transition, as the electron density increases [5]. These studies extend the concept of ferromagnetism to a new class of materials.

We have determined the exchange energy of ferromagnetic MoS_2 [5]. We stress that the host material MoS_2 is not magnetic – the magnetism arises via the mobile electrons. We find an exchange energy of 11 meV at low electron-density (corresponding to about 1 electron per 10,000 Mo atoms). This is a substantial energy: it corresponds to the thermal energy at about 100 K. This suggests that the ferromagnetism in MoS_2 survives at temperatures well above the temperature at which the experiment was performed (4.2 K).

The determination of the exchange energy relied on an interpretation of the optical behaviour, in particular the identification of the four spectral lines observed on illuminating gated MoS_2 with a weak red-laser [5]. Detective work was required to link each spectral line to a particular microscopic process. The essential guide is the Pauli principle: the two electrons in the trion cannot occupy the same state. This detective work resulted in a completely consistent account of the microscopic origin of the four trions [5]. It is also provided confirmation that the resident electrons all have the same spin. An examination of the photon energies, i.e., the "colour" of each spectral line, then allowed the exchange energy to be read off from this "bar code": the exchange energy is simply the energy separating two of the spectral lines.

This experiment on ferromagnetism in gated MoS_2 relies on the optical selection rules of MoS_2: it is not a universal approach to probing magnetism of mobile electrons in 2D. Furthermore, the probe, a red laser, may disrupt the ferromagnetism in subtle ways. The most obvious consequence of a ferromagnet is the magnetic field it creates in its vicinity. A direct measurement of this magnetic field would be ideal. Can it be detected? For iron this is trivial of course. The situation is completely different for electrons in a 2D semiconductor: the magnetic field is very small, and present samples are tiny. Detecting this magnetic field on MoS_2 would be a triumph in experimental physics. It would also open the door to probing magnetism in the general class of 2D electrons.

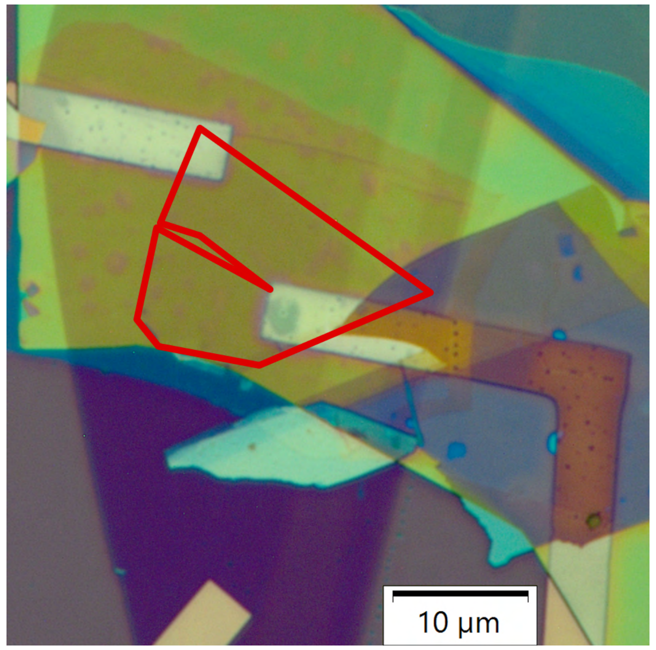

Fig. 1: Microscope image of a sample consisting of a stack of a few-layer graphite flake (purple), a thin bottom hBN layer (blue), monolayer MoS_2 (outlined in red), and the thick top hBN flake (yellow). One can also see the gold contacts to the few-layer graphite and the monolayer MoS_2. The scale bar is 10 µm.

The way forward is to use a state-of-the-art nano-magnetometer allowing the detection of ultrasmall magnetic fields with nanoscale spatial resolution. Noise will be an issue. The obvious way to reject noise is to turn the magnetism on and off by modulating the electron density at a particular frequency, rejecting signals at all other. Unfortunately, the present samples, shown in Fig. 1, cannot be modulated as the contact resistance is far too high. A new batch of device is currently being fabricated, replacing the high-resistance gold contacts with relatively low-resistance bismuth contacts. A schematic is shown in Fig. 2. The bismuth must be in intimate contact with the MoS_2. On success, modulation spectroscopy will be demonstrated in the optical domain, and subsequently magnetometry experiments will be designed.

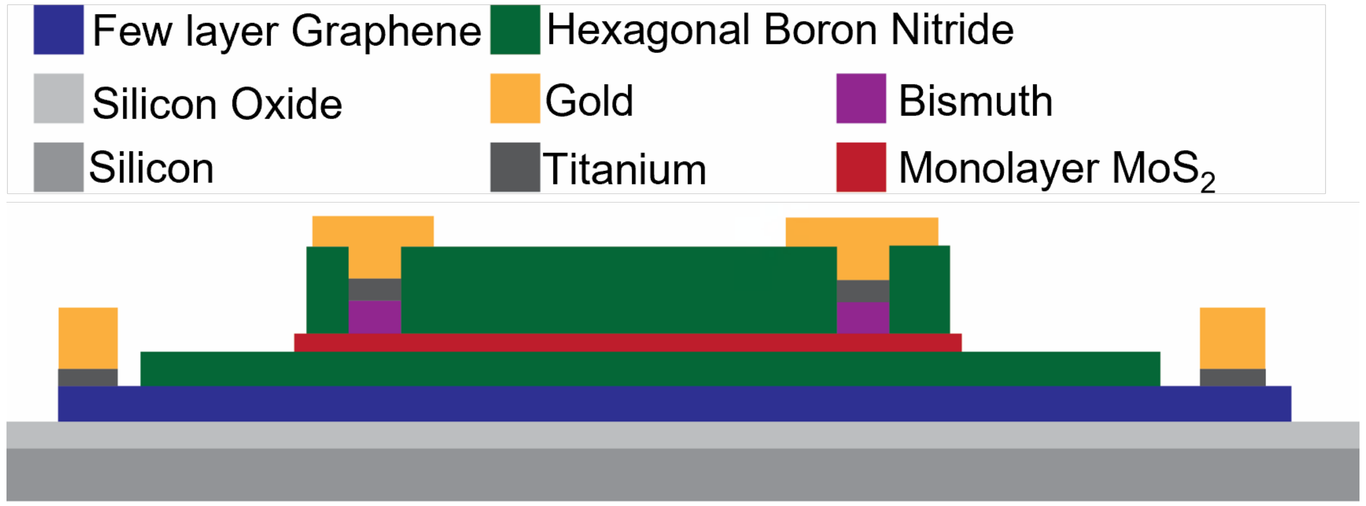

Fig. 2: Schematic of the fabrication process for bismuth contacts. The few-layer graphite is contacted with titanium/gold, and the MoS2 is contacted via an etched hole in the hBN with bismuth/titanium/gold contacts.

In our previous experiments, the ferromagnetism is stabilised by applying a large out-of-plane magnetic field [1,5]. This field determines the direction of the electron spins, either up or down. An alternative technique is to stabilise the ferromagnetism without an external field, relying instead on optical injection of either spin-up or spin-down electrons [3]. In a related material, local injection of spins resulted in a ferromagnetic phase extending over a large area [3]. It is presently unknown if this approach works also in the case of MoS_2. It is important to pump with red laser light at one location of the sample and to probe at a separate location. A cryogenic confocal microscope has been designed and built to achieve this. The pump spot can be positioned *in situ* with respect to the sample, and the probe spot can then be positioned *in situ* with respect to the pump, as shown in Fig. 3.

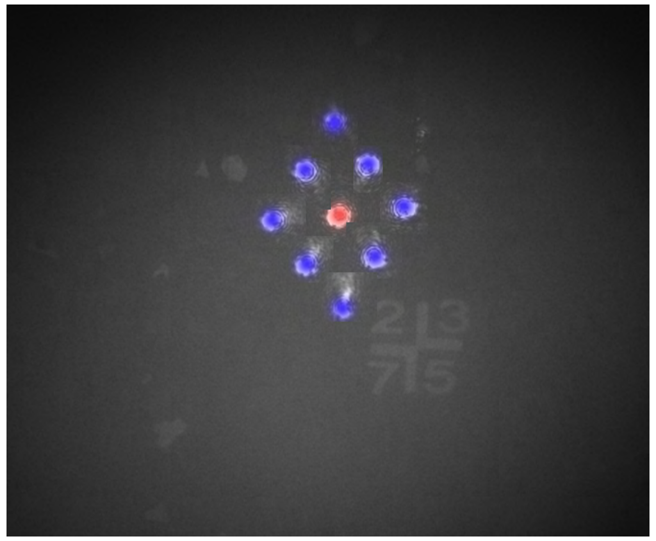

Fig. 3: Image of the probe spot, false coloured in blue, moved with respect to the pump spot indicated in red. The marker has a diameter of 20 µm.

References

[1] J. G. Roch, G. Froehlicher, N. Leisgang, P. Makk, K. Watanabe, T. Taniguchi, and R. J. Warburton, Spin-polarized electrons in monolayer MoS2, Nature Nanotechnology 14, 432 (2019)

[2] M. S. Hossain, T. Zhao, S. Pu, M. A. Mueed, M. K. Ma, K. A. Villegas Rosales, Y. J. Chung, L. N. Pfeiffer, K. W. West, K. W. Baldwin, J. K. Jain, and M. Shayegan, Bloch ferromagnetism of composite fermions, Nature Physics 17, 48 (2021)

[3] K. Hao, R. Shreiner, A. Kindseth, and A. A. High, Optically controllable magnetism in atomically thin semiconductors, Science Advances 8, eabq7650 (2022)

[4] A. L. Sharpe, E. J. Fox, A. W. Barnard, J. Finney, K. Watanabe, T. Taniguchi, M. A. Kastner, and D. Goldhaber-Gordon, Emergent ferro-magnetism near three-quarters filling in twisted bilayer graphene, Science 365, 605 (2019)

[5] N. Leisgang, D. Miserev, H. Mattiat, L. Schneider, L. Sponfeldner, K. Watanabe, T. Taniguchi, M. Poggio, and R. J. Warburton, Exchange Energy of the Ferromagnetic Electronic Ground State in a Monolayer Semiconductor, Physical Review Letters 133, 026501 (2024)

Iridium-porphyrin catalyzed prodrug activation

Project P2106: Innovative Catalytic Strategies to Combat Cancer
Project Leaders: T.R. Ward and M. Fani
Collaborator: D.A. Graf

Abstract

Most traditional cytotoxic anticancer drugs used in chemotherapy indiscriminately target rapidly proliferating cells. Their mode of action mainly relies on either impairment of mitosis or induction of DNA damage and, therefore, affects both rapidly proliferating cancer cells and healthy cells. By utilizing a prodrug therapy, where a less cytotoxic form of the anticancer drug is administered, the undesirable and unspecific death of healthy cells can be minimized. The precise accumulation and localized release of the cytotoxic drug in proximity to the diseased tissue are pivotal for the efficacy of the cancer therapy. The prerequisite for the active accumulation is the over-expression of a membrane-bound receptor that can be actively targeted by its natural ligand, antagonist, or antibody (ADC, SMDC, ADEPT, Figure 1).[1,2,3]

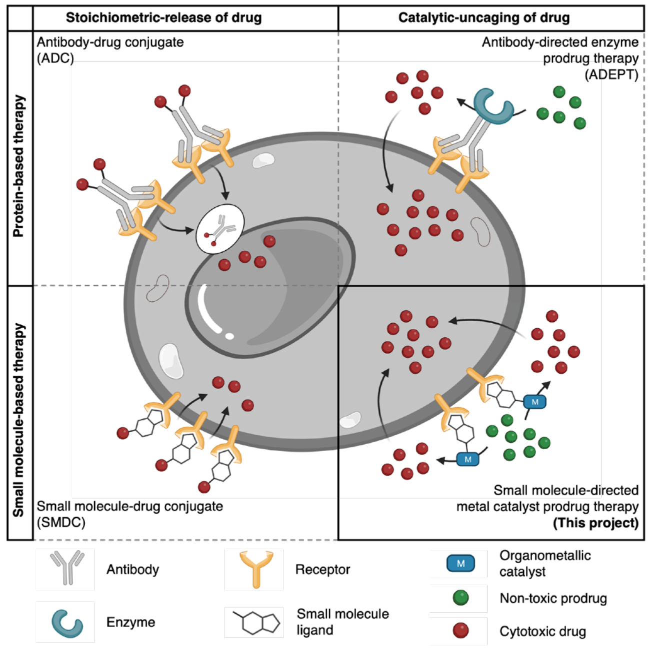

Fig. 1: Active targeting strategies to selectively accumulate chemotherapeutic drugs on cancer cells.

Our project is based on the development of an innovative therapy consisting of an organometallic catalyst conjugated to a targeting unit with a high affinity for a receptor over-expressed on the surface of cancer cells. Following selective accumulation at the surface of target cancer cells, the catalyst will site-specifically uncage a subsequently-administered non-toxic prodrug to release a potent cytotoxic drug. Notably, the small molecule-directed metal catalyst prodrug therapy (MCPT) is expected to be more selective than current chemotherapies. Further, compared to antibody-drug conjugates (ADC), the small molecule components are more straightforward and inexpensive to produce and tailored for a given target. They are also anticipated to exhibit greater tissue diffusion rates due to their low molecular weight. Building on the Ward group's expertise with *in cellulo* metal-catalyzed carbene-insertion reactions,[4,5] we set out to adapt this strategy to an intramolecular Buchner ring-expansion reaction of aryl diazoketones.

Cargo release upon Buchner ring-expansion

Previously, we have developed a synthetic sequence to access a substrate that undergoes a 1,6-elimination reaction upon Buchner ring expansion, Figure 2. Gratifyingly, this substrate efficiently releases a *para*-fluorobenzoic acid in the presence of an iridium porphyrin catalyst (Ir(mPIX)Me) within a few minutes in organic solvent. Intrigued by these initial results, we tested this scaffold to cage fluorophores and potent anti-cancer drugs (e.g., marina blue and epirubicin).

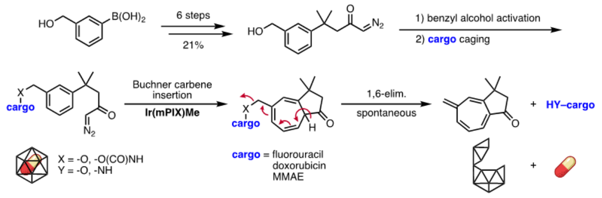

Fig. 2: Design and synthesis of an aryl diazoketone for cargo release via Buchner ring-expansion.

In vitro uncaging of fluorophores

A time-course experiment to monitor the kinetics of the uncaging reaction of pro6,8-F_2MU with varying concentrations of Ir(mPIX)Me resulted in the following observations: i) The reaction is compatible with an aqueous environment. ii) Using more than 10 nM Ir(mPIX)Me, the product release does not further increase after 2 h. iii) The catalyst reaches up to 1738 TON after 16 h, with a reduced yield.

Accumulation on cancer cells

The dimeric membrane-associated protein hCA IX is highly overexpressed under hypoxic conditions, a common feature of the microenvironment of solid cancer tumors. Outside of a tumor environment, hCA IX is virtually undetectable in normal adult tissues. It has been extensively studied as a target site for drug delivery using acetazolamide (AA) functionalized inhibitors. Importantly, these inhibitors are not internalized upon binding and are, therefore, well-suited to develop a MCPT.[6] For the selective accumulation of the organometallic catalyst, the carboxylic acids of the iridium porphyrin were conjugated through a linker with acetazolamide (AA–Ir(mPIX)Me). Fluorescence microscopy with the acetazolamide-bearing fluorophore AA–SRB further confirmed the selective binding on the cancer cell's surface in the presence of antibodies, Figure 4A & 4B. To further scrutinize the selective accumulation on the membrane protein hCA IX, we saturated all binding sites with free acetazolamide, resulting in no AA–SRB binding, Figure 4C.

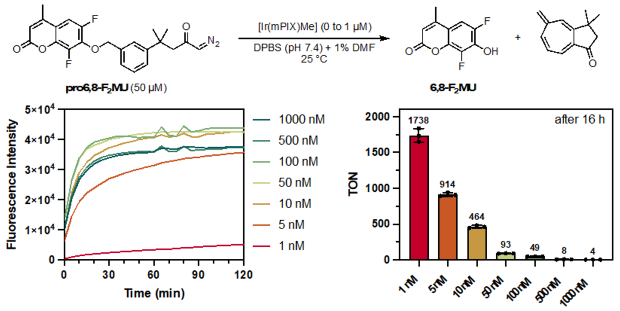

Fig. 3: Catalytic uncaging of pro6,8-F_2MU.

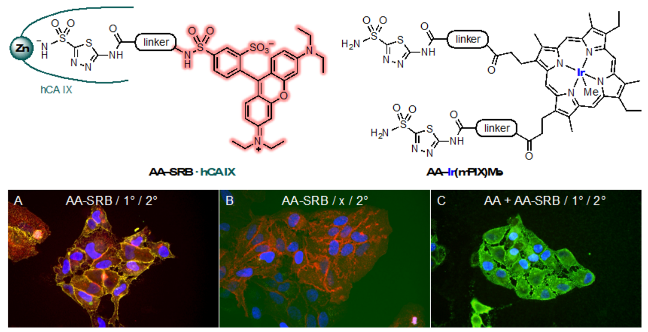

Fig. 4: Structure of acetazol-bearing fluorophore (AA–SRB) and iridium porphyrin (AA–Ir(mPIX)Me) and fluorescence microscopy images of hCA IX overexpressing cells (green: FITC functionalized 2nd antibody, red: AA–SRB, blue: nuclear stain DAPI).

On cellulo uncaging of prodrugs

We initiated the *on cellulo* studies by determining the IC_{50} values—at which concentration only 50% of the cells are viable—of epirubicin and pro-epirubicin (proEpi), Figure 5b. Thanks to the presence of the uncaging moiety, we were pleased that the toxicity of proEpi was significantly reduced, as reflected by its safety index (SI) value of 352.

Based on these promising results, we tested the catalytic uncaging of proEpi in the presence of AA–Ir(mPIX)Me bound to hCA IX on the surface of CT26.3E10 cells (AA-Ir(mPIX)Me · hCA IX), Figure 5a & 5c. The group of Dario Neri generously provided their transfected cell line, which over-expresses about 72'000 copies of hCA IX on its cell surface under normoxic conditions.[6] We incubated these cell lines, first with the cofactor AA–Ir(mPIX)Me for 20 min, followed by incubation with 10 µM proEpi for 48 h. The viability of hCA IX overexpressing cells reduced up to 50% in the presence of 10 nM of iridium cofactor. The control experiments with CT26.wt cells revealed no sufficient AA–Ir(mPIX)Me accumulation on the cell surface. Therefore, no toxic effect on the control cell line was observed.

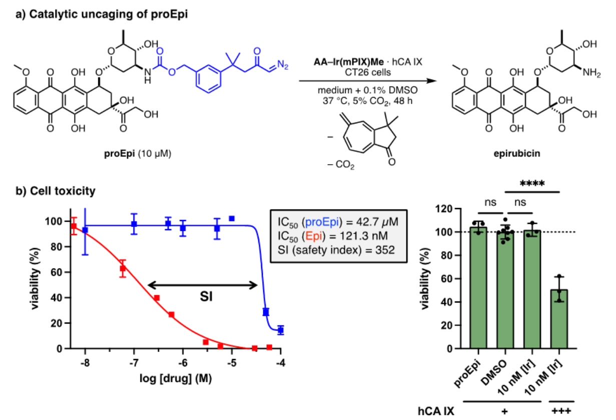

Fig. 5: In vitro uncaging a) of proEpi catalyzed by AA–Ir(mPIX)Me on the cell surface of hCA IX over-expressing cells, and b) cell toxicity of Epi (red) and proEpi (blue), ns: not significant, ****: P<0.0001 (one-way ANOVA).

Conclusion & Outlook

In the past year, we developed a novel bioorthogonal uncaging platform to release cytotoxic drugs on the cell surface of hCA IX overexpressing cells. We are currently preparing and evaluating different prodrugs to enhance the efficacy of this MCPT. This evaluation is expected to afford a drug/prodrug couple with a more stringent toxicity profile. Additionally, ICP-MS experiments will be carried out to confirm the accumulation of AA–Ir(mPIX)Me on the surface of CT26 cells and to determine the TON.

References

[1] J. Z. Drago, S. Modi and S. Chandarlapaty, "Unlocking the potential of antibody-drug conjugates for cancer therapy", Nat. Rev. Clin. Oncol. 18, 327–344 (2021)

[2] G. Casi and D. Neri, "Antibody-Drug Conjugates and Small Molecule-Drug Conjugates", J. Med. Chem. 58, 8751–8761 (2015)

[3] S. K. Sharma and K. D. Bagshawe, "Translating antibody directed enzyme prodrug therapy (ADEPT) and prospects for combination", Expert Opin. Biol. Ther. 17, 1–13 (2017)

[4] C. Rumo, A. Stein, J. Klehr, R. Tachibana, A. Prescimone, et al. "An Artificial Metalloenzyme Based on a Copper Heteroscorpionate Enables Sp3 C–H Functionalization via Intramolecular Carbene Insertion", J. Am. Chem. Soc. 144, 11676–11684 (2022)

[5] J. Zhao, D. G. Bachmann, M. Lenz, D. G. Gillingham and T. R. Ward, "An Artificial Metalloenzyme for Carbene Transfer Based on Biotinylated Dirhodium Anchored within Streptavidin", Catal. Sci. Technol. 8, 2294–2298 (2018)

[6] M. Wichert, N. Krall, W. Decurtins, R. M. Franzini, F. Pretto, et al. "Dual-display of small molecules enables the discovery of ligand pairs and facilitates affinity maturation", Nat. Chem. 7, 241–249 (2015)

Magnetic torque transducer in a phononic band-gap structure

Project P2107: High-sensitive torque magnetometry for 2D materials
Project Leaders: I. Zardo and M. Poggio
Collaborator: M. Claus (SNI PhD Student)

Introduction

Recent advancements in the fabrication and development of nanomechanical resonators have enabled exceptionally sensitive measurements of mass, force, and torque. These improvements are primarily attributed to the substantial reduction in the size of mechanical transducers over the past three decades. Smaller sizes and lower defect densities lead to reduced mechanical losses, which in turn enhance transducer sensitivity [1]. More recently, phonon engineering has emerged as a powerful tool to further minimize mechanical losses [2]. This approach employs patterned mechanical supports designed with a phononic band-gap tuned to the transducer's mechanical resonance frequency. These supports are also optimized to clamp the resonator effectively, further reducing losses. These innovative techniques have already been used to develop high-Q optomechanical devices [2] and are starting to find applications in the design of ultra-sensitive force sensors. However, their potential for torque sensing remains unexplored.

In this work, we aim to utilize advanced techniques to fabricate ultra-sensitive mechanical torque sensors specifically designed for investigating 2D materials, including 2D magnets and van der Waals (vdW) heterostructures. Our sensors will not only offer the sensitivity required to measure ultrathin magnetic materials but will also address a critical limitation of existing cantilever-based torque sensors by enabling electrical contact with the sample. This integration has been a significant challenge in previous designs, particularly for the most sensitive devices. A conceptual sketch of the proposed device is shown in Fig. 1.

Torque magnetometry is a well-established, highly sensitive method for studying nanomagnets, correlated metals, and superconductors [3]. Dynamic torque (frequency shift), which is proportional to the curvature of the magnetic free energy with respect to rotations, is a particularly effective observable for identifying magnetic phase transitions [4], because – just like the magnetic susceptibility – it exhibits discontinuities for both first- and second-order transitions. Torque magnetometry is also versatile, capable of measuring both magnetostatic effects and magnetization dynamics, including spin resonance and relaxation processes [5]. With the enhanced sensitivity of our planned torque sensors and the capability to integrate electrical leads and contacts with the sample, a wide range of experiments will become feasible. These include detecting superconducting and magnetic phase transitions in twisted bilayer graphene [5], van der Waals (vdW) heterostructures, and other 2D materials, such as the reported magnetic phase transition in gated monolayer MoS2 [6]. Our vision is to develop and apply a cutting-edge experimental platform to explore magnetic and superconducting phase transitions in 2D systems.

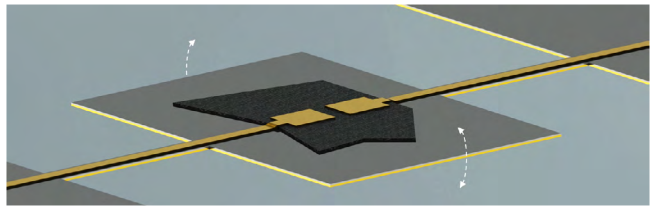

Fig. 1: Schematic diagram of a torque sensor with 2D sample, bottom back gate, and top contacts.

Goals

Sensitive torque magnetometry has been applied to study the magnetic properties of extremely small magnets [7], persistent currents in normal metal nanorings [8], and miniature superconducting structures [9]. However, this technique has not yet been utilized to investigate the emerging class of 2D van der Waals (vdW) materials and their heterostructures, which are too thin for conventional SQUID or torque magnetometers. These materials exhibit correlated states, including super-conductivity, highly insulating phases, and magnetism. Transitions between these states sometimes controllable via electrostatic gating. Our specially designed torque sensors aim to measure these phase transitions, providing detailed phase diagrams and new insights into these poorly understood condensed matter phenomena.

The objectives of this project are:

1. To fabricate torsional resonators that enable electrical contact with the sample and integrate them within phononic band-gap supports optimized for clamping;
2. To achieve state-of-the-art torque sensitivity on samples with electrical contacts;
3. To utilize these transducers to investigate magnetic and superconducting phase transitions in 2D materials as functions of gate voltage, magnetic field, and temperature.

Research in 2024

After developing fabrication techniques to make flexural and torsional mechanical resonators embedded inside a phononic band-gap from SiN, and studying their behavior during the first and second year, we have expanded the scope of our research to explore the magnetic properties of individual *Magnetospirillum gryphiswaldense* cells. These magnetotactic bacteria are known for their ability to sense Earth's magnetic field through chains of magnetic nanoparticles called magnetosomes, which act as biological compasses. Understanding their magnetic behavior has implications for both fundamental science and potential applications in biotechnology.

Using dynamic cantilever magnetometry (DCM), we measured the magnetic hysteresis of a single bacterium. These measurements, combined with transmission electron microscopy (TEM) and micromagnetic simulations, allowed us to analyze the magnetic configurations of the magnetosome chain. We identified key properties, such as the total magnetic moment, effective magnetic anisotropy, and the behavior of the chain under varying magnetic fields. Notably, we demonstrated that the chain's anisotropy stabilizes the bacterium's magnetic moment in Earth's field, a crucial feature for magnetotaxis.

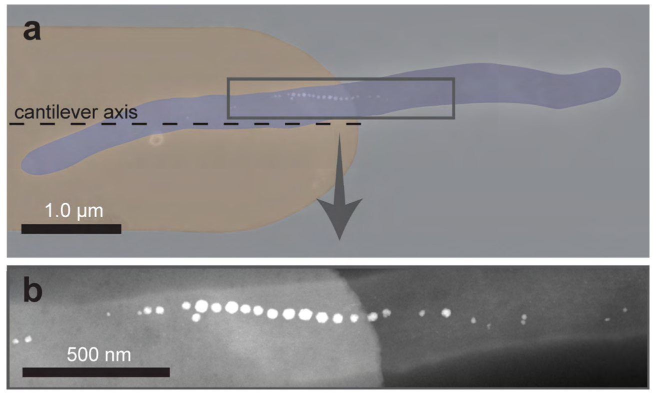

Fig. 2: a) False-color high-angle annular dark-field scanning transmission electron microscopy showing the bacterium (purple) attached to the apex of the cantilever (orange), and b) a close-up view of the magnetosome chain.

Our findings revealed the complex interplay between individual magnetosome properties and their collective magnetic behavior. This work not only enhances our understanding of magnetotaxis but also lays the groundwork for potential applications in biomedical devices, such as magnetically guided nano-robots or sensing platforms.

With this study, we validated our technique's ability to measure the magnetic properties of nanoscale systems with excellent precision. The insights gained from this research represent a significant milestone in applying high-sensitive torque magnetometry to biological systems.

Outlook

Looking ahead, we aim to return to study magnetic properties of 2D magnets and van der Waals heterostructures. To this end, we are currently fabricating few- to mono-layer samples of the antiferromagnetic vdW materials MnPS$_3$ and MnPSe$_3$, which will allow investigation of how the Néel temperature and the switching field of such materials depends on the number of interacting layers. Further, our investigation of the magnetic properties of a single *Magnetospirillum gryphiswaldense* cell has demonstrated the potential of dynamic torque magnetometry as an excellent tool for the study of magnetic phenomena in single-cell organisms, and nano-sized objects in general. This may motivate similar studies that incorporate other types of magnetotactic single-cell organisms in the future.

References

[1] F. R. Braakman and M. Poggio, "Force sensing with nanowire cantilevers", Nano-technology 30, 332001 (2019).

[2] Y. Tsaturyan, A. Barg, E. S. Polzik, and A. Schliesser, "Ultra-coherent nanomechanical resonators via soft-clamping and dissipation dilution", Nat. Nanotechnol. 12, 776 (2017)

[3] A. Mehlin, F. Xue, D. Liang, H. F. Du, M. J. Stolt et al., "Stabilized Skyrmion phase detection in MnSi Nanowires by Dynamic Cantilever Magnetometry", Nano Lett. 15, 4839 (2015).

[4] J. E. Losby, F. F. Sani, D. T. Grandmont, Z. Diao, M. Belov et al., "Torque-mixing magnetic resonance spectroscopy", Science 350, 798 (2015).

[5] U. Zondiner, A. Rozen, D. Rodan-Legrain, Y. Cao, R. Queiroz et al., "Cascade of phase transitions and Dirac revivals in magic-angle graphene", Nature 582, 203 (2020).

[6] J. G. Roch, D. Miserev, G. Froehlicher, N. Leisgang, L. Sponfeldner et al., "First-order magnetic phase transition of mobile electrons in monolayer MoS2", Phys. Rev. Lett. 124, 187602 (2020).

[7] A. Mehlin, B. Gross, M. Wyss, T. Schefer, G. Tütüncüoglu et al., "Observation of end-vortex nucleation in individual ferromagnetic nanotubes", Phys. Rev. B 97, 134422 (2018).

[8] A. C. Bleszynski-Jayich, W. E. Shanks, B. Peaudecerf, E. Ginossar, F. von Oppen et al., "Persistent currents in normal metal rings", Science 326, 272 (2009).

[9] J. Jang, D. G. Ferguson, V. Vakaryuk, R. Budakian, S. B. Chung et al., "Phase-locked cantilever magnetometry", Science 331, 186 (2011).

Effects of screened regions on the contact resistance to monolayer semiconductors

Project P2201: Strongly correlated electronic phases in twisted and stretched bilayer semiconductor nanostructures
Project Leaders: A. Baumgartner and P. Maletinsky
Collaborators: J.N. Sunil (SNI PhD Student), C. Schönenberger

Atomically thin, optically active semiconducting transition metal dichalcogenides (TMDCs), like MoS_2, can be used as ultimately thin transistors [1], and can host novel phases due to strong electron-electron interactions [2,3], especially predicted for artificially fabricated twisted bi-layer devices, which we aim to investigate in this project. However, experimental progress is frequently hindered by technical challenges, such as highly resistive contacts. In previous work, this issue was approached using intrinsically very clean interfaces [4], or semi-metal contacts [5] to lower the Schottky barrier between the metal contact and the semiconductor.

At this early stage of our project, we report our first combined optical and electrical transport experiments, based on which we identify another element that can result in large contact resistances, namely a region of the material that is screened by the electrical contacts and thus remains at lower carrier concentrations with a larger resistance than the bulk of the monolayer material.

Figure 1a shows a schematic of our typical devices: an MoS_2 monolayer flake is sandwiched between two insulating hexagonal Boron Nitride (hBN) flakes, and electrically connected to two surface contacts made of a 5nm layer of semi-metallic Bismuth, protected by 30nm gold. The actual contact areas are labeled “region I” in Fig. 1a. For fabrication reasons, these surface contacts overlap the top hBN layer by up to 100nm, which results in a different electron density in “region II” near the contact circumference, compared to “region III” far away from the contacts, as indicated by capacitor symbols. Only in “region III” one obtains a large lever arm, i.e. a strong effect of the graphite backgate.

This picture is very well supported by our optical and transport experiments performed on the same device and in the same cooldown, at temperatures of ~1.8K and in magnetic fields up to 9T (not discussed here). Figure 1b shows the micro-photoluminescence (µPL) intensity plotted as a function of the wavelength λ and the backgate voltage V_{BG}, with each spectrum normalized to the maximum value for each gate voltage. These spectra were recorded at a single spot roughly in the center of region III, with a spot diameter of ~200nm, i.e. quite locally on the several micrometer sized device (see Fig. 1a).

These measurements show the well-known PL emission from charge neutral excitons (X^0) for gate voltages $V_{BG}<0$, which then gets diminished between $V_{BG}=0$ and $V_{BG}=1V$. In the same interval the emission from negatively charged excitons (X^-) increases. This effect can be better observed in Fig. 2a, where the PL intensity is plotted as a function of V_{BG} for two fixed emission wavelengths (shown as dashed lines in Fig. 1b) that correspond to the two exciton emission center wavelengths (we do not discuss the energy shift with V_{BG} here). This transition from one emission type to the other starts at $V_{BG}\approx0$, which corresponds to $n\approx0$ [6] in the probed region III.

We now compare these optical experiments in region III to the differential conductance G measured between the two contacts and plotted in blue in Fig. 2a on the right axis. G is suppressed up to the much higher voltage $V_{BG}\approx1.25V$, well beyond the exciton transition point, and is then dominated by strongly gate-dependent oscillations up to $V_{BG}\approx2.0V$. Only for even larger gate voltages we find a smooth curve as expected for a homogeneous two-dimensional electron gas that saturates at a value determined by some contact resistance.

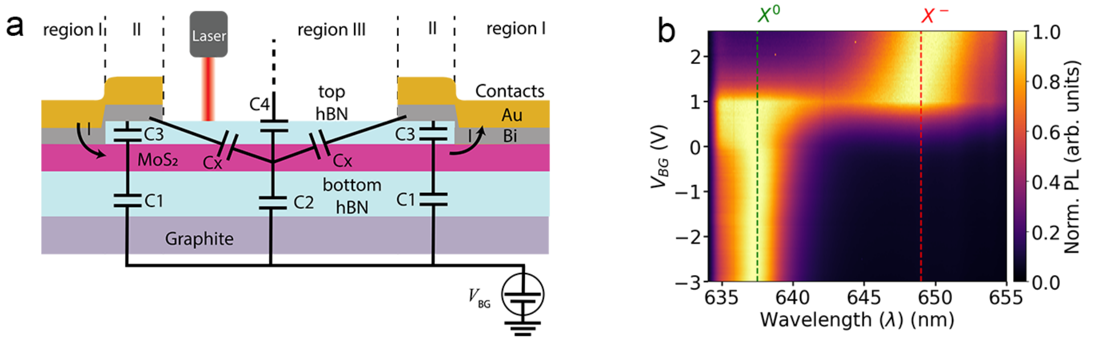

Fig 1 a) Schematic of a typical device with the discussed regions I, II and III. The MoS2 monolayer is shown in purple. While the µPL experiments necessarily probe a spot in region III, the current of a transport experiment necessarily passes through all regions sequentially. b) µPL intensity normalized to the maximum at each gate voltage, plotted as a function of the backgate voltage V_{BG} and the detection wavelength lambda. The labels X0 and X- label the charge neutral and the negatively charged exciton emission lines, respectively. The laser wavelength was 633nm and all data were recorded at a temperature of ~1.8K.

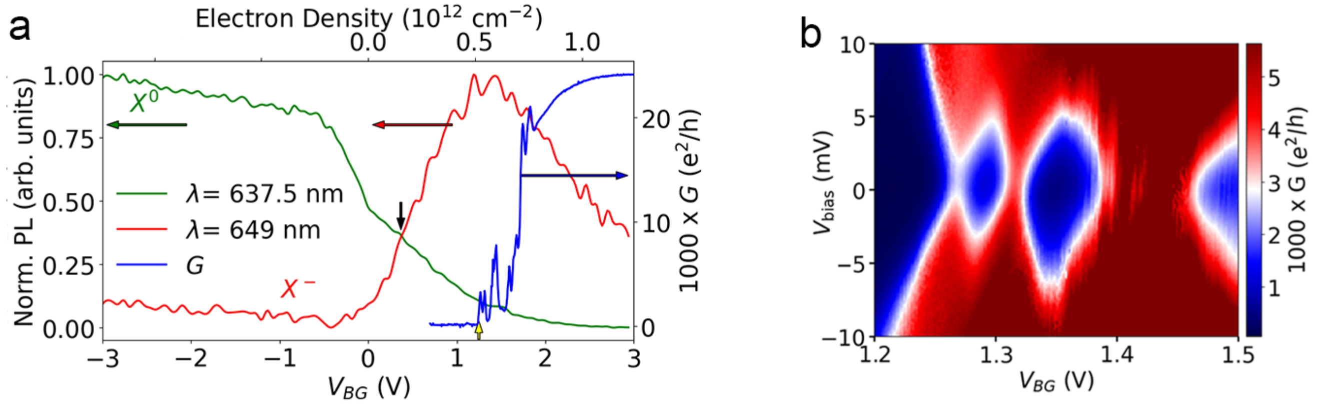

Fig 2 a) Left axis: µPL intensity of the charge neutral exciton (X0, green) at the wavelength lambda=637.5 nm and of the charged exciton (X-, red) at lambda=649.0nm, plotted vs the backgate voltage VBG, and normalized to the maximum value of each curve. The wavelengths are indicated in Fig. 1b for convenience. Right axis: differential conductance G as a function of VBG at zero bias voltage. b) G plotted as a function of the bias voltage Vbias and a small interval of VBG to investigate the conductance oscillations in Fig. a). All data were taken at a temperature of ~1.8K.

The discrepancy between the onsets of the conductance G and the PL emission from charged excitons in region III strongly suggests that the conductance oscillations at intermediate gate voltages stem from region II, which dominates the transport through the whole device. To investigate these oscillations in more detail, we plot G as a function of V_{BG} and the applied bias voltage V_{bias} between the two contacts in Fig. 2b. We attribute the regularly shaped, full suppression of the conductance at $V_{BG}<1.25V$ to a depletion of the electron density in a narrow region along the complete contact edge. This region must be close to the metal contact since the bias voltage also affects this conductance onset. In contrast, we identify the rather un-periodic conductance features at $V_{BG}>1.25V$ as overlapping Coulomb blockade diamonds (“Coulomb shards”), with addition energies on the scale of roughly 5meV, which can add up to fully blocked or quite conducting gate voltage intervals. Such Coulomb blockade features might occur due disorder in region II, which at the locally low electron densities (screened by contacts) dominates the transport properties of the system for all gate voltages.

While the effect of a badly gated contact region can result in inhomogeneous electrical doping in graphene, with various physical effects [7], in few-layer semiconductors it results in an unwanted, large contact resistance, but also in surprising Andreev bound state spectra if the contact material is superconducting [8]. For this project, we now aim to further improve the contact resistance in monolayer and bilayer MoS_2 electronic devices by minimizing the overlap of the contact material with the active channel material, which should then allow us to investigate novel exotic electronic phases in such systems using optical and transport techniques at the same time

References

[1] B. Radisavljevic and A. Kis, “Mobility engineering and a metal–insulator transition in monolayer MoS2”, Nature Materials 12, 815 (2013)

[2] J. Roch et al., “Spin-polarized electrons in monolayer MoS2”, Nature Nanotechnology 14, 432 (2019)

[3] N. Leisgang et al., “Exchange Energy of the Ferromagnetic Electronic Ground State in a Monolayer Semiconductor”, Phys. Rev. Lett. 133, 026501 (2024)

[4] M. Ramezani et al., “Superconducting Contacts to a Monolayer Semiconductor”, Nano Lett. 21, 5614 (2021)

[5] P.-C. Shen et al., “Ultralow contact resistance between semimetal and monolayer semiconductors”, Nature 593, 211 (2021)

[6] J. Klein et al., “Controlling exciton many-body states by the electric-field effect in monolayer MoS2”, Phys. Rev. Research 3, L022009 (2021) Phys.

[7] R. Du et al., “Tuning anti-Klein to Klein tunneling in bilayer graphene”, Rev. Lett. 121, 127706 (2018)

[8] I. Correa Sampaio et al., in preparation (2025)

Understanding the promoting role of sulfur in cobalt phosphide nanocatalysts

Project P2203: Towards Earth-Abundant Nanocatalysts for Hydrogenation Reactions: Understanding the Promoting Role of Sulfur in Cobalt Phosphide Nanocatalysts
Project Leaders: M. F. Delley and M. Nachtegaal
Collaborator: C. Yuan (SNI PhD Student)

Introduction

Hydrogenation reactions are widely used for the production of chemicals in the chemical industry. For the development of sustainable processes highly efficient and highly selective catalysts are needed that are made of earth-abundant elements. In particular, transition metal phosphide nanomaterials have recently shown great promise as catalysts for chemical transformations in energy-related applications, such as water splitting.[1] These materials have also shown high catalytic activity for hydrodesulfurization (HDS), in which heteroatoms are removed from organic fuels by reaction with H_2, and more recently also for the hydrogenation of C=C and C=O bonds in organic substrates.[2] Empirical studies have shown that the catalysis of water splitting by transition metal phosphides can be enhanced when a hetero-element, especially sulfur, is incorporated in the catalytic material (e.g. by doping).[3] Interestingly, a similar effect has been observed in HDS applications of these materials. During HDS sulfur is incorporated at the surface of transition metal phosphides and it is this in-situ formed phosphosulfide that is thought to be catalytically active.[4] However, due to the complexity of the sulfur-doped transition metal phosphide catalysts, it is challenging to establish clear structure-reactivity relationships for the sulfur-effect on the catalysis of these materials.

Goal of this research

We aim to develop a method for controlled sulfur doping of transition metal phosphide nanoparticles and understand the sulfur doping mechanism as well as Sulfur catalytic effect with operando X-ray-based spectroscopic analysis. We aim at constructing structure-activity/selectivity relationships and provide clear roadmap for the rational design of next generation catalysts.

Result and Discussion

We adapted a previously reported method for the synthesis of cobalt phosphide nanoparticles.[5] Here cobalt chloride as Co-precursor, 10 equivalents of triphenyl phosphite as P-precursor, and 10 equivalents of hexadecylamine (HDA) as ligand were dissolved and mixed in hexadecane. 4 equivalents of 1-octadecene were added as reductant. Hexadecane was chosen as solvent in order to avoid a possible oligomerization of the more typically used 1-octadecene solvent at 280 degree celsius.[6] The thereby prepared particles were characterized by a range of physicochemical methods. Transmission Electron Microscopy (TEM) showed the particles had quasi-spherical shapes with an average size of 4 ± 1 nm, while Energy Dispersive X-ray Spectroscopy (EDX) showed the bulk Co:P ratio is 1:1.5. The elemental mapping (figure 1) showed the Co and P signal matched each other. X-ray Photoelectron spectroscopy (XPS) showed the surface of particles contained more P than Co. Infrared spectroscopy (IR) and Nuclear Magnetic Resonance (NMR) showed the presence of the ligand in the particle, which was consistent with the XPS result.

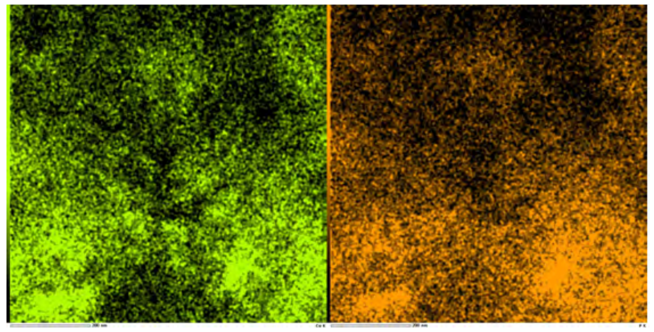

Fig. 1: Elemental mapping of CoP nanoparticles showing Co(green) and P(orange).

After successful synthesis of cobalt phosphide nanoparticles, we tried to modify the surface of the CoP with Sulfur. In short, we mixed the Sulfur-modification reagent and the particles in *d*-benzene and monitored the reaction at 80 °C by NMR spectroscopy. After the reaction, the particles were separated, washed and dried. The NMR spectrum and the XPS result (figure 2) both showed the successful S doping into the CoP particles, and the surface P/Co ratio dropped. The EDX result also showed a P content decrease from 1.85:1 to 1.5:1 after the modification. The surface S to Co ratio is around 0.1 according to XPS, but the oxidation of the phosphorous before the measurement may have changed the quantification ratio. Thus, we need to find a method to prevent exposure to air prior to the measurement. The NMR, IR and HRMS results all showed a loss of ligand during the S-modification.

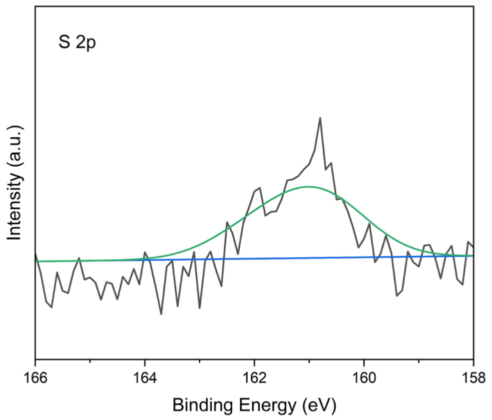

Fig. 2: The XPS result of the CoP after modification.

Moreover, we noticed that heating as synthesized CoP to 80 °C without S modification reagent can cause the loss of ligand and surface P species which was shown by the NMR and HRMS results (as shown in figure 3, we found the ligand peak in the washing mixture). With the addition of the S-modification reagent, it seemed there was less surface P loss, which was verified by EDX measurement. The P/Co ratio decrease from 1.85:1 to 1.25:1 after the heat treatment. No obvious size change of the as-synthesized nanoparticles, heat-treated particles and S-modified particles can be observed using TEM.

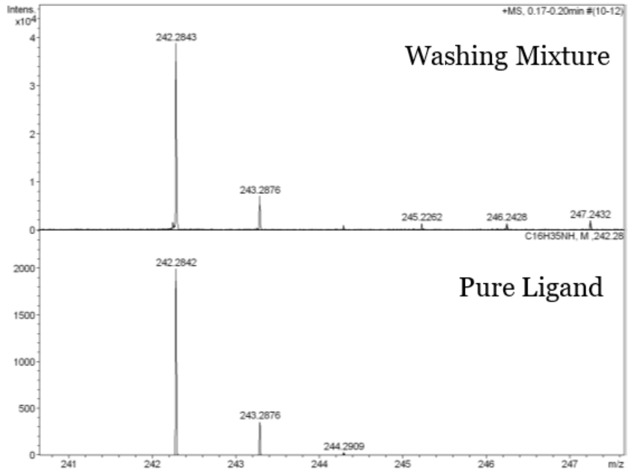

Fig. 3: The HRMS result of the washing mixture of the CoP after heat treatment.

We used hydrogenation of cinnamaldehyde as a probe reaction to investigate the role of Sulfur. The comparison was made between the CoP after S-modification and CoP after heating to 80 °C. The result showed that within the first hour, the S-modified CoP showed 100% selectivity to the thermodynamic unfavorable product cinnamyl alcohol, while the heat treated CoP showed 100% selectivity to thermodynamic favorable product, hydrocinnamaldehyde. This could be due to a changed electronic structure of Co sites through the S-modification of the surface of the nanoparticles, which may result in a favored adsorption of C=O bond to the surface over the C=C bond. [7] We are currently testing whether these results are reproducible.

Conclusion and Outlook

This year, we successfully developed a new method to modify the surface of CoP nanoparticles with Sulfur and used different characterization methods to investigate the chemistry of the Sulfur-doped material. We first plan to use ex-situ K-alpha X-ray Emission Spectroscopy (XES) to investigate the electronic structure of the modified S. We also propose to measure Operando Co K-beta XES to test whether the S-modification enhances C=O bond adsorption.

References

[1] T. Shi, B. Zhang, "Recent advances in transition metal phosphide nanomaterials: synthesis and applications in hydrogen evolution reaction", Chem. Soc. Rev., 45, 1529-1541 (2016)

[2] S. Oyama, T. Gott, H. Zhao, Y. Lee, "Transition metal phosphide hydroprocessing catalysts: A review", Catal. Today, 143, 94–107, (2009)

[3] J. Kibsgaard, T. Jaramillo, "Molybdenum Phosphosulfide: An Active, Acid-Stable, Earth-Abudant Catalyst for the Hydrogen Evolution Reaction", Angew. Chem. Int. Ed. 53, 14433-14437, (2014)

[4] X. Duan, Y. Teng, A. Wang, V. Kogan, X. Li, Y. Wang, "Role of sulfur in hydrotreating catalysis over nickel phosphide" J. Catal. 261, 232– 240, (2009)

[5] J. Liu, M. Meyns, T. Zhang, J. Arbiol, A. Cabot, A. Shavel, "Triphenyl Phosphite as the Phosphorus Source for the Scalable and Cost-Effective Production of Transition Metal Phosphides", Chem. Mater. 30, 1799-1807, (2018)

[6] E. Dhaene, J. Billet, E. Bennett, I. Van Driessche, J. De Roo, "The Trouble with ODE: Polymerization during Nanocrystal Synthesis", Nano Lett. 19, 7411-7417, (2019)

[7] W. Chen, Y. Che, J. Xia, L. Zheng, H. Lv, J. Zhang, H. Liang, X. Meng, D. Ma, W. Song, X. Wu, C. Cao, "Metal-Sulfur Interfaces as the Primary Active Sites for Catalytic Hydrogenations", J. Am. Chem. Soc. 146, 11542-11552, (2024)

Rubisco phase separation

Project P2204: NanoPhase
Project Leaders: B. Engel and M. Hondele
Collaborator: P. Van der Stappen (SNI PhD Student)

Small, dynamic, and liquid-like

Biomolecular condensation and liquid-liquid phase separation (LLPS) are now recognized as key processes driving the formation of membraneless organelles (MLOs) and organizing cellular architecture. These dynamic, membrane-free compartments enable essential biochemical functions like RNA processing and carbon fixation. LLPS is driven by weak, multivalent interactions, resulting in organelles that are highly dynamic, adaptable, and reversible. This versatility gives rise to a wide range of sizes, compositions, material properties, regulatory mechanisms, and functional roles [1].
Studies of biomolecular condensates, both reconstituted *in vitro* (Fig. 1) and observed in cells (Fig. 4), often use light microscopy methods like fluorescence recovery after photobleaching (FRAP) and passive microrheology to explore their microscale behavior. Our research aims to delve into the mechanisms of phase separation across scales, from cellular dynamics to molecular nanostructures.

The pyrenoid – a membraneless organelle fixes CO_2 in photosynthetic marine algae

Among the various biomolecular condensates, the pyrenoid [2] plays a critical role in Earth's carbon cycle. Located in algal chloroplasts, it houses large quantities of Rubisco (Ribulose-1,5-bisphosphate carboxylase/oxygenase), the enzyme responsible for photosynthetic CO_2 assimilation.
As a cornerstone of marine ecosystems, algae contribute significantly to carbon fixation, oxygen production, and the foundation and stability of aquatic food webs. Understanding the molecular basis of carbon fixation in algae – centered on the pyrenoid – can offer insights into natural carbon assimilation and inform strategies to enhance CO_2 fixation and biomass generation in natural and synthetic systems.

The model alga Chlamydomonas

Algae exhibit diverse pyrenoid morphologies (Fig. 1), yet only three essential Rubisco-condensing proteins, known as linkers, have been identified across species. These linkers are key drivers of Rubisco phase separation. The pyrenoid in *Chlamydomonas*, a unicellular green alga, is the most well-characterized system for detailed biophysical studies. This oraganism's genetic accessibility, ease of cultivation, and utility in studying photosynthesis, cellular motility, and metabolic pathways make it an ideal model for fundamental and applied research.

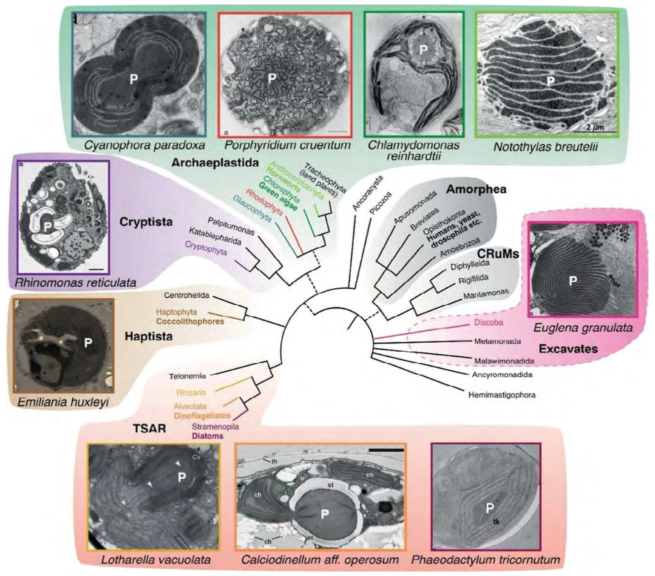

Fig. 1: Pyrenoid-containing algae are polyphyletic and found across the eukaryotic tree of life. Adapted from [2].

Intrinsically disordered proteins are key

In Chlamydomonas, it is known that an intrinsically disordered protein called EPYC1 interacts with Rubisco and is essential for the underlying phase separation that enables formation of the pyrenoid [3]. Figure 2 shows a schematic model of EPYC1 interacting with Rubisco and the resulting phase separation of these two components into droplets.
EPYC1 is a 30 kDa protein with intrinsically disordered regions (IDRs), high positive charge, and 5 repeating sequences. Each of these five repeats contains a Rubisco binding motif. This allows for weak multivalent interactions bridging adjacent Rubisco proteins, which enables condensate formation. These biochemical properties of IDRs are crucial for LLPS and are considered essential traits for the formation and function of biomolecular condensates in general, extending beyond pyrenoids to other MLOs.
The Rubisco binding motifs are called "stickers", and the amino acids between stickers are called "spacers". EPYC1 has 5 stickers and 5 spacers.

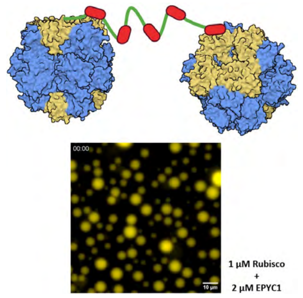

Fig. 2: Top showing schematic model of EPYC1 "crosslinking" Rubisco. Bottom showing fluorescent microscope image of the in vitro droplets.

However, such Rubisco linker proteins are not conserved between different algal clades. No homology sequences are known, but functional homologs exist that share common properties such as IDRs, weak multivalency, and a sticker-spacer model. Why evolution came up with a set number and length of stickers and spacers is a big mystery that we aim to explore in our project. We are keen to apply our multiscale techniques as well as an engineering approach to understand both the structural and biochemical mechanisms governing Rubisco phase separation in the Chlamydomonas pyrenoid.

Cryo-electron tomography and molecular ultrastructure of the Chlamydomonas pyrenoid

Rubisco is the most abundant protein in the world, and its copy number inside a single algal pyrenoid is high [4]. Additionally, the 550 kDa protein is big enough to be resolved by high-resolution cryo-electron tomography (cryo-ET, Fig. 3 & 4). By combining cryo-ET with different biophysical methods to study biomolecular condensates – such as FRAP and light microscopy – we aim to bridge our understanding of LLPS across scales.

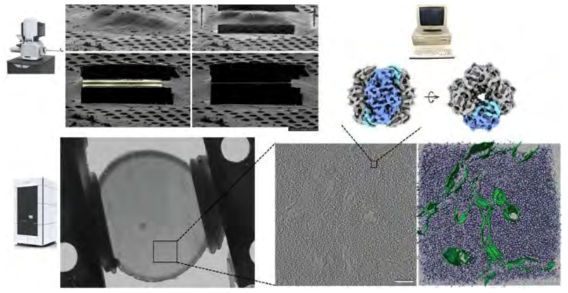

Fig. 3: Cryo-ET workflow: starting with thinning a vitreous cell (plunge frozen in liquid ethane) using a Focused Ion Beam (FIB). The ~200 nm thin "lamella" is imaged in a Transmission Electron Microscope (TEM), and the resulting 3D volume (tomogram) is analyzed by segmentation and/or subtomogram averaging. This can yield high-resolution native protein structures.

We developed a modular system based on golden gate cloning to create and test several sticker and spacer variants of EPYC1 on the LLPS of Rubisco both *in vitro* and *in vivo*. By combining micrometer-scale measurements of condensate dynamics with nanometer-scale analysis of Rubisco organization, we aim to bridge the gap between the liquid-like fluid properties of the condensate and the ultrastructural arrangement of its components. This would be a first in the field of phase separation, and would also provide new insights into the globally-important pyrenoid compartment.
The highly sophisticated cryo-ET workflow allows us to study ultrastructural organization of phase separated Rubisco in its native state both inside the cells and inside reconstituted condensates. One example of such analysis is our result showing short range distribution patterns of Rubisco inside the pyrenoid. This spatial distribution analysis is based on nearest-neighbor (NN) distances, as shown in Figure 4. The short range distance distribution pattern is typical for a liquid-like system.
In the near future, we are expanding this analysis to the engineered sticker and spacer variants of EPYC1. This will allow us the link between tunable "material" properties, phase separation behavior of Rubisco, and ultrastructural organization of various linker type Rubisco condensates.

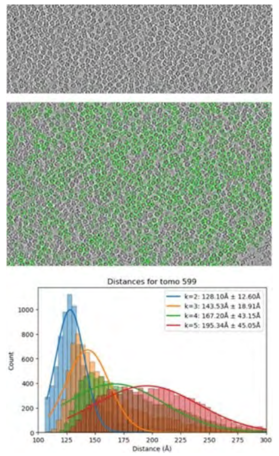

Fig. 4: Rubisco tomography. Identified particles circled in green. NN distances showing short range distributions.

References

[1] Shin Y, Brangwynne CP. "Liquid phase condensation in cell physiology and disease." Science (2017)

[2] Barrett, James, Philipp Girr, and Luke CM Mackinder. "Pyrenoids: CO2-fixing phase separated liquid organelles." Biochimica Et Biophysica Acta (BBA)-Molecular Cell Research (2021)

[3] Mackinder, Luke CM, et al. "A repeat protein links Rubisco to form the eukaryotic carbon- concentrating organelle." Proceedings of the National Academy of Sciences (2016)

[4] He, Shan, et al. "The structural basis of Rubisco phase separation in the pyrenoid." Nature plants (2022)

High aspect ratio arrays of silicon nanostructures by MacEtch in vapor phase

Project P2205: MAGNET. MacEtch based nAnofabrication of hiGh aspect ratio silicon Nanowires with magnEtic Tips
Project Leaders: L. Romano, M. Poggio and M. Stampanoni
Collaborator: B. Benz (SNI PhD student)

Introduction

Metal assisted chemical etching (MacEtch) [1,2] is pushing nanofabrication to new records. It is a nanofabrication method with great promise, and results in small feature sizes and high aspect ratios. Possible applications include solar cells, batteries, X-ray optics, and nanostructures for bio-compatible surfaces [1].

MacEtch consists of a local electrochemical reaction in the presence of an oxidant and etchant, causing the silicon substrate to be removed at the interface with the catalyst. We realized this process using oxygen and HF in vapor phase. Oxygen is catalytically reduced on platinum, thereby extracting electrons from silicon at the interface with Pt and making Si susceptible to removal in HF. This causes the catalyst to sink into the substrate, leaving an etched path. Thanks to this localized effect and anisotropic removal, deep etching with straight sidewalls and precision at nano-scale is possible in MacEtch.

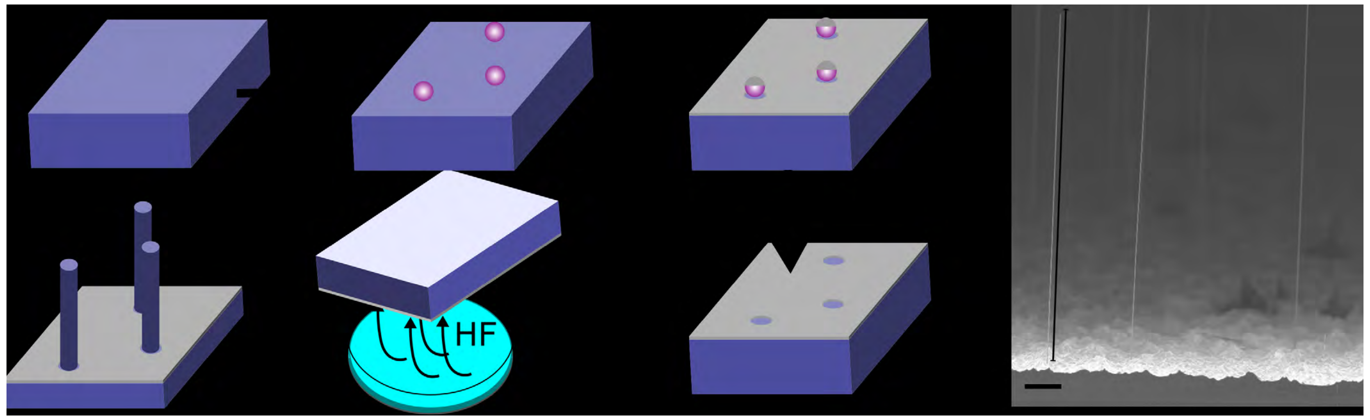

Fig. 1: Schematic of the microsphere lithography method and MacEtch in vapor. a) silicon substrate on which b) nanospheres are spread on the surface at a desired density. c) a platinum catalyst is deposited, the spheres block the deposition of the catalyst. d) The spheres were then removed, leaving a catalyst with holes. e) In the MacEtch step the catalyst sinks into the substrate. f) Si wires are formed with same diameter of the spheres at the location where the spheres were located. g) SEM image in cross section of formed Si nanowires (scale bar 10 µm). With a properly chosen density, we can thus create spaced Si nanowires, as seen on the right, with a diameter of 265 nm and height of 100 µm. The Pt catalyst (bright contrast in SEM) is visible at the bottom of the nanowires.

The vapor-based MacEtch utilized in this study has the advantage of being stiction-free. This solves the major issue of liquid MacEtch, i.e. nanostructures suffering of stiction during the drying after the etching because of capillary forces at liquid-solid interface. In vapor MacEtch, the reactants and products are both in the gas phase; therefore, this is not an issue. This enables a much higher aspect ratio to be achieved.

Recently, we showed that a carpet of random Si nanowires with feature sizes of 10 nm and aspect ratios of over 10’000:1 can be achieved [2] with smooth and straight sidewalls. This was achieved using a self-assembled pattern of the catalyst. However, several defects were observed in the etching of high-aspect-ratio patterned structures. Thus far, this has limited the use of MacEtch as a reliable silicon etching method. Controlling the etching quality of patterned structures in MacEtch is a key factor that allows for nano-structuring capabilities that go beyond the more conventional plasma etching. To address this issue, we developed new patterning methods for catalysts using microsphere and electron beam lithography [3]. This new method allows for a much cleaner process that improves the uniformity of the catalytic activity in the Pt pattern, resulting in more consistent Si etching and higher quality. This was applied to realize high aspect ratio nanowire arrays and gratings.

Nanowires as cantilever at nanoscale

In magnetic field microscopy, a nanowire with a magnetic tip can be used to detect magnetic fields [4]. If the magnet enters a field, it experiences a force that bends the wire. Two important parameters are the diameter and length of the wire: a smaller diameter and higher length lead to a higher displacement. Therefore, the smaller the wire and the higher the aspect ratio, the higher the sensitivity of the wire to magnetic fields.

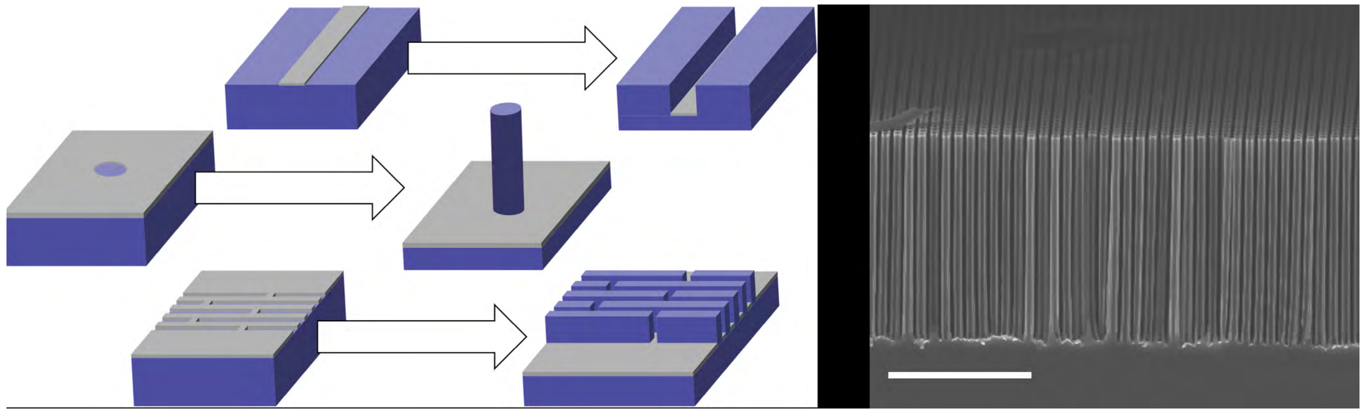

Fig. 2: The catalyst pattern defines the type of structure created during the MacEtch process (right side). Therefore, with an appropriate lithographic process, a multitude of structures can be created. As an example, we show an SEM image in cross section (right side) of a grating created with MacEtch. It has a linewidth of 120 nm, a pitch of 400 nm, and a depth of 13.6 µm. (scale bar 10 µm).

With the novel patterning method developed in this project [3] and a good etching control, MacEtch allows for the creation of Si nanowires with a diameter of 200 nm and aspect ratios greater than 500:1 (figure 1).

Compared with the more conventionally available wires for magnetic field microscopy, those produced by MacEtch are still connected to the substrate, allowing an easy handling and a complete control of their position.

Silicon gratings for X-ray Interferometry

X-ray grating interferometry relies on nanostructures to induce a phase shift in light [5]. For these gratings, we rely on small feature sizes and high aspect ratios, as this improves the sensitivity and resolution and allows the use of higher energy X-rays.

In the conventional method of deep reactive ion etching, we are limited to aspect ratios of 80:1 and feature sizes of 500 nm. MacEtch can improve both these aspects. Indeed, we have already achieved results with aspect ratios greater than 200:1 and feature sizes as small as 100 nm. A grating with similar features is shown in fig 2. It has a linewidth of 125 nm and a depth of 13.6 µm, giving an aspect ratio of >100:1. The sample was etched for 30 min using a pattern realized by electron beam lithography.

One limitation of vapor-MacEtch is the scaling up of the structured areas, which requires a larger amount of reactants. A larger grating area would allow a larger field of view in X-ray imaging applications. Using our new patterning method, we were able to increase the etched area and achieve gratings in the cm^2 range with good central uniformity. The etched structures show no tapering in depth, in contrast to conventional plasma etching. With this smooth and vertical grating sidewall, the performance of the grating-based X-ray interferometry can be improved.

This makes MacEtch a suitable choice for the realization of gratings, which will be investigated later in this project.

Conclusions and outlook

Progress has been made in the fabrication of nanostructures with high aspect ratios using vapor-MacEtch. Nanowires seem to be an ideal case for MacEtch, as they allow even and controlled etching. Thus, we successfully created nanowires in arrays with aspect ratios greater than 500:1. The final requirement for force-sensing applications is the creation of a magnetic tip on top of the nanowires.

In the field of gratings fabrication, we created gratings with smaller feature sizes and higher aspect ratios than those of conventional methods. Currently, the issue is the scaling up to a larger area with a functional etching time and uniformity. The edge effect is still the main issue, as there is a visible etch speed difference across the sample with edge etching at twice the etching speed. Further investigations are required to model etchant consumption as a function of area, catalyst porosity, and etching depth.

References

[1] R.P. Srivastava and D.-Y.Khang, “Structuring of Si into Multiple Scales by Metal-Assisted Chemical Etching“, Adv. Mater. 33, 2005932 (2021)

[2] L. Romano, Matias Kagias, Joan-Vila-Comamala, Konstantins Jefimovs, Li-Ting Tseng et al., “Metal assisted chemical etching of silicon in the gas phase: a nanofabrication platform for X-ray optics“, Nanoscale Horiz. 5, 869 (2020)

[3] L. Romano, B. Benz and M. Stampanoni, Methods of patterning for high aspect ratio catalyst assisted chemical etching, CH patent (2024)

[4] F. R. Braakman and M. Poggio., “Force sensing with magnetic cantilevers“, Nanotechnology 30, 332001 (2019)

[5] T. Thuering and M. Stampanoni, “Performance and optimization of X-ray grating interferometry“, Phil. Trans. R. Soc.A. 372, 20130027 (2014)

Towards NIR-light triggered nanocarriers

Project P2206: Multi-compartment nanofactories for on-site and on-demand drug synthesis and delivery
Project Leaders: O. Tagit and C. G. Palivan
Collaborator: A. Nikoletić (SNI PhD Student)

Introduction

Stimuli-responsive polymeric self-assemblies are promising drug delivery platforms offering on demand release with precise dose and spatiotemporal control over delivery. Thermoresponsive polymers with a lower critical solution temperature (LCST) are particularly promising as building block for such drug delivery systems. Polymers with LCST have hydrated polymer chains below the critical temperature (cloud point), but once heated beyond the LCST they undergo entropy-driven hydrophilic collapse and aggregation [1]. However, temperature can be used as an endogenous stimulus only in exceptional cases, creating a need for an external heating source that would trigger the thermoresponsive polymer [2]. Inorganic nanoparticles exhibit unique optical, electrical, thermal and magnetic properties at the nanoscale, allowing them to interact with various types of external stimuli and convert them to different physical, chemical, and mechanical forms, including heat. Inorganic nanoparticles can generate heat by various transduction mechanisms, one of the most studied being photothermal conversion of plasmonic nanoparticles. Gold nanorods (AuNRs) exhibit localized surface plasmon resonance (LSPR) and generate heat when excited with near-infrared (NIR) light. Furthermore, by modifying the size and aspect ratio of AuNRs, the LSPR peaks can be finely tuned to generate heat at specific NIR wavelengths. NIR light is ideal for biomedical applications due to its biocompatibility, deep tissue penetration, and low phototoxicity [3].
In this project, we aim to develop AuNR-thermoresponsive polymer hybrid nanoassemblies that can be triggered by NIR light for cargo release (Fig. 1). We are synthesizing novel thermoresponsive block copolymers that self-assemble into different nanostructures, to which we covalently attach AuNRs through appropriate end-group functionalization of polymers.

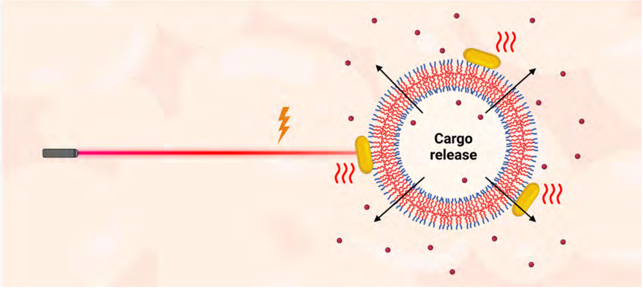

Fig. 1: Schematic illustration of the NIR light triggered release from thermoresponsive assemblies.

Hybrid nanoassemblies comprising different AuNRs and cargo will be co-encapsulated within giant unilamellar vesicles to form compartmentalized nanofactories (Fig. 2). Each nanocompartment can be selectively triggered at corresponding excitation wavelengths to precisely control the duration and sequence of release.

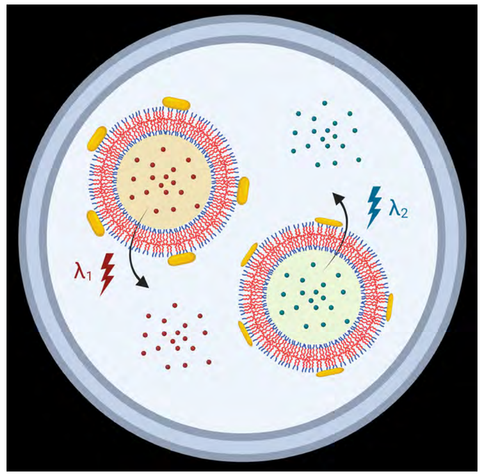

Fig. 2: Schematic illustration of the 'nanofactory'. Compartments with different AuNRs are triggered with light of different wavelengths.

Thermoresponsive block copolymers

We have synthesized libraries of thermoresponsive block copolymers based on hydrophobic polydimethylsiloxane (PDMS) and hydrophilic poly(di- and poly(triethylene glycol acrylate)s (PDEGA and PTEGA). The influence of block lengths on the LCST of resulting block copolymers and architecture of self-assembled structures was systematically investigated. We also explored different self-assembly methods for the fabrication of nanocompartments, prioritizing the formation of uniform nanoparticles, while ensuring high encapsulation efficiency for further experiments. The best control over size and size distribution of nanoassemblies was achieved with nanoprecipitation, where polymers are dissolved in an organic phase miscible with water, and then quickly added to aqueous phase under vigorous stirring, followed by evaporation of organic solvent. The resulting self-assemblies were characterized using dynamic light scattering (DLS) and transmission electron microscopy (TEM). For PDMS-*b*-PDEGA and PDMS-*b*-PTEGA with hydrophilic weight percentage of *f*=68%, we obtained uniform micelles (Fig. 3).

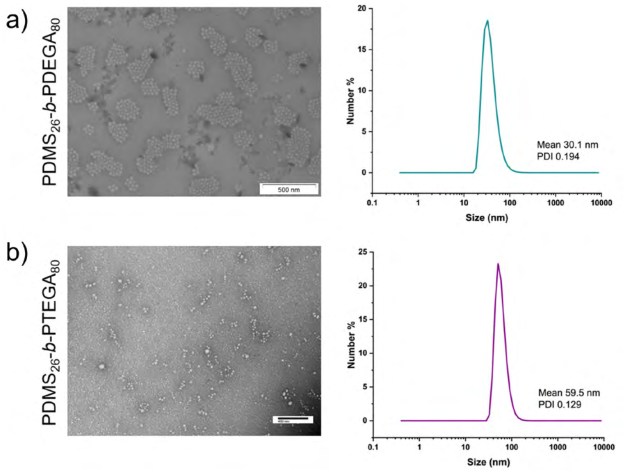

Fig. 3: Characterization of self-assemblies formed by nanoprecipitation of a) PDMS-b-PDEGA and b) PDMS-b-PTEGA using TEM (left) and DLS (right).

The thermoresponsive behaviour of PDMS-*b*-PDEGA and PDMS-*b*-PTEGA was evaluated through dynamic light scattering (DLS) and turbidimetry (cloud point) experiments conducted in aqueous solutions in H_2O, PBS, and in the presence of macromolecular crowders (sucrose and PEG). The cloud point determined using turbidimetry was 46 °C in H2O and 32 °C in PBS (Fig. 4a) for PDMS-*b*-PDEGA (*f*=68%), while it was 53 °C in PBS for PDMS-*b*-PTEGA (*f*=68%) (Fig. 4c). Analogous critical temperatures were obtained from DLS measurements, defined as the temperatures where sudden increase in size occurs due to aggregation and where PDI>0.5 (Fig. 4b and 4d). Block copolymers with longer PDMS blocks displayed lower LCST values due to increased hydrophobicity of copolymer. However, the main effect on LCST of copolymers was the length of hydrophilic PDEGA and PTEGA blocks, with longer block lengths resulting in higher LCST values. Furthermore, the end-group of the hydrophilic block significantly influenced the LCST.

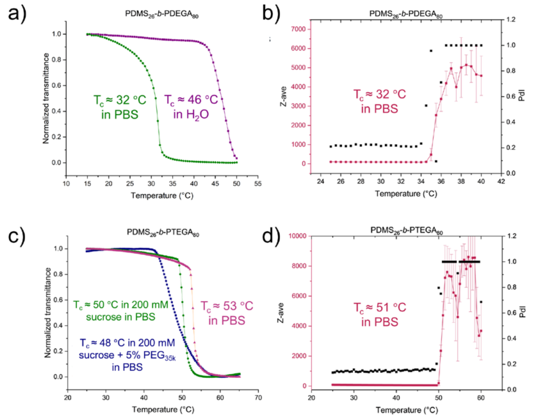

Fig. 4: Thermoresponsivity of PDMS-b-PDEGA and PDMS-b-PTEGA (f=68%) in aqueous solutions.

Moreover, we performed preliminary experiments to investigate triggered drug release. Before the NIR-light triggering, we tested thermoresponsive release from PDMS-*b*-PDEGA (*f*=68%) micelles. For that, we encapsulated anticancer drug Doxorubicin (DOX) during the self-assembly process and quantified concentration of released drug. Upon heating above LCST, the micelles aggregated releasing 41% of the cargo after 24h.

Gold nanorods

We have synthesized AuNRs in two steps using the seed-mediated growth method. Synthesized AuNRs had plasmonic resonance wavelength of ~800 nm, obtained by UV-Vis-NIR spectroscopy, which could be slightly tuned by varying the nanoparticle growth time. Size and aspect ratio of the prepared AuNRs were determined as 53.5 nm x 14.9 nm and 3.6 by SEM (Fig. 5) and TEM. The AuNRs synthesized using this method are stabilized with CTAB and dispersed in water (hydrophilic AuNRs). They can be made hydrophobic by dispersing them in organic solvent with phase transfer through liquid-liquid interface, during which the stabilizing ligands are exchanged. We used alkanethiols to stabilize AuNRs in organic solvents.

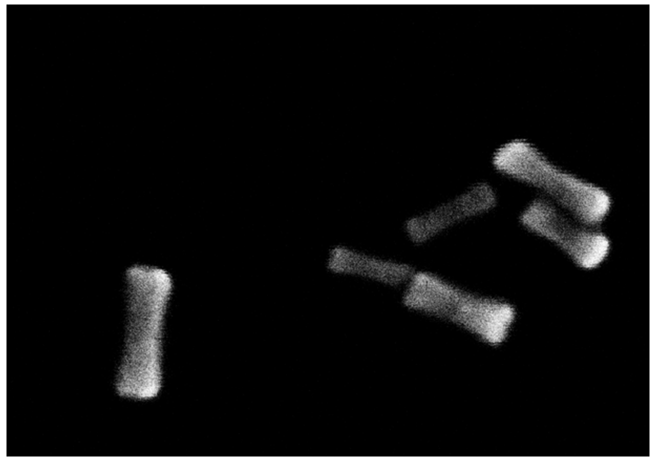

Fig. 5: SEM micrograph of AuNRs synthesized from 2h-aged seeds (aspect ratio 3.6).

Outlook

We are currently working on conjugation strategies to obtain polymer/AuNRs nanohybrids. In the next stage of the project, we will characterize such nanohybrids and use them for NIR-light triggered release studies. We will also synthesize gold nanorods with higher aspect ratios and higher LSPR wavelengths using different methodology. Finally, we will encapsulate polymer nanocompartments decorated with different AuNRs inside GUVs and test their selective release.

References

[1] A. Bordat, T. Boissenot, J. Nicolas, N. Tsapis, Thermoresponsive polymer nanocarriers for biomedical applications, Adv. Drug Deliv. Rev. 138, 167-192 (2019)

[2] M. Liu, H. Du, W. Zhang, G. Zhai, Internal stimuli-responsive nanocarriers for drug delivery: Design strategies and applications, Mater. Sci. Eng. C 71, 1267-1280 (2017)

[3] A. Saneja et al, Recent advances in near-infrared light-responsive nanocarriers for cancer therapy, Drug Discov. Today 23 (5), 1115-1125 (2018)

Scintillating core/shell HfO_2 nanoparticles for X-ray mediated optogenetics

Project P2207: Targeted scintillator nanoparticles for X-ray mediated optogenetics in behaving mice
Project Leaders: A. A. Wanner, J. De Roo and C. Padeste
Collaborator: E. Liari (SNI PhD Student)

In conventional optogenetics, optical tools are exploited in order to manipulate the activity and function of neurons in the brain. This is typically achieved by the activation of light switchable transmembrane proteins, such as channelrhodopsin, halorhodopsin or archaerhodopsin, with the assistance of visible light [1,2]. However, the visible light has a penetration depth limited to a few hundred micrometers and thus, to reach deeper brain structures, the light source has to be invasively implanted into the brain. This can lead to problems such as tissue damage and neuroinflammation. In this project, we are developing HfO_2 scintillating nanoparticles (SNPs) doped with Tb^{3+}, as an alternative non-invasive means of optogenetics. Utilizing their property of absorbing X-ray radiation due to the high atomic number of Hf (Z= 72) and the subsequent conversion to visible light by Tb^{3+}, we expect to achieve a non-invasive X-ray mediated optogenetic manipulation of brain cells [3].

Synthesizing scintillating nanoparticles (SNPs) for X-ray mediated optogenetics

Initially, HfO_2:Tb NPs of around 3 nm diameter were synthesized using a typical solvothermal reaction. After synthesis, the particles were further functionalized with the appropriate carboxylate ligand that makes them colloidally stable in non-polar solvents, so that they can be further studied [4]. Characterization of the particles was conducted by means of ^1H NMR spectroscopy to verify the surface functionalization, Dynamic Light Scattering (DLS) to confirm the hydrodynamic size, Transmission Electron Microscopy (TEM) to measure the diameter of the inorganic core and X-ray Photoelectron Spectroscopy (XPS) to confirm the presence and oxidation state of the elements in the crystal lattice.

The optical properties of the as-synthesized particles were initially measured using photoluminescence. In the excitation spectrum, two peaks are observed with the maximum peak at 235 nm and a shoulder at 275 nm, while in the emission spectrum (after excitation at 235 nm) 4 characteristic peaks are measured which correspond to the 4 transitions of Tb^{3+} (Figure 1A). The maximum emission peak at 545 nm is the peak of interest as it matches with the excitation range of the opsin that we want to utilize in the final application – ChRmine, a red-shifted channelrhodopsin, with a peak response at 520 nm. In addition, the lifetime measurements showed a decay time in the range of ms, which is characteristic for Ln^{3+}. After initial confirmation of the photoluminescence properties of the particles, the radioluminescence was measured using a custom setup with a tungsten X-ray tube, a sample holder, an optical fiber with collecting lenses and a spectrometer (Figue 1B). The SNPs exhibited a weak but yet reproducible signal at 545 nm (Figure 1C). Hence, it was crucial to increase the luminescence outcome of the particles.

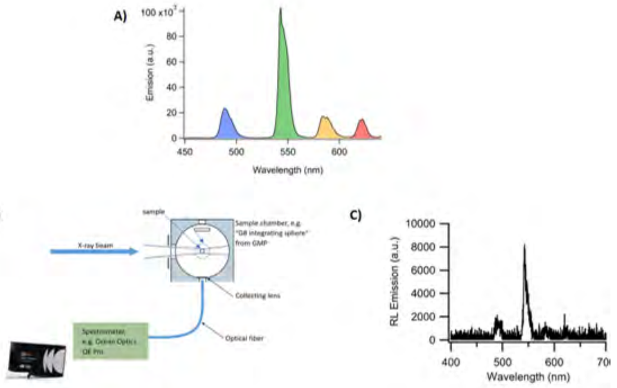

Fig. 1: A) Emission spectrum of HfO_2:Tb SNPs after UV irradiation, where the four peaks of Tb are visible, B) Custom setup for radio luminescence measurements which included an X-ray tube, a sample holder, an optical fiber with collecting lens and a spectrometer, C) Radio luminescence emission of HfO_2:Tb SNPs after X-ray irradiation, with a weak but yet reproducible emission peak at 545 nm.

Increase of the final photoluminescence was performed in two ways. Initially, the HfO_2:Tb core particles were co-doped with additional elements that serve as sensitizers. A sensitizer is an optically active element that can absorb a higher amount of energy, which can be further transferred to the activator for emission, which in this case is Tb. A second attempt to increase the photoluminescence efficiency of the particles was by coating the previously synthesized cores with an additional thin layer of approximately 0.5 nm in thickness of optically inactive HfO_2 shell (Figure 2A). The shell grows epitaxially on the surface of the particles and its main aim is to protect the quenching of Tb^{3+} luminescence from possible surface defects and surface molecules, such as the surface ligands or the solvent [5]. Both attempts led to a significant increase of photoluminescence as indicated by both the emission of the co-doped particles and the improved lifetime measurements, indicating that the non-radiative pathways due to surface phenomena were eliminated (Figure 2B).

Biofunctionalization of HfO_2 scintillating nanoparticles (SNPs)

The as-synthetized NPs are colloidally stable in non-polar solvents, such as toluene and cyclohexane. Since we aim to utilize them in a biomedical related application, they need to be colloidally stable in aqueous environments at physiological conditions (pH= 7.4), instead. The colloidal stability of the particles plays an important role in cellular uptake, cytotoxicity, targeting of a molecule of interest, particle aggregation, etc. Therefore, the carboxylate that is initially bound to the surface of the NPs will be exchanged with an appropriate ligand that will provide colloidal stability of the particles in a physiological environment.

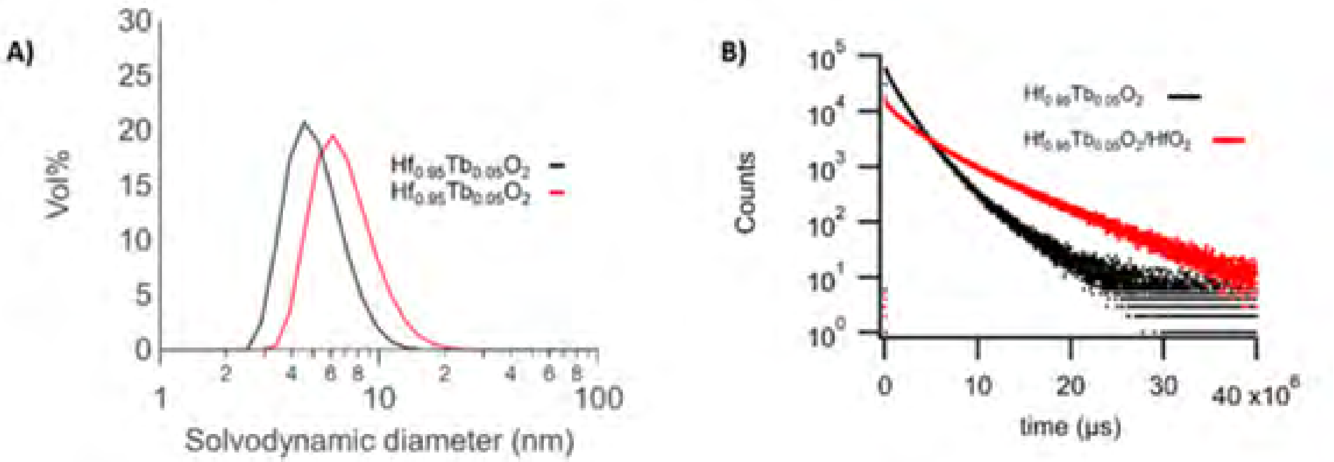

Fig. 2: A) Increase of the hydrodynamic diameter of a core-shell SNPs (red line) compared to the core SNPs (black line) as indicated by DLS measurements and B) Increase of lifetime measurements of the core-shell compared to the core after excitation at 235 nm and by monitoring the peak of interest at 545 nm.

In the past, the De Roo lab has investigated the colloidal stability offered by a plethora of ligands including amongst others carboxylates, phosphonates and catecholates. Some of these ligands do not offer the desired colloidal stability in physiological conditions, while the catecholate ligand that has been proven to bind tightly on the surface of the particles is quenching the final luminescence, which is of importance for the final application [6].

Hence, we are expanding our ligand library by synthesizing bidentate bisphosphonic acids as an alternative ligand, since they provide better colloidal stability compared to their monodentane phosphonic acid analogues and they do not quench the luminescence. Bisphosphonates have been reported in the literature to bind tightly on different NPs used for bioapplications, such as Au, Fe_3O_4 and $NaYF_4$, which is also another host matrix for Ln^{3+} [7]. Synthesized bisphosphonic acids with different ligand chains will be tested on the surface of non-doped HfO_2 particles. Undoped particles are preferred for this study, since they are compatible with ^1H NMR spectroscopy and their surface chemistry is similar to that of the core-shell doped particles. Thus, we will determine whether bisphosphonates should be used to bio-functionalize the surface of the particles and whether changing the organic ligand chain influences the final colloidal stability at physiological conditions.

In future, we will measure the radioluminescence of the SNPs with enhanced photoluminescence to verify whether this improvement is also achieved under X-ray irradiation. The bisphosphonate functionalized particles that are colloidally stable in H_2O will be end-functionalized with an appropriate moiety that can be chemically attached to specific molecules (e.g. SNAP tags) that will provide linkage of the NPs to the targeted protein in the brain. Lastly, the NPs will be tested first in vitro in acute coronal slices of mouse brain, where the generated photocurrents will be monitored by electrophysiological recordings and finally *in vivo* in behaving mice.

References

[1] J. Ditterich, et al., “Microstimulation of visual cortex affects the speed of perceptual decisions” Nature Neuroscience 6, 891–898 (2003).

[2] B. Chen, et al., “Recent advances in cellular optogenetics for photomedicine”, Advanced Drug Delivery Reviews 188, 114457 (2022).

[3] A. Kamkaew, et al., “Scintillating Nanoparticles as Energy Mediators for Enhanced Photodynamic Therapy”, ACS Nano 10, 3918–3935 (2016).

[4] A. Lauria, et al. , “Multifunctional Role of Rare Earth Doping in Optical Materials: Nonaqueous Sol-Gel Synthesis of Stabilized Cubic HfO2 Luminescent Nanoparticles“, ACS Nano 7, 7041-7052 (2013)

[5] C. Seno, et al., “Epitaxial core/shell nanocrystals of (europium-doped) zirconia and hafnia”, J. Am. Chem. Soc. 146, 20550-20555 (2024)

[6] L. Deblock, et al., “Mapping out the Aqueous Surface Chemistry of Metal Oxide Nanocrystals: Carboxylate, Phosphonate, and Catecholate Ligands“, JACS Au 2, 711–722 (2022)

[7] S. Kachbi-Khelfallah, et al., “Towards potential nanoparticle contrast agents: Synthesis of new functionalized PEG bisphosphonates”, Beilstein J. Org. Chem. 12, 1366–1371 (2016)

Breaking the size barrier in cryo-EM structure determination

Project P2301: NANO-PHOTO: NANOstructured protein materials for PHOTOcatalysis
Project Leaders: H.A. Bunzel, T.R. Ward, S. Panke
Collaborator: P. Elbers

Abstract

Cryo-electron microscopy (cryo-EM) enables reliable and straightforward structure determination for proteins with a molecular weight above 100 kDa. To overcome the size barrier in cryo-EM, we computationally design 3D protein nanospheres that display small proteins (<20 kDa) on their exterior. These oligomeric assemblies provide a robust platform for the structural elucidation of the displayed proteins. Preliminary cryo-EM data confirm the feasibility of our approach in overcoming the cryo-EM size barrier for protein structure determination.

Introduction

Cryo-EM has revolutionized structural biology by enabling the visualization of macromolecular complexes up to atomic resolution.[1] However, the technique faces a significant limitation when applied to small proteins, typically below 100 kDa. These proteins lack sufficient contrast and structural features for high-resolution structural elucidation, creating a critical gap in the structural determination of small biomolecules with cryo-EM.

Traditionally, structural elucidation of small proteins has relied on techniques such as X-ray crystallography and nuclear magnetic resonance spectroscopy (NMR, Fig. 1). While these methods have proven effective, they come with inherent limitations. X-ray crystallography requires high-quality crystals, which can be challenging to obtain. NMR, on the other hand, is well-suited for small proteins in solution but is challenging for larger assemblies or weakly interacting complexes. Cryo-EM offers a powerful alternative by capturing proteins in their native state without the need for crystallization. However, cryo-EM has been largely restricted to larger complexes due to the size barrier, necessitating innovative approaches to extend its application to smaller targets.

Computational protein design and structure prediction – recognized with the Nobel Prize in Chemistry in 2024 – is revolutionizing biology. Computational tools such as AlphaFold[2] and ProteinMPNN[3] now enable the reliable prediction of protein structures from amino acid sequences and the design of novel sequences that fold predictably into target structures. Nonetheless, computational structure prediction remains limited in addressing key functional aspects of proteins and enzymes, such as substrate binding, different conformational states, and dynamic interactions critical for activity.

To address these limitations, we integrate cutting-edge computational tools with experimental methodologies to develop a powerful approach for cryo-EM structure determination of small proteins. To that end, small proteins weighing less than 20 kDa are designed into oligomeric megadalton assemblies that can be readily detected by cryo-EM. To achieve this, we design 3D protein nanospheres that rigidly display the target small proteins on their exterior. By integrating experimental validation with cutting-edge computational design, our work bridges the gap between structural biology and advanced protein engineering.

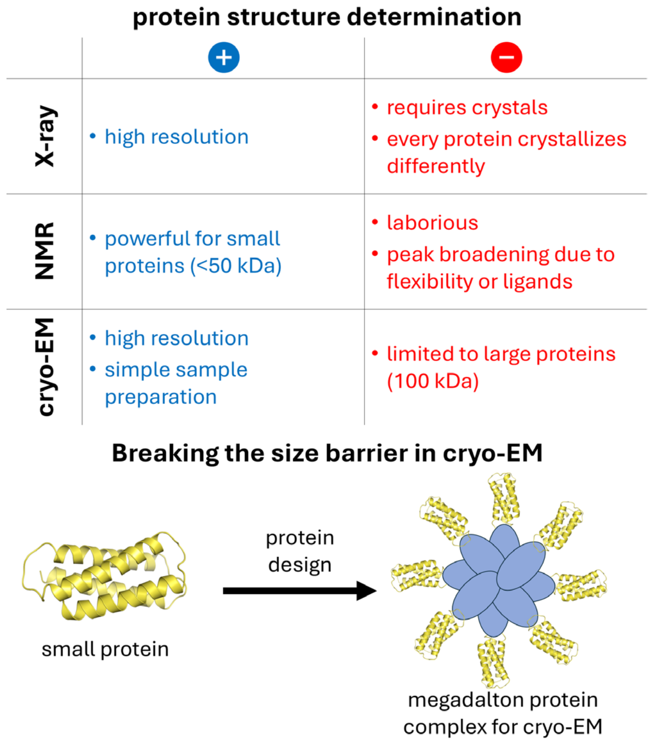

protein structure determination

	+	−
X-ray	high resolution	requires crystals every protein crystallizes differently
NMR	powerful for small proteins (<50 kDa)	laborious peak broadening due to flexibility or ligands
cryo-EM	high resolution simple sample preparation	limited to large proteins (100 kDa)

Breaking the size barrier in cryo-EM

Fig. 1: Protein structure determination. X-ray crystallography, NMR, and cryo-EM are common tools for experimental protein structure determination. X-ray crystallography requires protein crystals, which can be challenging to obtain. NMR is limited to small proteins, while cryo-EM typically works for proteins >100 kDa. Here, nanoscale design of 3D nanospheres is used to overcome cryo-EM's size limitation.

Results

Since the start of the project 10 months ago, significant progress has been made in developing a design pipeline to decorate 3D nanospheres with small proteins. By combining protein design with structure prediction algorithms, we successfully created a proof-of-concept nanosphere. Our protein design pipeline relied on AlphaFold to predict the structure of a protein nanosphere genetically fused to a helical bundle protein and ProteinMPNN to optimize the resulting structure. The scaffold protein nanospheres is a homomeric 60mer. After design, the nanosphere thus displays 60 copies of the small protein on its surface. During design, special attention was given to linking the small protein rigidly to the nanosphere while avoiding steric clashes. The developed design pipeline provides a strong foundation for future display of other proteins and a starting point for experimental validation of our approach.

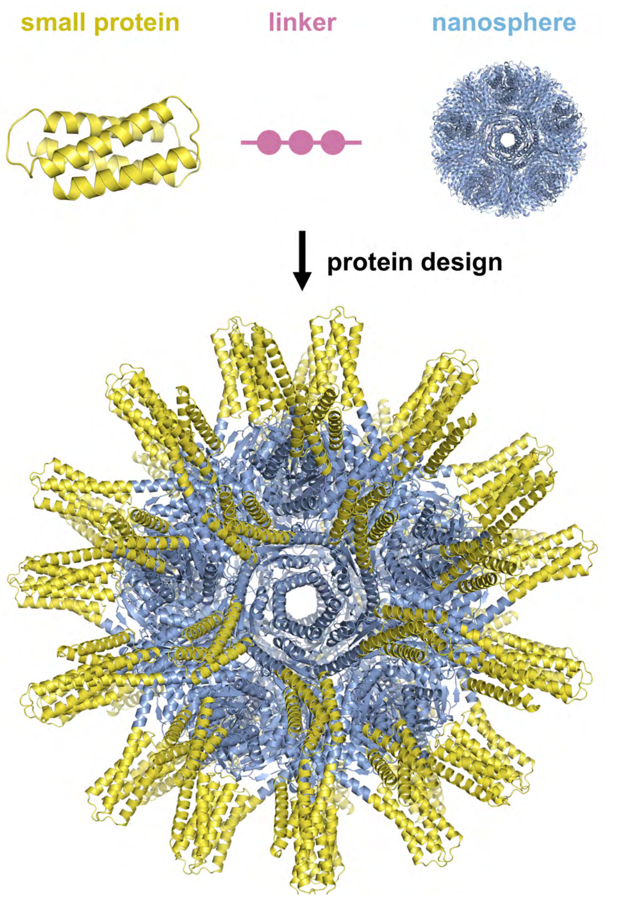

Fig. 2: Computational design of 3D nanospheres. AlphaFold and ProteinMPNN were used to genetically fuse a small protein (yellow) to 3D nanospheres (blue) via a rigid linker (pink). The resulting nanosphere rigidly displays the small protein for cryo-EM structure elucidation.

The designed 3D nanospheres were successfully produced and purified, with size exclusion chromatography confirming the correct size of the megadalton complex (Fig. 3). Individual particles of the correct size and shape were clearly visible in cryo-EM. While high-resolution reconstruction is ongoing, preliminary 2D classes and 3D reconstructions of a small test dataset already reveal distinct features of the displayed small protein (Fig. 3c+d). These results demonstrate the feasibility of using nanospheres for cryo-EM imaging and lay the groundwork for high-resolution structure determination.

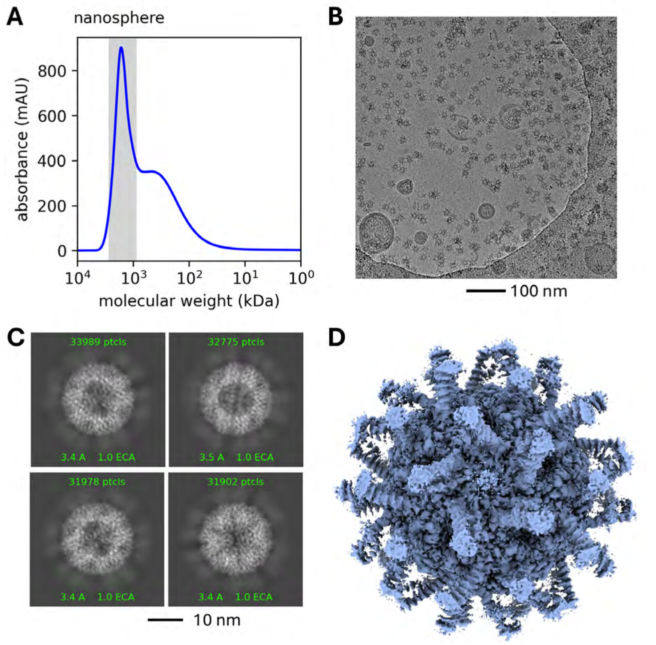

Fig. 3: Experimental analysis of the designed 3D nanospheres. (a) Size-exclusion chromatogram confirming the correct size of the megadalton complex. (b) Cryo-EM micrograph showing the individual particles. (c, d) Preliminary 2D classes and 3D reconstructions reveal distinct features of the displayed small protein.

Outlook

The successful design, production, and preliminary structural analysis of 3D nanospheres demonstrate their potential as a platform for overcoming the size barrier in cryo-EM. Moving forward, high-resolution reconstruction will be a key focus to validate the capability of these nanospheres for precise protein structure determination. Efforts will also be directed toward improving the modularity and versatility of the nanosphere platform, enabling broader applicability to diverse small proteins and functional complexes. By combining advanced computational design tools with experimental techniques, this approach holds significant promise for advancing cryo-EM applications for small proteins and providing new insights into the function of small proteins, ligand binders, and biocatalysts.

References

[1] Saibil, H. R.: "Cryo-EM in molecular and cellular biology",. Molecular Cell 82, 274, (2022).

[2] Abramson J, Adler J, Dunger J, Evans R, Green T, Pritzel A, Ronneberger O, Willmore L, Ballard AJ, Bambrick J, et al.: "Accurate structure prediction of biomolecular interactions with AlphaFold 3", Nature 630, 493 (2024).

[3] Dauparas J, Anishchenko I, Bennett N, Bai H, Ragotte RJ, Milles LF, Wicky BIM, Courbet A, de Haas RJ, Bethel N, et al.: "Robust deep learning–based protein sequence design using ProteinMPNN." Science 378, 49 (2022).

f

Chitosan-based scaffolds – new hope for alveolar bone augmentation?

Project P2302: Elucidating synergistic effects of nano topography and peptide immobilisation on osteogenesis
Project Leaders: A. G. Guex and M. Nash
Collaborator: I. Imhof (SNI PhD Student)

Introduction

In this project, we aim to gain control over the nano-architectural properties of electrospun fibres and elucidate their effect on protein adsorption, peptide tethering, and concomitant cell fate. Our goal is to understand the influence of a complex three-dimensional nano-environment on the osteogenic differentiation of mesenchymal stromal cells. This will ultimately contribute to deciphering the interplay between cell adhesion and lineage commitment. Eventually, these findings will allow us to develop scaffolds for a) in situ bone augmentation or b) in vitro model systems to evaluate new treatment strategies in oral implantology.

Dental implants provide excellent solutions to replace missing teeth. For long-term success, however, fast and permanent osseointegration within the host tissue is paramount, requiring at times in situ bone augmentation by means of biomaterials or bone grafts prior to dental implant placement. In both scenarios (material-based bone augmentation or implant osseointegration) surface topography, mechanical properties, and (bio)chemical composition of the chosen materials act in concert on cell adhesion. Specifically, the importance of micro- to nano-topographical properties on material surfaces to steer osteogenic differentiation has long been appreciated [1]. Topographical cues induce specific protein adsorption schemes that control integrin binding, focal adhesion formation, cytoskeletal development, and further downstream signalling to steer osteogenic differentiation via pathways known as mechanotransduction and intracellular tension. Understanding the first step of this cascade and gaining control over cell adhesion via specific peptide functionalisation routes on clearly defined substrates is thus suggested as a way forward to control differentiation. To date, most studies looking at surface topographies are performed on 2-dimensional solid substrates and disregard the importance of 3-dimensional, porous scaffolds during tissue formation. On 2 to 2.5-dimensional substrates, however, cells attain a state that is very different from their natural environment (Figure 1). Among other techniques, electrospinning has been used for decades to produce fibrous matrices that mimic the extracellular matrix. The method allows high control over material choice, fibre diameter and orientation, and post functionalisation methods [2]. In this PhD project we aim to engineer electrospun scaffolds with controlled architecture to elucidate the interplay between surface topography and protein/peptide adsorption or immobilisation on cell adhesion and osteogenic differentiation of mesenchymal stromal cells.

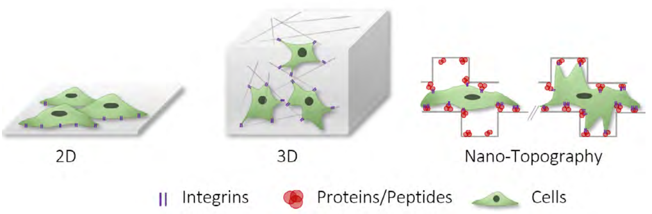

Fig. 1: Schematic representation of cells cultured on different substrates. Seeded on top of materials, cells experience a 2D environment, which is very different to their native environment. In porous scaffolds or hydrogels, a 3D environment can be provided.

Experimental setup and main research findings

During the first phase of the project, the aims have been to a) set up an electrospinner to process polymer solutions into fibrous scaffolds b) establish protocols for osteogenic differentiation and analysis thereof and c) develop scaffold production strategies that will allow for peptide immobilisation.

Initial experiments were carried out with Saos-2 osteoblastic cells as a model cell line. Saos-2 were cultured with differentiation or control medium, respectively. Samples were harvested at D7, D14, and D21. We characterised the calcium content, (indicative for mineralisation and thereby a strong hallmark for osteogenesis) using a calcium assay kit and Alizarin Red staining. We observed that the calcium content was significantly increased over time for Saos-2 cultured in differentiation medium, reaching values of 0.157 µg/µL on D21. This was also confirmed by Alizarin Red staining (Figure 2).

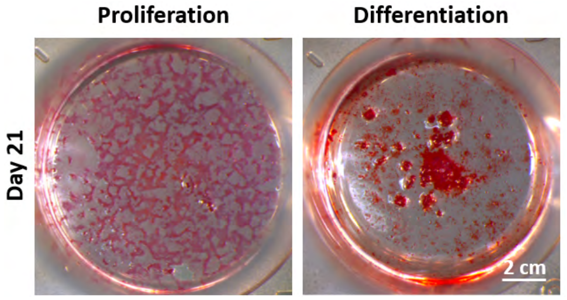

Fig. 2: Alizarin red staining of Saos-2 cells after 21 days in culture. Bright red spots indicate mineralisation. In the control group (proliferation) non-specific red colouration was observed.

Biofabricated cell-polymer constructs offer a promising approach for the regeneration of bone, and, if designed in a custom-tailored approach, allow for the control of cell spreading and subsequent differentiation. Here, we used chitosan (CS), which is known for its antibacterial properties and bears hydroxyl and amino groups for covalent immobilisation of peptides, and poly(epsilon-caprolactone) (PCL). In a first step, solutions at different ratios were produced to a) assess their viscosities and thereby determine spinnability, b) produce 2D films for first-line cell culture evaluation, and c) to explore hydrogels and aerogels as an alternative to electrospinning.

Solutions of different concentrations of chitosan (CS) (2 wt% or 8 wt%), PCL (10 wt%) or a blend thereof were prepared. The materials were dissolved in a mixture of acetic acid and formic acid at a ratio of 30/70. All polymer solutions were prepared at room temperature with overnight stirring. The viscosities of the solutions were assessed via frequency sweep on a Rheometer. An increasing chitosan concentration raised the viscosity by a factor of 10 (2 wt%) or 300 (8 wt%) compared to 10% PCL at a shear strain of 9.17%. The viscosity of the 2 wt% CS/10 wt% PCL blend (2467.8 mPa·s) was within the ideal range reported for electrospinning of chitosan composites, namely between 1000 – 7000mPa·s [3] and will thus be used in future experiments (Figure 3).

2D films were produced by drop-casting the solutions onto glass microscopy slides. Cells cultured on the polymer films presented a rounded morphology (mean roundness = 0.74 ± 0.15; mean circularity = 0.79, ± 0.15) compared to the control group on standard tissue culture plastic (mean roundness = 0.56 ±0.24; mean circularity = 0.71 ± 0.3), and a small average cell size ranging from 327.11 µm^2 (8 wt% CS/10 wt% PCL) to 1937.5 µm^2 (10 wt% PCL) compared to the control group (4302.8 µm^2).

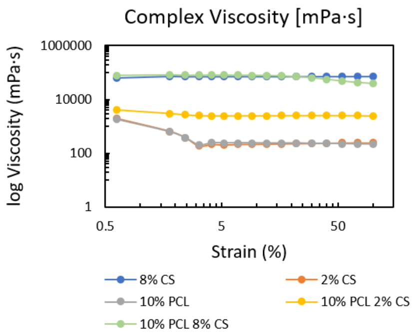

Fig. 3: Viscosities of different polymer solutions based on Amplitude Sweep Measurements.

To transition from 2D to 3D, Hydrogels were prepared by dissolving 2% CS in 2% acetic acid. The pH was adjusted to 5.5 in order to crosslink with either 175 mM or 200 mM Sodium Hydrogen Carbonate (SHC). Aerogels were prepared using the same dissolving strategy without pH adjustment. They were crosslinked with 175mM SHC either before or after lyophilizing for 24h. We observed that depending on the SHC concentration we were able change the degree of crosslinking of the hydrogels and thereby the mechanical properties (Figure 4A). Different to hydrogels, aerogels presented a macroporous structure, potentially allowing for cell migration and tissue formation (Figure 4B).

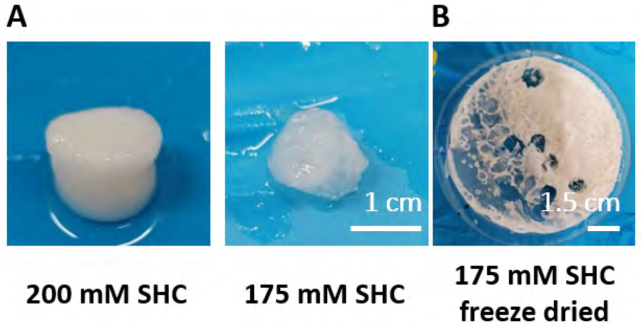

Fig. 4: Photographs of A) hydrogels and B) an aerogel crosslinked at different SHC concentrations.

Conclusions and Outlook

Saos-2 were shown to mature into mineralised osteoblasts under the established culture conditions. In future experiments, we will exploit the regenerative potential of progenitor cells and investigate how osteogenic hallmarks can be triggered by material properties. Based on the first data obtained from cells cultured on chitosan-based scaffolds, it is evident that functionalisation strategies are needed to enhance cell adhesion. While no indications for cytotoxic effects were observed, the round cell morphology is indicative for impaired cell adhesion. Furthermore, our preliminary studies demonstrated that non-toxic crosslinking agents such as SHC can be used to successfully crosslink CS. Further investigations will primarily focus on electrospinning different polymer blend systems and on establishing protocols to tether peptides that present specific adhesion motives to cells.

References

[1] M.J. Dalby, N. Gadegaard, R. Tare, A. Andar, M. O. Riehl et al., “The control of human mesenchymal cell differentiation using nanoscale symmetry and disorder“, Nature Materials 6(12), (2007)

[2] R. Weishaupt, J. Zünd, L. Heuberger, F. Zuber, G. Faccio et al., “Antibacterial, Cytocompatible, Sustainably Sourced: Cellulose Membranes with Bifunctional Peptides for Advanced Wound Dressings“, Advanced Healthcare Materials 9(7) (2020)

[3] L. Van der Schueren, I. Steyaert, B. De Schoenmaker, K. De Clerk, “Polycaprolactone/chitosan blend nanofibres electrospun from an acetic acid/formic acid solvent system“, Carbohydrate Polymers 88 (2012)

Programmable origami for regulated exchange (PORE): nuclear pore complex-inspired DNA nanopores

Project P2304: Selective new-to-nature nanopores enabled by biomolecular condensation
Project Leaders: R.Y.H. Lim and M. Hondele
Collaborator: L. Beckert (SNI PhD Student), K. Baumann, M. Siketanc, and D. Overwijn

Drawing inspiration from nature: The Nuclear Pore Complex

The nuclear pore complex (NPC) is a remarkable molecular assembly, mediating macromolecular transport between the nucleus and cytoplasm with unmatched selectivity [1]. Intrinsically disordered proteins (IDPs) termed phenylalanine-glycine nucleoporins (FG Nups) facilitate this process by engaging in rapid, transient interactions with nuclear transport receptors (karyopherins or Kaps) to enhance NPC transport efficiency [2]. Non-specific cargoes are excluded by the NPC permeability barrier organized by a liquid dynamic nanocluster of FG Nups and Kaps known as the central plug [3].
More generally, RNA and proteins form phase-separated liquid-like biomolecular condensates (BMC) in vitro and membraneless organelles in vivo. Interestingly, BMCs also display enhanced selectivity towards specific molecules (clients) but can exclude non-specific molecules. Like the central plug in NPCs, BMCs also contain localized, slow-moving nanodomains where RNA and proteins experience restricted diffusion. These nanodomains create distinct microenvironments that influence residence times and biochemical interactions [4].
Our objective is to engineer BMC-like selectivity in NPC-like DNA origami nanopores and explore how scaffold-client systems where specific molecules such as RNA or IDPs can function as "scaffolds", generating a selective diffusion barrier for client molecules-of-interest. In this way, we aim to reveal a general principle that governs selective transport control in nanopores.

From concept to structure: Engineering DNA origami nanopores

At the core of our work is the "Octagon," a DNA origami nanopore designed as a modular platform for attaching a diverse range of scaffold molecules, including IDPs, RNA, and double-stranded DNA (dsDNA). DNA origami is a nanotechnology method that uses the programmed self-assembly of a long, single-stranded circular DNA molecule folded into precise shapes with the help of hundreds of short complementary "staple" strands [5,6]. This technique enables the creation of highly customizable nanoscale structures with defined geometries and functional properties.

To replicate the organization of FG Nups within the NPC, the Octagon channel incorporates up to 64 attachment sites, ensuring precise positioning and functionalization of scaffold molecules (Fig. 1).

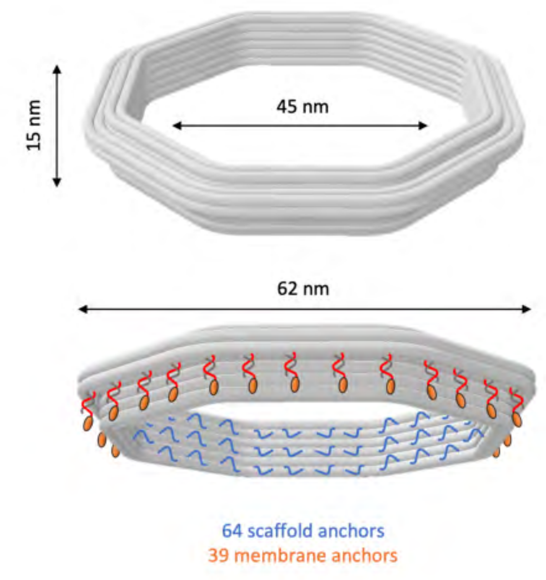

Fig. 1: A schematic representation of the Octagon DNA origami nanopore, featuring 64 scaffold anchors to enable functionalization with various scaffold types and 39 membrane anchors to ensure stable insertion into lipid bilayers, highlighting its modular design and functionality.

Unveiling inner pore dynamics by High-Speed AFM and interaction studies

High-speed atomic force microscopy (HS-AFM) revealed the dynamic fluctuations of RNA-scaffold molecules within individual Octagons in real time [7]. These fluctuations may reflect short-lived structural rearrangements or localized interactions (Fig. 2). Such behaviour aligns with the properties of the NPC, where flexibility and transient binding are key to the speed and bidirectionality of selective transport.
Complementary insights were obtained through surface plasmon resonance (SPR) studies, which quantified the interaction kinetics of RNA scaffolds and FUS (fused in sarcoma). FUS was chosen as a client molecule due to its well-characterized RNA-binding domain and its role in exerting multivalent, transient interactions within biomolecular condensates.

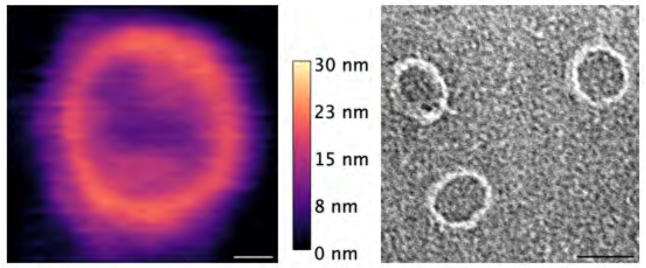

Fig. 2: Left: High-speed AFM image of the functionalized Octagon nanopore decorated with 150 nt long RNA sequences, showing dynamic fluctuations and a physical barrier within the pore. Scale bar: 10 nm. Right: Transmission Electron Microscopy (TEM) image of the empty Octagon nanopore, providing structural confirmation of the pore architecture. Scale bar: 50 nm.

Overcoming challenges and broadening applications

Future experiments will focus on integrating these nanopores into lipid bilayers, as a means to selectively regulate transport into lipid vesicles.
However, creating stable insertions of Octagons into lipid bilayers remains a challenge in the field. Although cholesterol-based anchoring strategies facilitate the initial attachment, they frequently prove ineffective in forming transmembrane channels with reliable stability (8).
To enhance integration, we are investigating the potential of pneumolysin-functionalized nanopores for robust and stable incorporation into membranes (9). Pneumolysin is a pore-forming protein derived from *Streptococcus pneumoniae* that naturally creates transmembrane channels by assembling into ring-like structures, making it an ideal candidate for enhancing nanopore stability.

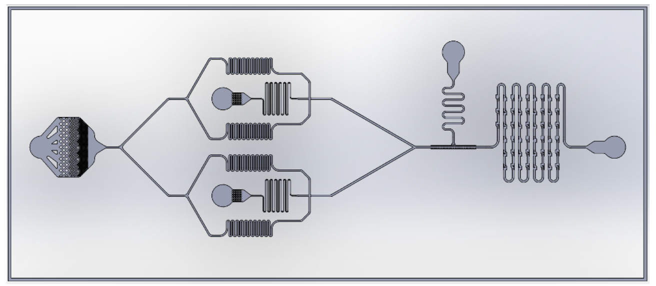

Fig. 3: Schematic representation of the Octagon DNA origami nanopore with 39 membrane anchors for stable insertion into lipid bilayers, illustrating its modular design and functionality.

In parallel, microfluidic approaches are being developed to enable high-throughput assembly and analysis of nanopores in lipid vesicles, enhancing the reproducibility and scalability of transport studies.

Concluding remarks

This project represents a significant step towards replicating the selective transport mechanisms of the NPC. Our programmable DNA origami-based platform exploits the nanoporous confinement of dynamic scaffold-client interactions to regulate selective transport in non-biological environments. This promises to pave the way for transformative applications in diagnostics, molecular sorting, and drug delivery. Continued refinement of scaffold design and bilayer integration will bring us closer to realizing these ambitious goals.

References

[1] B. W. Hoogenboom et al., "Physics of the Nuclear Pore Complex: Theory, Modeling and Experiment", Phys Rep 921, 1-53 (2021)

[2] L. E. Kapinos, et al., "Karyopherin-Centric Control of Nuclear Pores Based on Molecular Occupancy and Kinetic Analysis of Multivalent Binding with FG Nucleoporins", Biophysical Journal 106, 1751-1762 (2014)

[3] T. Kozai, et al., „Dynamic molecular mechanism of the nuclear pore complex permability barrier", bioRxiv (2023)

[4] G. Gao, et al., "Single molecule tracking reveals nanodomains in biomolecular condensates", bioRxiv (2024)

[5] P. W. Rothemund, et al., "Folding DNA to create nanoscale shapes and patterns", Nature 440, 297-302 (2006)

[6] A. Fragasso, et al., "Reconstitution of Ultrawide DNA Origami Pores in Liposomes for Transmembrane Transport of Macromolecules", ACS Nano 15, 12768–12779 (2021)

[7] Q. Feng, et al., "Channel width modulates the permeability of DNA origami based nuclear pore mimics", Sci. Adv. 10, eadq8773 (2024)

[8] E. Georgiou, et al., "DNA Origami - Lipid Membrane Interactions Controlled by Nanoscale Sterics", Small, e2404720 (2024)

[9] Q. Shen, et al., "Functionalized DNA-Origami-Protein Nanopores Generate Large Transmembrane Channels with Programmable Size-Selectivity", ACS 145, 1292-1300 (2023)

Synthesis of a novel carcerand suitable for metal ion encapsulation

Project P2306: Enabling the challenging separation of radionuclides via the entrapment inside molecular containers
Project Leaders: K. Tiefenbacher and P. Steinegger
Collaborator: A. Kharchenko (SNI PhD Student)

Introduction

Nuclear medicine demands efficient and durable methods for separating radionuclides. Traditional 44Ti/44Sc generators, which rely on adsorption-based separation techniques, face challenges such as limited chemical stability, radiolysis, and decreasing separation efficiency over time. To overcome these limitations, a novel molecular encapsulation/destruction method for radionuclide separation has been proposed. This strategy involves the irreversible encapsulation of radionuclides, followed by the breakdown of the molecular container (carcerand) during radionuclide decay, thereby releasing the daughter product (Fig. 1). The potential for encapsulating Cs cations in carcerands was previously demonstrated by Cram D.J.1

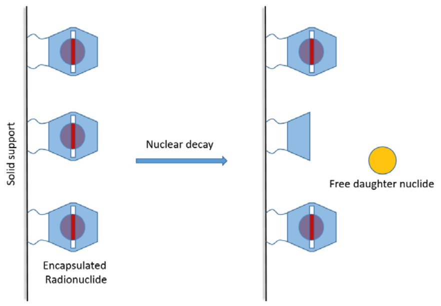

Fig. 1: Proposed molecular encapsulation/destruction method for radionuclide separation.

Given the smaller radii of most radionuclide cations, including Ti, our initial efforts have focused on synthesizing a novel calix[4]arene-based carcerand 1 (depicted in Fig. 2). Calix[4]arene is widely recognized for its ability to bind metal ions2, and a carcerand formed by two calix[4]arene units offers a smaller internal cavity with narrower openings, potentially providing advantages for encapsulating smaller cations. Similar structures have been theoretically calculated.3 However, despite synthesis attempts, they have yet to be isolated.4

Synthesis of carcerand 1

To obtain carcerand 1, several approaches were explored. Base-catalyzed tetramerization with formaldehyde is the standard approach for calixarene synthesis. The same conditions were applied to bisphenol-F 2 in an attempt to directly access carcerand 1. Unfortunately, only insoluble polymer was obtained as a result of this reaction. Similarly, polymeric material was also observed in the reaction of bisphenol-F 2 with formaldehyde catalyzed by TiCl4 under high-dilution conditions.

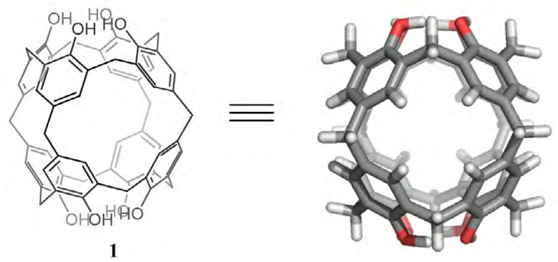

1

Fig. 2 Structure of new carcerad 1 for encapsulation of metal ions.

Another approach to synthesizing carcerand 1 involved "stitching" two calix[4]arenes together. Lewis acid-catalyzed condensation of unsubstituted calix[4]arenes 3 resulted in polymeric material, with no detectable product. Similar results were observed in acid- and base-catalyzed reactions of paramethylenechloridecalix[4]arene 4 with unsubstituted calix[4]arene 3 (Fig. 3; Table 1.).

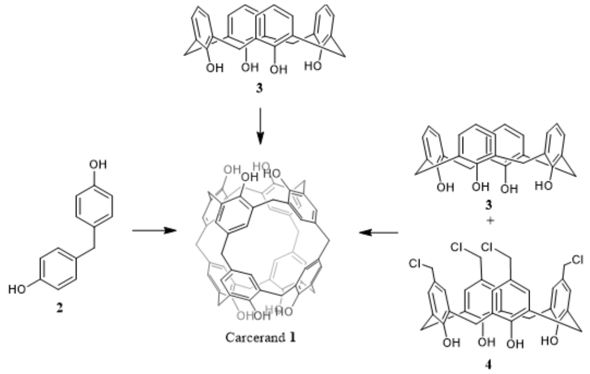

Fig. 3: Initial approaches to carcerand 1 synthesis.

Table 1. Screened conditions for carcerand 1 synthesis.

N	Reaction	Cat., eq	Conditions	Yield %
1	**3->1**	BF_3*OEt_2, 0.2	DCM, Paraform 2.2 eq, r.t. 13 h	0
2	**3->1**	PTSA, 0.2	DCM, Paraform 2.2 eq , r.t. 30 min	0
3	**3->1**	$TiCl_4$, 1	Dioxane, Paraform 2.2 eq reflux 4 h	0
4	**2->1**	NaOH, 0.04	Formaline, Ph_2O 260 °C 6 h	0
5	**2->1**	$TiCl_4$, 1	Paraform, Dioxane, refluxe 12 h	0
6	**4+3->1**	$ZnCl_2$, 4.5	DCM, r.t. 12 h	0
7	**4+3->1**	$ZnCl_2$, 4.5	DCM, 120 °C, 30 min	0
8	**4+3->1**	K_2CO_3, 4.5	Acetone/DCM, 70 °C 24 h	0

Since formation of polymeric by-products where observed in all cases, we next used more pre-organized starting materials. The previously described5 5,11,17,23-Tetrakis[4-hydroxybenzyl]-25,26,27,28-tetrapropoxycalix[4]arene 5 were synthesized and reacted with formaldehyde and its analogs to get n-Pr functionalized carcerand 6 (Fig. 4). During the screening of different conditions for the closure of 5, product formation was detected by mass spectroscopy. However, under these conditions, cleavage of the propyl groups from the starting material was observed, and no product could be detected by NMR (Table 2).

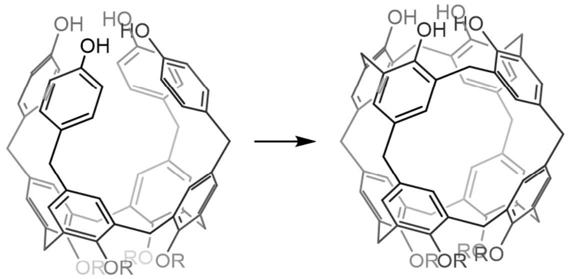

5 R = *n*-Pr
7 R = H

6 R = *n*-Pr
1 R = H

Fig. 4: Synthesis of carcerand from more pre-organized starting material.

1. Lewis acids tested: ZnCl2, AlCl3, BF3*OEt2, Mg(TfO)2, Sc(OTf)3, B(PhF5)3, MsOH, TFA, KHSO4, TMSOTf. 2. Formation of polymeric material no product observed. 3. Product detected by HR-MS. 4. Yield determined by NMR.

To overcome this issue, the same reaction was performed starting from 5,11,17,23-Tetrakis[4-hydroxybenzyl]-25,26,27,28-tetrahydroxycalix[4]arene 7 yielding product in 3% yield. Further optimization gave closed carcerand 1 containing DCM as guest with 8% yield (Fig. 4; Table 2).

Table 2. Conditions for synthesis of carcerands 1 and 6.

N	Reaction	Conditions	Yield %[4]
1	**5->6**	Lewis acids[1], formaldehyde, DCM, r.t. -60°C	0[2]
2	**5->6**	NaOH, Formaline, Ph_2O, ref	0
3	**5->6**	PTSA, formaldehyde, DCM, r.t.	0
4	**5->6**	PTSA, Dimethoxymethane, r.t.	0
5	**5->6**	PTSA, trioxane, DCM, r.t.	SM
6	**5->6**	PTSA, trioxane, DCM, 120 °C, 30 min	Traces[3]
9	**7->1**	PTSA, trioxane, DCM, 1 h	8.2

Conclusion

In summary, the first successful synthesis and isolation of the novel carcerand 1 were achieved. Work is currently underway to improve the reaction yield and to encapsulate various guests, including cations of potential radionuclides.

References

[1] D. J. Cram, S. Karbach, Y. H. Kim, L. Baczynskyj, K. Marti, et al., Host–Guest Complexation: Carcerands and Carcaplexes, the First Closed Molecular Container Compounds, J. Am. Chem. Soc. 110, 2554–2560 (1988).

[2] Z. Shi, C. A. Olson, N. R. Kallenbach, Cation–π Interaction in Model α-Helical Peptides, J. Am. Chem. Soc. 124, 3284–3291 (2002).

[3] A. Saal, T. Jarrosson, O. Ouamerali, C. A. Daul, Molecular hydrogen encapsulation in spherophanes, Chem. Phys. Lett. 480, 225–230 (2009).

[4] M. Hugo, Synthesis towards spherical molecules, Doctoral Thesis, University of Basel, Faculty of Science, (2024).

[5] A. Arduini, G. Giorgi, A. Pochini, A. Secchi, F. Ugozzoli, Anion Allosteric Effect in the Recognition of Tetramethylammonium Salts by Calix[4]arene Cone Conformers, J. Org. Chem. 66, 8302–8308 (2001).

Theragnostic nanobody-polymer-conjugates targeting B7-H3 – The next steps

Project A17.01: B7H3 Nanobody PC (CIS Biopharma AG, Bubendorf, FHNW Muttenz, Paul Scherrer Institut, Kinderspital Zürich)
Project Leader: C. Geraths
Collaborators: M. Behe, T. Villiger, O. Germershaus, J. Nazarian

Background and Concept

Conventional tumor chemotherapy or radiotherapy are efficient at eradication of tumor cells but often lack target cell specificity, resulting in significant side effects. Theragnostics are modalities which may be used for both diagnosis and treatment, facilitating improved disease management, and reducing risks and costs of cancer therapy.

B7-H3 is a transmembrane protein, acting as a suppressor of T-cell activation and proliferation as well as a potential checkpoint inhibitor ligand, which is overexpressed in different tumors, e.g., non-small cell lung cancer and prostate cancer. [1] Nanobodies are derived from heavy-chain antibodies from Camelidae and are characterized by low molecular weight, high stability, low immunogenicity, excellent affinity and specificity as well as high solubility. [2] Therefore, nanobodies represent ideal targeting moieties in the development of immunoconjugates.

The aim of this project is the development of a nanobody-polymer conjugate targeting B7-H3 and allowing attachment of diagnostic tracers such as radionuclides and/or therapeutic agents such as cytotoxic drugs (Fig 1.). By employing suitable polymeric carriers, the blood half-life of the conjugate may be tailored according to diagnostic or therapeutic requirements, off-target effects may be reduced and ultimately penetration of the blood-brain barrier may be achieved. Following the optimization of the B7-H3 nanobody production in the first year, polymer synthesis and radiolabeling were subsequently performed and further optimized. In the last year, the coupling of the polymer to the nanobody and first functional test on brain cancer cells were conducted.

Cell culture experiment with radiolabeled Nanobody

The nanobody was modified in the first step with an azide group at a surface-exposed cysteine by maleimide DOTA chelator. This chelator modified conjugate was then radiolabeled with ^{177}Lu with approx. 64 % radiochemical yield. After purification by a PD-10 desalting column, a radio purity of approx. 90% was achieved, which was suitable for cell culture experiments. For this A-172 glioblastoma cells incubated with radiolabeled nanobody-conjugate to identify the cell uptake (Fig 2.) [3]. Unfortunately, specific binding to B7-H3 expressing cells was low (<0,5 %) which might be a result of reduced affinity due to linker attachment. Further experiments have to be conducted to optimize binding e.g. affinity maturation or alternative linker design.

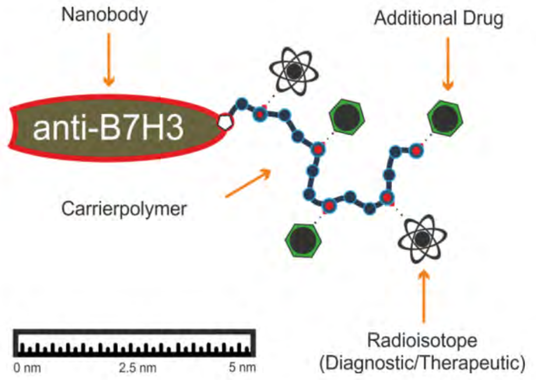

Fig. 1: Concept of B7-H3-nanobody-polymer conjugate.

First coupling experiment with model polymer carrier

Model polymer carriers comprising biocompatible monomers were synthesized by a controlled radical polymerization technique (RAFT polymerization). Subsequently polymer analog reactions for the attachment of 2 different active moieties were performed resulting in the model polymer carrier modified with 3 fluorophore tracers and 5 DOTA chelators for immobilization of radio nuclides. In the next step this model polymer carrier was functionalized successfully with a DBCO group at its headgroup for coupling to an azide-modified nanobody by a click reaction. Although this led to the formation of the desired nanobody-polymer conjugates the reaction suffered from low yields and the formation of nanobody dimers (Fig 3.). In the future this reaction will have to be optimized especially in regard to purification (= remove of non-reacted polymer carrier) which tends to elute similar to the conjugate in the SEC. Subsequently cell culture experiments, e.g. internalization, can be initiated using the purified conjugates. These experiments represent a good basis for future projects since critical process steps, such as polymer-nanobody coupling, were identified and optimization strategies, such as improved polymer purification, determined.

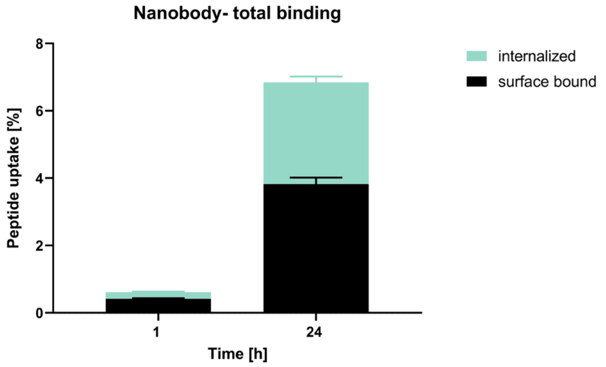

Fig. 2: Binding &Internalization of Nanobody: Total cell uptake of the radiolabelled nanobody which is increasing from 1 to 24 h. The specific uptake was below <0,5 %.

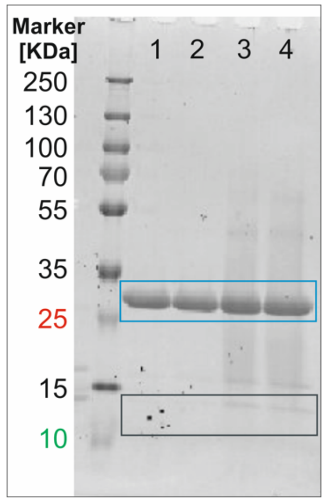

A SDS PAGE of Nanobody coupling

1: Nanobody (non-functionalized); 2: Nanobody azide functionalized, 3: Nanobody polymer modified; 4: Nanobody polymer modified (purification attempt)

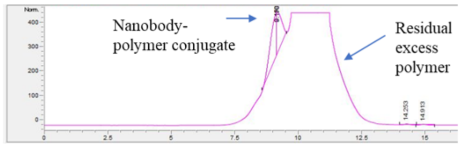

B: SEC analysis

Fig 3: Characterization of NB-polymer conjugates

Summary

During the 2nd year of the project a lead was identified out of several nanobody candidates. This candidate was radiolabeled and tested on brain tumor cells in the 3rd year of the program (cost neutral prolongation). Further first coupling experiments with the polymer carrier were conducted but the process has to be optimized. The experiments revealed that the target binding may be affected by the used linkers as the binding to living cells was impaired. This could be a result of the lower target affinity of the candidate in the first run. CIS Biopharma therefore decided to initiate an affinity maturation separated from the project to support the program. This ongoing process led to first nanobody candidates indicating higher affinity than the parent nanobody, which will be verified by surface plasmon resonance (SPR) to determine their K_D. Also, these candidates could not be further tested due to time & budget constraints; the SNI program laid the foundation for an application for a 1.2 Mio CHF Innosuisse project which was granted recently. With this we aim to develop the product further giving patients with brain tumors a new perspective.

References

[1] S. Yang, W. Wei, Q. Zhao, “B7-H3, a checkpoint molecule, as a target for cancer immunotherapy”, Int. J. Biol. Sci. 16, 1767 (2020).

[2] S. Sun, Z. Ding, X. Yang, et al., “Nanobody: A Small Antibody with Big Implications for Tumor Therapeutic Strategy”, Int. J. Nanomedicine 16, 2337 (2021).

[3] Lindmo, T., Boven, E., Cuttitta, F., Fedorko, J. & Bunn, P. A. Determination of the immunoreactive function of radiolabeled monoclonal antibodies by linear extrapolation to binding at infinite antigen excess. J. Immunol. Methods 72, 77–89 (1984).

Functional sample preparation for analysis of cellular ultrastructures

Project A17.03: FuncEM (University of Basel, Paul Scherrer Institut, CryoWrite AG, Basel)
Project Leader: T. Braun
Collaborators: I. Takashi, N. Zimmermann, A. Fränkl, L. Rima, Ch. Bechthold, A. Lorca, A. Engel

Introduction

Sample preparation of minute amounts of sample, e.g., from single cells, is essential in biomedical experiments for basic and applied research. Here, we present the amended version of the cryoWriter system for sample preparation by combining bottom-up (microfluidics) and top-down (robotics) approaches for the gentle preparation of biological samples for the subsequent analysis by electron microscopy (EM) [1,2] and mass spectrometry (MS) [3]. Notably, this system also allows the visual characterization of the sample before preparation, enabling correlative analysis.

Single and few-cell lysis and uptake

We optimized our previous development for single-cell lysis and uptake [4]. We tested the amended system for the lysis of adherent eukaryotic cells, which were previously "infected" by fluorescently labeled amyloid nanoparticles (Fig. 1). Subsequently, the lysate is prepared for EM (proteome ultrastructure) or MS (metabolomics).

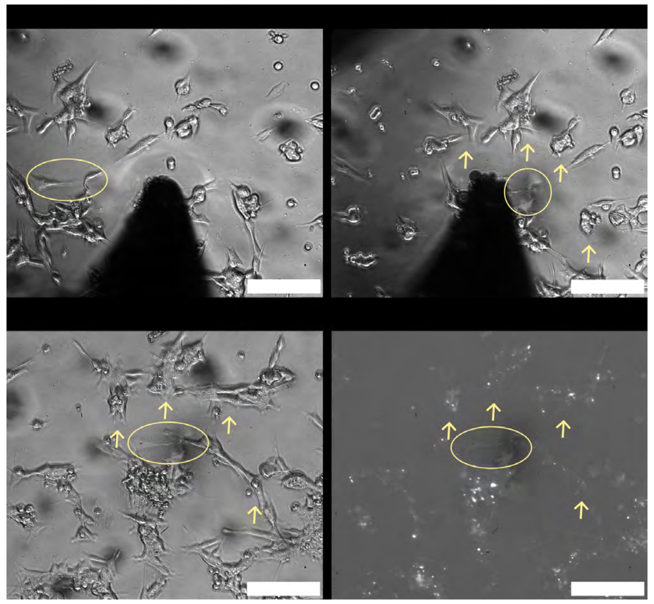

Fig. 1: Monitoring effects of the single-cell electroporation of amyloid-infected cells on neighboring cells after lysis. An individual cell was electroporated (yellow circle) and aspirated into the microcapillary. Afterward, the cell culture was placed in the incubator for an additional 12 h cell growth (recovery), and the same place was imaged again by light microscopy. The results show that (i) cells in proximity (>50 µm distance to the lysis center) are still able to divide and proliferate (yellow arrows), and (ii) the fluorescence-labeled amyloid particles remain in the cells. Figure adapted from Rima et al., 2024 [4].

Fig. 1 shows that the method for single-cell lysis of adherent eukaryotic cells is fast (< 1 s) and maintains the integrity of surrounding cells. Furthermore, the microscopy information (DIC and fluorescence channel) is essential for correlating the biological experiments with the EM and MS results.

Lysate analysis by MS and EM

Fig. 2 shows results from the single-cell experiments for metabolite detection by MS (here: Glutamine and Dopamine, two neurotransmitters) and proteins by visual proteomics (here: uptaken seeds extracted from a single cell). During the FuncEM project, we produced high-quality cryo-EM grids with single-cell lysate suitable for high-resolution processing.

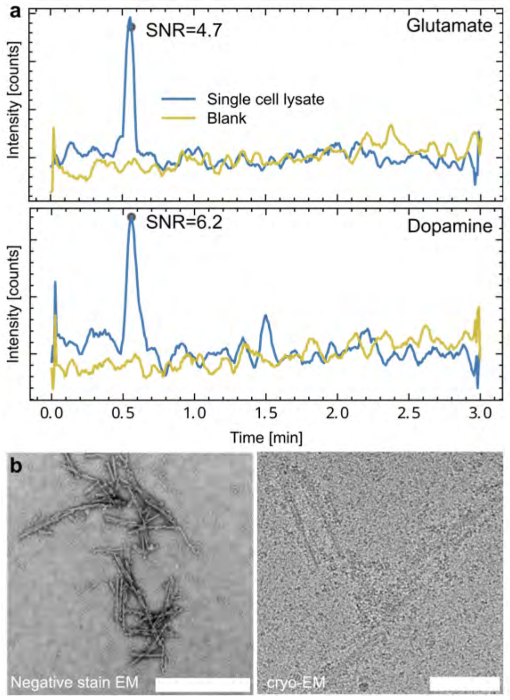

Negative stain EM

cryo-EM

Fig. 2: Single-cell analysis by mass spectrometry (a) for metabolomics and EM (b) for visual proteomics. a) MS spectra for targeted metabolomics of a single cell; the neurotransmitters Dopamine and Glutamate are detected simultaneously [4]. b) Single-cell visual proteomics. Cells were seeded with fluorescently labeled amyloid particles, and an individual cell was selected according to the fluorescence signal in the light microscope, lysed, and prepared for EM (see Fig. 1).

Whole cell vitrification

Complete cells can be grown on cryo-EM carriers (grids), vitrified, and a thin lamella is milled by a focused ion beam into the cell for subsequent analysis by electron tomography. We developed a platform for the miniaturized cultivation of adherent eukaryotic cells that is compatible with the semi-automated preparation by the cryoWriter system. For preparation, the surplus liquid is removed using the cryoWriter's pump system, thinned with a temperature-controlled gas stream, and automatically withdrawn and plunged into liquified ethane.

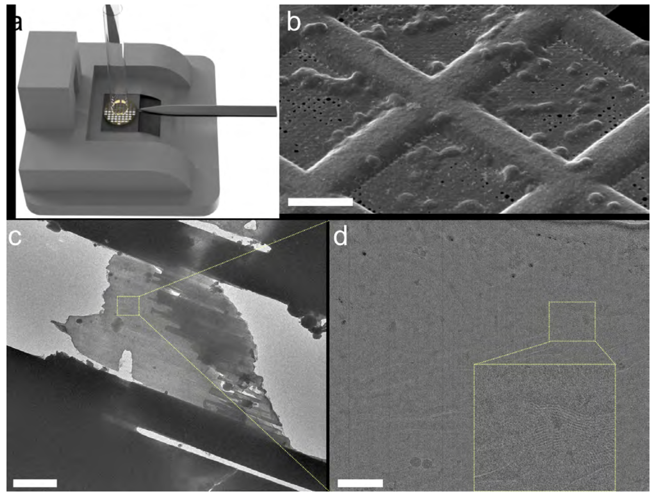

Fig. 3: Whole cell vitrification platform workflow. a) Miniaturized platform for cell growth on the cryo-EM grid, the surplus liquid is gently removed by a microcapillary, followed by a controlled gas flow over the grid. Subsequently, the robotics withdraws the grid, flips it 90°, and vitrifies it by plunging it into liquid ethane. b) SEM overview of vitrified eukaryotic cells. Scalebar: 30 µm. c) Focused ion beam milled lamella. Scale bar: 1 µm. d) section through the 3D reconstruction of the lamella with visible membrane stacks. Scale bar: 100nm.

Functional Cryo-EM Sample Preparation for Flagellar Axoneme

Eukaryotic flagella are complex and sensitive structures. They mainly consist of a bundle of microtubule pairs with attached dynein motor proteins. These axamers are natively surrounded by a biomembrane. Demembranization makes the structure accessible for ATP, allowing activity tests of the isolated examiners but further destabilizing the structural integrity of isolated cilia. Therefore, the preparation for cryo-EM is delicate; in particular, the paper blotting step used in classical preparation methods disturbs, flattens, or disrupts the ultra-structure. The cryoWriter system allows the systematic optimization of the layer thickness, as shown in Fig. 4.

Prototype of commercial cryoWriter

Importantly, we received the new commercial prototype of the cryoWriter system developed by the cryoWriter AG (Fig. 5). Compared to our in-house developed system, the new device has significant advantages. First, a much larger sample area can be covered for electron microscopy. Second, the newly designed high-precision pump system allows the precise, virtually backlash-free uptake and dispensing of nL sample volumes. Third, the system is entirely automated, which is particularly interesting for automated whole-cell vitrification. Lastly, a prototype of an interferometer was developed for the real-time monitoring of the layer thickness, which will be of great interest.

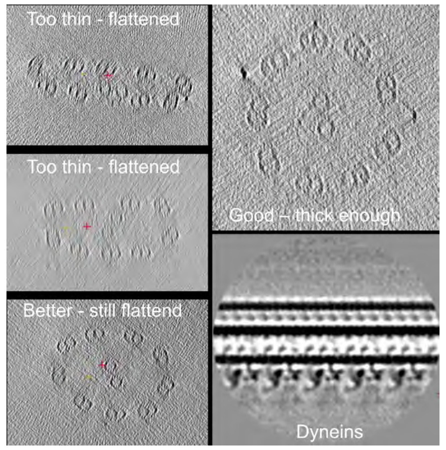

Fig. 4: cryo-EM sample preparation for electron tomographical analysis of de-membranized cilia structures (axamers). The specimen thickness is crucial to maintaining sample integrity. Here, a section through the 3D reconstruction is shown. The cryoWriter allows the adjustment of the ice thickness, preserving the global cilia structure. The soft, blotting-free preparation additionally preserves the dynein motor proteins.

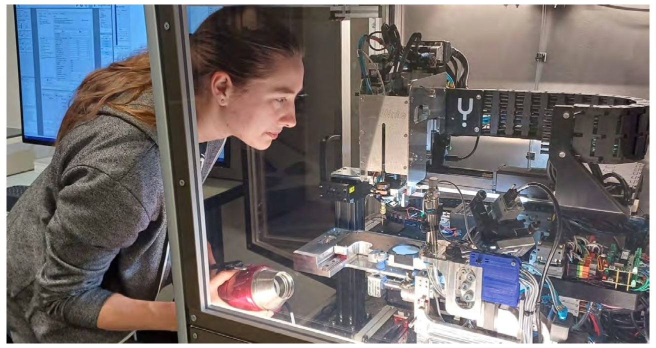

Fig. 5: Elaine Schneider (PhD student Biozentrum & cryoWrite AG) operating the new cryoWriter system.

References

[1] C. Schmidli, S. Albiez, L. Rima, R. Righetto, I. Mohammed, et al., " Microfluidic Protein Isolation and Sample Preparation for High-Resolution Cryo-EM", Proc. Natl. Acad. Sci. U.S.A. 116(30), 15007 (2019)

[2] L. Rima, M. Zimmermann, A. Fränkl, T. Clairefeuille, M. Lauer, et al., "cryoWriter: A Blotting Free Cryo-EM Preparation System with a Climate Jet and Cover-Slip Injector", Faraday Discussiona (2022)

[3] L. Rima, Ch. Berchtold, S. Arnold, A. Fränkl, R. Sütterlin, et al., "Single and few cell analysis for correlative light microscopy, metabolomics, and targeted proteomics", Lab Chip 24, 4321-4332 (2024)

Phase-shifting metasurfaces for flexible and foldable displays

Project A17.04: META-DISPLAYS (CSEM SA, Paul Scherrer Institut, Rolic Technologies Ltd., Allschwil)
Project Leader: B. Gallinet
Collaborators: L. Ciric, G. Basset, E. Glushkov, I. Giannopoulos, D. Kazazis, F. Federspiel, R. Frantz, D. Pires

Introduction

The growing demand for thin, flexible, and foldable displays has driven the search for advanced fabrication technologies. To ensure flexibility, the displays thickness must be significantly reduced. In displays, suppressing the back reflection and enhancing the image contrast are of primordial importance. This is usually realized by placing above the display emitter layer a polarizer and a phase-retarding layer (Fig. 1). Additionally, the suppression of ambient light reflection must be minimized for a broad range of angles, ensuring that contrast is maximized at any viewer position. The phase-retarding layer, a quarter waveplate, must also have high transmission to maximize the brightness of the OLED display.

Standard phase-retarding materials based on liquid crystal technology typically have thicknesses of a several microns. Metasurface-based layers have the potential to replace existing bulky phase-retarding plates, by achieving the same functionality within several hundred nanometers [1], [2].

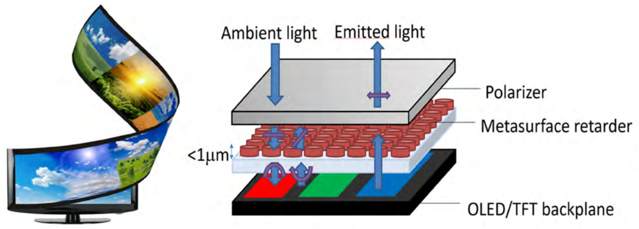

Figure 1: Left, foldable screen illustration. Right, phase retardation stack with metasurface layer. Unpolarized light passes through a linear polarizer, becomes anticlockwise circularly polarized after 1/4 waveplate. Reflection from LED backplane results in clockwise polarization, which is further transformed back to linear polarization but orthogonal to the initial linear polarization, thus preventing any light reflection.

Design

Phase retarders based on metasurfaces have been designed and simulated. Fig. 2 illustrates simulation results of phase retardation and their minimal dependence on the incident angle of light, meeting the target requirements. These simulations demonstrate the feasibility of implementing these structures in various materials and substrates, providing additional flexibility.

A cost-effective and high-throughput approach involves UV nanoimprint lithography (UV-NIL) directly on the foil (Fig. 2, left). This method allows for the transfer of metasurface structures onto high refractive index material coated on a thin, flexible, transparent foil. Preliminary tests reveal challenges in sustaining the replication fidelity of high aspect ratio structures required for such metasurface designs.

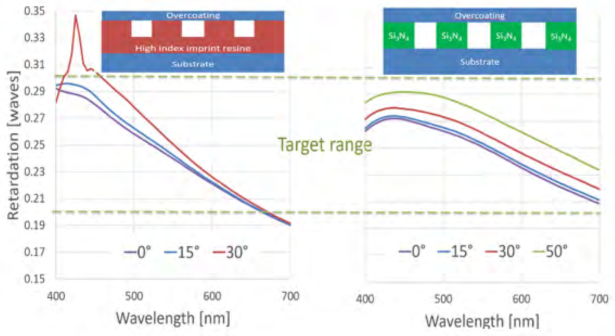

Figure 2: Simulation of EM phase retardation with wavelength/angle of incidence. Left: case of UV-NIL of high refractive index foil. Right: case of NIL approach on rigid dielectric (green color code). Between the dashed green lines is the range of retardation that is acceptable. It should have a low angle and wavelength dependence.

The focus has thus been made on a wafer-based approach that would involve thermal NIL (Fig.2, right), which represents also a cost-effective approach potentially interesting for industrial applications.

Fabrication

The wafer scale process is based on thermal NIL with reactive ion etching (RIE) pattern transfer.

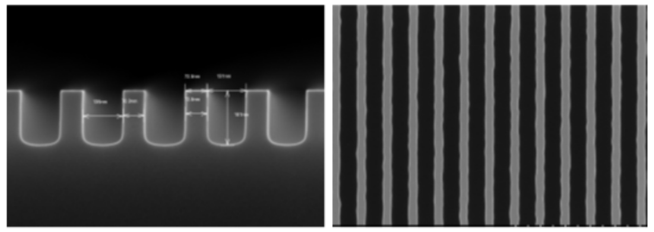

Figure 3: Scanning electron micrographs of 1x1 inch master structures fabricated in Si, after RIE and EBL. On the left one can see the cross section of the 35% duty cycle grating having the period of 200nm. On the right top view of the grating lines.

The primary requirement for thermal NIL is a preparation of high-quality stamp, which is usually done as a double copy of the master using a hybrid (ceramic-organic) UV-curable polymer. Master structures are realized via EBL patterning of PMMA and transfer of the pattern into the Si substrate via RIE (Fig.3, 4).

As the final device is to be integrated into a demonstrator with macroscopically visible effects of the metasurface phase retarder with a polarizer film the nanostructured master surface was chosen to be 1x1 inch.

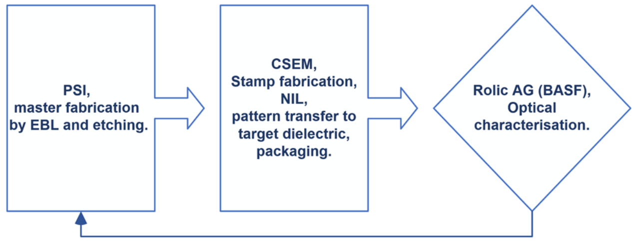

Figure 4: Fabrication and collaboration scheme.

A low-loss dielectric SiNx (deposited via PECVD) was chosen with a refractive index of 2.04 (Fig. 2, right). Achieving accurate pattern transfer into SiNx required several steps, including the deposition of a dual mask layer (metal and oxide), imprinting a NIL polymer with precisely tuned thickness of the residual layer, and adding a third mask layer on top of the imprint to ensure that pattern fidelity is not altered after residual layer etching. This step ensured proper pattern transfer while opening the NIL pattern via RIE.

After extensive optimization of the imprint and etching steps, including systematic iterations, we developed a process flow that ensures a more stable and reproducible RIE process. This marks significant progress toward achieving the project's objectives.

Results and discussion.

Fig. 5 reports optical characterization of the fabricated wafers. The plotted curves demonstrate a strong dependence on the etching time of residual layer after the NIL step. The distinct behavior of the red curve aligns well with changes in etching time. Conversely, the process outcome is quite robust with respect to variations in mask layer thickness, as all plotted curves correspond to different mask thicknesses. Measurements closely follows the reference sample (orange curve, Fig. 5) in terms of phase retardation, achieving the predicted and desirable value of approximately 0.25 waves at 550 nm. However, transmission is generally lower than expected (~90%) and is wavelength-dependent, ranging between 44% and 78%. This reduction in transmission is most likely due to scattering caused by defects. However, the dependence of retardance on the incident angle of light is minimal, with variations of only ~1% up to 20° and ~9% at 40°.

When compared to the reference sample, the results show a chromatic dependence comparable to the reference. The measured retardance values (0.18–0.39) exceed the target range specified in the project (0.2–0.3), as shown in Fig. 2 (right).

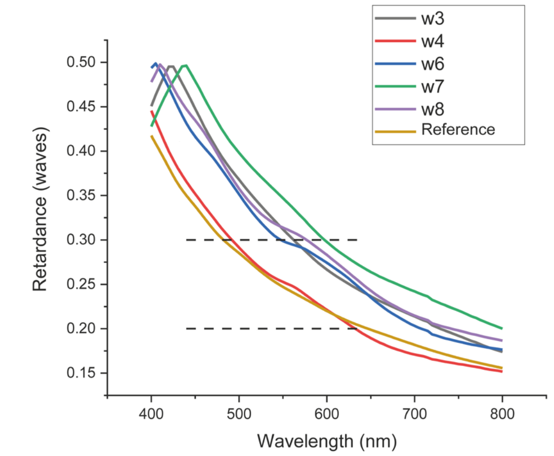

Figure 5. Retardance in the function of wavelength. The plot illustrates 5 wafers with similar but slightly different thickness of etching mask and residual imprint layer The reference device is based on liquid crystal technology.

Simulation results predict lower chromatic dependence than measured, and stronger angular dependence with higher transmission values. This points to the role of defects in both increasing chromatic dependency and reducing angular dependency.

Conclusions and outlook

In this project, we demonstrated that current technological solutions for phase retarders can be significantly enhanced, particularly by achieving a thickness reduction of at least an order of magnitude. Importantly, the incident angular dependence of retardance shows excellent stability achieved with deep-subwavelength features. Further development of the fabrication process is envisioned to improve the chromatic stability and transmission and bring it to the level predicted by simulations.

Despite the demanding and challenging nature of the fabrication process, we successfully stabilized it, creating a foundation for further advancements. The positive outcome of this project opens up new possibilities for scaling up the production and fabrication of these surfaces. For example, our initial high refractive index (HRI) foil-based solution could be further refined, and the current wafer-based thermal NIL approach could be replaced by UV NIL, offering greater versatility, a broader choice of materials, enhanced process control, and potentially improved metasurface quality.

Acknowledgements

The project partners (CSEM, Paul Scherrer Institute (PSI) and Rolic AG) express sincere gratitude to the Nano-Argovia program for funding the project.

References

[1] A. Arbabi, Y. Horie, M. Bagheri, A. Faraon, Dielectric metasurfaces for complete control of phase and polarization with subwavelength spatial resolution and high transmission, Nature Nanotechnology 10, 937- 943 (2015)

[2] F. Lütolf, F. Friebel, I. Kuznetsov, B. Rudin, F. Emaury et al., Wafer-scale replicated gratings for compressing ultrafast laser pulses at telecom wavelengths, Optics Continuum 1, 1051- 1059 (2022)

Smooth focusing mirrors for X-rays

Project A18.01: CAPOFOX (Paul Scherrer Institut, FHNW Muttenz, XRnanotech AG, Villigen)
Project Leader: H. Schift
Collaborators: S. Saxer, F. Döring

In the Nano Argovia project CAPillary Optics for FOcusing of X-rays (CAPOFOX), an interdisciplinary team is developing lithographic methods to produce micro-optical components with extreme low surface roughness. Researchers from the Paul Scherrer Institute PSI, the School of Life Sciences at the University of Applied Sciences and Arts, Northwestern Switzerland FHNW and the industrial partner XRnanotech are aiming for a process that produces tiny capillary mirrors suitable for both ultraviolet and X-rays. Hollow glass tubes that are shaped like a funnel, or segments from such tubes that are shaped like ellipsoidal mirrors, can serve as focusing elements for X-ray beams (Fig 1) [1]. Yet, there is a restricted range of available geometrical shapes. In 2024, the different partners were focusing on advancing both, fabrication and characterization methods. Progress has been made towards the assessment of 4 nm roughness on laser-patterned three-dimensional (3D) resist structures. First designs of 10 mm long and 80 µm deep slopes for capillary optics have been made.

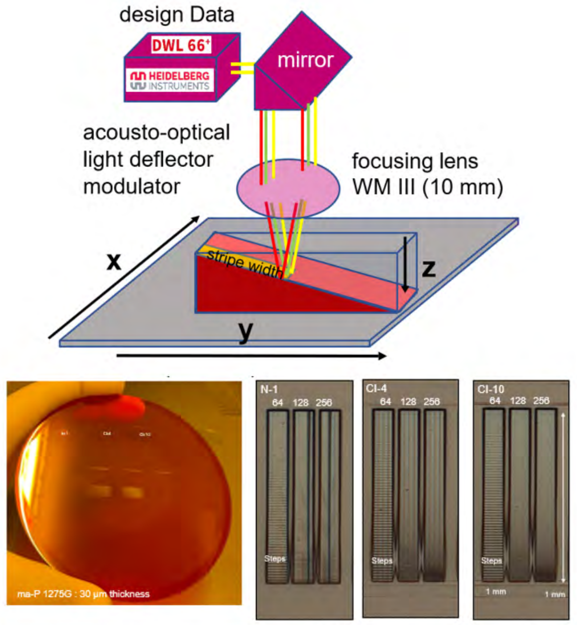

Fig. 1: Top: Schematic setup of the scanning laser direct writing lithography (DWL) tool. Bottom left: Resist coated wafer (ma-P 1275 G). Right: Optical micrographs of 1 mm long, 100 µm wide and 15 µm deep linear flat slopes in 30 µm thick resist with different writing strategies and number of steps with different gray values (64, 128, 256).

Arbitrary 3D shapes by gray-tone lithography

Gray-tone lithography allows to reproduce a 3D surface topography from a computer aided design and could create surfaces, e.g., with parabolic shapes in lateral (x-y) direction, that could focus light more precisely (Fig. 1). This can be done by exposing photosensitive materials (photoresists) with a scanning laser of rapidly varying laser intensity and then etching the exposed resist away, leading to a ready to use 3D structure. In CAPOFOX, the project team wants to establish methods that are a) capable of generating such geometries with a limited number of gray values and b) characterize and optimize the roughness in the nanometer range, to finally achieve smooth waveguide structures in polymers that are similar or even better than those of glass capillaries. For the fabrication, the team at PSI led by Dr. Helmut Schift employed a novel resist from micro resist technology GmbH that could be patterned to more than 100 µm depth instead of the 20 µm so far [1]. This was a big step towards designs that would be closer to the capillaries used for curved focusing mirrors. The actual glass capillaries used so far have diameters of up to 1 mm but narrow down to a few 10's of µm. Therefore, an inverted cylinder ("half-pipe") of over 50 µm height would already allow to come close to such a setup.

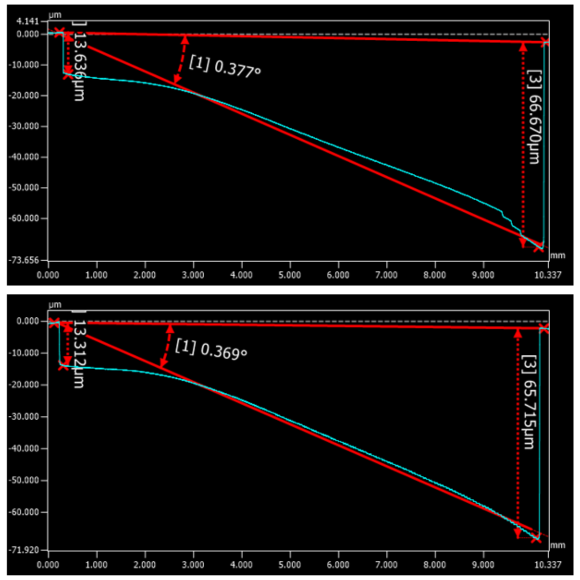

Fig. 2: Confocal scanning laser microscope (Keyence VK-X3100) longitudinal (y) cross-sections of two slopes produced with direct laser lithography (Heidelberg Instruments DWL 66+) in 120 µm thick ma-P 22_XP novolak resist with 1'024 GVs. Top: Linear flat slope. Bottom: Linear concave slope with 150 µm constant radius (in x), thus creating a taper along y starting from 5 µm at the top to 300 µm width at the bottom.

The new resist, although chemically similar, required the establishment of a modified process scheme. Thick resists are typically more prone to air inclusions and to mechanical stress during processing. Air bubbles are created by casting viscous resist and during the post-bake of the exposed resist and had to be eliminated by introducing long settling times and vacuum steps before exposure. Particular attention is required for the linearization of the slopes and the transfer of this knowledge from flat linear flat to concave slopes (Fig. 2). Overall, the new resist, which goes to the limits of what is possible with novolak chemistries, is a huge progress for applications such as micro-optics and microfluidics that require channel sizes with depths over 50 µm.

Roughness measurement by SFM

Atomic force microscopy (AFM) allows for measuring nanoroughness essential for applications utilizing the 13.5 nm EUV wavelength. Currently, the steps generated by the discretization of a 3D structure using 1'024 gray values are, however, found to be larger. In theory. a 10 mm long, 60 µm high linear slope would result in 10 µm long and 60 nm high steps. The step length is longer than the 1.4 µm beam width of the scanning laser, and the height is more than 4 times higher than the EUV wavelength. Instead, 10'000 GVs would result in 1 µm long steps that are 6 nm high. The laser beam would then overlap different steps and enable an inherent blurring. In addition, the generation of narrow, deeper, and steeper slopes are a challenge for high resolution AFM. Dr. Sina Saxer (FHNW) and her team managed this by using specific structures that enabled them to measure at different depths of the slope. Three distinct structural features caused by the laser writing were observed: a) vertical tiling stripes (TS), b) horizontal gray values (GV) and c) random roughness of the resist (Fig. 3). The TS roughness of 22 nm, constituted by all GVs within a long slope and stitching errors stemming from the 30 µm wide stripes generated by overlapping exposures due to the DWL writing strategy. Without such artifacts, i.e., an area of 20×20 µm2, the GV roughness reduces to 8 nm. Neglecting both, stitching lines and GVs (Fig. 3c), resulted in a promising 4 nm roughness caused by the resist properties. After thorough analysis, we can now identify this value as a roughness inherent to the novolak resist, and different from design- and process-related limitations. Although 4 nm would be suitable roughness for many applications, the use of such a surface for reflecting EUV or even X-rays with minimized scattering requires a lower roughness of below 1 nm. Since it is not easy to switch to graytone resists with different chemistry, a possible alternative is therefore to convert the novolak topography into the surface of a different polymeric material and use a smoothening process that is able to flatten the 4 nm locally. Such a process was established previously for polymethyl methacrylate (PMMA), a polymer with linear chains that can be reflown by selective thermal annealing (TASTE process) [2]. This could also flatten out surface steps and artifacts without affecting the overall design of the slope.
As the next step, a concave reflective mirror for EUV will be fabricated using a higher number of GVs (Fig. 3) and tested with X-rays. We will see what effect the optimized results from linear slopes will have on these more complex 3D shapes. The results will contribute to the development of ultra-smooth mirrors for focusing X-rays, which can be used in material processing, for example.

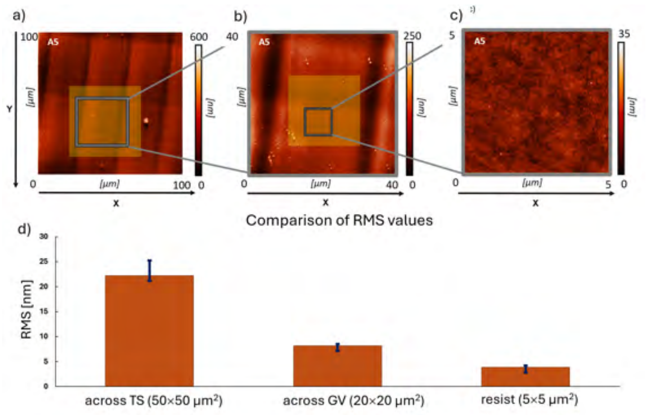

Fig. 3: AFM images and roughness analysis of linear slope: a-c) Surface roughness measurements using a NTEGRA in tapping mode at a frequency of 0.5 Hz and analyzed by NOVA software (both by NT-MDT). A 3rd-order polynomial subtraction was applied to the data using the to ensure proper flattening before analysis. Cantilever tips (RTSPA 150, Bruker) with a nominal resonance frequency of 150 kHz, a force constant of 5 N/m, and a tip radius of approximately 8 nm were employed for the measurements. The roughness values were calculated exclusively from the yellow-highlighted areas. The images with gray borders visually indicate the location and dimensions of the analyzed regions. For visualization purposes, images from one area (A5) are shown, while the roughness values were obtained by evaluating multiple images for each condition: a) 22 nm RMS on a 50×50 µm² area, calculated over four images spanning two tiling gaps (distance between TS 28 µm) b) 8 nm RMS on a 20×20 µm² area, calculated within a tiling stripe (distance between GV 9.4 µm) c) 4 nm RMS on a 5 × 5 µm² area, calculated in the flat region between two steps. d) Comparison between RMS values of different surface areas.

This project allows XRnanotech to advance its X-ray optics technology through significant achievements in surface quality: "The CAPOFOX project has driven remarkable improvements in reducing surface roughness over the past year, enabling us to achieve very smooth surfaces that strongly enhance our product developments. This innovative approach not only ensures high performance but also opens the door to impactful applications in the future. We are excited to be part of such transformative progress," said Dr. Florian Döring, CEO and founder of XRnanotech.

References

[1] C. Schuster, G. Ekindorf, A. Voigt, A. Schleunitz, G. Grützner, Pushing deep greyscale lithography beyond 100 µm pattern depth with a novel photoresist, Proc. SPIE 12497 (2023) 124970P.

[2] A. Schleunitz, V.A. Guzenko, M. Messerschmidt, H. Atasoy, R. Kirchner, H. Schift, Novel 3D micro- and nanofabrication method using thermally activated selective topography equilibration (TASTE) of polymers, Nano Convergence 1(7) (2014)

Tissue assembly with diffractive nano-optics tweezers and Fs alexandrite laser – NanoFemto tweezers

Project A18.05: NanoFemto Tweezers (FHNW Windisch, FHNW Muttenz, TLD Photonics AG, Villigen)
Project Leader: B. Resan
Collaborators: T. Grätzer, M. Gullo, R. Carreto

Abstract

We aim to build holographic optical tweezers by employing diffractive nano-optics and a novel ultra-short pulsed alexandrite laser. The optical tweezers will be able to manipulate multiple types of cells allowing for multi-cellular tissue assembly with minimal thermal impact due to a newly developed ultra-short pulsed alexandrite laser pumped by red laser diodes.

Introduction

Personalized medicine aims to tailor treatments, reducing adverse effects, using patient-derived organoids for drug testing. Yet, organoids alone can't replicate intricate inter-organ interactions. Body-on-chip platforms are vital, integrating multiple organoids in microfluidic setups, which requires precise bio fabrication, aligning diverse cell types with micrometer accuracy. Holographic optical tweezers offer promise, using lasers to manipulate cells. Conventional lasers risk cellular damage due to heat. To counter this, we propose femtosecond lasers, giving a minimal heat impact. Enhanced by nano-diffractive optical elements, lasers can form optimal trapping patterns. This synergy aims to establish a gentle holographic optical tweezer system towards body-on-chip creation.

The alexandrite oscillator developed for this application uses red laser diodes to pump the crystal directly. This provides multiple benefits to other pumping setups currently in use, such as flash lamps, green laser diodes, and frequency doubled YAG-lasers. Pumping by red laser diodes provides superior quantum efficiency, lower cost, and complexity. Multi-watt level red laser diodes have become commercially available in recent years and have thus enabled the direct pumping of alexandrite lasers.

Continuous-wave and Q-switched pulsed operation of alexandrite lasers pumped by red laser diodes has already been demonstrated [1]. SESAM modelocked operation of alexandrite, which is a method used for achieving ultrashort pulses in the femto- and picosecond range, has so far only been demonstrated using green pump light from expensive frequency-doubled solid-state lasers [2]. Diode-pumped femtosecond alexandrite could become a cost-effective and efficient alternative to the currently widely used ti:sapphire lasers for generating ultrashort pulses in the near-infrared spectrum.

Experimental Setup

The experimental setup consists of a scientific setup of the diode-pumped alexandrite oscillator (see Figure 1 and an optical tweezer setup (Fig. 4a). The alexandrite oscillator is pumped by a fiberized output laser diode module with 5 W of nominal optical output. The cavity design was adapted from ti:sapphire oscillators by considering the upper state lifetime and emission cross-section of alexandrite. The crystal is normal incidence and anti-reflection coated for the pump and lasing wavelengths.

Figure 1: Scientific setup of the red diode pumped alexandrite oscillator.

Results

An 84 MHz pulse repetition rate alexandrite laser oscillator was designed, and a scientific setup has been built, as shown in Figure 1. The laser achieved 1.2 W of output power in CW mode at 8 W of pump power using a 1% output coupler. Using a SESAM as one of the end mirrors and incorporating GVD mirrors for dispersion compensation, we have achieved modelocked operation centered at 747 nm with a spectral width (FWHM) of 6.6 nm (see Figure 2a). Assuming a sech^2-shaped pulse, this corresponds to ~95 fs pulse width (FHWM) as can be deduced from the autocorrelation measurement in Figure 2b. The output power was 315 mW, corresponding to a pulse energy of 3.8 nJ and a peak power of 35 kW.

We've also achieved much shorter, sub 50 fs pulses using Kerr-lens modelocking, but at a lower average output power of 110 mW. [3]

To project holograms for optical trapping foci, nano diffractive optical elements (nDOE) were computed based on a kinoform addition algorithm. The previously developed phase mask algorithm has been improved and adapted for high precision two photon nano lithography able to project graduated intensities and force fields, compared to singe points (figures 3a-c). The 3d nDOE was computed and could be directly fabricated by 2-photon lithography (figure 3d). The pixel resolution could be increased form 10x10 µm^2 to 1x1 µm^2. At the same time the division of a singular phase shift pixel has been improved from 128 to 256 discrete levels, according to a vertical precision of 5 nm. Also, the process was optimized to fabricate a relatively large 1x1cm^2 nDOE with nanometric resolution and features. These refinements allow to achieve nDOE with finer details and allow to better shape the optical filed into smaller (figure 4c-d) and more complex traps such as vortex traps and trap fields.

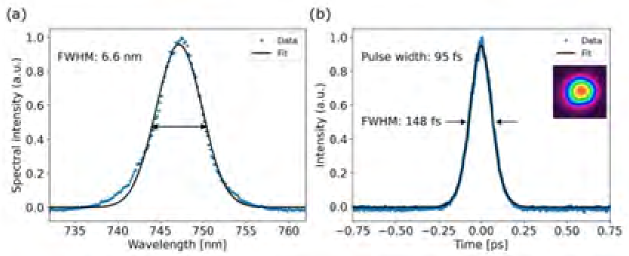

Figure 2: a) Spectrum of the modelocked alexandrite laser. b) Autocorrelation measurement and inset the beam profile. Taken from [3]

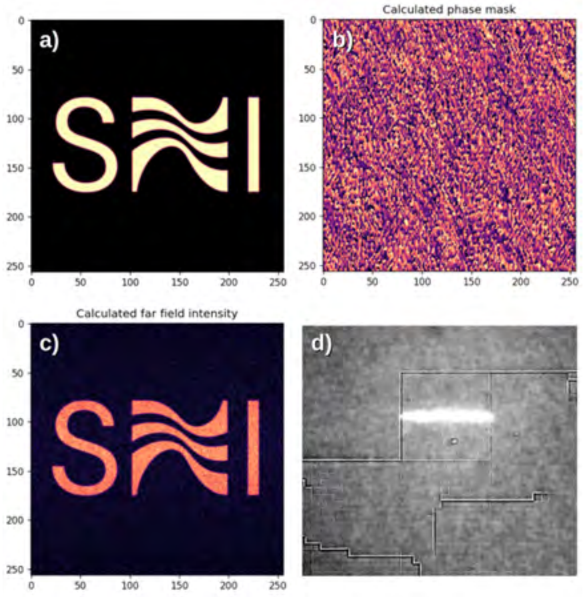

Figure 3 Target intensity of the hologram projection of an example filed (SNI logo); b) Calculated phase masks with improved lateral and vertical resolution; c) Calculated intensity form phase mask b, showing the improved quality of the nDOE; d) Snapshot of nano lithography process of phase mask.

The basic optical tweezer setup was improved to allow easier and better alignment. The low power pilot laser was replaced by a 200mW 820nm laser to achieve stronger optical traps allowing the manipulation of microbeads and ultimately cells. To permit the trap arrangement modulation, e.g., trap distance, several nDOEs were fabricated side by side to enable switching between different configurations by lateral shifting of the nDOE plate. In addition. the nDOEs were mounted on a carousel to allow swift switching. The microscope camera and illumination were improved to allow better monitoring of the trapping process. Finally, a dedicated sample stage holder was fabricated for mounting and translating glass bottom cell culture dishes. Microbeads with a diameter of 8µm were successfully trapped as cell surrogates (Figure 4d-f). The system is now ready for trapping and assembling neuron cells. Integration with a two-photon microscope will be evaluated as a remaining step. First components evaluation is already completed in this regard.

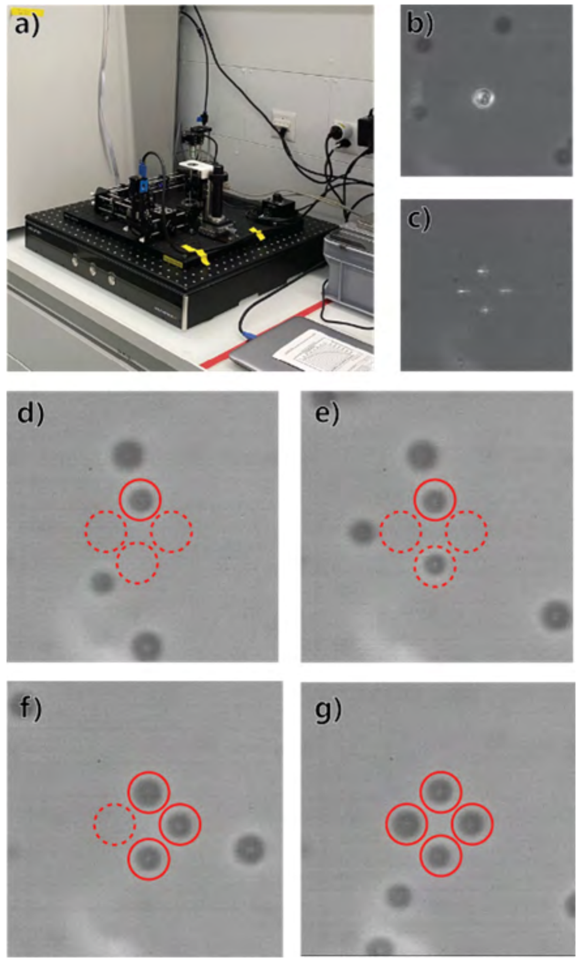

Figure 4 a) advanced optical trap setup in biosafety lab; b-c) Single optical trap foci with a focal spot size of 3µm, four optical traps with 1µm spot size; d-g) Consecutive trapping of microspheres (dotted lines are empty spots)

References

[1] A. Teppitaksak, A. Minassian, G. M. Thomas, and M. J. Damzen, “High efficiency >26 Wf diode end-pumped Alexandrite laser,” Opt. Express 22, 16386-16392 (2014).

[2] Shirin Ghanbari, Ksenia A. Fedorova, Andrey B. Krysa, Edik U. Rafailov, and Arkady Major, “Femtosecond Alexandrite laser passively mode-locked by an InP/InGaP quantum-dot saturable absorber,” Opt. Lett. 43, 232-234 (2018).

[3] Tobias Grätzer, Manuel Zeyen, Daniel Hug, and Bojan Resan, "Red diode-pumped SESAM and Kerr-lens modelocked alexandrite lasers," Opt. Express 32, 47033-47040 (2024)

NanoHighSens: using nanoscale spintronic magnetic sensor for high bandwidth current measurements

Project A18.06: NanoHighSens (FHNW Muttenz, FHNW Windisch, Camille Bauer Metrawatt AG, Wohlen)
Project Leader: J. Pascal
Collaborators: H. Nicolas, A. Grana, J.-B. Kammerer, R. Sousa, S. Gorenflo, M. Ulrich

Introduction

The measurement of electrical current at a high-frequency and low noise have recently received new quality standard requirements (e.g., IEC62020-1), requiring the measurement of high-frequency harmonics in electrical currents networks above 100 kHz. This becomes challenging to achieve with existing technologies. To overcome these difficulties the NanoHighSens project targets the use of new nanoscale devices called spin transfer torque magnetic tunnel junctions (STT-MTJs) as nanoscale magnetic sensors combining both high bandwidth as well as high resolution.

Magnetic Tunnel Junctions

The innovative principle of using STT-MTJs as magnetic sensing units relies in the fact that the switching voltages are proportional to the external field. A low amplitude (± 350 to 400 mV) triangular voltage signal at high frequency is then applied across the MTJ, typically at a frequency of 100 kHz and above, leading to periodical reversal of the magnetization of the storage/free layer [1]. These reversals of the magnetization lead to a change in the resistance of the device, alternating from low resistive state to high resistive state and inversely. Such alternating behaviour between the two resistive states, combined with the proper dedicated electronics, results in a signal proportional to the external magnetic field [2] (Fig. 1).f

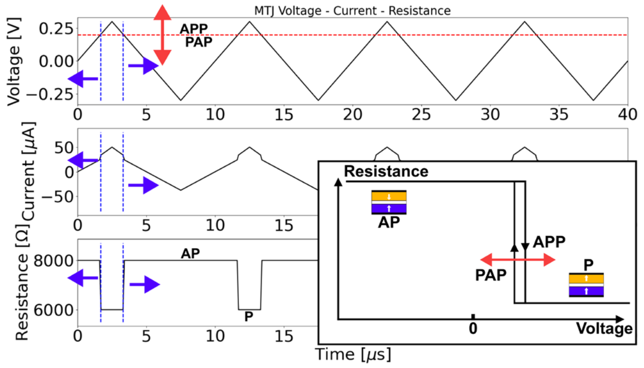

Fig. 1: STT-MTJ magnetic sensing principle.

Electronics and Signal Processing Platform

Dedicated conditioning electronics have been developed, including the MTJ reading electronics and a ring-shaped PCB (printed circuit board), for the measurements of multiple sensing units.

The conditioning electronics includes all the required analog hardware circuitry to operate the MTJ and to output a signal proportional to the magnetic field, as depicted in Fig. 2. This electronic circuit is based exclusively on operational amplifiers combined with resistors, diodes and capacitors, making the design fully compatible with future CMOS monolithic integration. Since these MTJs were originally designed for memory applications, they remain also fully compatible with CMOS standard processes.

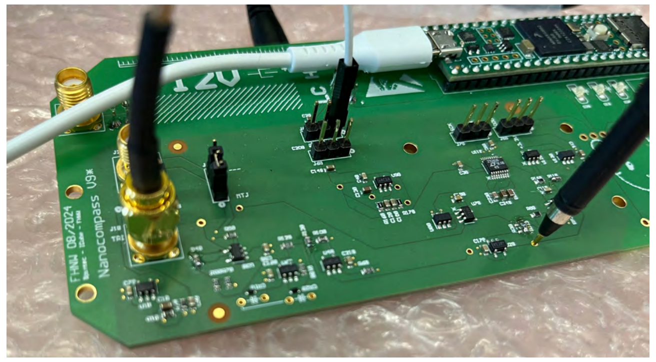

Fig. 2: Conditioning electronics for the magnetic sensing of STT-MTJs.

On the other hand, the signal processing electronics consists in multiple larger sensing units, embedding microcontrollers and memories, each capable of handling the measurement of a sensing unit, creating the complete current probe prototype (Fig. 3). Each unit can measure the MTJs at a sampling frequency of 250 kHz, offering a bandwidth of up to 125 kHz, with synchronous measurements through all the other units. This results in seven synchronous data point from multiple sensing units, each of them resulting from an array of MTJs, allowing the noise to be substantially lowered. The eighth controller is in charge of reading and controlling the entire system and does not include the eighth sensing unit at the moment. Consecutive sample points are then stored until the embedded memory of the microcontrollers is completely full, then quickly read-out, and sent to the computer for more advanced signal processing and analysis (e.g., FFT, averaging or digital filtering). The output of the entire system is therefore a single reconstructed signal proportional to the external field (i.e., current) with low noise and high bandwidth, allowing the assessment of high harmonics in the monitored power network.

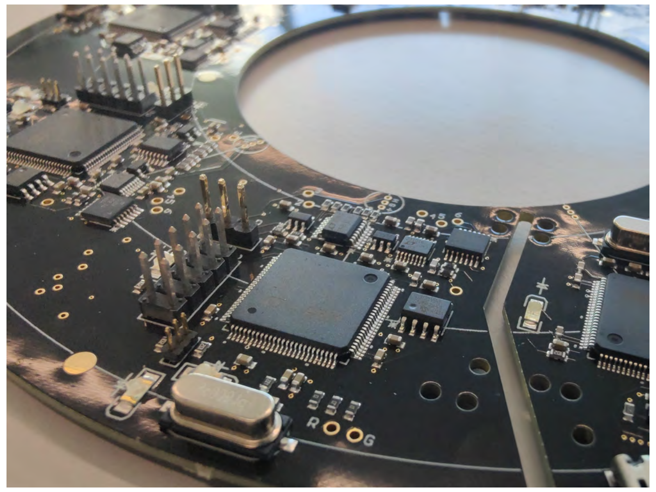

Fig. 3: Ring-shaped PCB containing seven sensing units with a main microcontroller. The primary current conductor is placed at the center of the device.

Results

Using the presented STT-MTJs combined with the conditioning electronics, sensitivities of the devices could be measured (i.e., output characteristics), up to 5 mV/mT with noise level as low as 2 to 5 $\mu T/\sqrt{Hz}$ on a single MTJ presenting nominal diameter ranging from 50 to 100 nm (Fig. 4). Further tests and analysis are being conducted to assess the different ways of optimizing the electronics and the stack of the junction to enhance the performance of these sensing elements (i.e., reduce the noise and increase the dynamic range).

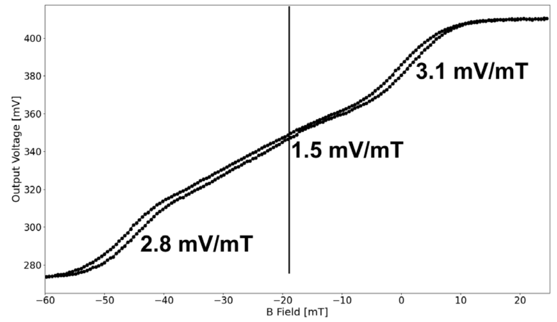

Fig. 4: Output characteristics of the proposed conditioning electronics of a single MTJ.

Due to technological challenges to combine MTJs with the electronics at this stage of the project, MTJ-arrays were replaced with commercially available sensors (TMR sensors) as reference. Finally, measurements, performed at Camille Bauer Metrawatt facility, using the ring-shape PCB also showed successful results and working principle, by allowing the detection of an ac current through a wire, positioned at the centre of the device (Fig. 5). Current consumption, when considering the sensing element only, remains typically in the µW range, making such technology significantly low power in comparison to existing technologies. This also makes the prototype and MTJs compatible for future arrays of multiple junctions, as the total power consumption of such array will remain in the order of 1-5 mW, easily manageable in an integrated circuit. Typical dynamic range of such sensing devices are between ± 8 mT to ± 30 mT. However, these MTJs present a offset field that needs to be further investigated.

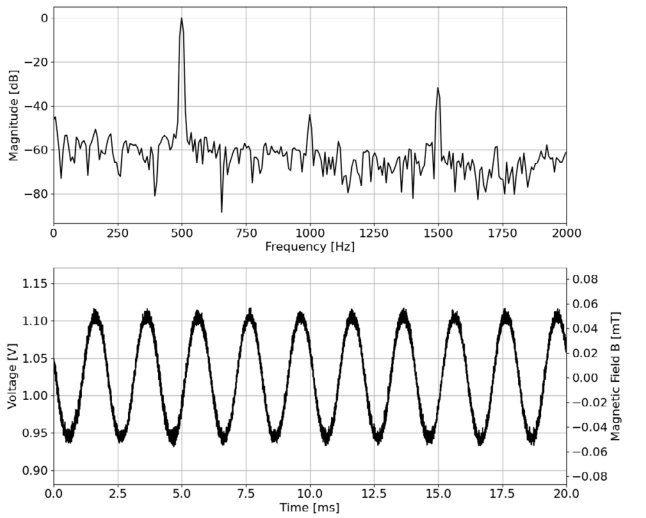

Fig. 5: Measurement of a 500 Hz sine wave current in a wire at ± 10 A. The second and third harmonics are visible. The signal is reconstructed from the seven synchronous individual sensors measurements.

Conclusion

Using newly developed MTJs presenting low coercive fields, associated with the dedicated reading circuitry, a high-bandwidth magnetic sensing element could be demonstrated achieving a high bandwidth (100 kHz to 1 MHz) with a noise as low as a 2 $\mu T/\sqrt{Hz}$, while offering a low power consumption (< 25 µW) combined with nanoscale diameters (50 up to 100 nm). Thanks to these dimensions, an array of multiple MTJs can now be fully considered, allowing the resolution to be lowered down by the square root of the number N of sensing elements ($\propto 1/\sqrt{N}$). Such array of sensing units will then be mounted and connected on the described ring-shaped PCB of the current probe to create the complete current sensing probe, offering both high-bandwidth and low noise performance. However, further different improvements are still required to obtain a lower noise, almost exclusively induced by the stochasticity of MTJs in the reversal events.

References

[1] H. Nicolas et al., “Conditioning Circuits for Nanoscale Perpendicular Spin Transfer Torque Magnetic Tunnel Junctions as Magnetic Sensors”, IEEE Sensors Journal 23, (2023).

[2] H. Nicolas et al., “Low-Coercivity Perpendicular Spin Transfer Torque Magnetic Tunnel Junctions as Nanoscale Magnetic Sensors”, IEEE Intermag 2023, (2023).

Quantum sensors for brain imaging

Project A18.07: QSBI (Paul Scherrer Institut, CSEM SA, Qnami AG, Muttenz)
Project Leader: K. Moselund
Collaborators: S. Kim, J. Meirer, M. Munsch

Introduction

Our goal in the QSBI project was to develop a new generation of MEG system, combining quantum sensors (NV centres) and artificial intelligence (AI). Such systems would enable measurements of brain activity in noisy environments and may be integrated into nano-probes for brain or cardiac endoscopy.

We focused on two key components. The first component is the development of a new quantum sensor based on optically addressable atomic defects in diamond known as NV centres. NV-diamond quantum sensors have the potential to revolutionize MEG by providing high enough sensitivity to measure signals from the brain while simultaneously having high enough dynamic range to enable measurements outside of magnetically shielded rooms. Further, the sensors could be mounted on a headcap and adjusted to patient's head shape. However, the high refractive index of diamond, as well as the low absorption cross section of NV-centers means that getting enough light out of the crystal is a challenge. The conversion efficiency from excitation photons to detected readout photons is typically 1-3%. Ultimately this is one significant factor currently limiting sensitivity, and both excitation efficiency and photon collection efficiency needs to improve to reach the sensitivity needed to detect magnetic signals from the brain.

The second key focus involved advancing AI algorithms to reconstruct 3D brain activity maps with high fidelity and robustness to noise. This task poses a significant challenge: decoding tiny (picotesla) brainwave signals from MEG data, despite interference from much larger ambient fields (micro-teslas) generated by the earth as well as environmental noise from nearby instrumentation and vehicles. To overcome these challenges, we employ a two-step approach using machine learning. First, we enhance the signal quality using tailored algorithms to improve the signal-to-noise ratio of raw sensor data, delivering cleaner readouts for subsequent analysis. We then localize brain activity using advanced machine learning methods to decode the sensor signals and accurately localize their origins within the brain. Through benchmarking experiments, we systematically evaluate and identify the best-performing methods for achieving high fidelity and reliability in brain activity reconstruction.

Results & discussion

1) Design an optical assembly structure

Qnami finished the design of a light collection system compatible with sensor packaging and miniaturization. The design consists of two parts: An NV-sensor diamond crystal cut into the shape of an elongated diamond rod with square end facets. The elongated shape and the high refractive index of diamond ensures that the majority of the photoluminescence from the crystal is guided towards the 2 square facets. Second, contacted with one of the facets is a parabolic light guide that reduces the NA of the emitted PL (while increasing the area). The lightguide is designed to optimize coupling into a 0.52 NA optical fiber. Large core diameter fibers with 0.52 NA are easily accessible commercially. Ray tracing simulations indicate that using this optical system we should be able to achieve a conversion ratio of green photons to collected red PL of 23%.

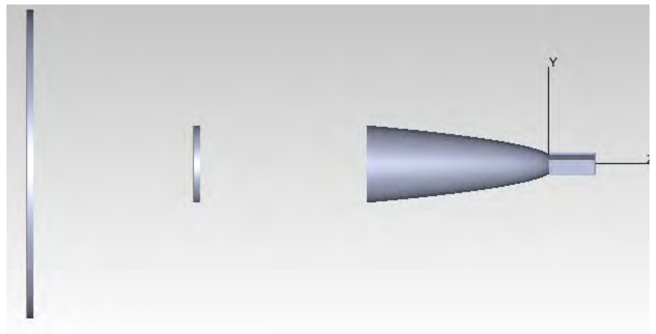

Fig. 1. The optical assembly design. Taken from a ray-tracing simulation. The cylindrical parabola is a diamond light guide, while the square rod represents the NV containing diamond crystal. The vertical planes are used to measure the angular distribution and intensity of the light that is coupled out of the diamond. This design is upgraded from the elliptical design we envisioned at the start of the project. Careful simulations showed that the performance of the elliptical design would be unsatisfactory.

2) Design and fabricate advanced photonic nanostructures on the diamond surface.

In order to selectively optimize the excitation and collection efficiencies we designed and fabricated wavelength dependent optical structures on the diamond. We evaluated different design approaches by simulation, developing structures both based on photonic bandgaps as well as optimized scattering. Qnami and PSI jointly developed fabrication routes to produce the designed structures. Based on our investigation of nanophotonic surface patterning, we believe this is a more promising route to improve efficiency rather than the simple solution of coating.

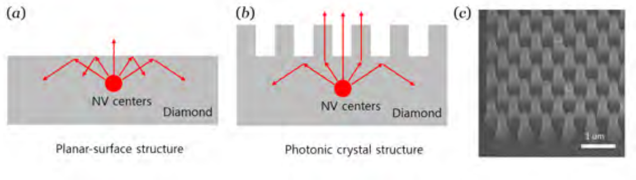

Fig, 2 (a) illustration of the challenge of out-coupling light due to the high refractive index of diamond, the out-coupling efficiency of the light is very low, which results in a low sensitivity. (b) illustration of the concept of how scatterers at the surface or photonic crystals might optimize out-coupling efficiency. (c) example of a diamond photonic crystal lattice fabricated in QSBI.

3) Optical characterization of the effect of nanopatterning of the diamond surface

In the first phase PSI developed an optical set-up and test methodology which was used to assess the impact of nano patterning of the diamond surface [1]. In 2024 we evaluated a number of different designs, including heights of the nanopillars and explored the effects of the size of nanopillars and the photonic crystal lattice periodicity, defined by the parameter "a". The results are shown in Fig. 3.

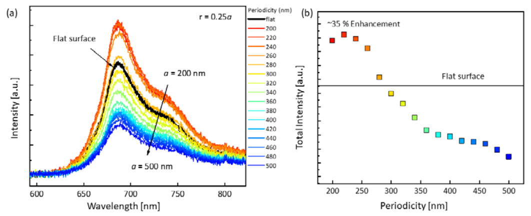

Fig. 3. (a) intensity read-out of the lightemitted from the NV centers as a function of wavelength. (b) enhancement of the signal at 690 nm compared to a flat surface as a function of the periodicity a.

As illustrated in Fig. 3.a a clear difference can be observed between nanopatterned and flat regions of the diamond surface, in that particular image it appears brighter as more light escapes from the surface. Form figures 3.c and 3.b it can be observed that the degree of enhancement or depression of the collected NV signal compared to a flat surface strongly depends on the periodicity of the photonic crystal lattice. For the maximum wavelength around d690 nm and a fairly tight lattice with a periodicity of 225 nm we observe an enhancement of the collected signal of up to 35% - in line with the goals of the QSBI project. Whereas for larger lattice spacings exceeding 300 nm we observe a reduction of the collected light compared to a flat surface. It is clear that nanopatterning can act as an important enhancement factor for improving the sensitivity of sensors based on NV centers in diamond.

What we could not establish from these results alone is whether the improved sensitivity stems from an improved activation efficiency (better at keeping the green laser light inside the structure to experience multiple passes within the diamond medium) or an improved extraction efficiency of the red light emitted from the NV centers. Most likely it is a combination of both factors.

To further elucidate the mechanisms behind the enhancement PSI carried out simulations of the transmission of the periodic structures Maximum transmission occurred around 240-250 nm periodicity, roughly similar to the peak enhancement observed in the experimental data, thus we believe we can tie the enhancement observed in the light intensity to an improved extraction efficiency.

4) Inferring Brain activity using Machine Learning

The AI for Life Science team of CSEM has developed machine learning algorithms to achieve non-invasive, 3D localization of neuronal brain activity using MEG (magnetoencephalography) sensors. To lay the foundation, we built a physical model that translates electromagnetic currents within the brain into their corresponding sensor readouts in the MEG system. This model allowed us to generate realistic simulated data, enabling early progress without depending on actual sensor data while the next-generation MEG sensors are being developed. Building on this groundwork, we developed machine learning algorithms capable of interpreting sensor readouts to localize active regions of the brain cortex. Our approach explored a variety of advanced methods tailored specifically to MEG data, including deep learning architectures such as Bidirectional Long Short-Term Memory networks (BiLSTMs) and Convolutional Neural Networks (CNNs), alongside specialized mathematical models. To validate our methods, we evaluated their performance using both simulated and semi-realistic datasets. The latter employed a "phantom head," a device equipped with magnetic dipoles to generate controlled, artificial brain signals, allowing for the precise knowledge of signal locations. Our benchmarking showed that the top-performing approach was a mathematical model called FLEX-MUSIC [2]. This algorithm, excels in identifying signal sources while accounting for spatially extended neuronal activity – a common feature in MEG data. These developments resulted in a computational pipeline to produce highly accurate 3D maps of brain activity, a crucial component in many downstream applications. For example, these tools could improve epilepsy detection, where precise localization of abnormal activity is critical, or functional brain mapping, supporting and improving our understanding of the dynamics of our brain.

Conclusion

In order to develop a sensor compatible with MEG application, we investigated different design approaches by simulation and measured qualitatively an enhancement of PL emission. Our findings in the computational analyses demonstrate that state-of-the-art machine learning algorithms outperform currently used methods in reconstructing 3D brain activity maps with high fidelity. Looking ahead, these algorithms can be used to improve the signal-to-noise ratio of next-generation MEG sensors and enable precise, non-invasive analyses of brain activity.

We also found that nanopatterning of the diamond surface can enhance the light extraction by up to 35%, but that the degree of enhancement or depression of the signal is highly dependent on the periodicity of the nanofeatures. Altogether we believe that we have successfully achieved the objectives of the QSBI project, by proving the applicability of the different concepts.

References

[1] S. Kim, G. Seniutinas, J. Meirer, T. Sjölander, K. Moselund, Quantum Sensors for Brain Imaging, Swiss Quantum Days (2024)

[2] Hecker, Lukas, Ludger Tebartz van Elst, and Jürgen Kornmeier. Source localization using recursively applied and projected MUSIC with flexible extent estimation. Frontiers in Neuroscience 17 (2023)

Overcoming drug delivery barriers with SmartCoat™

Project A18.08: SmartCoat (FHNW Muttenz, Paul Scherrer Institut, Palto Therapeutics AG, Allschwil)
Project Leader: J. Mosbacher
Collaborators: G. Lipps, R. Benoit, Palto Therapeutics AG

The challenge

The efficient and targeted delivery of nucleotide-based therapeutics (NBTs) to diseased cells remains an unresolved challenge. Small NBTs like antisense oligomers or siRNAs are rapidly degraded, do not readily penetrate biological barriers and can cause side-effects when accumulating in non-diseased tissue.

Development of improved SmartCoats

Palto Therapeutics is developing a novel approach to overcome these issues using so-called SmartCoats™ which are protein-based carriers comprising modules for siRNA binding, protection, and targeting (Figure 1). The team therefore aimed to design and produce SmartCoats capable of binding to and protecting siRNA, targeting siRNAs to specific cancer cells where they release the siRNA into the cytoplasm for robust target gene knock-down.

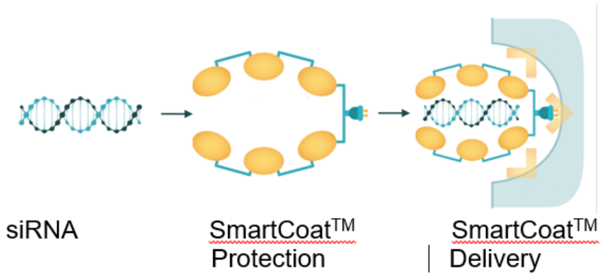

Figure 1: Chemically unmodified therapeutic siRNA (left) is encapsulated in a single protective layer that protects the RNA (middle, SmartCoat™) and shuttles the RNA to specific surface epitopes on target cells (right).

In the first year, we generated three versions of peptidic siRNA binders with increasing complexity, developed biophysical assays like size exclusion chromatography (SEC), Fluorescence Polarization Anisotropy (FPA) and Dynamic Light Scattering (DLS) for molecular characterization, as well as functional experiments to show serum stability, cell targeting, target gene knock-down and anti-proliferative efficacy in cancer cell lines.

The best of the three versions showed siRNA binding affinity of 150-300 nM which was far higher than anticipated. While the construct provided a decent siRNA serum stability, no target gene knock-down could be detected.

Building up on results from the first year, we optimized the initial design of fusion protein constructs using *in silico* structural modeling. We incorporated additional siRNA-binding modules and improved the linker regions between these modules. The newer-generation SmartCoats showed a single band in the SDS-PAGE (Figure 2A), had more predictable biochemical and biophysical properties, represented in a clear main peak in the SEC spectrum (Figure 2B), and exhibited significantly improved siRNA-binding affinity (Figure 2C). Notably, these carriers did not aggregate, as determined through dynamic light scattering and analytical gel filtration chromatography (not shown). Furthermore, SmartCoat-siRNA complexes were shown to stay associated in the presence of serum whereas naked siRNA rapidly degraded (data not shown).

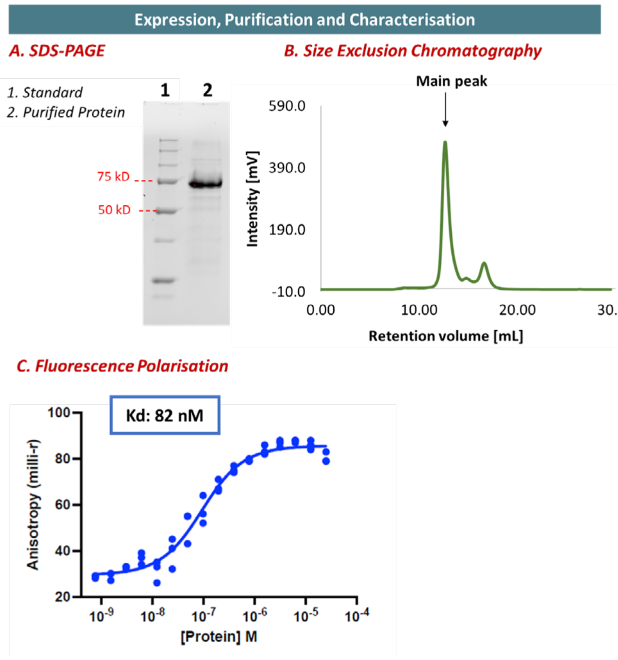

Figure 2: Newer-generation SmartCoats can be efficiently produced and purified (A), are monodisperse (B) and tightly bind siRNA (C).

Using a modified GFP-tagged SmartCoat construct, we could show in confocal imaging experiments that the peptide was able to attach to or enter SKOV-3 cells, an ovarian cancer cell line expressing specific surface markers that the SmartCoat construct targets (Figure 3). After 24 hours incubation, still quite high concentrations were needed to show SmartCoat signals in the majority of cells (Figure 3: upper panels for SC 400 nM and 800 nM). Compared to standard *in vitro* transfection agents like lipofectamine, we estimated that we need about 30-fold higher concentrations when using our current constructs as siRNA shuttles.

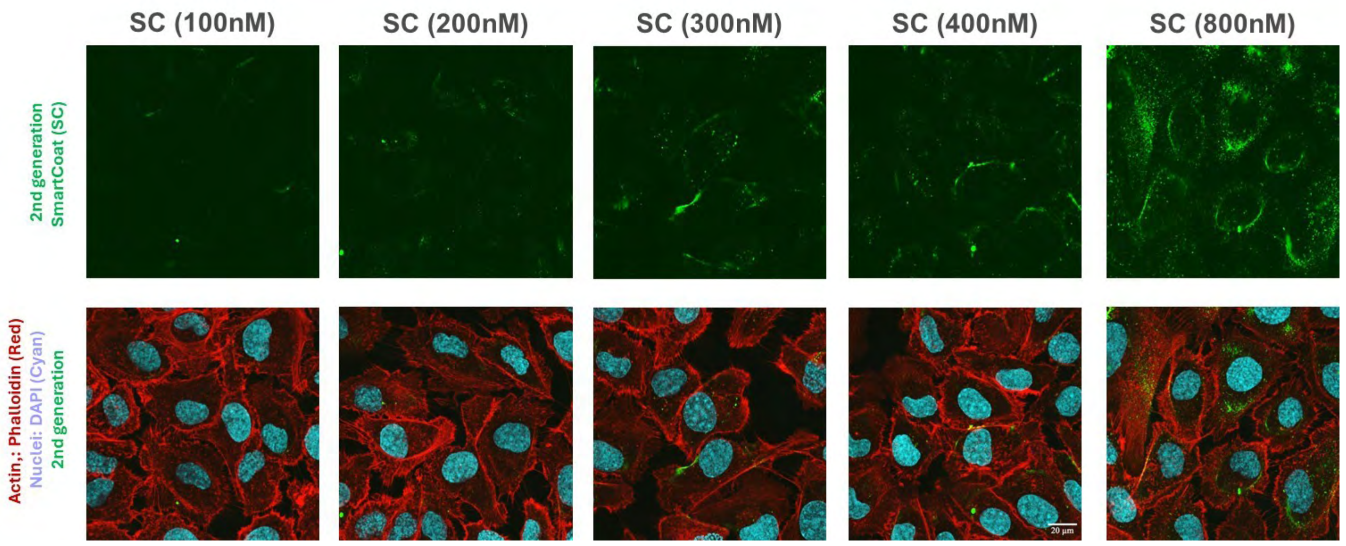

Figure 3: Cell targeting of newer generation SmartCoat to SKOV-3 cells. Upper panels: Fluorescent signals from eIGFP-tagged SmartCoats (named SC) at increasing concentrations after 24h incubation to cultured SKOV-3 cells. Lower panels: Super-imposed confocal images showing DAPI (blue; nuclei), phalloidin (red; f-actin in the cytoplasm) and SmartCoat (green) from same experiment as upper panel. Image size 0.12x0.12 mm.

This low "transfection efficiency" may be the main reason why we were not able to see any functional gene knock-down efficiency using an oncogene-targeting siRNA aggregated with the newer SmartCoat generation ("SC3" in Figure 4). While lipofectamine-mediated siRNA transfections ("L" in Figure 4) consistently showed target knock-down of about 80%, no significant knock-down was detected in the SC3-siRNA-treated SKOV-3 cell cultures. In fact, lipofectamine-transfected siRNA could already induce similar knock-down levels at 5 nM concentrations, again about 30-fold lower than those necessary to detect any cell signals of labeled peptide constructs (compare Fig. 3).

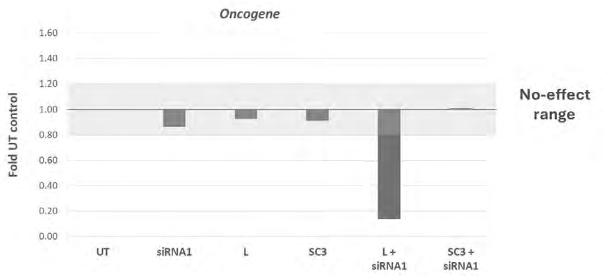

Figure 4: Target oncogene knock-down by siRNA incubated with standard lipofectamine (L) or newer generation SmartCoat (SC3). qPCR data was normalized to untransfected controls (UT) and shown as mean data from 2 biological and 3 technical replicates. SKOV-3 cells were plated 24h prior to transfection, incubated with siRNA for 5h in serum-free OptiMem conditions, then re-supplied with RPMI medium with serum for further 20h, lysed and processed for qPCR quantification. Similar data was obtained from experiments with 48h incubation.

Consequently, we could not observe any functional anti-proliferative efficacy of SmartCoat-shuttled siRNA (Figure 5). For this experiment, we had to combine four different siRNAs targeting different oncogenes as single oncogene knock-down was insufficient to reduce SKOV-3 growth rates.

In summary, we generated peptidic siRNA shuttles combining modules for binding, protection and cell targeting. We have been able to improve structural and binding properties, as well as serum stability. Still, we have neither been able to reach binding affinities of published reference constructs (see e.g. Liu et al., 2014), nor could we show siRNA-mediated knock-down with our current construct. This might be due to the lack of high affinity binding but may also be due to poor cell membrane permeability or slow release of siRNA once the complex reaches the cytoplasm.

Outlook

Drug delivery of RNA-based therapeutic molecules remains a major challenge for the pharmaceutical industry. Peptide-based shuttles hold promises to provide siRNA protection and targeting. We have established a robust engine to design, express, and purify such shuttles, combined with biophysical and *in vitro* cellular assays for structural and functional characterization. More data from more constructs are necessary to understand how eventually biophysical data could guide construct design in a way to achieve functional efficacy in cellular assays and ultimately in patients.

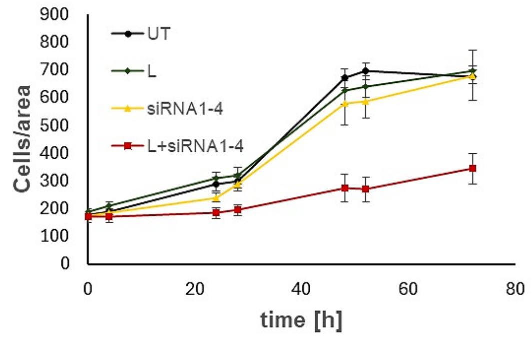

Figure 5: Inhibition of cell proliferation by oncogene knock-down. SKOV-3 cells were plated at t= -24h before incubation with 4 siRNAs targeting different oncogenes (siRNA1-4) Phase contrast images were taken daily at 2 timepoints and cells counted automatically. While Lipofectamine (L) or siRNAs alone did not change cell growth compared to untreated (UT) controls, L+siRNA1-4 mixtures significantly reduced proliferation (mean ± SEM , n=4)

References

Liu DV, Yang NJ, Wittrup KD. A nonpolycationic fully proteinaceous multiagent system for potent targeted delivery of siRNA. Mol. Ther. Nucleic Acids. 2014; 3: e162.

Development of functional nano-layers for Gen 4 anode-less all-solid-state batteries

Project A19.01: BatCoat (Paul Scherrer Institut, FHNW Windisch, Oerlikon Metco AG, Wohlen)
Project Leader: M. El Kazzi
Collaborators: K. Löffel, K. Yalamanchili

Project motivation

Following the EU approval of an effective ban on new fossil-fuel cars from 2035, there is an urgent need to develop a safe, efficient and eco-friendly electric mobility solution. Recent investigations show that for both passenger cars and heavy-duty trucks, battery-powered vehicles are the most efficient solutions to achieve the targets of net zero CO_2 emissions.

However, the current generation 2 and 3 of Li-ion battery technology using graphite or silicon-graphite composite as an anode (Fig. 1) and liquid-based electrolyte cannot meet the user requirements in terms of range, price, safety and more importantly sovereign, and sustainable supply chain. There is a consensus, indicating that by replacing the conventional anodes with anode-less lithium metal batteries (AL-LMB)[1] in Gen4 cells, using solid electrolytes (SE)[2], and just Cu as anode current collector (CC) an energy density of 500 Wh/kg (Fig. 1) could be achieved, simultaneously reducing the cost to < 80-100 CHF/kWh at cell level with an improved safety. As a result, AL-LMB technology is considered the holy grail for rechargeable batteries. Yet, the current limitations to realize AL-LMB cells are related to the ability to plate and strip metallic lithium for more than 500 cycles at an efficiency of more than 99%.

The BatCoat project aims to solve this challenge by using nanoscale functional layers (10 to 100 nm) deposited on the surface of the Cu CC to be tested in all-solid-state (ASSB) cells. First, a lithiophilic material called nucleation layer, is deposited directly on top of the Cu, allowing a uniform Li plating/stripping by improving the Li wettability. This is then followed by a second layer, having good ionic conductivity but being electrically insulating, which acts as a barrier layer between deposited Li and the solid electrolyte, preventing them to react with each other (Fig 1). Finally, a three-dimensional (3D) Cu CC will be designed (Fig. 2) and optimized with aspect ratio features in the 100s of nm scale to reduce the local current density at high charging rates.

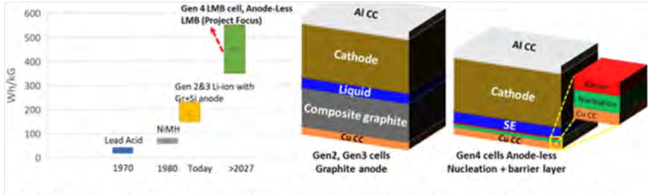

Figure 1: Energy density comparison of the AL-LMB with their predecessors, and the sketch of the current Gen2, Gen 3 compare to Gen 4 cells.

Fig. 1: Energy density comparison of the AL-LMB with their predecessor technologies, and sketch of the current Gen2, Gen3 compared to Gen4 cells.

Project goals

We list below the major challenges to overcome for achieving the BatCoat KPIs (Exceptional according to in Table 1) considered as a minimum requirement of commercial battery for car industry:

(i) Reduce the local current density at the anode, because higher current favors the Li dendrite growth.

(ii) Suppress the formation of inactive Li caused by the plated Li reaction with the SE.

(iii) Mitigate the large volume change (~15 µm of Li equivalent thickness) during plating and stripping leading to an important strain accumulation at the interface with the SE and causing cracks formation.

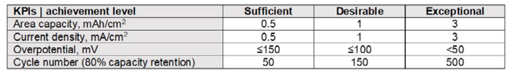

KPIs | achievement level	Sufficient	Desirable	Exceptional
Area capacity, mAh/cm^2	0.5	1	3
Current density, mA/cm^2	0.5	1	3
Overpotential, mV	≤150	≤100	<50
Cycle number (80% capacity retention)	50	150	500

Table 1: Technological key performance indicator (KPIs) target at different success levels

Table 1: BatCoat technological key performance indicator (KPIs) target at different success levels.

The novelty of BatCoat in addressing those challenges is the use of a 3D current collector with the appropriate coating of nucleation and barrier layers. This is the gap that Oerlikon Metco (OM) our industrial partner also would like to fill, by developing, and commercializing technical and economically compelling high throughput nucleation, and barrier coater thereby enabling the Gen 4 anode-less technology.

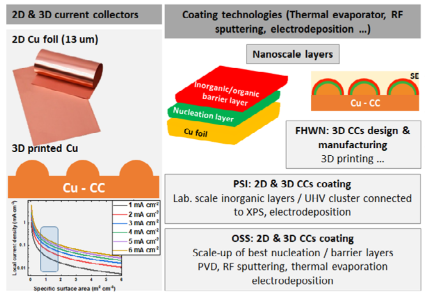

Figure 2. The sketch is summarizing the PSI, FHWN and OSS approaches to enable the anode-less concept for Gen 4 ASSBs. 1st by exploring the role of the CC morphology (2D foil vs. 3D), 2nd thin films nucleation and barrier layers, 3rd deposition fabrication techniques (PVD, RF sputtering, electrodeposition and e-gun evaporators).

Fig. 2: BatCoat approaches to enable the anode-less concept for Gen4 ASSBs. 1st by exploring the role of the CC morphology (2D vs. 3D), 2nd thin films nucleation and barrier layers and 3rd thin film deposition employed techniques.

The 3D CC will help to reduce drastically the local current density which is proportional to the surface area. Fig. 2 shows the local current density drop as a function of the surface area increase, using a very simplistic calculation by just dividing the current collector specific area by the cycling current applied on the cathode. As a matter of fact, already a surface area around 1 m^2/cm^3 is enough to reduce the current density by a factor of 30. Finally, 3D CC is expected to help reducing the interface strain induced by the large volume change of the plated Li, and when is combined with a nanoscale nucleation and barrier layers coating, the Li wettability, surface diffusivity will improve and prevent the reactivity of the Li with the electrolyte which is essential to increase the coulombic efficiency of the plated/stripped Li and the cycle life.

BatCoat 1st year achievements

The milestones of the 1st year have been achieved and some obtained results even outperformed the promised milestones. A summary of the main achievements is presented in the Fig. 3. PSI explored and tested the nucleation and barrier layers on the 2D current collector (CC). From the first screening 100 nm Ag as a nucleation layer provided the best cycling performance in terms of critical current density achieving 0.8 mA/cm^2. When adding 130 nm LiF as barrier layer on top of the Ag the critical current density was doubled achieving 1.5 mA/cm^2. Based on those promising results, a first full ASSB cell assembly were tested, composed of NCM811 as cathodes, LPSCl as solid electrolyte combined either with (i) bare Cu (Fig 3.a) or (ii) 100 nm Ag/130 nm LiF deposited on Cu (Fig 3.b) as CCs. The cycling protocol of the cells was the following: progressive increase of the current density or also so-called cycling rate (C) from 0.075 mA/cm^2 (C/20) up to 1.5 mA/cm^2 (1C), and for each cycling rate, 3 cycles were performed. The cells were cycled in galvanostatic mode, (Fig 3.a and 3.b) providing excellent capacity at C/20 rate between 160 and 180 mAh/g. It is obvious that the cell with the bare Cu CC shorted at C/3 or at 0.5 mA/cm^2 (Fig 3.a) while the cell with modified Cu surface with Ag and LiF (Fig 3.b) survived the 1C rate (1.5 mA/cm^2) which is beyond the desirable KPIs (Table 1). Furthermore, the long cycling performance of the Ag/LiF modified Cu was tested at a current density of 0.5 mA/cm^2 and areal capacity of 1 mAh/cm^2 presented in Fig 3.c. At those cycling conditions the cell survived 200 cycles before achieving 80% capacity retention which is also beyond the desirable KPIs (Table 1) in terms of areal capacity and number of cycles. Those achievements are the best reported up to this day, without yet optimization of the nucleation and barrier layers thicknesses and cathode surface coating. Thus, thanks to those results PSI has fully achieved the milestones promised for the 1st year.

Moreover, FHNW succeed to manufacture a series of 3D Cu current collectors (CC) with sinusoidal shape (Fig 3.d), by employing pulsed laser surface structuring. Those 3D Cu CCs are currently under final optimization (e.g., improving surface roughness, surface cleaning), afterward early next year will be sent to PSI for applying the Ag and LiF nucleation and barrier layers and for the electrochemical testing as well as for comparison with the results obtained on the 2D Cu CC. Additionally, FHNW performed simulation of the current density and strain distribution at the interface between 3D CC and the solid electrolyte (Fig 3.e).

Since the coating on Cu is not currently modeled in the simulation, this effect cannot be computationally captured now. However, computational modeling of the battery system is paramount in further optimization.[3] The coating therefore needs to be accounted for in the simulation; this shall be additionally undertaken by FHNW in the 2nd year.[4]

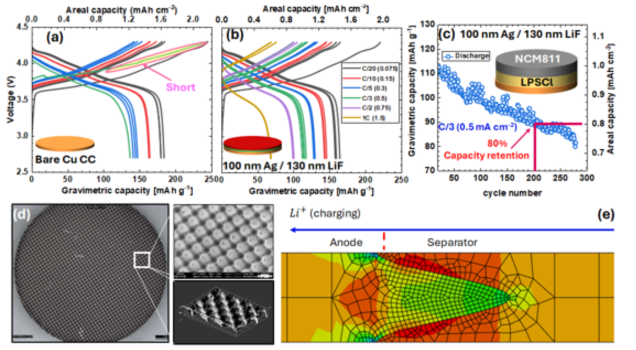

Fig. 3: Galvanostatic cycling performance at different current density of all-solid-state anode-less full cell using NCM811 as a cathode and 2D Cu as anode (a) bare Cu and (b) 100 nm Ag/130 nm LiF coated Cu. (c) long cycling performance of the best coated Cu at 0.5 mA/cm2 and 1 mAh/cm2. (d) SEM of the 3D Cu current collector. (e) Simulation of horizontal normal stress during charging at the interface between 3D CC and solid electrolyte (red: tension; blue: compression).

Conclusions

As mentioned above, the 1st year of the BatCoat was very fruitful in acquiring scientific knowledge and technically very successful where most of the planned experiments have been performed without major problems. Moreover, all the challenges have been overcome thanks to the excellent collaborative efforts between PSI, FHNW and OM, and the regular meetings, discussions, and the exchanged ideas.

For the 2nd year, PSI will further improve the electrochemical performance by additional optimization of the nucleation and barrier layers and evaluate them on the 3D CC. FHNW will finalize the strain and current density distribution simulation on the 3D CC and manufacture the best optimized 3D CC morphology for the final electrochemical testing to achieve the exceptional KPIs. Lastly, knowledge transfer to OM regarding the best nucleation and barrier layers to be reproduced and optimized at large scale.

References

[1] S. Kim, et al., "Lithium-Metal Batteries: From Fundamental Research to Industrialization", Advanced Materials 35, 2206625 (2023)

[2] N. Lee, et al., "Anode-less all-solid-state batteries: recent advances and future outlook", Materials Futures 2 (1), 013502 (2023)

[3] M. Martí-Florences, et al., "Modelling and Estimation in Lithium-Ion Batteries: A Literature Review", Energies 16 (19), 6846 (2023)

[4] S. E. Sandoval, et al., "Structural and electrochemical evolution of alloy interfacial layers in anode-free solid-state batteries", Joule 7 (9), 2054-2073 (2023)

Pushing the limits of electron microscopy with high-Z sensors

Project A19.03: HiZfEM – High-Z sensors for electron-microscopy (Paul Scherrer Institut, University of Basel, DECTRIS AG, Baden)
Project Leader: D. Greiffenberg and E. van Genderen
Collaborators: K.A. Paton, S. Fernandez, J.P. Abrahams

Introduction

Hybrid pixel detectors (HPD) caused a revolution in photon science when they were first used at light sources almost two decades ago [1]. More recently, they have been widely adopted in electron microscopy for diffraction-based experimental modalities thanks to their high dynamic range, fast frames rates (>kHz), and good radiation hardness compared to the current state-of-the-art CMOS cameras. However, their spatial resolution is limited by the multiple scattering of primary electrons in their thick (≥ 300 µm) silicon sensors, necessary to ensure their radiation hardness [2].

The aim of this project is to replace the relatively light silicon sensors (atomic number Z=14) with heavier sensors, which have greater stopping power due to their increased electron density. Using such sensors should improve the image quality by reducing the range of incident electrons and therefore image blurring. Well understood high-Z sensor materials are chromium-compensated GaAs (Z=31/33) and CdZnTe (Z=48/30/52). Another point that can negatively impact the detector efficiency is backscattering of the primary electron out of the sensor which probability increases for heavier elements. GaAs:Cr is therefore a particularly promising sensor material as its average atomic number is sufficiently high to reduce the range of incident electrons but not so high as to cause a significant reduction in detector efficiency due to increased electron backscattering.

Materials and Methods

Broadly speaking, there are two different categories of HPDs available: Charge-integrating (CI) and single photon counting (SPC) readout chips. CI readout chips provide a precise measurement of the deposited energy per pixel, making it possible to clearly see how a single electron has deposited its energy along its trajectory in the sensor. This gives us precise information about the shape and length of the primary electrons' tracks. SPC readout chips increment a digital counter if the deposited energy in a single pixel exceeds a predefined energy threshold. If the energy threshold is properly set, single photon counters operate effectively noise free and are capable of extremely high (> MHz) count rates.

This project consists of two parts which are largely characterized by the readout chip used: In the first stage of the project, GaAs:Cr sensors were bonded to the CI readout chip JUNGFRAU1.0 [3], which has a pixel size of 75 x 75 µm². During this phase, the sensors were initially characterized with photons to determine their detector properties and with electrons to study their charge release during the absorption process in detail (Fig. 1). To test the sensors' response to electrons with energies up to 200 keV, dedicated mechanics were constructed for installing devices on the JEOLJEMF200 (S) TEM located at the Paul Scherrer Institut and operated by the University of Basel (Fig. 2).

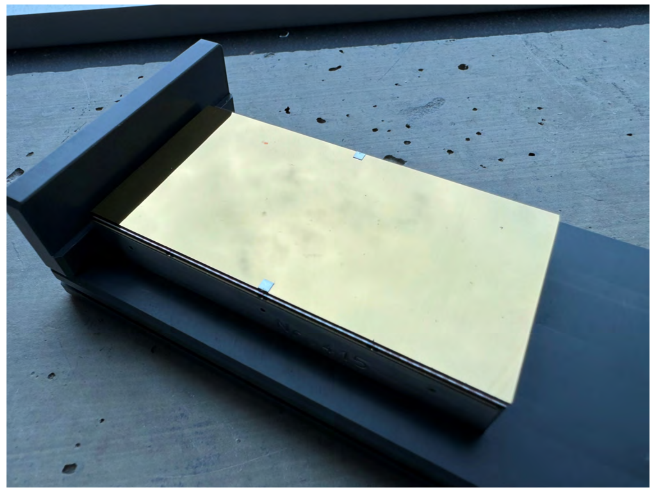

Fig. 1: Picture of a full GaAs:Cr module (8x4 cm²) mounted on eight JUNGFRAU readout chips.

One of the open research questions with GaAs:Cr is whether it is possible to make use of the defined charge spread within the sensor which results in different signal amplitudes in adjacent pixels depending (most dominantly) on the lateral absorption position of incident quanta (both photons and electrons). In silicon sensors it has been successfully demonstrated that spatial resolutions of few microns can be obtained via interpolation when using photons. However, the lateral scatter of high-energy electrons means that to localize the entry point of electrons in silicon sensors requires advanced machine learning based methods [4]. If the reduced lateral scatter of electrons in GaAs:Cr means interpolation can be applied to localize the electron entry point in GaAs:Cr sensor, then this would be far more computationally efficient than current methods used with silicon sensors.

However, CI detectors rely on short acquisition times when localizing incident electrons to be sure that the electron tracks are clearly separated in space, limiting their suitability for many experiments. The second part of the project will aim to transfer interpolation techniques to a SPC multiple energy thresholds to obtain an electron detector that combines high spatial resolution with their high count and frame rates.

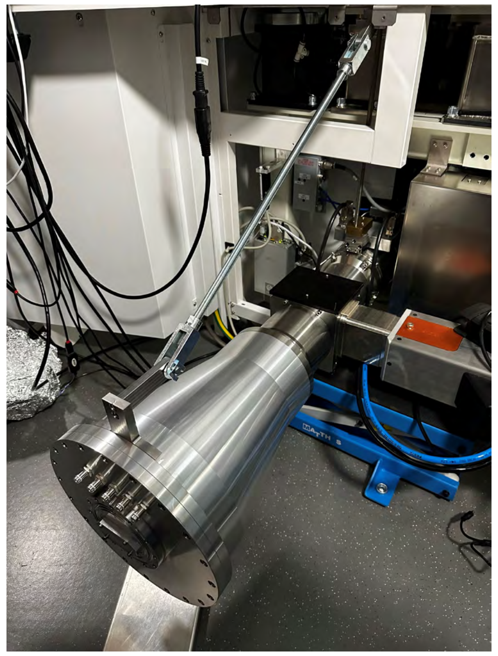

Fig. 2: Photo of the mechanics for testing different detectors installed on the JEOL JEM F200 (S)TEM.

Results

The results of the initial characterization with photons confirm the high quality and good uniformity of the GaAs:Cr sensors provided by DECTRIS. The relevant performance parameters such as the charge transport properties (µ×τ product) of the electrons of 4×10^{-4} cm²/V meet or even exceed the values of state-of-the-art GaAs:Cr from other suppliers [5].

Interpolation tests with photons with GaAs :Cr were successful and the improvement in spatial resolution is clearly visible when comparing the imaging results measured at a microfocus X-ray tube (Fig. 3). The phantom is a lead besom consisting of 0.02 mm thick lead with open tapered lines transparent to X-ray photons. The upper part of Fig. 3 shows the image with the physical 75 µm pixel pitch while in the lower part the same image with a virtual pixel pitch of 25 µm is seen. The Nyquist frequency is the spatial frequency above which aliasing sets in and it is 1/(2×pixel pitch) or 6.67 lp per mm for a 75 µm pixel pitch. As predicted by theory, the besom lines cannot be resolved for spatial frequencies above the Nyquist frequency (indicated by black numbers above the besom), while for the virtual pixel pitch of 25 µm the resolution is clearly pushed to higher spatial frequencies above the physical Nyquist frequency.

In addition to the work at PSI, GaAs:Cr and silicon sensors were installed on a TECNAI F30 TEM at the Johannes Gutenberg University in Mainz to characterize their response to 300 keV electrons. Comparing the sizes of the pixel clusters due to individual, isolated 300 keV electrons (Fig. 4), it can be seen that the size of the average pixel cluster for GaAs:Cr is over 30 % smaller than that of silicon.

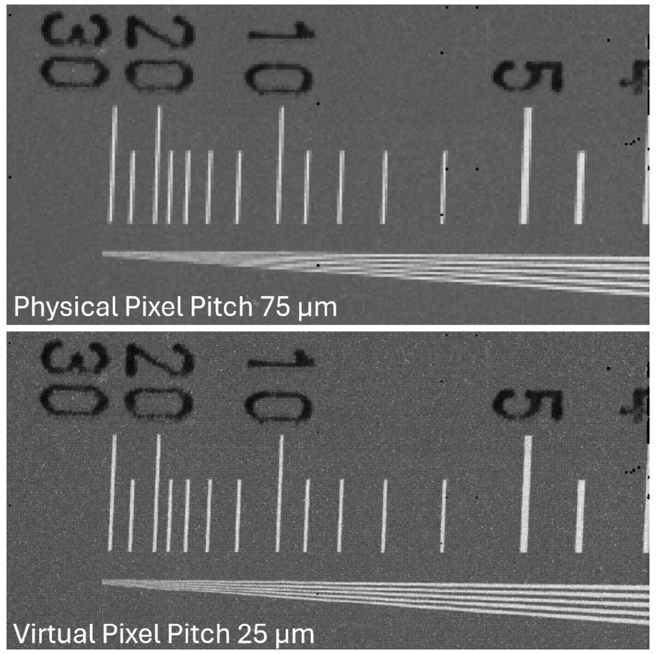

Fig. 3: X-ray image of a phantom with tapered lead lines to determine the spatial resolution. The black numbers on top are an indication of the spatial separation of the besom lines below. (top) Image with the native 75 µm pixel pitch (bottom) Interpolated image with a virtual pixel pitch of 25 µm

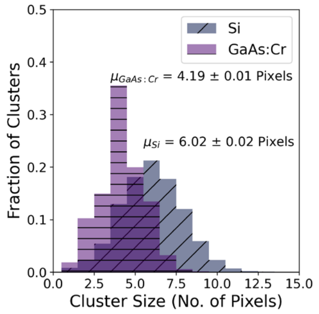

Fig. 4 Histograms showing the distribution of pixel cluster sizes for 300 keV electrons in both GaAs :Cr and silicon sensors. Each dataset consisted of ~ 5 ×10⁵ clusters.

References

[1] C. Broennimann, et al., "The PILATUS 1M detector", Journal of Synchrotron Radiation 13 (2006)

[2] B. D. A. Levin, "Direct detectors and their applications in electron microscopy for materials science", Journal of Physics:Materials 4 (2021)

[3] A. Mozzanica, et al., "The JUNGFRAU detector for applications at synchrotron light sources and XFELs", Synchrotron Radiation News 31(6) (2018)

[4] X. Xie, et al., "Enhancing spatial resolution in MÖNCH for electron microscopy", Journal of Instrumentation, 19(01) (2023)

[5] D. Greiffenberg, et al., "Characterization of chromium compensated GaAs sensors with the charge-integrating JUNGFRAU readout chip

Nanobiocatalysts for PET recycling

Project A19.05: NANOdePET (FHNW Muttenz, FHNW Windisch, INOFEA AG, Muttenz)
Project Leader: P. Shahgaldian
Collaborators: M. Grob, R. Correro

Introduction

Despite growing public awareness and stricter policies, plastic use continues to rise. Beyond significant fossil fuel consumption and greenhouse gas emissions, plastics present a major environmental challenge. Low cost, lightweight, and excellent mechanical properties make polyethylene terephthalate (PET) a polymer of choice for packaging applications. Industrialized countries recycle PET mechanically, but recycled materials' quality declines with every recycling round, limiting reuse. This highlights the need for better PET recycling solutions.

NANOdePET scope

The NANOdePET project builds upon INOFEA's proprietary enzyme protection technology, which encapsulates enzymes within a soft and porous organosilica layer [1]. This protective layer shields enzymes from chemical and physical stressors but also preserves their activity by allowing efficient substrate diffusion. Furthermore, it enables straightforward recovery and reuse of the nanobiocatalyst. A recent breakthrough in this technology was the integration of an artificial chaperone building block, β-cyclodextrin (β-CD), into the protective layer [2]. This significantly improved enzyme stability under various conditions. In the NANOdePET project—a collaboration between HLS, HT, and INOFEA—the primary objective is to further refine and advance the enzyme engineering approach to develop next-generation nanobiocatalysts designedspecifically to degrade PET materials into their monomeric components, namely terephthalic acid (TPA), mono(2-hydroxyethyl) terephthalate (MHET), and bis(2-hydroxyethyl) terephthalate (BHET). Beyond optimizing enzyme performance, the project seeks to benchmark this technology with current standard recycling methods.

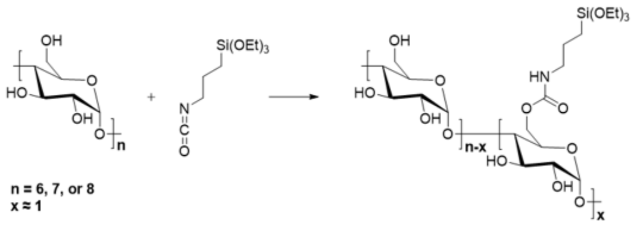

Fig. 1: Synthesis pathway of CD-based (alpha, beta, and gamma; n = 6, 7, and 8, respectively) building block of the organosilica layer.

Results

To produce stable nanobiocatalysts capable of degrading PET, we first focused on improving the building blocks composing the protective layer. We further developed our chaperone-based engineering approach to simultaneously achieve high productivity, selectivity in reaction products, enzyme stability and recycling. We produced a series of novel cyclodextrin derivatives bearing triethoxysilane building blocks (Fig. 1). To assess the effect of CD macrocycle size, we used alpha, beta, and gamma- derivatives composed of 6, 7 and 8 glucose units, respectively. Native CDs were reacted with 3-isocyanatopropyl-tri-methoxysilane to yield CD-TES. Characterization results (1H NMR and elemental analysis) revealed an average of 1.02, 1.23 and 1.08 substituents for alpha, beta, and gamma- CD, respectively.

Next, we selected five esterase enzymes known to have PET hydrolytic activity, namely leaf compost cutinase (LCC), Lipase 9 from the *Bacillus* genus (Lip9), *Candida antarctica* lipase B (CalB), hydrolase from *Candidatus bathyarchaeota* (PET46), and *Humicola insolens* cutinase (HiC). Those enzymes were immobilized and shielded using the synthetic strategy shown in Fig. 2. Among the enzymes tested, Lip9 and PET46 yielded nanobiocatalysts with the highest activity retention, reaching 100% after shielding. LCC was immobilized with 60% activity retention. Immobilization of HiC and CalB posed challenges, but approximately 30% activity retention was achieved for both enzymes. Despite these variations, HiC and LCC demonstrated the highest PET degradation efficiency. Consequently, optimizations for immobilization and shielding were initially prioritized for the LCC enzyme, followed by the HiC enzyme. Additionally, we investigated the incorporation of hydrophobic organosilica building blocks into the protective layer – namely octyl-, propyl-, and benzyl-triethoxysilanes – to enhance interactions between nanobiocatalysts and hydrophobic PET materials, particularly PET foils. This approach aimed to further improve PET degradation efficiency.

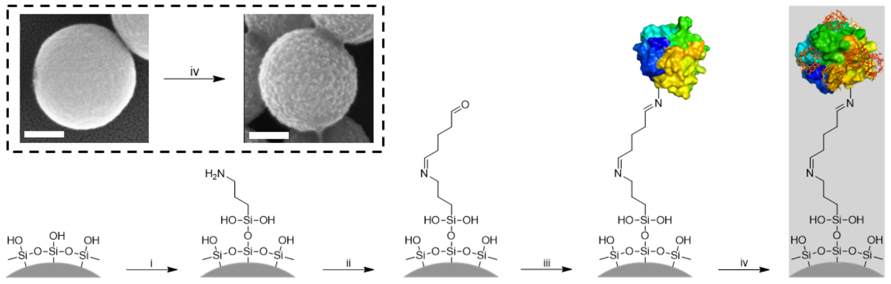

Fig. 2: Principle of enzyme protection with CD (shown in red) embedded in an organosilica layer. The amine functions introduced by the reaction of bare silica particles (i) with aminopropyltriethoxysilane (APTES) are utilized to form imine bonds with glutaraldehyde (ii). Free aldehyde functions of this crosslinker further react with primary amine functions of lysine residues of the protein to covalently conjugate the protein on the surface of the particles (iii). The protective organosilica shield is grown using tetraethyl orthosilicate (TEOS), APTES and CD-TES (iv). The insert shows SEM images of a core SNP, and a shielded SNP obtained after immobilization and layer growth (step iv); scale bars represent 100 nm.

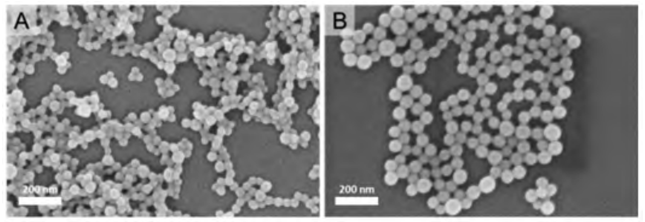

Fig. 3: SEM images of PET particles from Low intrinsic viscosity PET and bottle grade PET (B).

The next step involved conducting PET degradation tests using two types of PET substrates: PET particles with a diameter of 70 nm (Fig. 3) and commercial PET foils. The PET particles were prepared by dissolving various PET materials in hexafluoropropanol, followed by precipitation in water to achieve the desired size.

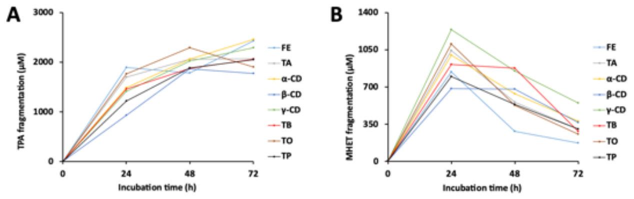

Fig. 4: Production of TPA (A) and MHET (B) fragments of PET particles with soluble enzymes (FE), or enzymes shielded with TEOS and APTES (TA), CD-TES alpha-,beta-, and gamma-CD), benzylsilane (TB), propylsilane (TP), and octylsilane (TO).

PET particles' degradation was investigated by incubating PET nanoparticles with 2 U of biocatalysts (either soluble or shielded LCC enzymes) for 3 days at 50 °C in buffer (pH 8.0). The degradation efficiency was evaluated by quantifying the main degradation fragments – TPA, MHET, and BHET – using HPLC (Fig. 4). The results revealed that after 72 hours, alpha-CD- and gamma-CD-supported nanobiocatalysts outperformed the soluble enzyme in total fragmentation (TPA and MHET), achieving a degradation level 15% higher than the soluble enzyme. The hydrophobic nanobiocatalysts (TB; shielded with benzylethoxy silane and TP; shielded with propylethoxy silane) demonstrated degradation efficacy comparable to the soluble enzyme. A clear trend emerged across all biocatalyst types: TPA content increased steadily, while MHET content gradually decreased after the first 24 hours. This suggests that biocatalysts shifted to converting oligomers into monomers after the initial phase of PET particle degradation, achieving an overall degradation of 80%. The termination of degradation may be attributed to retroinhibition, wherein degradation fragments restrict substrate accessibility. Optimization efforts are ongoing to achieve complete PET degradation. Noteworthy is that activity retention studies showed that nanobiocatalysts maintained 70% of their initial activity after 5 days under degradation conditions. They also retained full activity for 4 days of storage. The soluble enzyme was less stable with activity retention of 60% after the same treatment.

We also studied PET foil degradation at different crystallinity levels (7% and 40%, as determined by differential scanning calorimetry). Foils were incubated with a soluble LCC enzyme or TP nanobiocatalyst at 50 °C (Figure 5). HPLC analyses revealed that PET foils with 7% crystallinity were degraded equally well by both biocatalysts, achieving a degradation efficiency of 22% after 3 days. However, for PET foils with 40% crystallinity, significant differences were observed. The soluble enzyme showed no measurable degradation, whereas the hydrophobic TP nanobiocatalyst exhibited significant degradation levels. This suggests that the enhanced interaction between the nanobiocatalyst and the hydrophobic PET surface favors degradation. This is facilitated by nanobiocatalyst tailored hydrophobic properties. The hydrophobic interaction between the nanobiocatalyst and PET foils was confirmed by SEM analysis after degradation, followed by thorough washing with water (Fig. 5). On 7 % crystalline foils, the affected and degraded areas were clearly visible. On 40 % crystalline foil, the particles remained attached to the PET foil even after washing.

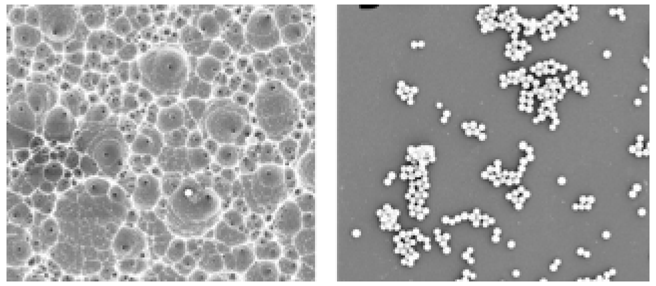

Fig. 5: SEM micrographs of PET foils with 7% (A) and 40% (B) crystallinity after treatment with shielded LCC enzyme within a hydrophobic organosilica layer (TP).

In summary, the first phase of NANOdePET allowed improved PET degradation using nano-engineered enzymes. Work is underway to improve degradation rates and benchmark the technology with currently established methods.

References

[1] M. R. Correro, N. Moridi, H. Schützinger, S. Sykora, E. M. Ammann, et al., "Enzyme Shielding in an Enzyme-thin and Soft Organosilica Layer", Angew. Chem. Int. Ed., 55, 6285 (2016)

[2] A. Foroutan Kalourazi, S. A. Nazemi, A. R. Unniram Parambil, R. Muñoz-Tafalla, P. Vidal, et al., "Exploiting cyclodextrins as artificial chaperones to enhance enzyme protection through supramolecular engineering", Nanoscale, 16, 5123 (2024)

Advancing electron diffraction unveiling the role of hydrogen atoms in protein-ligand interactions through protein nanocrystals

Project A19.07: ProtEDinNanoxtals (Paul Scherrer Institut, University of Basel, ELDICO Scientific AG, Allschwil, and leadXpro AG, Villigen)
Project Leader: V. Panneels
Collaborators: G. Fiorini, R. Cheng, J.P. Abrahams, E. van Genderen, G. Steinfeld, M. Hennig

Introduction & aim

Hydrogen atoms and protons are crucial in biological chemical reactions. However, visualizing them in proteins is challenging. Spectroscopy struggles due to background noise and difficulties in interpretations of spectroscopic shifts, X-ray and conventional electron crystallography need perfect microcrystals and do not reveal the exact positions of very light elements like the hydrogen atoms, and neutron crystallography requires large crystals. In this Nano-Argovia project, we aim to enhance electron diffraction (ED) for studying hydrogen roles in protein-ligand interactions, especially in important membrane proteins. A first milestone was reached with diffraction up to 1.2 Å.

Electron diffraction is ideal because electrons interact strongly with matter, offer a high signal-to-noise ratio, and scatter at hydrogen atoms effectively. ED was already employed in the 1970s, showcasing for the first time the seven tilted alpha-helices of the membrane protein bacteriorhodopsin within the purple membrane of archaebacteria at a resolution of 7Å [1]. Shortly thereafter, X-ray crystallography for proteins gained attraction, overshadowing ED. In contrast to ED, single particle electron microscopy has recently carved out a niche within structural biology for examining large macromolecular complex structures (https://www.ebi.ac.uk/emdb/), and its usage has been growing for approximately the last decade. ED of organic compounds saw a resurgence since 2015 and is now widely utilized in chemistry and pharmacology for analyzing small compounds, especially active pharmaceutical ingredients [2].

State of the art of Electron Diffraction

With recent developments of detectors, sample preparation and general improvements in system and data collection pipelines [3], ED has been demonstrated at average resolution for a few small protein prototypes such as lysozyme and insulin [4, 5], paving the way for measurements on other protein targets. However, the challenge in protein structural determination using 3D-ED lies in both optimizing the sample and the device. The crystals need to be thin enough, in the order of hundreds of nanometers, to reduce multiple scattering events [2]. On the other hand, many scientists and industries harvest already showers of tiny submicron crystals that are too small for X-ray diffraction. Especially for these very small crystals and to overcome beam damage and gaining a high resolution per frame, serial 3D-ED crystallography appears ideal [2].

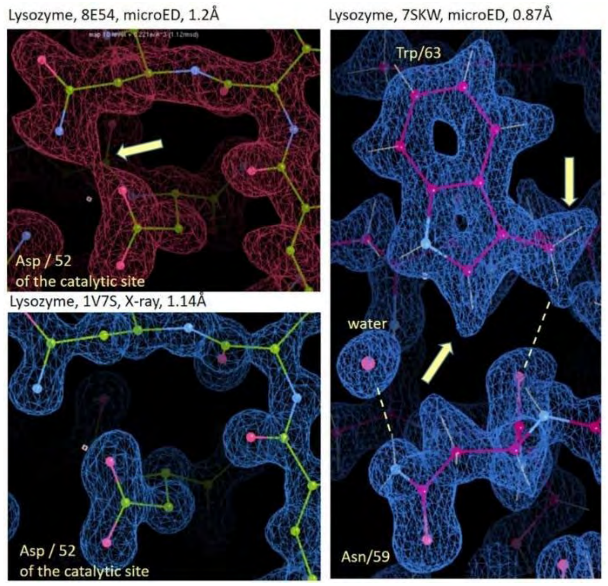

Fig. 1: Comparison of electron density from ED- and X-ray datasets recorded on lysozyme. Upper left : electron density of the catalytic site of lysozyme at a resolution of 1.2Å, obtained with microED (pdb-8E54). The yellow arrows highlight electron density that correspond to a hydrogen atom. Lower left: the same view from a measurement with X-ray diffraction (pdb- 1V7S) at a resolution of 1.14 Å. Right panel: highest resolution data until today (0.87 Å) obtained for lysozyme using microED (pdb-7SKW).

Beyond the ability to collect data on many small crystals, optimizing the settings for serial crystallography, another significant advantage of 3D-ED is the high signal-to-noise ratio and the capability to detect hydrogen atoms [2-5]. **Fig. 1** illustrates a few published electron densities from X-ray versus ED data on lysozyme: the right panel displays density for hydrogen atoms from a lysozyme crystal, with a resolution reaching 0.87 Å.

Compared to the electron density of the 2Fo-Fc map obtained with X-ray diffraction (lower left), which primarily displays the electron density around the larger atoms like carbon, oxygen, and nitrogen, the upper left panel shows additional electron density signals at the presumed hydrogen locations.

Challenging the ED method for proteins

The larger dimensions of proteins, as opposed to small molecules, makes the use of Electron Diffraction for protein structural studies challenging[2]. In addition, protein crystals are fragile and need a cryo-environment. In the ProtEDinNanoxtals consortium, two out of the four partners are specializing in ED and already collaborators in the study referred as [3]: one partner from academia (UniBas) and the other from industry (ELDICO Scientific, AG). The goal is to test protein nanocrystals on both 1) the ED-set-up of a JEOL F-200 Transmission Electron Microscope (TEM) located at the PSI, and 2) a dedicated Electron Diffractometer of radical new design (lens, stage, tilt, no distortion, cryo) belonging to the ELDICO industrial partner. ELDICO was the first company to produce commercially available devices that are dedicated to ED crystallography.

Since half a year, the role of the Nano-Argovia postdoc, expert in crystallography, has been to optimize crystals quality and dimensions for her ED -measurements at very high resolution and dataset collection on small proteins and later, pharmaceutically relevant targets. First ED measurements have been conducted on the ED setup, based on a JEOL F-200 Transmission Electron Microscope (TEM), that is owned by Basel University and housed in the BIO department of the PSI. Micron-sized crystals, achieving resolutions up to 1.6Å (X-ray diffraction data collected by us at the European Synchrotron Research Facility, ESRF), were used for initial ED experiments with minimal basic preparation methods aimed at reducing the crystals size to sub-micron. The crystals diffracted electrons to a higher resolution than X-rays, up to 1.2 Å when assessed on the TEM (**Fig 2**). The next step towards collecting a complete dataset requires now the generation of optimized nanocrystal(s) in order to achieve a size of low hundreds of nanometers. However, many different improvements will also be necessary at the electron microscope, tuning the electron beam shape, testing different energies, ensure a stable location of the sample, testing different detectors and automatizing data collection.

Summary and Outlook

ED has the potential to deliver diffraction signals at very high resolution, with enhanced contrast of light elements - most importantly for hydrogen. In our consortium, we collaborate, exchange experience, and collect data from crystals that may have to be precisely nano-shaped by the primary academic partner (PSI) using cryo- FIB milling. In the next phase, we will also engage with and acquire data from specific proteins of interest from the drug discovery industrial partner LeadXpro, AG.

Monthly knowledge transfer is promoted by exchanges within the network from ED-measurements of protein nanocrystals with electron microscopes to the electron diffractometer team and the pharma partner. This collaborative approach is aimed at broadening the expertise across both academia and industry, driving forward our understanding and capabilities in ED and protein crystallography in Switzerland.

The postdoc G. Fiorini is being trained to independently acquire data on the JEOL F-200 at the PSI and is gaining experience on data collection and processing with other ED-devices from abroad. Partially disordered crystals will be scanned with a narrower parallel electron beam to tackle local disorder and imperfections.

SNI is thereby supporting forefront ED methods development and research in structural biology, following the successful use of it in material science and small drug compounds.

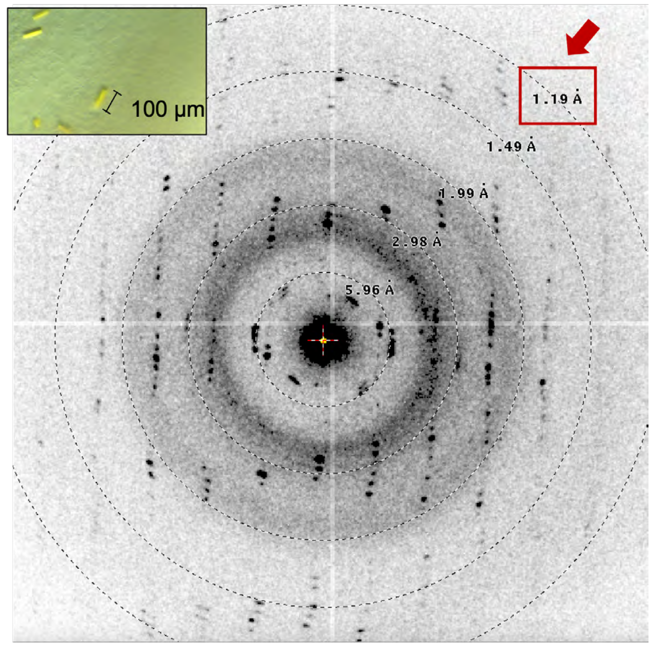

Fig. 2: Electron diffraction images of protein crystals measured at the F200 electron microscope and picture showing the protein crystals (inset) prior to dimension optimization.

References

[1] Henderson, R. & Unwin, P. N. Three-dimensional model of purple membrane obtained by electron microscopy. Nature 257, 28-32 (1975).

[2] Gemmi, M. et al. 3D Electron Diffraction: The Nanocrystallography Revolution. ACS Cent Sci 5, 1315-1329 (2019).

[3] T. Gruene et al Rapid Structure Determination of Microcrystalline Molecular Compounds Using Electron Diffraction. Angew. Chem. Int. Ed. 2018, 57, 16313.

[4] Clabbers, M. T. B. et al. Protein structure determination by electron diffraction using a single three-dimensional nanocrystal. Acta Crystallogr D Struct Biol 73, 738-748 (2017).

[5] Palatinus. Hydrogen positions in single nanocrystals revealed by electron diffraction. Science 355,166-(2017).

Small but mighty – zirconia nanostructures

Project A19.11: ZIRYT (University of Basel, FHNW Muttenz, Straumann Group, Basel)
Project Leader: N. Rohr
Collaborators: A.G. Guex, M. de Wild, R. Wagner

Nanostructures on zirconia dental implants

For dental and orthopaedic implants, titanium-based materials are considered gold standard with successful osseointegration and minimal failure rates. Promising ceramic solutions have emerged to meet patient-specific demands for improved aesthetics or to avoid aversions to metallic implants. Zirconia (ZrO_2) is a high-strength oxide ceramic that is used as implant material as well as for patient-specific restorations on dental implants and natural teeth.
Once inserted to the oral cavity, the material is in direct contact with human hard and soft tissue and exposed to thermal, (bio)chemical, and mechanical loads. This complex environment imposes significant biological demands on the design of dental implant materials, with surfaces of zirconia to be structured to a) provide an ideal environment to promote cell growth and attachment of fibroblasts and keratinocytes in the gingival region, b) induce differentiation of bone progenitor cells and facilitate osseointegration in the endosseous part without pronounced inflammatory response, and c) to potentially inhibit bacterial attachment along the entire implant surface (Fig. 1).

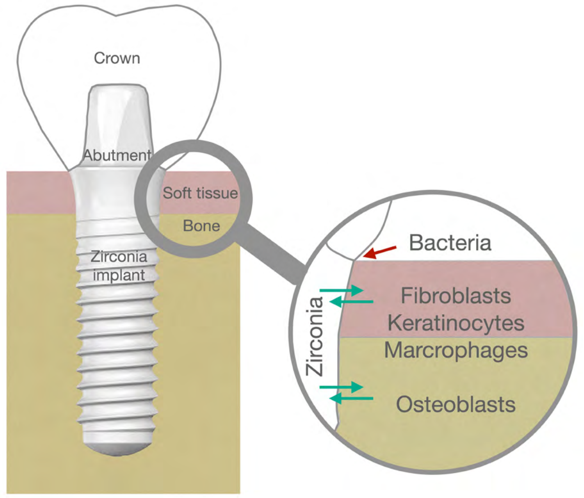

Fig. 1: The surface of zirconia dental implants is in direct contact with the bone and soft tissue, hence the material-cell interaction is crucial for long-term integration.

To achieve optimal biological interaction, major emphasis has been placed on the topographical surface characteristics of ceramic implants. Traditional structuring approaches used by dental implant manufacturers are sandblasting, acid-etching, laser-ablation or by additive sintering of a ceramic slurry [1]. However, those production steps are hazardous due to the high acid concentration and temperatures needed to etch zirconia, labor intense, reduce mechanical strength and significantly increase the final costs for zirconia implants. Therefore, it is of high interest to simplify the production steps without loss of function and performance.
Zirconia is a polymorphic material as it appears in three crystal phases: monoclinic, tetragonal, and cubic. The presence of each crystal phase is mainly influenced by the particle size of the un-sintered material, thermal treatment and dopants added to the material. Crystal phases of zirconia are metastable, therefore stress induction by thermal, hydrothermal or mechanical loading can result in spontaneous phase transformations [2]. The most common dopant used with zirconia in dentistry is yttria (Y_2O_3). The addition of 3 mol% yttria stabilizes zirconia mainly in the tetragonal phase. The addition of 4 mol% or 5 mol% to zirconia has been introduced to increase the grain size and thus the translucency, and therefore improve the aesthetical appearance in the oral cavity. An increase in yttria concentration however reduces the tetragonal phase ratio and increases the cubic proportion, reducing strength. Additionally, the existing crystallographic phase also influences the nanostructure, which in turn affects the surface topography after heat treatment: The growth of grains is equipping the material surface with a defined nano- (20 nm) to microstructure (3 µm) without the need for hazardous treatment protocols.

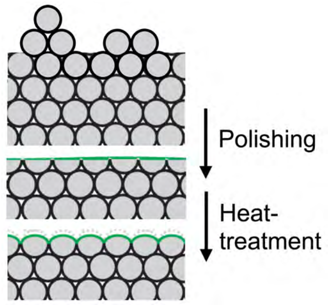

Fig. 2: Effect of polishing and heat-treatment on grain- and surface-structure of zirconia.

Controlling the surface topography and evaluate the effect on mechanical and biological properties is of high interest to find the optimal surface finish for zirconia and its wide applications in dentistry. Hence, the aim of the ZIRYT project is to understand the underlying mechanisms of how crystallinity, yttria dopant concentration and heat-treatment affect the nanostructure, and ultimately osteogenesis, soft tissue integration and immune reaction.
Within the first year of the ZIRYT project we produced disk-shaped specimens out of four different zirconia materials with varying yttria contents. Three different surfaces were created by sintering, subsequent polishing, or polishing and heat-treatment (Fig. 2).

By characterizing the chemical, topographical, mechanical and crystallographic properties of the materials with the different surface treatments, we were able to gain an in-depth understanding of the effects of surface treatments and initial material composition on nanostructured zirconia surfaces. Specimens that were polished and subsequently heat-treated displayed a smooth surface with varying nanostructures (S_a in the range of ~5 to 15 nm) due to the re-appearance of the crystal grains (Fig. 3) as observed in atomic force microscope (AFM) images. A positive correlation was observed between grain size and yttria content, with increasing yttria concentrations yielding progressively larger grains.

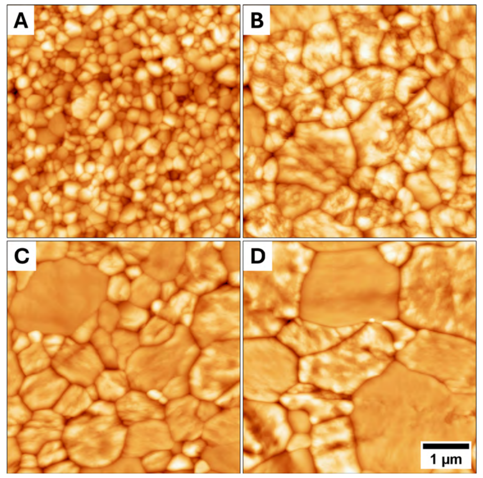

Fig. 3: AFM images showing larger grain sizes for zirconia with higher yttria content. A) and B) are zirconia materials containing 3 mol% yttria, while C) contains 4 mol% and D) 5 mol%.

By analyzing the crystal phase composition with X-ray diffraction (XRD), a higher tetragonal phase (80%) was observed in 3 mol% yttria-doped zirconia, compared to 4 or 5 mol% yttria-doped zirconia (70%). The yttria-content as well as the different surface treatments also affected mechanical properties of the materials. When conducting scratch testing, chipping of the 4-5 mol% yttria materials occurred (Fig. 4), which was not observed on the other materials.

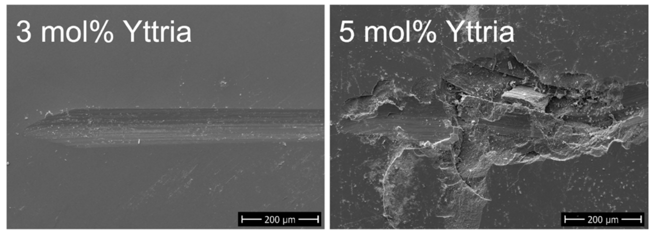

Fig. 4: Scanning electron microscope image of zirconia surfaces after scratch-testing, revealing chipping for the 5 mol% yttria material next to the scratch, while the 3 mol% material remained intact.

The polishing procedure increased biaxial flexural strength, while it was again slightly reduced after heat-treatment. Weibull analysis revealed that highest strength and reliability is achieved for materials with 3 mol% yttria. Surprisingly, hardness HV1 was not affected by the yttria content and the heat-treatment.
Subsequently, those surfaces were evaluated in cell culture using human gingival fibroblasts (HGF-1). Initial cell spreading observed after 4 hours did not reveal contact guidance by the grain structure (Fig. 5). Ongoing experiments focus on the culture of osteogenic precursor cells to gain a first understanding of the osseointegration potential of these materials.

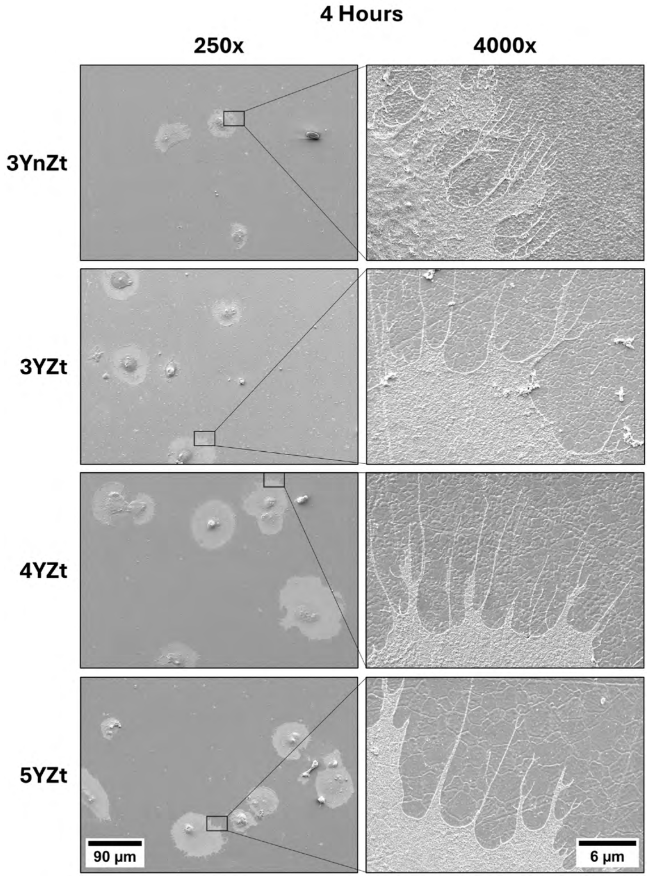

Fig. 5: Scanning electron microscope images of HGF-1 cells fixed after 4 hours on zirconia with varying in yttria content.

In summary, our first-year results indicate a strong dependence of surface topography on yttria content and process parameters, allowing to control the interface for cell or tissue adhesion upon implantation. Combined, these results underpin our initial hypothesis that cell response can be controlled by distinct zirconia chemical composition and heat-treatment. This paves the way towards industrial translation of heat-treated zirconia implants and restorations to achieve tight hard and soft tissue adhesion. As main targets in 2025, we will investigate the immune response and further exploit injection-molding as a new avenue for zirconia implant production, as this is currently the most promising technique to lower costs and increase efficiency. The applicability of the "best" surface topography found in this project to injection-molded specimens will be targeted in the second year.

References

[1] F. H. Schünemann, et al., "Zirconia surface modifications for implant dentistry", Mater Sci Eng C 98, 1294-305 (2019)

[2] S-H. Guan, et al., "Energy landscape of zirconia phase transitions", J Am Chem Soc 137, 8010-3(2015)

Publication list

Ahn, Seungkuk, Akanksha Jain, Krishna Chaitanya Kasuba, Makiko Seimiya, Ryoko Okamoto, Barbara Treutlein, and Daniel J. Müller. “Engineering Fibronectin-Templated Multi-Component Fibrillar Extracellular Matrices to Modulate Tissue-Specific Cell Response.” Biomaterials 308 (July 1, 2024): 122560. https://doi.org/10.1016/j.biomaterials.2024.122560.

Alter, Claudio Luca, Claudia Lotter, Ramya Deepthi Puligilla, Jan Stephan Bolten, Jaroslaw Sedzicki, Jason Marchese, Valentin Schittny, et al. “Nano Plasma Membrane Vesicle-Lipid Nanoparticle Hybrids for Enhanced Gene Delivery and Expression.” Advanced Healthcare Materials 14, no. 1 (2025): 2401888. https://doi.org/10.1002/adhm.202401888.

Apostolidis, P., B. J. Villis, J. F. Chittock-Wood, J. M. Powell, A. Baumgartner, V. Vesterinen, S. Simbierowicz, J. Hassel, and M. R. Buitelaar. “Quantum Paraelectric Varactors for Radiofrequency Measurements at Millikelvin Temperatures.” Nature Electronics 7, no. 9 (September 2024): 760–67. https://doi.org/10.1038/s41928-024-01214-z.

Astasov-Frauenhoffer, Monika, Laurent Marot, Fabien Sanchez, Roland Steiner, Birgit Lohberger, Michael M. Bornstein, Raphael S. Wagner, Sebastian Kühl, and Khaled Mukaddam. “Effects of Nanomodified Titanium Surfaces Considering Bacterial Colonization and Viability of Osteoblasts and Fibroblasts.” Journal of Biomedical Materials Research Part A 112, no. 12 (2024): 2160–69. https://doi.org/10.1002/jbm.a.37768.

Bagani, Kousik, Andriani Vervelaki, Daniel Jetter, Aravind Devarakonda, Märta A. Tschudin, Boris Gross, Daniel G. Chica, et al. “Imaging Strain-Controlled Magnetic Reversal in Thin CrSBr.” Nano Letters 24, no. 41 (October 16, 2024): 13068–74. https://doi.org/10.1021/acs.nanolett.4c03919.

Budakian, Raffi, Amit Finkler, Alexander Eichler, Martino Poggio, Christian L Degen, Sahand Tabatabaei, Inhee Lee, et al. “Roadmap on Nanoscale Magnetic Resonance Imaging.” Nanotechnology 35, no. 41 (July 2024): 412001. https://doi.org/10.1088/1361-6528/ad4b23.

Carulla, Maria, Rebecca Barten, Filippo Baruffaldi, Anna Bergamaschi, Giacomo Borghi, Maurizio Boscardin, Martin Brückner, et al. “Quantum Efficiency Measurement and Modeling of Silicon Sensors Optimized for Soft X-Ray Detection.” Sensors 24, no. 3 (January 2024): 942. https://doi.org/10.3390/s24030942.

Cerioli, Nicola, Wissem Bououdina, Alessandro Mereu, Evangelos Natsaridis, Jeannette Salsetta, Agata Cova, Gianpiero Lupoli, et al. “Reprogramming the Melanoma and Immunosuppressive Myeloid Cells with Esomeprazole-Loaded PLGA Nanoparticles.” iScience 28, no. 1 (January 17, 2025). https://doi.org/10.1016/j.isci.2024.111559.

Chahib, Outhmane, Yuling Yin, Jung-Ching Liu, Chao Li, Thilo Glatzel, Feng Ding, Qinghong Yuan, Ernst Meyer, and Rémy Pawlak. “Probing Charge Redistribution at the Interface of Self-Assembled Cyclo-P5 Pentamers on Ag(111).” Nature Communications 15, no. 1 (August 2, 2024): 6542. https://doi.org/10.1038/s41467-024-50862-4.

Chakraborti, Himadri, Cosimo Gorini, Angelika Knothe, Ming-Hao Liu, Péter Makk, François D Parmentier, David Perconte, et al. “Electron Wave and Quantum Optics in Graphene.” Journal of Physics: Condensed Matter 36, no. 39 (July 2024): 393001. https://doi.org/10.1088/1361-648X/ad46bc.

Chang, Cynthia Sin Ting, Marcus Wyss, Michal Andrzejewski, Geoffrey Darut, Lukas Graf, Vladimir Novak, Margie Olbinado, et al. “Microstructures, Phase and Mechanical Characterisation of Al2O3-ZrO2-TiO2 Coating Produced by Atmospheric Plasma Spraying.” Open Ceramics 20 (December 1, 2024): 100698. https://doi.org/10.1016/j.oceram.2024.100698.

Cheung, L. Y., R. Haller, A. Kononov, C. Ciaccia, J. H. Ungerer, T. Kanne, J. Nygård, et al. “Photon-Mediated Long-Range Coupling of Two Andreev Pair Qubits.” Nature Physics 20, no. 11 (November 2024): 1793–97. https://doi.org/10.1038/s41567-024-02630-w.

Christensen, D V, U Staub, T R Devidas, B Kalisky, K C Nowack, J L Webb, U L Andersen, et al. “2024 Roadmap on Magnetic Microscopy Techniques and Their Applications in Materials Science.” Journal of Physics: Materials 7, no. 3 (June 2024): 032501. https://doi.org/10.1088/2515-7639/ad31b5.

Ciaccia, Carlo, Roy Haller, Asbjørn C. C. Drachmann, Tyler Lindemann, Michael J. Manfra, Constantin Schrade, and Christian Schönenberger. “Charge-4e Supercurrent in a Two-Dimensional InAs-Al Superconductor-Semiconductor Heterostructure.” Communications Physics 7, no. 1 (January 22, 2024): 1–8. https://doi.org/10.1038/s42005-024-01531-x.

Dönges, Laura, Atharva Damle, Andrea Mainardi, Thomas Bock, Monica Schönenberger, Ivan Martin, and Andrea Barbero. “Engineered Human Osteoarthritic Cartilage Organoids.” Biomaterials 308 (July 1, 2024): 122549. https://doi.org/10.1016/j.biomaterials.2024.122549.

Erbe, M., R. Berrazouane, S. Geyer, L. Stasi, F. van der Brugge, G. Gras, M. Schmidt, et al. “Mo-Si Superconducting Nanowire Single-Photon Detectors on $\mathrm{Ga}\mathrm{As}$.” Physical Review Applied 22, no. 1 (July 29, 2024): 014072. https://doi.org/10.1103/PhysRevApplied.22.014072.

Feng, Qingzhou, Martin Saladin, Chunxiang Wu, Eason Cao, Wei Zheng, Amy Zhang, Pushpanjali Bhardwaj, et al. “Channel Width Modulates the Permeability of DNA Origami–Based Nuclear Pore Mimics.” Science Advances 10, no. 46 (November 13, 2024): eadq8773. https://doi.org/10.1126/sciadv.adq8773.

Ferraresi, Lorenzo J. A., Gökhan Kara, Nancy A. Burnham, Roman Furrer, Dmitry N. Dirin, Fabio La Mattina, Maksym V. Kovalenko, Michel Calame, and Ivan Shorubalko. “AFM-IR of Electrohydrodynamically Printed PbS Quantum Dots: Quantifying Ligand Exchange at the Nanoscale.” Nano Letters 24, no. 35 (September 4, 2024): 10908–14. https://doi.org/10.1021/acs.nanolett.4c02631.

Foroutan Kalourazi, Ali, Seyed Amirabbas Nazemi, Ajmal Roshan Unniram Parambil, Manuel Ferrer, S. Shirin Shahangian, and Patrick Shahgaldian. “Exploring the Potential of Various Cyclodextrin-Based Derivatives in Enzyme Supramolecular Engineering.” ChemBioChem n/a, no. n/a (n.d.): e202400840. https://doi.org/10.1002/cbic.202400840.

Glover, Hannah, Torben Saßmannshausen, Quentin Bertrand, Matilde Trabuco, Chavdar Slavov, Arianna Bacchin, Fabio Andres, et al. “Photoswitch Dissociation from a G Protein-Coupled Receptor Resolved by Time-Resolved Serial Crystallography.” Nature Communications 15, no. 1 (December 30, 2024): 10837. https://doi.org/10.1038/s41467-024-55109-w.

Goossens, Eline, Loren Deblock, Lisa Caboor, Dietger Van den Eynden, Iván Josipovic, Pablo Reyes Isaacura, Elizaveta Maksimova, et al. “From Corrosion Casting to Virtual Dissection: Contrast-Enhanced Vascular Imaging Using Hafnium Oxide Nanocrystals.” Small Methods 8, no. 10 (2024): 2301499. https://doi.org/10.1002/smtd.202301499.

Grätzer, Tobias, Manuel Zeyen, Daniel Hug, and Bojan Resan. “Red Diode-Pumped SESAM and Kerr-Lens Modelocked Alexandrite Lasers.” Optics Express 32 (December 11, 2024): 47033–40. https://doi.org/10.1364/OE.542834.

Grisan Qiu, Y Y, P Biasin, P Mantegazza, S Baronio, M Heinrich, M K Muntwiler, and E Vesselli. “Seeking Borophene on Ni3Al(111): An Experimental Characterization of Boron Segregation and Oxidation.” Journal of Physics: Materials 7, no. 2 (February 2024): 025004. https://doi.org/10.1088/2515-7639/ad278c.

Heuberger, Lukas, Maria Korpidou, Ainoa Guinart, Daniel Doellerer, Diego Monserrat López, Cora-Ann Schoenenberger, Daela Milinkovic, Emanuel Lörtscher, Ben L. Feringa, and Cornelia G. Palivan. “Photoreceptor-Like Signal Transduction Between Polymer-Based Protocells.” Advanced Materials 37, no. 3 (2025): 2413981. https://doi.org/10.1002/adma.202413981.

Hinaut, Antoine, Sebastian Scherb, Xuelin Yao, Zhao Liu, Yiming Song, Lucas Moser, Laurent Marot, et al. “Stable Au(111) Hexagonal Reconstruction Induced by Perchlorinated Nanographene Molecules.” The Journal of Physical Chemistry C 128, no. 44 (November 7, 2024): 18894–900. https://doi.org/10.1021/acs.jpcc.4c03812.

Hiret, Paul, Patrik Tognina, Eric Faudot, Roland Steiner, Artem Dmitriev, Laurent Marot, and Ernst Meyer. “Variations of Plasma Potential in RF Discharges with DC-Grounded Electrode.” Plasma Sources Science and Technology 33, no. 7 (July 2024): 075019. https://doi.org/10.1088/1361-6595/ad6691.

Huang, Shuyu, Zhiyong Wei, Zaoqi Duan, Chengdong Sun, Yongkang Wang, Yi Tao, Yan Zhang, et al. “Reexamination of Damping in Sliding Friction.” Physical Review Letters 132, no. 5 (January 30, 2024): 056203. https://doi.org/10.1103/PhysRevLett.132.056203.

Huang, Wenhao, Tathagata Paul, Mickael L Perrin, and Michel Calame. “Eliminating the Channel Resistance in Two-Dimensional Systems Using Viscous Charge Flow.” 2D Materials 11, no. 3 (April 2024): 033001. https://doi.org/10.1088/2053-1583/ad3e09.

Hug, Daniel, Andreas Dax, Alexandre Trisorio, Romain Carreto, Thomas Südmeyer, and Bojan Resan. “Thermal Lensing and Small Signal Gain Measurements in a Pulsed Blue Diode Pumped Ti:Sapphire Amplifier at Room Temperature.” Optics Express 32, no. 22 (October 21, 2024): 39887–95. https://doi.org/10.1364/OE.536823.

Jani, Hariom, Jack Harrison, Sonu Hooda, Saurav Prakash, Proloy Nandi, Junxiong Hu, Zhiyang Zeng, et al. “Spatially Reconfigurable Antiferromagnetic States in Topologically Rich Free-Standing Nanomembranes.” Nature Materials 23, no. 5 (May 2024): 619–26. https://doi.org/10.1038/s41563-024-01806-2.

Kalourazi, Ali Foroutan, Seyed Amirabbas Nazemi, Ajmal Roshan Unniram Parambil, Ruben Muñoz-Tafalla, Paula Vidal, S. Shirin Shahangian, Victor Guallar, Manuel Ferrer, and Patrick Shahgaldian. “Exploiting Cyclodextrins as Artificial Chaperones to Enhance Enzyme Protection through Supramolecular Engineering.” Nanoscale 16, no. 10 (2024): 5123–29. https://doi.org/10.1039/D3NR06044F.

Kapinos, Larisa E., Joanna Kalita, Elena Kassianidou, Chantal Rencurel, and Roderick Y. H. Lim. “Mechanism of Exportin Retention in the Cell Nucleus.” Journal of Cell Biology 223, no. 2 (January 19, 2024): e202306094. https://doi.org/10.1083/jcb.202306094.

Kara, Gökhan, Patrik Rohner, Erfu Wu, Dmitry N. Dirin, Roman Furrer, Dimos Poulikakos, Maksym V. Kovalenko, Michel Calame, and Ivan Shorubalko. “Scaling of Hybrid QDs-Graphene Photodetectors to Subwavelength Dimensions.” ACS Photonics 11, no. 6 (June 19, 2024): 2194–2205. https://doi.org/10.1021/acsphotonics.3c01759.

Kaur, Yashpreet, Saeko Tachikawa, Milo Yaro Swinkels, Miquel López-Suárez, Matteo Camponovo, Alicia Ruiz Caridad, Wonjong Kim, Anna Fontcuberta i Morral, Riccardo Rurali, and Ilaria Zardo. “Thermal Rectification in Telescopic Nanowires: Impact of Thermal Boundary Resistance.” ACS Applied Materials & Interfaces 17, no. 1 (January 8, 2025): 1883–91. https://doi.org/10.1021/acsami.4c14920.

Kroonen, Camiel C. E., Antoine Hinaut, Adriano D’Addio, Alessandro Prescimone, Daniel Häussinger, Gema Navarro-Marín, Olaf Fuhr, Dieter Fenske, Ernst Meyer, and Marcel Mayor. “Toward Molecular Textiles: Synthesis and Characterization of Molecular Patches.” Chemistry – A European Journal 30, no. 69 (2024): e202402866. https://doi.org/10.1002/chem.202402866.

Le Bohec, Mickaël, Roland Steiner, Hiroki Natsume, Shin Kajita, Marwa Ben Yaala, Laurent Marot, and Marie-Hélène Aumeunier. “Relationship between Topographic Parameters and BRDF for Tungsten Surfaces in the Visible Spectrum.” Optik 303 (May 1, 2024): 171750. https://doi.org/10.1016/j.ijleo.2024.171750.

Leisgang, Nadine, Dmitry Miserev, Hinrich Mattiat, Lukas Schneider, Lukas Sponfeldner, Kenji Watanabe, Takashi Taniguchi, Martino Poggio, and Richard J. Warburton. “Exchange Energy of the Ferromagnetic Electronic Ground State in a Monolayer Semiconductor.” Physical Review Letters 133, no. 2 (July 8, 2024): 026501. https://doi.org/10.1103/PhysRevLett.133.026501.

Li, Chao, Vladislav Pokorný, Martin Žonda, Jung-Ching Liu, Ping Zhou, Outhmane Chahib, Thilo Glatzel, et al. “Individual Assembly of Radical Molecules on Superconductors: Demonstrating Quantum Spin Behavior and Bistable Charge Rearrangement.” ACS Nano 19, no. 3 (January 28, 2025): 3403–13. https://doi.org/10.1021/acsnano.4c12387.

Liu, Jung-Ching, Chao Li, Outhmane Chahib, Xing Wang, Simon Rothenbühler, Robert Häner, Silvio Decurtins, et al. “Spin Excitations of High Spin Iron(II) in Metal–Organic Chains on Metal and Superconductor.” Advanced Science n/a, no. n/a (n.d.): 2412351. https://doi.org/10.1002/advs.202412351.

Lotter, Claudia, Evrim Ümit Kuzucu, Jens Casper, Claudio Luca Alter, Ramya Deepthi Puligilla, Pascal Detampel, Juana Serrano Lopez, Alexander Sebastian Ham, and Jörg Huwyler. “Comparison of Ionizable Lipids for Lipid Nanoparticle Mediated DNA Delivery.” European Journal of Pharmaceutical Sciences 203 (December 1, 2024): 106898. https://doi.org/10.1016/j.ejps.2024.106898.

Maffeis, Viviana, Andrea Otter, André Düsterloh, Lucy Kind, Cornelia Palivan, and Sina S. Saxer. “High-Throughput Silica Nanoparticle Detection for Quality Control of Complex Early Life Nutrition Food Matrices.” ACS Omega 9, no. 16 (April 23, 2024): 17966–76. https://doi.org/10.1021/acsomega.3c09459.

Marchiori, Estefani, Giulio Romagnoli, Lukas Schneider, Boris Gross, Pardis Sahafi, Andrew Jordan, Raffi Budakian, et al. “Imaging Magnetic Spiral Phases, Skyrmion Clusters, and Skyrmion Displacements at the Surface of Bulk Cu2OSeO3.” Communications Materials 5, no. 1 (September 28, 2024): 1–12. https://doi.org/10.1038/s43246-024-00647-5.

Mattiat, Hinrich, Lukas Schneider, Patrick Reiser, Martino Poggio, Pardis Sahafi, Andrew Jordan, Raffi Budakian, et al. “Mapping the Phase-Separated State in a 2D Magnet.” Nanoscale 16, no. 10 (March 7, 2024): 5302–12. https://doi.org/10.1039/D3NR06550B.

Mihali, Voichita, Piotr Jasko, Michal Skowicki, and Cornelia G. Palivan. “Controlled Enzymatic Reactions by Programmed Confinement in Clusters of Polymersomes and Janus Nanoparticles.” Materials Today 80 (November 1, 2024): 201–17. https://doi.org/10.1016/j.mattod.2024.08.020.

Mora-Castaño, Gloria, Mónica Millán-Jiménez, Andreas Niederquell, Monica Schönenberger, Fatemeh Shojaie, Martin Kuentz, and Isidoro Caraballo. “Amorphous Solid Dispersion of a Binary Formulation with Felodipine and HPMC for 3D Printed Floating Tablets.” International Journal of Pharmaceutics 658 (June 10, 2024): 124215. https://doi.org/10.1016/j.ijpharm.2024.124215.

Mortelmans, Thomas, Balz Marty, Dimitrios Kazazis, Celestino Padeste, Xiaodan Li, and Yasin Ekinci. “Three-Dimensional Microfluidic Capillary Device for Rapid and Multiplexed Immunoassays in Whole Blood.” ACS Sensors 9, no. 5 (May 24, 2024): 2455–64. https://doi.org/10.1021/acssensors.4c00153.

Niederquell, Andreas, Susanne Herzig, Monica Schönenberger, Edmont Stoyanov, and Martin Kuentz. “Computational Support to Explore Ternary Solid Dispersions of Challenging Drugs Using Coformer and Hydroxypropyl Cellulose.” Molecular Pharmaceutics 21, no. 11 (November 4, 2024): 5619–31. https://doi.org/10.1021/acs.molpharmaceut.4c00592.

Nigro, Arianna, Eric Jutzi, Nicolas Forrer, Andrea Hofmann, Gerard Gadea, and Ilaria Zardo. “High Quality Ge Layers for Ge/SiGe Quantum Well Heterostructures Using Chemical Vapor Deposition.” Physical Review Materials 8, no. 6 (June 5, 2024): 066201. https://doi.org/10.1103/PhysRevMaterials.8.066201.

Nigro, Arianna, Eric Jutzi, Fabian Oppliger, Franco De Palma, Christian Olsen, Alicia Ruiz-Caridad, Gerard Gadea, Pasquale Scarlino, Ilaria Zardo, and Andrea Hofmann. “Demonstration of Microwave Resonators and Double Quantum Dots on Optimized Reverse-Graded Ge/SiGe Heterostructures.” ACS Applied Electronic Materials 6, no. 7 (July 23, 2024): 5094–5100. https://doi.org/10.1021/acsaelm.4c00654.

Parambil, Ajmal Roshan Unniram, Rohan Pokratath, Muhammed Jibin Parammal, Evert Dhaene, Dietger Van den Eynden, Sandor Balog, Alessandro Prescimone, Ivan Infante, Patrick Shahgaldian, and Jonathan De Roo. “Atomically Precise Surface Chemistry of Zirconium and Hafnium Metal Oxo Clusters beyond Carboxylate Ligands.” Chemical Science 15, no. 42 (October 30, 2024): 17380–96. https://doi.org/10.1039/D4SC03859B.

Pereira, Camila Faria de Amorim, Michelle Nonato de Oliveira Melo, Vania Emerich Bucco de Campos, Ivania Paiva Pereira, Adriana Passos Oliveira, Mariana Souza Rocha, João Vitor da Costa Batista, et al. “Self-Nanoemulsifying Drug Delivery System (SNEDDS) Using Lipophilic Extract of Viscum Album Subsp. Austriacum (Wiesb.) Vollm.” International Journal of Nanomedicine 19 (December 31, 2024): 5953–72. https://doi.org/10.2147/IJN.S464508.

Perrin, Mickael L., Anooja Jayaraj, Bhaskar Ghawri, Kenji Watanabe, Takashi Taniguchi, Daniele Passerone, Michel Calame, and Jian Zhang. “Electric Field Tunable Bandgap in Twisted Double Trilayer Graphene.” Npj 2D Materials and Applications 8, no. 1 (February 27, 2024): 1–8. https://doi.org/10.1038/s41699-024-00449-w.

Ranni, Antti, Subhomoy Haldar, Harald Havir, Sebastian Lehmann, Pasquale Scarlino, Andreas Baumgartner, Christian Schönenberger, et al. “Decoherence in a Crystal-Phase Defined Double Quantum Dot Charge Qubit Strongly Coupled to a High-Impedance Resonator.” Physical Review Research 6, no. 4 (November 14, 2024): 043134. https://doi.org/10.1103/PhysRevResearch.6.043134.

Rima, Luca, Christian Berchtold, Stefan Arnold, Andri Fränkl, Rosmarie Sütterlin, Gregor Dernick, Götz Schlotterbeck, and Thomas Braun. “Single and Few Cell Analysis for Correlative Light Microscopy, Metabolomics, and Targeted Proteomics.” Lab on a Chip 24, no. 18 (September 10, 2024): 4321–32. https://doi.org/10.1039/D4LC00269E.

Romankov, Vladyslav, Moritz Bernhardt, Martin Heinrich, Diana Vaclavkova, Katie Harriman, Niéli Daffé, Bernard Delley, et al. “Orientation-Driven Large Magnetic Hysteresis of Er(III) Cyclooctatetraenide-Based Single-Ion Magnets Adsorbed on Ag(100).” Small Science 4, no. 8 (2024): 2400115. https://doi.org/10.1002/smsc.202400115.

Ruggiero, Luigi, Arianna Nigro, Ilaria Zardo, and Andrea Hofmann. “A Backgate for Enhanced Tunability of Holes in Planar Germanium.” Nano Letters 24, no. 42 (October 23, 2024): 13263–68. https://doi.org/10.1021/acs.nanolett.4c03493.

Sanchez, Fabien, Laurent Marot, Artem Dmitriev, Roland Steiner, and Ernst Meyer. “Formation of Nano-Tendril Bundle (NTB) by Evaporation of Tungsten in Neutral Gases.” Fusion Engineering and Design 200 (March 1, 2024): 114187. https://doi.org/10.1016/j.fusengdes.2024.114187.

Scherb, Sebastian, Antoine Hinaut, Yanwei Gu, J.G. Vilhena, Rémy Pawlak, Yiming Song, Akimitsu Narita, Thilo Glatzel, Klaus Müllen, and Ernst Meyer. “The Role of Alkyl Chains in the Thermoresponse of Supramolecular Network.” Small 20, no. 51 (2024): 2405472. https://doi.org/10.1002/smll.202405472.

Sojo-Gordillo, Jose M., Yashpreet Kaur, Saeko Tachikawa, Nerea Alayo, Marc Salleras, Nicolas Forrer, Luis Fonseca, Alex Morata, Albert Tarancón, and Ilaria Zardo. “TEM-Compatible Microdevice for the Complete Thermoelectric Characterization of Epitaxially Integrated Si-Based Nanowires.” Nanoscale Horizons 9, no. 7 (June 24, 2024): 1200–1210. https://doi.org/10.1039/D4NH00114A.

Song, Yiming, Xiang Gao, Rémy Pawlak, Shuyu Huang, Antoine Hinaut, Thilo Glatzel, Oded Hod, Michael Urbakh, and Ernst Meyer. “Non-Amontons Frictional Behaviors of Grain Boundaries at Layered Material Interfaces.” Nature Communications 15, no. 1 (November 2, 2024): 9487. https://doi.org/10.1038/s41467-024-53581-y.

Song, Yiming, Jin Wang, Antoine Hinaut, Sebastian Scherb, Shuyu Huang, Thilo Glatzel, Erio Tosatti, and Ernst Meyer. “Nonmonotonic Velocity Dependence of Atomic Friction Induced by Multiple Slips.” Physical Review Letters 133, no. 13 (September 24, 2024): 136201. https://doi.org/10.1103/PhysRevLett.133.136201.

Thakkar, Pooja, Vitaliy A. Guzenko, Peng-Han Lu, Rafal E. Dunin-Borkowski, Jan Pieter Abrahams, and Soichiro Tsujino. “Electrostatic Interference Control of a High-Energy Coherent Electron Beam Using Three-Element Boersch Phase Shifters.” Japanese Journal of Applied Physics 63, no. 10 (October 2024): 104501. https://doi.org/10.35848/1347-4065/ad7341.

Trippmacher, Simon, Serhiy Demeshko, Alessandro Prescimone, Franc Meyer, Oliver S. Wenger, and Cui Wang. “Ferromagnetically Coupled Chromium(III) Dimer Shows Luminescence and Sensitizes Photon Upconversion.” Chemistry – A European Journal 30, no. 31 (2024): e202400856. https://doi.org/10.1002/chem.202400856.

Tschudin, Märta A., David A. Broadway, Patrick Siegwolf, Carolin Schrader, Evan J. Telford, Boris Gross, Jordan Cox, et al. “Imaging Nanomagnetism and Magnetic Phase Transitions in Atomically Thin CrSBr.” Nature Communications 15, no. 1 (July 17, 2024): 6005. https://doi.org/10.1038/s41467-024-49717-9.

Tsujino, Soichiro, Yohei Sato, Shichao Jia, Michal W. Kepa, Sofia Trampari, and Takashi Tomizaki. “Inertial Mixing of Acoustically Levitated Droplets for Time-Lapse Protein Crystallography.” Droplet 3, no. 3 (2024): e132. https://doi.org/10.1002/dro2.132.

Ungerer, J. H., A. Pally, A. Kononov, S. Lehmann, J. Ridderbos, P. P. Potts, C. Thelander, et al. “Strong Coupling between a Microwave Photon and a Singlet-Triplet Qubit.” Nature Communications 15, no. 1 (February 5, 2024): 1068. https://doi.org/10.1038/s41467-024-45235-w.

Vervelaki, Andriani, Kousik Bagani, Daniel Jetter, Manh-Ha Doan, Tuan K. Chau, Boris Gross, Dennis V. Christensen, Peter Bøggild, and Martino Poggio. “Visualizing Thickness-Dependent Magnetic Textures in Few-Layer Cr2Ge2Te6.” Communications Materials 5, no. 1 (March 19, 2024): 1–8. https://doi.org/10.1038/s43246-024-00477-5.

Vito, G. de, D. M. Koch, G. Raciti, J. M. Sojo-Gordillo, A. Nigro, R. Swami, Y. Kaur, et al. “Suspended Micro Thermometer for Anisotropic Thermal Transport Measurements.” International Journal of Heat and Mass Transfer 224 (June 1, 2024): 125302. https://doi.org/10.1016/j.ijheatmasstransfer.2024.125302.

Weegen, Moritz, Martino Poggio, and Stefan Willitsch. “Coupling Trapped Ions to a Nanomechanical Oscillator.” Physical Review Letters 133, no. 22 (November 25, 2024): 223201. https://doi.org/10.1103/PhysRevLett.133.223201.

Wu, Congyu, Seyed Amirabbas Nazemi, Natascha Santacroce, Jenny A. Sahlin, Laura Suter-Dick, and Patrick Shahgaldian. “Reduction-Responsive Immobilised and Protected Enzymes.” Nanoscale Advances 7, no. 1 (2025): 89–93. https://doi.org/10.1039/D4NA00580E.

Yurgens, Viktoria, Yannik Fontana, Andrea Corazza, Brendan J. Shields, Patrick Maletinsky, and Richard J. Warburton. “Cavity-Assisted Resonance Fluorescence from a Nitrogen-Vacancy Center in Diamond.” Npj Quantum Information 10, no. 1 (November 7, 2024): 1–8. https://doi.org/10.1038/s41534-024-00915-9.

Zannier, V., J. Trautvetter, A. K. Sivan, F. Rossi, D. de Matteis, B. Abad, R. Rurali, L. Sorba, and I. Zardo. “InAs–InP Superlattice Nanowires with Tunable Phonon Frequencies.” Advanced Physics Research 3, no. 6 (2024): 2300157. https://doi.org/10.1002/apxr.202300157.

Žaper, Liza, Peter Rickhaus, Marcus Wyss, Boris Gross, Kai Wagner, Martino Poggio, and Floris Braakman. “Scanning Nitrogen-Vacancy Magnetometry of Focused-Electron-Beam-Deposited Cobalt Nanomagnets.” ACS Applied Nano Materials 7, no. 4 (February 23, 2024): 3854–60. https://doi.org/10.1021/acsanm.3c05470.

Zheng, Han, Luk Yi Cheung, Nikunj Sangwan, Artem Kononov, Roy Haller, Joost Ridderbos, Carlo Ciaccia, et al. “Coherent Control of a Few-Channel Hole Type Gatemon Qubit.” Nano Letters 24, no. 24 (June 19, 2024): 7173–79. https://doi.org/10.1021/acs.nanolett.4c00770.

Protein Partnerships
Protein-protein interactions in human thyroid epithelial cells are visualized using an innovative fluorescence technique (BiFC) (green). This approach highlights the precise cellular localization of the interactions and emphasizes the dynamic complexity of protein partnerships in mammalian cells, bridging the gap between nanotechnology and molecular biology. F-actin (red), DNA (blue). (Image: Ahmed H.H.H. Mahmoud, Biozentrum University of Basel)

About this publication
Design concept: STUDIO NEO
Text and layout: C. Möller and M. Poggio
with support of PIs and PhD students
Translations and proof-reading: UNIWORKS
(Erlangen, Germany)
Images: if not referenced C. Möller

Educating
Talents
since 1460.

University of Basel
Petersplatz 1
4001 Basel
Switzerland

www.unibas.ch

Swiss Nanoscience Institute
University of Basel
Klingelbergstrasse 82
4056 Basel
Switzerland

www.nanoscience.ch